

**A PIEZORESISTIVE MICROCANTILEVER ARRAY
FOR CHEMICAL SENSING APPLICATIONS**

A Dissertation
Presented to
The Academic Faculty

by

Arnab Choudhury

In Partial Fulfillment
of the Requirements for the Degree
Doctor of Philosophy in the
Woodruff School of Mechanical Engineering

Georgia Institute of Technology
December 2007

Copyright 2007 by Arnab Choudhury

**A PIEZORESISTIVE MICROCANTILEVER ARRAY
FOR CHEMICAL SENSING APPLICATIONS**

Approved by:

Dr. Peter J. Hesketh, Advisor
School of Mechanical Engineering
Georgia Institute of Technology

Dr. Jiri Janata
School of Chemistry and Biochemistry
Georgia Institute of Technology

Dr. Levent Degertekin
School of Mechanical Engineering
Georgia Institute of Technology

Dr. Lawrence Bottomley
School of Chemistry and Biochemistry
Georgia Institute of Technology

Dr. Zhoumin Zhang
School of Mechanical Engineering
Georgia Institute of Technology

Dr. Zhiyu Hu
Biosciences Division
Oak Ridge National Laboratory

Date Approved: November 5, 2007 □

To
My parents for life, love and for always being my guiding stars
And to
My brother and all his dreams

ACKNOWLEDGEMENTS

I started my journey through graduate school at Georgia Tech six years ago. These years have been more than just another step on the educational ladder as I'd thought at the start- it has been an opportunity to take a plunge at the deep end and explore whatever I chose to. For this opportunity, I cannot thank my advisor, Dr. Peter Hesketh, enough. Also, while he allowed me to choose my direction with several aspects of this work, he was always very involved in helping me solve various problems related to every aspect of this work. Dr. Hesketh's ability to figure out the cause of problems sitting right under my nose has often left me astounded and his love of science, work ethic, patience (in particular with all the times I've been late with work) and good humor have made this a rewarding endeavor. I'd also like to thank my co-advisor, Dr. Zhiyu Hu with who I've worked very closely on this project and some others. He kept me going with words of encouragement when I came back disappointed from the cleanroom and caution when I was tempted to rush into things. Also the opportunity to work on several different projects with him has been an enriching experience.

I am very grateful to other members of my PhD thesis committee- Dr. Jiri Janata, Dr. Larry Bottomley, Dr. Levent Degertekin and Dr. Zhoumin Zhang for their suggestions and constructive criticism of my work- all of which helped me understand the issues involved better. I am extremely grateful for allowing me extra time while I got my thesis together.

My peers at Georgia Tech were perhaps the greatest fillip to this work and I am extremely grateful to all the people who at various times egged me on and helped my

with different aspects of my thesis. I'd like to thank past and present member of my group, in particular Dr. Rajesh Luharuka, Dr. Heungjoo Shin, Dr. Moses Noh, Dr. Sang Kyung Kim, Zhungchun Peng and Surajit Kumar for their help with almost everything I did and learnt. Also I'd like to thank Krishna Tunga who was my go-to man for all things ANSYS-related. Thanks are also due to numerous cleanroom users- Kianoush Naeli, Houri Johari, Mina Raiszadeh, Karan Kacker, Dr. Yoonsu Choi, Dr. Reza Abdolvand, Logan MacLeod and many others- for their help with various aspects of fabrication. I am immensely grateful to Gary Spinner, Vinh Nyugen, Charlie Suh and other members of the cleanroom staff who have helped me with numerous problems all these years. I'd also like to thank Dr. Siva Gurram, Baris Bicen, Caesar Garcia and Rasim for helping me with various aspects of testing. My early faltering steps at testing of my device were steadied by Guclu Onaran, who has been an immense help all this work. I can hardly begin to thank him for all his time, help and a completely loony sense of humor; Shaolin Soccer and the Turkish Star Wars were definitely a welcome respite from the trials and travails of graduate school. I've also had the opportunity of working with two summer students- Ryan Newcomb and Robin Vujanic- these last two years both of who contributed greatly to this work. Robin put in a lot of enthusiasm and effort in the work on thermal characterization and his inputs in this work have been invaluable.

I'd like to thank all those who've made these years at graduate school enjoyable and complete: my roomies over the years- Manas, Jitesh, Harpreet, Sanjeev, Saketh and Kunal, the gang from ME- Mark, Joe, Logan, Brent, Harry and Kasi (honorary ME) and other pals around GT- Manav, Vikrant, Saurabh, Rithika, Anandita, Dinesh, Anandraj, Deepti and hordes of others at GT and around.

I'd also like thank Papuda and Ruchi babhi, and Chandankaku and Kakima for never letting me feel too far from home. Finally I'd like to thank my parents for forever being supportive of my decisions in life and for being my pillar of strength.

TABLE OF CONTENTS

ACKNOWLEDGEMENTS	IV
LIST OF TABLES	XIII
LIST OF FIGURES	XIV
NOMENCLATURE.....	XXIV
SUMMARY	XXVI
CHAPTER 1: INTRODUCTION.....	1
1.1 Micro Total Analysis Systems.....	3
1.1.1 Elements of a μ TAS.....	4
1.1.2 Sensors and Selectivity	5
1.2 Microcantilever Chemical Sensors.....	6
1.2.1 Piezoresistive Microcantilever Surface Stress Sensing	6
1.3 Scope Of This Dissertation.....	8
1.3.1 Motivation for Study.....	8
1.3.2 Research Objectives.....	9
1.4 Structure Of The Thesis	10
1.5 References.....	11
CHAPTER 2: BACKGROUND AND PREVIOUS WORK.....	14
2.1 Sensor Classification.....	14
2.2 Surface Stress-Based Sensing.....	16
2.2.1 The Phenomenon of Surface Stress	16
2.2.2 Surface Modification for Chemical Sensing.....	18
2.3 Microcantilever Transducers.....	19
2.3.1 Operational Modes.....	20
2.3.2 Methods of Signal Readout.....	20
2.4 Microcantilever-based Chemical and Biochemical Sensing	21
2.4.1 Biosensors	22

2.5	Piezoresistive Microcantilevers for Chemical Sensing	23
2.5.1	Piezoresistance in Silicon	23
2.5.2	Existing Piezoresistive Microcantilevers for Surface Stress Measurement..	24
2.6	Array-based Detection Systems	25
2.7	References	26
CHAPTER 3: MATERIAL DESIGN AND NOISE ISSUES		33
3.1	Elements of Piezoresistive Microcantilever Design	34
3.1.1	Geometry of the Piezoresistive Microcantilevers	34
3.2	Material Design	35
3.2.1	State of Stress in the Microcantilever	36
3.2.2	Effect of Doping on Piezoresistor Response	37
3.3	Sources of Noise in Piezoresistive Microcantilevers	40
3.3.1	Johnson Noise	40
3.3.2	Hooge Noise.....	40
3.3.3	Vibration Noise.....	43
3.3.3.1	Vibration Noise in a Microcantilever-based Piezoresistive Surface Stress Sensor	43
3.3.3.2	Noise in Piezoresistive Readout.....	44
3.3.4	Total System Noise	47
3.4	Effect of Doping Parameters.....	49
3.4.1	Minimum Detectable Stress in Piezoresistive Microcantilevers	50
3.5	Conclusions.....	52
3.6	References.....	52
CHAPTER 4: DESIGN OF THE PμCA.....		54
4.1	Surface Stress Sensitivity	54
4.2	A New Cantilever Bending Model.....	55
4.3	Effect of Geometric Parameters on Surface Stress Response.....	58
4.3.1	Surface Stress Distribution in ANSYS Model.....	59
4.3.2	Effect of Geometric Parameters on Surface Stress Response.....	62
4.3.3	Design Rules for Piezoresistive Microcantilevers	65
4.4	Microfluidic Design.....	66
4.4.1	Design of Flow Cell	66
4.4.2	Other Considerations	68

4.5	Final Device Design	69
4.5.1	Design of Piezoresistive Microcantilever Array.....	69
4.5.2	Matrix of Device Designs.....	69
4.6	Double-Sided Surface Stress Measurement	69
4.6.1	Concept of Double-Sided Sensing.....	69
4.6.2	Design Issues.....	71
4.7	Conclusion	72
4.8	References	73
CHAPTER 5: FABRICATION OF THE PμCA		75
5.1	Materials and Process Flow	75
5.2	PμCA Fabrication	75
5.3	Salient Features of PμCA Fabrication Process	82
5.3.1	Tight control on layer dimensions.....	82
5.3.2	Robust design.....	83
5.4	Fabrication Issues	84
5.4.1	Scheme of Stress Compensation.....	84
5.4.2	Functionalization of Cantilevers.....	88
5.5	Conclusions	90
5.6	References	91
CHAPTER 6: MECHANICAL AND THERMAL CHARACTERIZATION		92
6.1	Mechanical Characterization	92
6.1.1	Measurement of Natural Frequency of Cantilevers.....	92
6.1.2	Measurement of Gauge Factor of Cantilevers.....	93
6.1.2.1	Calculation of Gauge Factor.....	93
6.1.2.2	Experimental Evaluation of Deflection Sensitivity.....	96
6.2	Thermal Characterization	97
6.2.1	Introduction.....	97
6.2.2	Background.....	97
6.2.3	Model for Heat Transfer from Piezoresistive Microcantilevers.....	98
6.2.4	Device Details.....	101
6.2.5	Experimental Design.....	101
6.2.6	Measurement Setup.....	102
6.2.7	Characterization of Measurement Setup.....	103
6.2.7.1	Characterization of the Input Source.....	103

6.2.7.2	Characterization of the Ballast Resistor.....	103
6.2.8	Measurement of Cantilever Resistance.....	105
6.2.9	Thermal Characterization of Microcantilevers	106
6.2.9.1	Thermal Calibration of Devices.....	106
6.2.9.2	DC Calibration.....	109
6.2.9.3	Evaluation of Effective Heat Transfer Coefficient.....	109
6.2.9.4	Cantilever Response to Sinusoidal Inputs.....	111
6.2.9.5	Analysis of Sinusoidal Response.....	113
6.2.10	Measurement in Flow Conditions.....	113
6.2.11	Array Operation	115
6.2.11.1	Demonstration of Array Operation.....	115
6.2.11.2	Thermal Cross-talk in Array	115
6.3	Measurement Space for Piezoresistance Measurement	116
6.4	References.....	118
CHAPTER 7: MEASUREMENT SETUP.....		120
7.1	Electrical Measurement.....	120
7.1.1	PSD Methods for Noise Reduction.....	121
7.1.1.1	Noise Measurement with PSD Methods.....	122
7.1.2	Electrical Measurement Setup	123
7.1.3	External Noise Sources.....	127
7.2	Chemical Flow Setup	129
7.2.1	Chemical Flow Cell	132
7.3	Experimental Protocol.....	133
7.4	Conclusions.....	134
7.5	References.....	135
CHAPTER 8: CHEMICAL SENSING EXPERIMENTS		136
8.1	Background	136
8.1.1	Surface Stress on Gold.....	136
8.1.2	Reaction Kinetics of Alkanethiols on Gold	137
8.2	Chemical Sensing with Microcantilevers.....	137
8.2.1	General Microcantilever Response.....	137
8.2.1.1	Response to 6-Mercapto-1-hexanol	138
8.2.2	Effect of Cantilever Geometry on Surface Stress Response.....	141
8.2.2.1	Effect of Clamping Distance.....	141
8.2.2.2	Effect of Cantilever Length	142
8.2.3	Effect of Resistor Length.....	143

8.3	Other Chemical Sensing Schemes	144
8.3.1	Single and Double-Sided Sensing.....	144
8.3.2	Chemical Sensing with a Thermal Array.....	145
8.3.2.1	Background.....	145
8.3.2.2	Estimation of Reaction Parameters.....	146
8.3.2.3	Thermal Array Measurement: Results.....	147
8.3.2.4	Thermal Array Measurement: Analysis.....	150
8.3.2.5	Thermal Array Measurement: Limitations and Recommendations.....	151
8.4	Conclusions.....	152
8.5	References.....	153
CHAPTER 9: SUMMARY AND RECOMMENDATIONS.....		155
9.1	Summary.....	155
9.2	Research Contributions.....	156
9.2.1	Design.....	156
9.2.2	Fabrication.....	156
9.2.3	Thermal Characterization.....	157
9.2.4	Measurement.....	157
9.2.5	Application.....	158
9.3	Recommendations for Improvement of Sensor Performance	158
9.4	Recommendations for Future Work.....	159
9.5	References.....	162
APPENDIX A: DESIGN DETAILS.....		163
A.1	Masks Layouts for PμCA.....	163
APPENDIX B: FABRICATION DETAILS.....		166
B.1	Process Flow	166
B.2	Important Photoresist Recipes.....	172
APPENDIX C: THERMAL MODELS.....		173
C.1	Closed-Form Transient Solution for Microcantilever Heating	173
C.1.1	Sinusoidal input	174
C.2	References.....	177

APPENDIX D: ELECTRICAL CIRCUIT LAYOUT	178
D.1 Electrical Circuit Layout of Measurement Box	178

LIST OF TABLES

Table 2.1 Existing piezoresistive microcantilever sensors for surface stress detection. ..	25
Table 3.1. Longitudinal (π_x) and transverse (π_y) piezocoefficients in [110] silicon ^a . Surface stress sensitivities for various boundary conditions show the advantage of n-type doping.	37
Table 4.1 Matrix of cantilever designs. Cantilever length, piezoresistor length and distance from the clamped end of the cantilever were varied.....	69
Table 5.1. Specifications for SOI wafer. ^a	75
Table 5.2. Mechanical properties and residual stress in various layers of the cantilever.	87
Table 6.1 Design parameters of cantilever chips used in experiments. Cantilevers have been referred to as ‘Cant’ in this table. All dimensions are in microns.....	101

LIST OF FIGURES

Figure 1.1 The tricorder from the TV series Star Trek [8]. This handheld device could be used for chemical, radiation and biological sensing.	3
Figure 1.2 Components of a micro total analysis system (μ TAS).	4
Figure 1.3 Scheme of surface stress detection with a piezoresistive microcantilever. π_L and π_T are the piezoresistive coefficient of the piezoresistor in the longitudinal and transverse direction. Generally the longitudinal direction is taken along the axis of the cantilever.	6
Figure 1.4 Reference cantilevers allow for filtering of noise in the measurement. The analyte binds selectively to the functionalized cantilever on the left. No binding takes place on the reference cantilever on the right.	7
Figure 2.1 Scheme for chemical sensing: The transducer converts the chemical signal into an analytically useful signal.	15
Figure 2.2 Chemical sensing and biosensing methods [4].	16
Figure 2.3 Three methods of analyte interaction with the modified surface of the surface stress sensor: A- Interaction with a surface monolayer, B- Interaction with an analyte permeable layer and C- Interaction with surface-immobilized colloids.	18
Figure 2.4 Operation modes and methods of signal transduction in microcantilever sensors (EM- electromagnetic).	19
Figure 2.5 Piezoresistive coefficients in silicon at room temperature: A. n-type, B. p-type [57].	23

Figure 3.1 Comparison of loading effects in A. AFM-type cantilever and B. surface-stress based cantilevers. The cantilever deflects due to surface stress associated with analyte binding.	33
Figure 3.2 P μ CA schematic and geometric parameters. (A) A ten-cantilever array. (B) An individual cantilever. (C) Close-up of the piezoresistor.	35
Figure 3.3 Longitudinal and transverse stress (in the piezoresistor) along the length of a 200 \times 50 μ m microcantilever under uniform surface stress of 60 N/m.	38
Figure 3.4 Piezoresistor response for different resistor lengths (l_R). Here $\delta = 0$. Use of n-type silicon is advantageous for $l_R > 93.6 \mu$ m.	38
Figure 3.5 Piezoresistor response for different resistor positions (δ) with a fixed resistor length ($l_R = 50 \mu$ m). Use of n-type silicon piezoresistors is advantageous for $\delta > 18.4 \mu$ m.	39
Figure 3.6 A. Device with four substrate resistors used for measurement of 1/f noise. B. Schematic of circuit used for measurement of 1/f noise.	41
Figure 3.7 1/ f noise spectrum measured using substrate resistors.	42
Figure 3.8 Schematic of piezoresistive microcantilever beam.	45
Figure 3.9 Variation of vibration noise with length of the piezoresistor (l_R).	47
Figure 3.10 Variation of various noise sources with resistor length at 10 kHz with a bandwidth of 10 Hz.	48
Figure 3.11 Variation of noise sources with frequency of electrical excitation of the piezoresistive microcantilever.	48

Figure 3.12 Effect of doping level and temperature on n-doped silicon [3].....	49
Figure 3.13 Minimum detectable surface stress as a function of piezoresistor length (l_R).	51
Figure 3.14 Variation of minimum detectable stress with doping concentration.	51
Figure 4.1 Stress in the x - direction in the silicon piezoresistor cause by a surface stress of 1 N/m in the gold layer. The first 10 μm of the cantilever (left) is clamped. All units are in MPa.	59
Figure 4.2 Stress in the y - direction in the silicon piezoresistor cause by a surface stress of 1 N/m in the gold layer. The first 10 μm of the cantilever (left) is clamped. All units are in MPa.	60
Figure 4.3 Surface stress sensitivity for p-type silicon piezoresistors.	61
Figure 4.4 Surface stress sensitivity for n-type silicon piezoresistors.	61
Figure 4.5 A. Parameters that were varied to evaluate the effect of resistor placement and geometry on surface stress sensitivity. B. A finite element plot showing n-type surface stress sensitivity in the region chosen for evaluation of effect of geometric parameters (all units in MPa).	62
Figure 4.6 Effect of piezoresistor length on surface stress response.	63
Figure 4.7 Effect of piezoresistor distance from the clamped end of the cantilever on surface stress response.	63
Figure 4.8 Effect of piezoresistor width on surface stress response.. Large piezoresistor width creates a larger piezoresistive response.	64

Figure 4.9 Effect of variation of gap between piezoresistors.	64
Figure 4.10 Effect of variation of cantilever length for the same length of the piezoresistors. If $l \approx l_r$, the piezoresistive response is reduced to fringe effects in the stress profile in the piezoresistor.....	65
Figure 4.11 A. Base of flow cell used for integration of the P μ CA. B. CAD image of the two halves fo the flow cell with the integrated P μ CA.....	66
Figure 4.12 A. Schematic for flow model, B. Results of flow of air in the flow channel at 19.8 cms ⁻¹ . The flow profile at the inlet was uniform.....	67
Figure 4.13 A. 10-cantilever P μ CA, B. A single piezoresistive microcantilever.....	68
Figure 4.14 A. Cantilever deformation under SSS and DSS, B. Layer structure of cantilever beam structure used in this work. (σ_s - surface stress).....	70
Figure 4.15. Calculated SSS and DSS surface stress sensitivity for varying bottom nitride thickness.....	71
Figure 4.16. Calculated SSS and DSS surface stress sensitivity for different oxide layer thickness. Surface stress sensitivity of the fabricated microcantilevers are indicated.....	72
Figure 5.1. P μ CA fabrication process flow.	76
Figure 5.2 Doping profile of SOI wafer after doping and annealing. The measured profiles are compared to the profile evaluated theoretically.....	77
Figure 5.3. Resistivity measured from the doping profile measurement made using spreading resistance analysis (SRA).....	77

Figure 5.4. Change in silicon nitride stress with N ₂ flow rate on Unaxis PECVD system.	78
Figure 5.5. Piezoresistive microcantilever embedded in membrane released by TMAH etch.....	79
Figure 5.6. Microcantilever definition is performed using the buried aluminum mask. The bottom aluminum layer prevents etching of the underside of the cantilever in the nitride etch plasma.....	80
Figure 5.7 Piezoresistive microcantilever in the PμCA. The distance from the clamping point (δ) is 250 μm in this cantilever.	81
Figure 5.8 The ten-cantilever piezoresistive microcantilever array (PμCA). Evidence of TMAH etching can be seen in the edge of the silicon portion of the chip.	82
Figure 5.9. Cross section of the cantilever, showing the layer structure (with the piezoresistor).....	83
Figure 5.10. PμCA microcantilever. A. $\delta = 0 \mu\text{m}$ and $\delta' \sim 0 \mu\text{m}$, B. $\delta = 50 \mu\text{m}$ and $\delta' =$ 10-15 μm. Correct design of the cantilever parameter, δ , ensures that the surface stress sensitivity of the cantilever shown in B is unaffected by small errors in etching of the bulk silicon ($ \delta - \delta' < 10 \mu\text{m}$).....	84
Figure 5.11. A. Layer structure of the cantilever. B. Curvature of a cantilever fabricated without the appropriate stress compensation for flat cantilevers.....	85
Figure 5.12. Variation of surface stress sensitivity with thickness of bottom nitride layer.	86

Figure 5.13. Change in radius of curvature with increasing thickness of bottom (tensile) nitride layer. At approximately 200 nm, it approaches infinity; i.e., the cantilever is almost flat.....	88
Figure 5.14 Delamination of gold from cantilever surface due to large interfacial stresses.	89
Figure 5.15. Scheme for metallization of the piezoresistive microcantilevers after fabrication.	90
Figure 6.1 Measurement of natural frequency of a 517 μm cantilever. Phase response of the cantilever is overlain in the plot.....	93
Figure 6.2 Schematic showing cantilever cross-section and the method of deflection of piezoresistive microcantilever. A known deflection is achieved by using a stiff AFM probe.	94
Figure 6.3 Voltage sensitivity of the 10-channel CMOS chip to resistance change in the piezoresistive microcantilever [2]. The voltage sensitivity at 3.46 k Ω is 4.4×10^{-4} V/ Ω . .	96
Figure 6.4 Schematic of heat transfer from a piezoresistive microcantilever.....	99
Figure 6.5 Circuit for measurement of cantilever resistance. The circuit capacitances were evaluated using impedance analysis.	102
Figure 6.6 Frequency spectrum of the signal generator output for a 1V output at 1 kHz.	103
Figure 6.7 Impedance characteristics of ballast resistor.	104
Figure 6.8 Temperature-resistance calibrations of cantilevers with different resistor lengths.....	107

Figure 6.9 Temperature coefficient of resistivity of the cantilevers.	108
Figure 6.10 Cantilever average temperatures for various voltage inputs. Since thermal calibration was performed up to 150 °C, voltage values that are associated with higher temperatures are not shown.	108
Figure 6.11 Flow-chart for minimization routine used to evaluate thermal dependence of heat transfer coefficient.....	109
Figure 6.12 Temperature dependence of heat transfer coefficient for different piezoresistor lengths.....	110
Figure 6.13 Amplitude of resistance response at different excitation frequencies.	111
Figure 6.14 Average resistance of the piezoresistor for resistive heating at different frequencies.	112
Figure 6.15 Comparison of simulation results with experimentally measured values. Top: Resistance amplitude of the piezoresistor. Bottom: Average resistance of the piezoresistor.	113
Figure 6.16 Thermal response of the cantilever, in the flow measurement setup, to DC excitation at different flow rates.	114
Figure 6.17 Measurement setup for investigation of effect of heating on adjacent cantilevers.	116
Figure 6.18 Prediction of variation of resistance amplitude with excitation frequency for a voltage amplitude of 0.25 V across the piezoresistor. The prediction was based on the thermal model.	117

Figure 6.19 Prediction of variation of average resistance with excitation frequency for a voltage amplitude of 0.25 V across the piezoresistor. The prediction was based on the thermal model. 118

Figure 7.1 Normalized noise spectrum measured from a thin film resistor. 1/f noise at low frequencies is very high. 122

Figure 7.2 A. Measurement box used for measurement with 10-channel CMOS chip, B. Close-up of CMOS chip wirebonded on a DIP package [4], C. DIP package that is used with the measurement box [4]..... 123

Figure 7.3 System for measurement of resistance from the cantilevers using PSD. A. The three independent power supplies (SG1-3) allow for heating of the cantilevers to different temperatures (each signal generator can have a different DC bias), B. Each cantilever is placed on a 3/4th Wheatstone bridge, represented here by the blue rectangle. 124

Figure 7.4 Instruments used for resistance measurement: A. Computer with LabVIEW for data acquisition, B. Signals generators and lock-in amplifier, C. SIM 925 multiplexer which is connected to D. Measurement box with Wheatstone bridge circuits. 125

Figure 7.5 Measurement box used for implementation of Wheatstone bridge circuits and to heat cantilevers to different temperatures. A. ZIF connector and internals of the measurement box, B. BNC connectors for connection to piezoresistors and power supply to the Wheatstone bridge circuits. Three independent power supplies with different DC bias may be used. C. BNC connectors for connection to SIM 925 multiplexer. Each channel has an A and B line for differential measurement at the lock-in amplifier. 126

Figure 7.6 Screenshot of LabVIEW program used for data acquisition and control of the multiplexer. 127

Figure 7.7 Noise measured on the various channels of the data acquisition setup with thin films resistors. The time period of this noise signal is approximately 1600 seconds. 128

Figure 7.8 1.25 MHz noise signal measured using two signal generator sources with the lock-in amplifier.....	129
Figure 7.9 The chemical testing setup for exposure of the cantilevers in the SLA package to controlled concentrations of the analyte.	130
Figure 7.10 A. The complete flow setup used for control of analyte concentration, B. Mixing chamber with the effusion vial, C. Flow cell inside the Faraday cage and D. Flow cell with clips for connection to measurement box, and 4-way crossover valve.....	131
Figure 7.11 A. SLA flow cell top and base, B. PuCA wirebonded on the flowcell base, C. Flow cell placed connected to flow system and placed inside Faraday cage, D. Connection of flowcell leads to measurement box.	133
Figure 8.1 Response from a gold-coated and uncoated reference cantilever when both are exposed to 55 ppb of mercaptohexanol (flowrate 2sccm).	138
Figure 8.2 Differential measurement of surface stress by subtracting surface stress response of gold-coated cantilever from reference cantilever. This plot is generated by subtracting the surface stress response of the gold-coated cantilever from that of the reference cantilever in Figure 8.1.	139
Figure 8.3 Response curve associated with analyte absorption at 55 ppb at 10 sccm for a short time. The jump in resistance of the piezoresistor at the start and end of analyte flow is due to a change in flow rate in the system. The piezoresistance changes at the end of analyte exposure.....	140
Figure 8.4 Effect of clamping distance (δ): The seemingly smaller response for $\delta = 0$ μm is due to use of incorrect surface stress sensitivity. Analyte concentration: 55 ppb, flowrate: 2 sccm.....	141

Figure 8.5 Effect of resistor length: The response for the two cantilevers with different cantilever lengths is near identical. The higher stresses here are on account of measurement at a concentration of 400 ppb (flowrate: 2 sccm).	143
Figure 8.6 The voltage change in the cantilevers (top) and the piezoresistive response (bottom) of single- and double-sided cantilevers to 55 ppb of mercaptohexanol.....	144
Figure 8.7 Effect of concentration: The equilibrium stress and reaction rate are larger at high concentrations. Flowrate: 2 sccm.....	148
Figure 8.8 Adsorption reactions on the cold and heated cantilevers. The reaction curves are fitted with Langmuir isotherms. These measurements were made at 55 ppb at 5 sccm.	149
Figure 8.9 Desorption curves for desorption of analyte from the saturated sensors in dry nitrogen. Flow rate: 5 sccm.....	149
Figure 8.10 Variation of piezoresistive coefficient with doping concentration (for n-type silicon) and temperature. The y-axis plots the ratio of the piezoresistive constant at a given concentration and temperature to piezoresistive constant at 300 K for a doping level of 10^{15} cm^{-3} [15].	150
Figure 8.11 Spatial temperature profile of a 750 μm long cantilever with an average temperature of 50 $^{\circ}\text{C}$	152
Figure 9.1 Schematic of Pt_{μ}CA cantilever. The outer loop is the piezoresistive sensor while the inner loop is the Pt RTD.....	161
Figure 9.2 MOF coating cantilevers. The MOF used in this coating is MOF-5 [2]. MOFs of different grain sizes have been grown: A- 50 μm , B- 5 μm	161

NOMENCLATURE

δ	Designed piezoresistor distance from the clamped end of cantilever
δ'	Actual piezoresistor distance from the clamped end of cantilever
ε	Strain in the cantilever at a given point
ε^0	Strain at any point in midplane of the cantilever
χ	Curvature of the cantilever at a given point
$\varepsilon_x, \varepsilon_y, \varepsilon_{xy}$	Strain components along x and y axes
$\chi_x, \chi_y, \chi_{xy}$	Curvature components along x and y axes
π_a	Piezoresistive coefficient in direction “a”
σ	Stress in the cantilever at a given point
$\sigma_{i,k}$	Residual stress in the k^{th} layer of the cantilever
σ_s	Surface stress acting on the cantilever
σ_s^+, σ_s^-	Magnitude of surface stress on the top and bottom surfaces of the cantilever
ν_k	Poisson ratio of the k^{th} layer of the cantilever
A	Stretching stiffness matrix
B	Bend-stretching coupling matrix
D	Bending stiffness matrix
E_k	Young’s modulus of k^{th} layer
h	Thickness of the cantilever
h_k	Thickness of the k^{th} layer
h_R	Thickness of the piezoresistor
l	Cantilever length
l_R	Length of resistor
N	Axial force in the cantilever
M	Planar moment in the cantilever
$\tilde{\mathbf{Q}}$	Stress-strain tensor for isotropic materials

$S_{Clamped}, S_{Free}$	Stress sensitivities at the clamped and free ends of the cantilever
R	Resistance of piezoresistor
ΔR^s	Piezoresistance change due to surface stress
u	Deformation along the x-axis
v	Deformation along the y-axis
w	Deflection of the cantilever mid-plane along the z-axis
b	Width of cantilever
b_R, w_R	Width of resistor
z_k	Distance of the mid-plane of the k^{th} layer from the cantilever mid-plane
z_R	Distance of the mid-plane of the piezoresistor from the cantilever mid-plane
<i>AFM</i>	Atomic force microscopy
<i>BSA</i>	Bovine serum albumin
<i>DNA</i>	Deoxyribonucleic Acid
<i>EM</i>	Electromagnetic
<i>GOx</i>	Glucose oxidase
<i>IgG</i>	Immunoglobulin G
<i>IR</i>	Infrared
<i>PDMS</i>	Poly-dimethylsiloxane
<i>PECH</i>	Poly-epichlorohydrin
<i>PSD</i>	Phase sensitive detection
<i>PμCA</i>	Piezoresistive microcantilever array
<i>QCM</i>	Quartz crystal microbalance
<i>RIE</i>	Reactive ion etch
<i>RTD</i>	Resistance temperature detector
<i>SAW</i>	Surface acoustic wave
<i>TCR</i>	Temperature coefficient of resistance
<i>TMAH</i>	Tetra-methyl ammoniumhydroxide
<i>VOC</i>	Volatile organic compounds

SUMMARY

Numerous applications in the present day ranging from testing humidity in air to detecting miniscule quantities of potentially hazardous chemical and biological agents in the air or water supplies require the development of chemical sensors capable of analyte detection with high sensitivity and selectively. Further, it has become desirable to create lab-on-chip systems that can detect multiple chemical agents and allow for sampling and testing of environments at locations distant from conventional laboratory facilities. Current challenges in this area include design, development and characterization of low detection limit sensors, development of low-noise readout methods, positive identification of analytes and, identification and reduction of the effect of various noise sources - both intrinsic and extrinsic to the sensor.

The current work examines the performance limits of a 10-cantilever piezoresistive microcantilever array (P μ CA) sensor. The microcantilevers measure analyte concentration in terms of the surface stress associated with analyte binding to the functionalized cantilever surface.

The design, fabrication, characterization and testing of this measurement platform is presented. A novel aspect of the sensors developed is the use of n-type doping which increases the sensitivity of the device by one order of magnitude. In addition, design rules for surface stress-based chemical sensors have been developed. Extensive thermal characterization of the piezoresistive microcantilevers has been performed for DC and AC electrical excitation and values of heat transfer coefficient for the associated microscale phenomena are reported.

Further, a method of low-noise measurement of cantilever resistance has been developed based on phase-sensitive detection techniques and this has been integrated with a multiplexing circuit to measure piezoresistance change in multiple cantilevers.

Finally, the two novel techniques of chemical sensing- double-sided sensing and thermal array-based sensing have been investigated. These methods are presented as a means of extending the applicability and functionality of piezoresistive microcantilever sensors for chemical sensing.

CHAPTER 1

INTRODUCTION

As human society grows in size and complexity, so does the need to keep all its technological elements functioning effectively. Failure to do so can adversely affect millions of lives. Sensors and sensor systems are used to monitor almost every aspect of human activity and our immediate environment. In today's world, monitoring the quality of air, water and our food supplies is of vital importance. Also, with industrial products forming the backbone of society, industrial monitoring systems are also crucial. This has become particularly true given the tremendous potential that industrial systems have for damage to human life and the environment [1, 2]. Further, our endeavors to expand the horizons of human knowledge outwards, in the area of space exploration, and inwards, in the areas of diagnostics, genetics and drug delivery, require specialized sensing systems. More recently terrorism and security concerns have created a great urgency in the search for better and more versatile chemical sensing systems.

This dissertation discusses issues related to chemical sensing in fluids. Such sensor systems are also referred to as the electronic nose (for vapor phase detection) and the electronic tongue (for liquid phase detection) [3]. The requirements of a 'good chemical sensor' are as follows:

1. Ability to measure in a variety of media: Potential applications for these sensors range from analysis of air and water quality, monitoring of food quality, in vitro monitoring of human health and medical diagnostics. Hence sensors that are able to perform equally well in all fluid environments are desirable. Also this requirement implies that the sensor is compatible with these environments.
2. Ability to detect multiple analytes simultaneously: In most potential applications for chemical sensors, sampling is to be done at the site of investigation. Due to the relatively simple sample preparation operations possible in field studies, in vitro diagnostics, etc., the sensor has to be able to differentiate between and measure different analyte concentrations present in the sample.

3. Label-free detection: In numerous detection schemes, the analyte is 'labeled' with a fluorescent, chemiluminescent or radioactive marker. Measurement of analyte concentration is achieved by measuring the concentration of the marker bound on the sensor via the analyte binding mechanism. However labeling can be a very complex and analyte-specific process. Hence sample preparation is extensive and these methods are not amenable to most field applications. Methods of detection that do not require labeling of the analyte are preferred.
4. High sensitivity: High device sensitivity coupled with low noise in the measurement allows for low detection limit measurement of analyte concentration. While this is not required for most commonplace applications such as measurement of air and water quality, with issues of national security and bioterrorism (associated with low detection-limit measurement of chemical and biohazards) growing in importance, development of versatile sensors with high sensitivity is essential.
5. High selectivity: Selectivity is a crucial issue with sensor devices. Most sensors respond to numerous analytes in the same way. Sensors that allow for positive identification of specific analytes are required.
6. Portability and low-power operation: These are twin requirements that have driven research in the direction of microscale sensors. The need for field measurements necessitates portable sensors with self-contained power, sampling, measurement and readout units. Simple detection schemes with limited hardware requirements are key to achieving these needs.
7. Robustness: Robust sensor design that allows for accurate measurements in different environmental conditions such as variation in temperature, fluid properties, vibration, etc. is desirable.
8. Low-cost: Cost of a chemical sensor depends on cost of manufacture (fabrication facilities, complexity of the device, cost of raw materials and labor), cost of use (need to simple or extensive instrumentation) and reusability of the sensor. All three are important considerations in the design of any chemical sensor.

1.1 Micro Total Analysis Systems

Chemical analysis systems, today, are a broad class of sensors systems for detection of different classes of measurands and are based on diverse principles of measurement. Detection of the chosen analyte involves operations starting with sample preparation and ending in data representation. Gas chromatography [4] and mass spectrometry [5] are two commonly used techniques that allow for accurate and highly sensitive analyte detection and measurement. However these traditional systems tend to be large. In recent years portability has also become an important design requirement for this class of sensors, with the need to make measurements at locations far from conventional laboratory facilities. Hence there is a growing interest in miniaturizing existing chemical analysis systems and developing new and novel ones [6, 7]. These systems are referred to as ‘micro total analysis systems’ (μ TAS).

It has often been said that science fiction has a habit of turning into scientific fact. This has happened at a growing pace in recent years. Gene Rodenberry’s breakthrough science fiction in the 1960s, Star Trek, introduced the tricorder to the world. This was a portable, handheld device that could perform simultaneous chemical, radiation and biological scans in a given area.



Figure 1.1 The tricorder from the TV series Star Trek [8]. This handheld device could be used for chemical, radiation and biological sensing.

While in the 1960s this was merely a figment of human imagination, interest in the creation of real micro total analysis systems or ‘lab-on-chip systems’ that can perform label-free detection of multiple chemical or biological agents, in a variety of analytes in different media, has grown manifold in recent years. Some of the best known μ TASs are the MicroChemLab™ developed at Sandia National Laboratories for detection of chemical and biological toxins [9] and the SniffEX™ developed at Oak Ridge National Laboratories for explosive detection [10].

1.1.1 Elements of a μ TAS

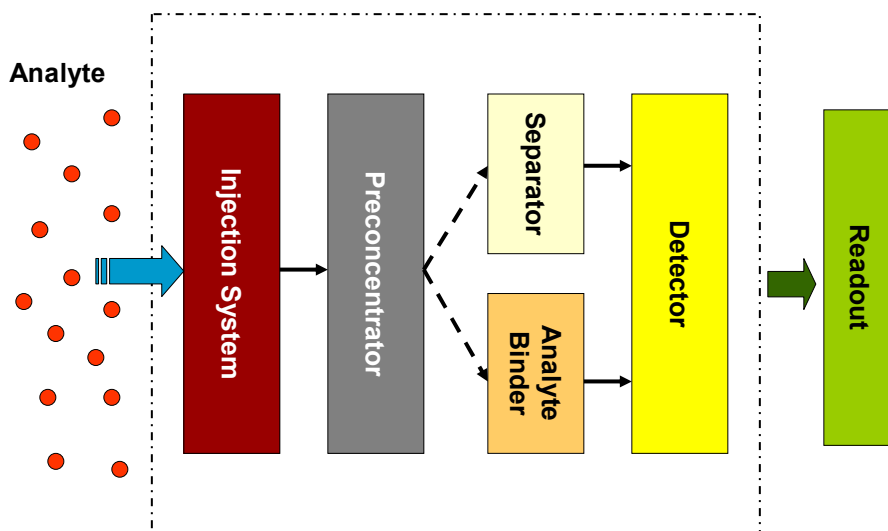


Figure 1.2 Components of a micro total analysis system (μ TAS).

The functional elements comprising a μ TAS are shown in Figure 1.2. Injection and flow control in the system is achieved by one of a variety of pumping mechanisms (off-chip liquid chromatography pumps, electroosmotic pumps, AC magnetohydrodynamic pumps, resistive heating-based pumps, centrifugal pumps, piezoelectric pumps, etc.) and microvalves. Preconcentration of the analyte is required to ensure that the concentration is within the detector’s dynamic range of operation. Currently there are two classes of detectors- ones that are targeted to detection of a single

analyte from an analyte mixture and others that respond to multiple analytes in a mixture. Since the first class of sensors is analyte-specific, no separation of the analyte from the mixture is required. The second class of sensors, however, requires means of isolation of each analyte to be detected. While the preconcentrator and separator have been shown as separate units, some systems use chromatography, electrophoresis, magnetic [7], temperature gradient focusing [11], etc. to perform one or both functions. Systems with analyte-specific detection systems, in theory, do not need separation system. However, for practical systems, purification of the sampled analyte mixture to remove ions, molecules and particles that might result in erroneous measurement is desirable.

1.1.2 Sensors and Selectivity

At the heart of the μ TAS is the sensor/detector. The options for chemical detection systems employed in a μ TAS are discussed in greater detail in Chapter 2. The method and nature of detection often limits the media in which sensors may be deployed as well as the limits of detection.

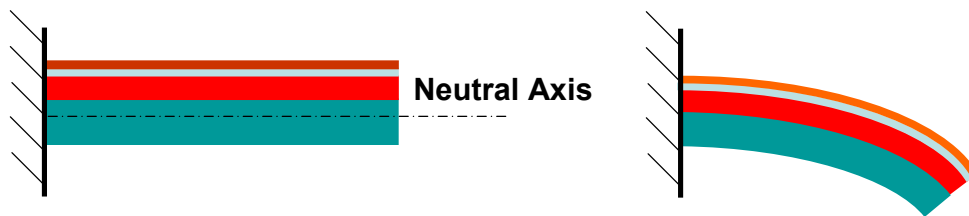
A very important aspect of sensing systems is selectivity. This refers to the ability of the sensor to detect a single analyte or a class of analytes from a mix of systems. This is typically a function of the selective coating or ‘analyte-binder’ on the sensor. Currently work suggests that finding selective coatings for each individual analyte is both extremely difficult and impractical. The use of sensor arrays to measure analytes wherein each sensor of the array is coated or ‘functionalized’ with a different binder allows for measurement of a chemical signature associated with each analyte [12]. Another method of improving selectivity of current sensor systems is to add orthogonal sensors to the system that allow for measurement of multiple measurands [13]. The system can then measure multiple physical or chemical properties associated with the analyte and identification and measurement of the analyte can be carried out based on a lookup table prepared using a calibrated sample. Thus the use of sensor arrays can enhance the specificity of current sensing systems.

1.2 Microcantilever Chemical Sensors

Microcantilevers are an extremely simple yet versatile class of sensors. All measurements made with cantilever sensors revolve around static bending or measurement of resonant frequency of the cantilever. Microcantilever sensors have been applied to measurement of mechanical, electrical, electrochemical, chemical, thermal and electromagnetic properties and phenomena.

Microcantilever sensors are also an excellent platform for chemical and biochemical detection [14]. Since the demonstration of the high sensitivity of microcantilevers, by Thundat et al. [15] and Barnes et al. [16], they have been applied to the detection of a variety of analytes. Two possible modes of cantilever operation are possible- dynamic and static. This work utilizes the latter by measuring out-of-plane cantilever deflection resulting from surface stress associated with the interaction of the analyte with a ‘functionalized’ cantilever surface. Functionalization refers to the modification of the microcantilever surface so as to allow for selective binding to specific analytes. Every binding event is associated with a change in Gibbs free energy that in turn results in a change in surface stress (related by the Shuttleworth equation, refer § 2.2.1). Hence measurement of surface stress may be used a definitive means of detection and measurement of analytes.

1.2.1 Piezoresistive Microcantilever Surface Stress Sensing



$$\frac{\Delta R}{R} = \pi_L \sigma_L + \pi_T \sigma_T$$

Figure 1.3 Scheme of surface stress detection with a piezoresistive microcantilever. π_L and π_T are the piezoresistive coefficient of the piezoresistor in the longitudinal and transverse direction. Generally the longitudinal direction is taken along the axis of the cantilever.

The cantilever bending due to surface stress on the cantilever can be measured using a variety of detection methods (refer § 2.3). Most methods infer surface stress from the measured cantilever tip deflection using simple beam theory [17]. Piezoresistive detection is different from methods such as optical and capacitive detection in that surface stress may be measured directly. The schematic in Figure 1.3 demonstrates how surface stress on the cantilever results in stress in the piezoresistor and a change in piezoresistance. In a cantilever with a piezoresistive strain gage (resistance, R) the surface stress ($\sigma_{\text{surface stress}}$) may be related to the change in piezoresistance (ΔR^s) by the surface stress sensitivity ($S_{\text{cantilever}}$) by

$$\frac{\Delta R^s}{R} = S_{\text{cantilever}} \sigma_{\text{surface stress}} \quad (1.1)$$

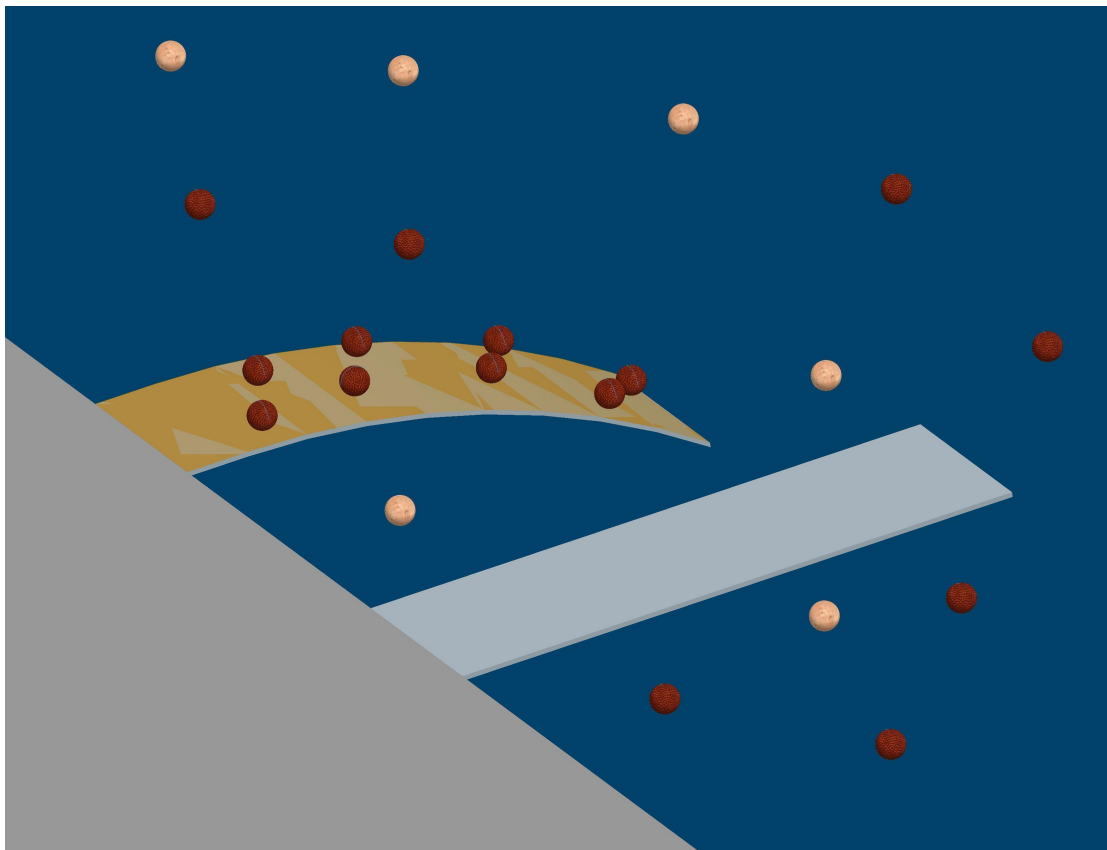


Figure 1.4 Reference cantilevers allow for filtering of noise in the measurement. The analyte binds selectively to the functionalized cantilever on the left. No binding takes place on the reference cantilever on the right.

Thus piezoresistive microcantilevers can be used to investigate surface stresses due to analyte interaction directly. Further, since the piezoresistor is built into the cantilever, fluid properties (optical, dielectric, viscosity, etc.) do not limit detection in environments such as blood, ionic solvents, etc.

Typically a second cantilever is used in conjunction with the functionalized cantilever. This does not interact with the analyte and acts as a reference cantilever and helps filter thermomechanical noise in the measurement (Figure 1.4).

1.3 Scope Of This Dissertation

For effective use of microcantilevers as chemical or biochemical sensors, both a sensitive, well-characterized platform for measurement and an analyte-specific, functionalized cantilever surface are required. This work details the design and development of the former. While understanding of piezoresistive microcantilever-based chemical and biochemical sensors has progressed significantly, numerous questions related to sensor design, operation and application remain unanswered that need to be addressed adequately to be able to fully assess their potential. Further cantilever-based chemical sensors are one element of a huge class of chemical sensors available today. It is extremely likely that other types of sensors are better suited for certain applications. Hence understanding the limits of performance and operation of piezoresistive microcantilever arrays will create benchmarks that allow for comparison with other sensor systems.

Some design choices were made at the very outset of this work. A piezoresistive microcantilever array design was chosen over the other modes of signal readout to ensure operation was not limited by fluid properties (refer § 2.3.2). Also, the fabrication issues with construction of optical, capacitive, magnetic and electron tunneling devices make these less attractive options for signal readout.

1.3.1 Motivation for Study

Based on the survey of literature in the area, the following issues merit further investigation:

- Design: A majority of current endeavors in design of piezoresistive cantilevers for surface stress sensing are based on designs of AFM based cantilevers and are not optimized for surface stress measurements. This is partly true because no broad rules for design of surface stress sensitive cantilevers exist. Also material design for surface stress sensing issues has not been given much importance in existing work.
- Thermal characterization: No work exists on thermal issues associated with piezoresistive cantilevers for surface stress measurement. Piezoresistive microcantilevers can be used as a calibrated thermal array for chemical sensing. However no studies on this area exist. Also, thermal noise issues in piezoresistive measurement have been addressed incorrectly thus far.
- Measurement techniques: All current work in literature relies on DC measurement of resistance. AC resistance measurement for low-noise piezoresistive surface stress measurement merits study.
- Alternative schemes of measurement: Work by Rasmussen et al. [18] suggests that alternative schemes of measurement may be applied to surface stresses measurement with piezoresistive microcantilevers. No further work has been reported on this issue. The idea of double-sided surface stress sensing, design for such cantilevers and potential applications are examined in this work.

1.3.2 Research Objectives

Several important questions remain unanswered in the area of microcantilever-based sensing. These are related to the twin aspects of piezoresistive microcantilever-based surface stress sensors:

- Design, fabrication, characterization and operation of the piezoresistive microcantilever transducer
- Design of the surface functionalization that results in high analyte specificity and results in large surface stress in these systems.

This work deals with the first. The objectives of this work, then, are:

1. To design and fabricate a highly sensitive piezoresistive microcantilever-based chemical sensing platform for chemical sensing applications.

2. To characterize the electrical, mechanical and thermal behavior of the piezoresistive microcantilever array.
3. To evolve rules for design and operation of this sensor platform to achieve higher measurement sensitivity and low-noise measurement.
4. To investigate new schemes of sensing with existing piezoresistive microcantilever systems with a view to enhance the measurement sensitivity and functionality of the piezoresistive microcantilever array.

1.4 Structure Of The Thesis

This thesis consists of four major components- design, process development and fabrication, characterization and finally testing of the P μ CA. Chapter 1 has introduced the motivation, needs and direction of the current work.

Chapter 2 discusses to background to chemical sensor systems and cantilever-based chemical sensors in particular. Also it serves to justify some of the initial design choices made in this work.

Issues related to design of the P μ CA have been taken up in Chapters 3 and 4. Chapter 3 takes up the discussion of material related issues in design of the piezoresistive microcantilevers and noise in the microcantilever and design for the same is discussed. Chapter 4 is devoted to geometric design issues in the microcantilever. A new model for surface stress detection is presented here and this has been used to devise design rules for surface stress based cantilever sensors. This chapter proposes an optimal design for the piezoresistive microcantilever based on sensitivity and signal-to-noise considerations. Considerations for design of microfluidics in the system are presented here.

Chapter 5 presents the fabrication of the P μ CA. Process development, fabrication problems and their solutions, and fabrication results. In order to preserve the continuity of this chapter, details of several standard and non-standard processes and other processing related details have been omitted from the chapter. These have been compiled, instead, and presented in Appendix B.

Chapter 6 discusses the mechanical and thermal characterization of the P μ CA. This analysis forms the basis of choice of measurement conditions used in this work.

Chapter 7 presents the methods used in work for electrical measurement and the flow system used to expose the P μ CA to the chosen analyte and a controlled concentration.

Chapter 8 presents results of the chemical testing of the P μ CA in vapor phase. Also it serves to validate some design ideas and detection schemes presented in previous chapters.

Finally, Chapter 9 draws conclusions on effectiveness of ideas presented in this work and presents recommendations for future work and directions in this research area.

Details of various steps in the design process, design parameters, mask details, etc. have been compiled in Appendix A. Details of the fabrication process and process steps have been compiled in Appendix B.

Appendix C presents an analytical solution used for calculation of thermal behavior of the cantilevers. This may be used for transient analysis of the cantilever. This closed form solution is limited in that it requires that the heat transfer coefficient be independent of temperature.

Some of the circuit designs and layouts used in this work are compiled in Appendix D.

1.5 References

- [1] V. R. Dhara and R. Dhara, "The Union Carbide disaster in Bhopal: A review of health effects," *Archives of Environmental Health*, vol. 57, pp. 391-404, 2002.
- [2] V. Drozdovitch, A. Bouville, N. Chobanova, V. Filistovic, T. Ilus, M. Kovacic, I. Malatova, M. Moser, T. Nedveckaite, H. Voelkle, and E. Cardis, "Radiation exposure to the population of Europe following the Chernobyl accident," *Radiation Protection Dosimetry* vol. 123, pp. 515-528, 2007.
- [3] T. C. Pearce, S. S. Schiffman, H. T. Nagle, and J. W. Gardner, *Handbook of machine olfaction*: Wiley-VCH, 2003.
- [4] R. P. W. Scott, *Introduction to analytical gas chromatography*: CRC Press, 1998.
- [5] E. d. Hoffmann and V. Stroobant, *Mass Spectrometry: Principles and applications*: John Wiley & Sons, 2001.

- [6] D. R. Reyes, D. Lossifidis, P.-A. Auroux, and A. Manz, "Micro total analysis systems. 1. Introduction, theory and technology," *Analytical Chemistry*, vol. 74, pp. 2623-2636, 2002.
- [7] P.-A. Auroux, D. Lossifidis, D. R. Reyes, and A. Manz, "Micro total analysis systems. 2. Analytical standard operations and applications," *Analytical Chemistry*, vol. 74, pp. 2637-2652, 2002.
- [8] "http://memory-alpha.org/en/wiki/TR-560_Tricorder_VI#23rd_century", (October, 2007)
- [9] R. P. Manginell, P. R. Lewis, D. R. Adkins, R. J. Kottenstette, D. Wheeler, S. Sokolowski, D. Trudell, J. Byrnes, M. Okandan, J. M. Bauer, and R. G. Manley, "Recent advancements in the gas-phase MicroChemLab," in *Proceedings of the SPIE: Lab-on-a-Chip: Platforms, Devices, and Applications*, 2004, pp. 44-55.
- [10] L. A. Pinnaduwege, D. L. Hedden, A. Gehl, V. I. Boiadjev, J. E. Hawk, R. H. Farahi, T. Thundat, E. J. Houser, S. Stepnowski, R. A. McGill, L. Deel, and R. T. Lareau, "A sensitive, handheld vapor sensor based on microcantilevers," *Review of Scientific Instruments*, vol. 75, pp. 4554-4557, 2004.
- [11] A. J. d. Mello, "Free zone protein separations," *Lab On A Chip*, vol. 5, pp. 12-13, 2005.
- [12] M. K. Baller, H. P. Lang, J. Fritz, C. Gerber, J. K. Gimzewski, U. Drechsler, H. Rothuizen, M. Despont, P. Vettiger, F.M. Battiston, J. P. Ramseyer, P. Fornaro, E. Meyer, and H.-J. Guntherodt, "A cantilever array-based artificial nose," *Ultramicroscopy*, vol. 82, pp. 1-9, 2000.
- [13] U. Weimar and W. Göpel, "Chemical imaging: II. Trends in practical multiparameter sensor systems," *Sensors and Actuators B*, vol. 52, pp. 143-161, 1998.
- [14] N. V. Lavrik, M. J. Sepaniak, and P. G. Datkos, "Cantilever transducers as a platform for chemical and biological sensors," *Review of Scientific Instruments*, vol. 75, pp. 2229-2253, 2004.
- [15] T. Thundat, R. J. Warmack, G. Y. Chen, and D. P. Allison, "Thermal and ambient - induced deflections of scanning force microscope cantilevers," *Applied Physics Letters*, vol. 64, pp. 2894-2903, 1994.

- [16] J. R. Barnes, R. J. Stephenson, M. E. Welland, C. Gerber, and J. K. Gimzewski, "Photothermal spectroscopy with femtojoule sensitivity using a micromechanical device," *Nature*, vol. 372, p. 79, 1994.
- [17] J. Gere and S. Timoshenko, *Mechanics of materials*, Fourth ed. Boston: PWS Publishing Company, 1997.
- [18] P. A. Rasmussen, A. V. Grigorov, and A. Boisen, "Double sided surface stress cantilever sensor," *Journal of Micromechanics and Microengineering*, vol. 15, pp. 1088-1091, 2005.

CHAPTER 2

BACKGROUND AND PREVIOUS WORK

This chapter serves to review the background and prior work related to various components of this study. This review also serves to justify some of the initial design choices made in this work and to identify gaps in current understanding of issues related to piezoresistive microcantilever-based chemical sensing. Literature review of some topics related to design or measurement issues have been taken up in the pertinent sections of this thesis.

2.1 Sensor Classification

A vast array of sensors has been developed based on different transduction principles. These find application in almost every human endeavor. These may be classified into physical, chemical and biological sensors in terms of the measurand [1]. The following definitions [2] will help clarify the nature and purview of the current work:

Physical sensor- A device that provides information about a physical property of the system.

Chemical sensor- A chemical sensor is a device that transforms chemical information, ranging from the concentration of a specific sample component to total composition analysis, into an analytically useful signal. The chemical information, mentioned above, might originate from a chemical reaction of the analyte or from a physical property of the system investigated.

Biological sensor- A biological sensor is a device that is able to transform information on biomass into a useful analytical signal.

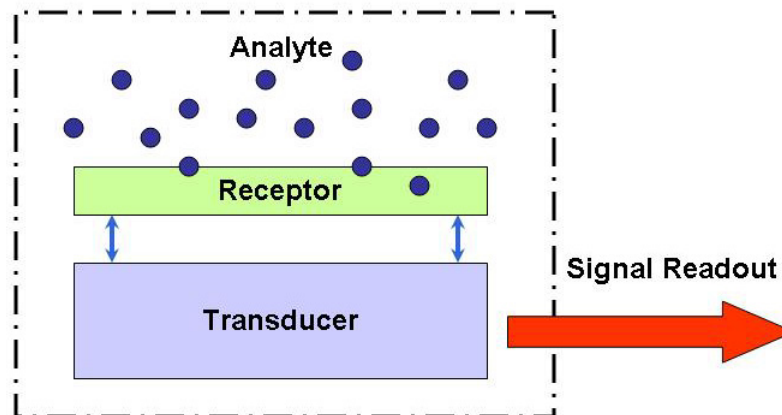


Figure 2.1 Scheme for chemical sensing: The transducer converts the chemical signal into an analytically useful signal.

The elements of a chemical sensor are the *receptor*, which transforms the chemical information to a form of energy that can be measured by the *transducer* (Figure 2.1). The latter transforms the energy carrying chemical information into a useful analytical signal. Ordinarily the transducer does not have any selectivity. Further, the principle of transduction is typically physical. The receptor of a chemical sensor is based on one of the following principles [2]:

Physical- No chemical change takes place. Detection is based on change of a physical property such as absorbance, refractive index, conductivity, mass change, temperature, etc.

Chemical- A chemical reaction occurs with the participation of the analyte resulting in an analytical signal.

Biochemical- A biochemical reaction is the source of analytical signal. These maybe be considered a subset of chemical receptors. These are also referred to as biosensors [3].

Most available literature treats biological sensors and biosensors (biochemical sensors) as a single class of sensors. Several biological parameters such as mechanical properties of cells or label-based biosensing techniques such as fluorescence, chemiluminescence or radiative detection use physical sensors for detection and

measurement and do not fall under the purview of chemical sensors. In this text, biological sensors will be defined as above and biosensors or biochemical sensors will be treated as subset of chemical sensing.

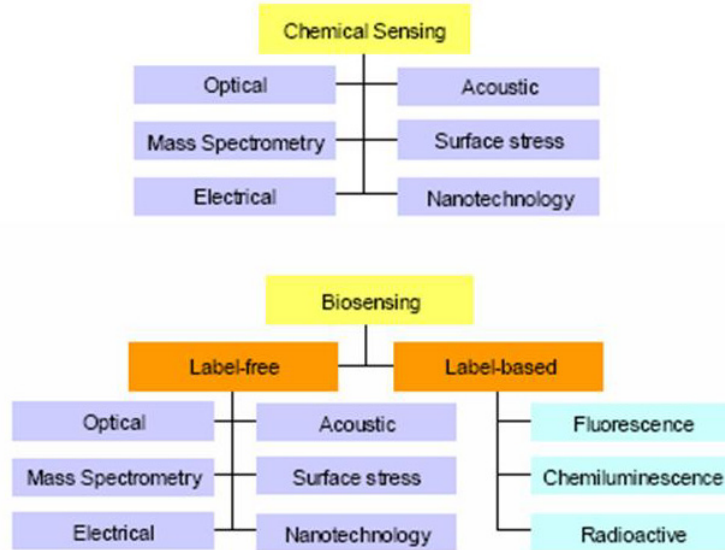


Figure 2.2 Chemical sensing and biosensing methods [4].

2.2 Surface Stress-Based Sensing

The varied methods of chemical and biochemical sensing are categorized in Figure 2.2. Surface stress measurement is a label-free method of chemical and biochemical detection and is the method of analyte detection chosen in this work. This section presents current understanding of the phenomenon of surface stress. This review is based on the seminal work of Shuttleworth [5] and numerous review papers [6-10]. Also current sensor devices for measurement of surface stress and surface modification used in such devices are surveyed.

2.2.1 The Phenomenon of Surface Stress

Current definitions of surface and interface stresses are based on the work of Gibbs. Surface free energy (γ) is defined as reversible work per unit area to create a surface, exposing new atoms. Surface stress (f), however, is the reversible work per unit area to stretch a surface elastically. If a fluid surface is stretch new atoms come to the

surface keeping the atoms per unit area constant and the surface free energy is equal to surface stress. For a solid however the actual number of atoms is constant and the number of atoms per unit area is altered and $f \neq \gamma$. In liquids, since $f = \gamma$, these terms are used interchangeably and sometimes referred to as ‘surface tension’. In solids, however f and γ can be different by upto a factor of 3.

Surface stress may be defined in terms of change in the bulk stress tensor near a surface or interface. If the surface lies in the $x-y$ plane and the z axis is perpendicular to the surface, surface stress is defined by

$$\tau_{ij}^s = \int_{-\infty}^{+\infty} (\tau_{ij}(z) - \tau_{ij}^b) dz \quad (2.1)$$

where, τ_{ij}^s is surface stress tensor, $\tau_{ij}(z)$ is the bulk stress tensor which may be different from the bulk stress tensor τ_{ij}^b in the vicinity of the surface and i and j represent tensor components in the x and y directions. This definition also implies that the units of surface stress are force per unit length rather than force per unit area. This definition lends itself to experimental determination of surface stress using numerous mechanical methods of investigation based on elastic deformation theory [11]. The thermodynamic definition of surface stress is obtained by considering the work δW associated with straining a thin crystal plate of thickness t by $\delta \varepsilon_{ij}$,

$$\delta W = A \int_{-t/2-0}^{+t/2+0} dz \sum_{i,j} \tau_{ij}(z) \delta \varepsilon_{ij} \quad (2.2)$$

where A is the area of the plate. Now the work may be expressed as the sum of bulk and surface work and in turn the sum of bulk and surface stress energies as:

$$\delta W = \delta W^s + \delta W^b = \delta F^s + \delta F^b = 2A \sum_{i,j} \delta \varepsilon_{ij}^s + At \sum_{i,j} \delta \varepsilon_{ij}^b \quad (2.3)$$

The surface free energy (F) may be expressed in terms of the specific free energy (γ) as

$$\delta F^s = \delta(\gamma A) = \delta \gamma A + \gamma \delta A \quad (2.4)$$

At a specific value of strain ε_{ij} , the surface stress and the free energy may be related by the Shuttleworth equation [5]:

$$\tau_{ij} = \gamma \delta_{ij} + \frac{\partial \gamma}{\partial \varepsilon_{ij}} \quad (2.5)$$

2.2.2 Surface Modification for Chemical Sensing

Sensors used for chemical or biochemical sensing applications are used in conjunction with different chemistries to modify the surface. Three different models have been proposed for analyte binding for chemical sensing [12]. These are based on the nature of the surface modification used as the chemically sensitive layer.

1. Interaction with a surface monolayer: These interactions are primarily surface phenomena. Analyte adsorption can be a physisorption (binding energy < 0.1 eV) or a chemisorption process (binding energy > 0.3 eV) which is true of most chemical bonding. The Shuttleworth equation relates change in surface stress on chemisorption to change in the Gibbs free energy. The spontaneous adsorption process of alkanethiols is driven by the excess interfacial free energy and results in a reduction in interfacial stress and causes surfaces to expand (Figure 2.3.A). This results in the development of compressive surface stress. Compressive stresses have been noticed in the interaction of alkanethiols on gold-coated cantilevers [13, 14]. Other analytes may cause tensile stresses.

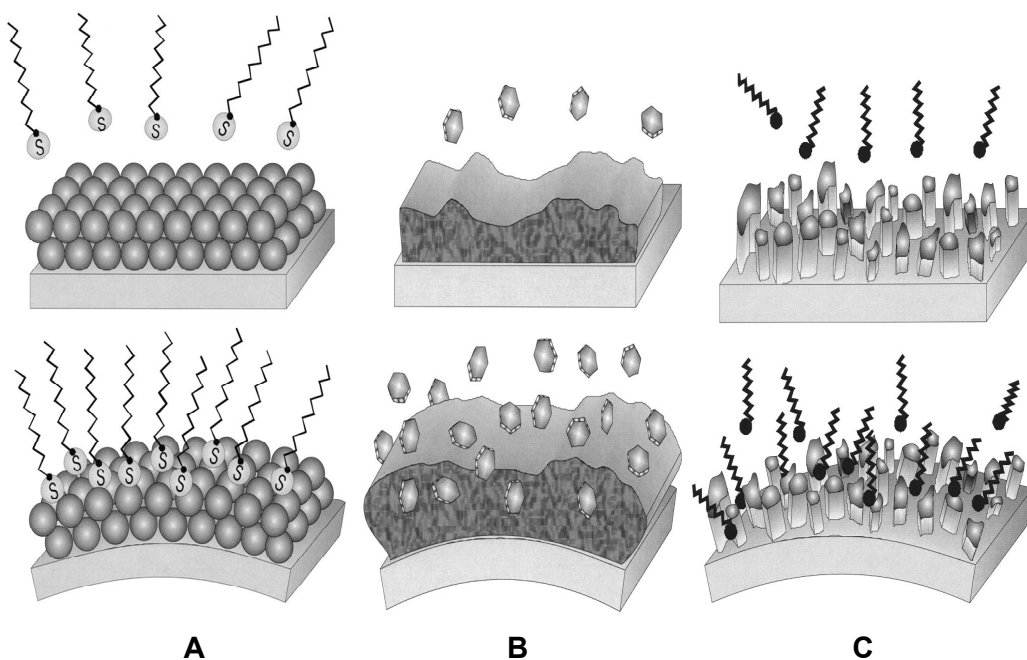


Figure 2.3 Three methods of analyte interaction with the modified surface of the surface stress sensor: A- Interaction with a surface monolayer, B- Interaction with an analyte permeable layer and C- Interaction with surface-immobilized colloids.

2. Interaction with a thick analyte-permeable layer: When the analyte molecules interact with a permeable surface layer, the analyte is physically absorbed in the layer in addition to any chemical interaction that might occur (Figure 2.3.B). This results in swelling of the layer and cantilever deflection on account of this swelling [15-21].

3. Interaction with surface-immobilized colloids: Colloids have been found to be a very promising class of responsive phases for cantilever-based chemical detection [22]. Analyte interaction with structured phases combines bulk, surface and intersurface processes. This results in very efficient conversion of receptor-analyte interaction into mechanical energy for cantilever deflection (Figure 2.3.C).

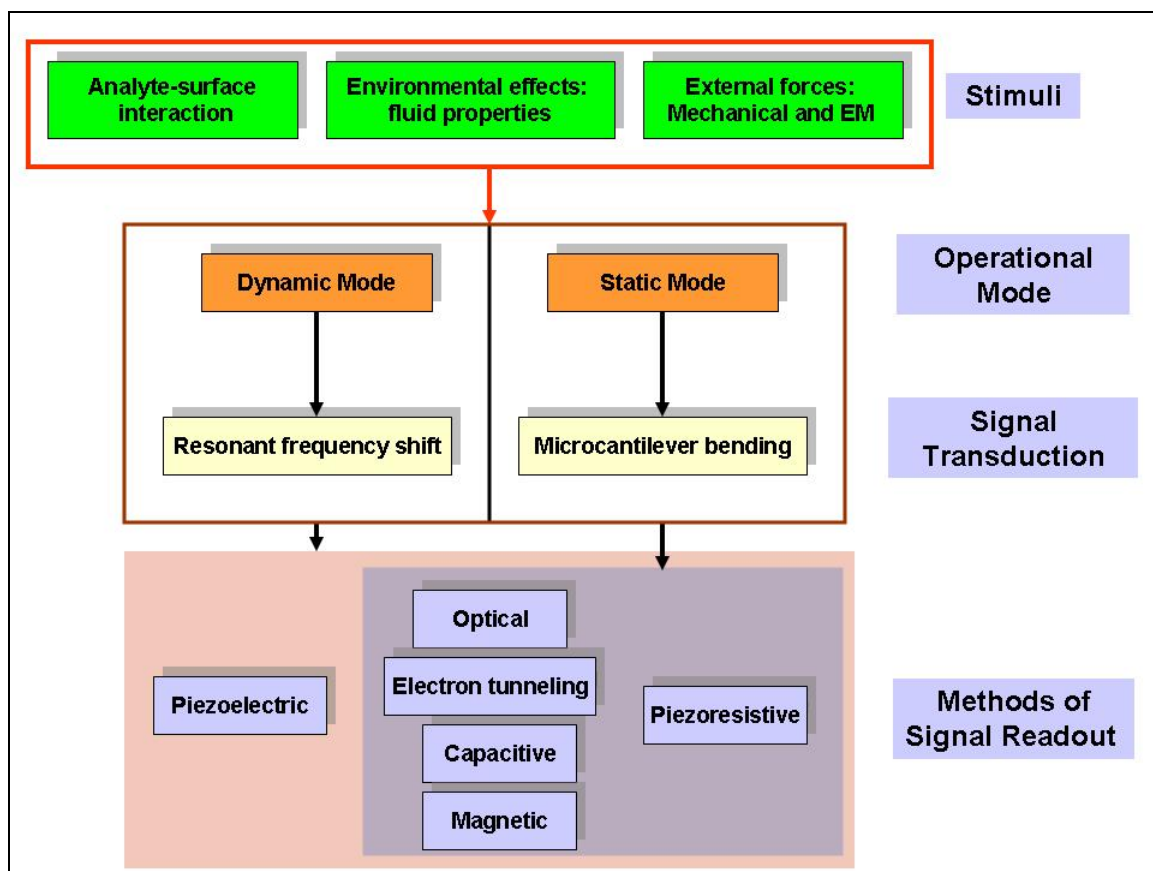


Figure 2.4 Operation modes and methods of signal transduction in microcantilever sensors (EM- electromagnetic).

2.3 Microcantilever Transducers

Microcantilever transducers are micromechanical devices with high mechanical sensitivity, low thermal mass, simple design (making them easy to modify) and fabrication, and flexibility of operation. This makes them amenable to a variety of

sensing applications. Microcantilever sensors have been shown to be more sensitive than QCMs and SAW devices [23]. Microcantilevers have been used for applications as varied as metrology [24], thermal sensing and imaging [25, 26], scanning electrochemical microscopy [27], chemical sensing and biosensing applications [12, 14, 28-38], material characterization, etc.

2.3.1 Operational Modes

Microcantilever transducers can be operated in two detection modes- dynamic and static (Figure 2.4). In dynamic mode, the cantilever is used as a micromechanical oscillator and the effect of mass loading, stress, temperature change, the fluid environment or external forces is evaluated in terms of the shift in resonant frequency of the cantilever and/or the quality factor (Q) in various environments. In static mode detection, change in the desired measurand results in cantilever bending. This bending is picked up using the signal readout mechanism employed.

2.3.2 Methods of Signal Readout

Given the simplicity of microcantilever design and operation in static and dynamic modes, a variety of methods of signal readout may be employed. These are:

Optical- Optical readout is the most common form of signal measurement given its high sensitivity and extensive use in most commercial AFM (Atomic Force Microscope) systems. These use the position of the laser beam, reflected off the cantilever beam, on a photodiode to evaluate cantilever deflection. Interferometric schemes have also been implemented that allow for measurement of deflection as small as 0.01 Å. Limitations of these devices are associated with interference and attenuation in the media of detection. These cannot be used effectively in media with varying refractive index, high opacity and high turbidity.

Capacitive- Capacitive readout is based on measurement of deflection in terms of change in the gap between the cantilever and a fixed conductor. Capacitive microcantilever-based detection is also limited by interference caused by variation in the dielectric constant or density of the medium. Further these cannot be used in electrically conductive media.

Magnetic- Magnetic readout with cantilever systems has been used to measure deflection in static mode or as an actuation mechanism for resonant mode measurement. In the latter change in resonance is used to measure change in properties of the cantilever or environment. Magnetic readout, like capacitive readout is affected by properties of the fluid environment. In addition to this it requires a current loop on the cantilever which might result in heating of the cantilever and in cantilever deflection. For these reasons, it is not a preferred method of signal readout.

Electron Tunneling- Electron tunneling has been used extensively for highly sensitive deflection measurements in AFM studies. Deflections as small as 10^{-4} nm have been measured with such systems. However the tunneling characteristics are dependent on the media of detection. Further the dynamic range of measurement is extremely limited which makes this a poor choice for chemical sensing applications.

Piezoelectric- Piezoelectric readout is carried out via the deposition of a piezoelectric material such as ZnO. Deformation of the piezoresistor induces transient charge in the ZnO. When using in dynamic mode, the mechanical resonance of the device may be interrogated. This yields information on mass addition to the cantilever, surface stress, properties of the fluid media, etc. However operation in liquids results in loss in sensitivity. Also the ZnO thickness required for large signal output is often much larger than is acceptable for the optimal mechanical characteristics of the sensor.

Piezoresistive- Piezoresistivity refers to the change in bulk resistivity of certain materials on the application of stress. This has been used extensively in AFM probes for deflection measurement, gravimetric applications, flow measurement, measurement of fluid properties and the like. It is unaffected by properties of the medium of detection. However interrogation of resistance change requires flow of current through the piezoresistor and can result thermal fluctuation in the cantilever and in deformation of the cantilever and result in piezoresistance change.

2.4 Microcantilever-based Chemical and Biochemical Sensing

Microcantilever sensors have been used in a variety of chemical and biochemical detection applications. While some work has been done on pH sensors [34] and microcalorimetric sensors (to measure heat of reaction on the cantilever surface) [39], a

majority of the literature is related to chemical and biochemical sensing in liquids and gases wherein the analyte binding to a modified cantilever surface is measured.

In most surface stress-based cantilever sensors, the receptor of the microcantilever sensor allows for selective binding to the cantilever surface, resulting in surface stresses. The binding interaction with different surface modifications has been described in § 2.2.2. In order to evaluate the effect of analyte binding to the surface, microcantilevers can be used in static or dynamic mode. In static mode, mass sensitivity of cantilevers is extremely low and the measured parameter is surface stress associated with the interaction. In dynamic mode, mass sensitivity is very high and a large volume of literature is related to detection of analyte in terms of mass addition to the cantilever via the analyte-surface binding. However the cantilever may be designed so that surface stresses maybe evaluated while operating the cantilever is dynamic mode. Recent work by McFarland et al. [40] has shown steady state stresses of 0.48 mN/m for alkanethiols in liquid phase detection. If the temperature changes because of the chemical reaction on the cantilever surface, this can be evaluated using a calorimetric cantilever [26, 39, 41, 42].

2.4.1 Biosensors

Microcantilever sensors afford the possibility of label-free sensing of biological analytes [12, 38, 43]. Biosensing applications are normally carried out in liquid media. Detection of glucose has been carried out with glucose oxidase (GOx) immobilized on a cantilever [44]. Moulin et al. [45] reported on the development of compressive tensile stresses associated with nonspecific adsorption of immunoglobulin G (IgG) and bovine serum albumin (BSA) on gold-coated microcantilevers. Fritz et al. [46] reported on sensitive and specific monitoring of oligonucleotide hybridization using arrays of functionalized cantilevers and were able to detect a single base-pair mismatch. To demonstrate applicability of these methods to real biodetection problems, detection of low concentrations (0.2 ng/ml) of prostate specific antigen (PSA) was carried out in background buffered solutions containing physiological levels of both human serum albumin and human plasminogen [47].

2.5 Piezoresistive Microcantilevers for Chemical Sensing

Piezoresistance is the change in bulk resistivity due to mechanical stress or strain in a material [48-51]. The piezoresistive property of silicon has led to its application in pressure sensors [52], gyroscopes [53], accelerometers [54], AFM and other cantilever based probes, etc. This section introduces the specifics of piezoresistive properties of silicon, measurement techniques and related issues.

2.5.1 Piezoresistance in Silicon

Piezoresistive properties of silicon have been a topic of study for over fifty years now since work by Smith on the piezoresistance of silicon and later work by Tufte et al on the piezoresistive constants of heavily doped n-type silicon [55, 56]. Models for behavior of piezoresistance and second and higher order piezoresistance effects in p- and n-doped silicon have been developed by Kanda [48, 57-60] and others. A graphical representation was developed by Kanda which shows the magnitude of the various piezocoefficients of silicon along the different crystal directions Figure 2.5.

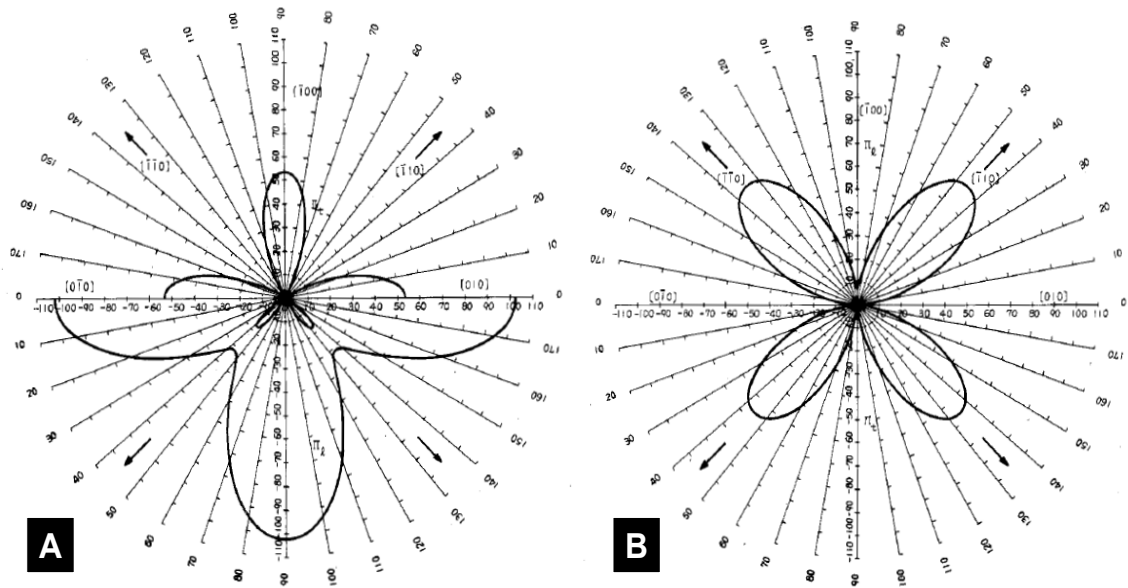


Figure 2.5 Piezoresistive coefficients in silicon at room temperature: A. n-type, B. p-type [57].

On the (100) plane of silicon the piezoresistive constants in the [110] and perpendicular to it are given by

$$\pi_{t,110} = \frac{1}{2}(\pi_{11} + \pi_{12} + \pi_{44}) \text{ and } \pi_{t,110} = \frac{1}{2}(\pi_{11} + \pi_{12} - \pi_{44}) \quad (2.6)$$

where π_{11} , π_{12} and π_{44} are the elements of the resistivity tensor for silicon. Most piezoresistive devices are fabricated on the (110) plane of silicon and the piezoresistive response of these devices may be evaluated as

$$\frac{\Delta R}{R} = \pi_l \sigma_l + \pi_t \sigma_t \quad (2.7)$$

2.5.2 Existing Piezoresistive Microcantilevers for Surface Stress Measurement

Most cantilever sensors used for chemical detection are based on optical detection of deflection. Given the limitations of optical sensors in numerous liquid phase and biological applications (§ 2.3.2), in recent years a number of groups have taken recourse to surface stress detection based on piezoelectric and piezoresistive microcantilever detection schemes [36, 37, 61, 62].

All existing piezoresistive microcantilever sensors for surface stress detection use p-type doping [37, 61-63]. This is surprising given the piezocoefficients associated with n-type silicon are much larger (Figure 2.5). As will be shown in Chapter 3, p-type doping is an excellent choice for measurement of stress at the clamped end of a cantilever as is often required in AFM-based probes. However n-type doping is more conducive to surface stress applications.

Surface stress sensitivity in cantilever-based surface stress measurement is evaluated using plates or beam models [64]. In existing work the effect of boundary conditions on surface stress sensitivity is ignored. This can result in an erroneous estimate of surface stress sensitivity of the cantilever sensor. The work of several groups in the area of piezoresistive microcantilever based surface stress sensing in

Table 2.1. As pointed out earlier all the silicon-based sensors use p-type doping. Hence the reported values of surface stress sensitivity (all of which are based on the Stoney equation [6] or related models) may be higher than the actual surface stress sensitivity of the piezoresistive cantilever sensors.

Table 2.1 Existing piezoresistive microcantilever sensors for surface stress detection.

Authors	Device Details	Novel Aspects/ Applications	Device Sensitivity
Thaysen et al. [29]	Multilayered P μ CA using polysilicon piezoresistors. Dimensions: 180 μ m x 100 μ m	- Integrated into a SU-8 flow cell for liquid phase detection - Polysilicon piezoresistor	4.4×10^{-4} (N/m) ⁻¹ [35]
Thaysen et al. [65]	SU-8-based cantilever with a gold strain gauge. Dimensions: 200 μ m x 100 μ m	- Use of lower Young's modulus of SU-8 for higher surface stress sensitivity	3×10^{-4} (N/m) ⁻¹ [65]
Volden et al. [32]	All-silicon cantilever. Dimensions: 300 μ m x 300 μ m. Thickness: 3 μ m	- Integrated with on-chip CMOS circuitry for measurement. - Integrated Wheatstone bridge.	Not available
Li et al. [63]	SOI-based multilayered piezoresistive microcantilever. Dimensions: 21 μ m x 91 μ m	- Use of XeF ₂ for bulk etching of silicon.	8.37×10^{-4} (N/m) ⁻¹

2.6 Array-based Detection Systems

Another development in the area of cantilever-based chemical and biochemical detection is the use of large arrays of cantilevers. This allows for numerous advantages over single cantilever detection [66]. Array can be used to analyze a complex mixture of analyte with separate cantilevers functionalized so that each is sensitive to a single chemical in the mixture. Further it has been seen that single- cantilever measurements may not be repeatable and use of cantilever arrays allow for detection of 'chemical signatures' that may also be used for positive identification and quantification of chemicals effectively creating an electronic nose [67]. Finally, the use of 'reference cantilevers' within the array, in which some cantilever are not functionalized, allows for thermal and mechanical filtering of environmental noise.

2.7 References

- [1] R. M. White, "A sensor classification scheme," *IEEE Transactions on Ultrasonics, Ferroelectrics and Frequency Control*, vol. UFFC-34, pp. 124-126, 1987.
- [2] A. Hulanicki, S. Glab, and F. Ingman, "Chemical sensors definitions and classification," *Pure and Applied Chemistry*, vol. 63, pp. 1247-1250, 1991.
- [3] D. R. Thévenot, K. Tothb, R. A. Durstc, and G. S. Wilson, "Electrochemical biosensors: recommended definitions and classification," *Biosensors and Bioelectronics*, vol. 16, pp. 121-131, 2001.
- [4] S. Satyanarayana, "Surface stress and capacitive MEMS sensor arrays for chemical and biological," in *Mechanical Engineering Berkeley*: University of California, 2005.
- [5] R. Shuttleworth, "The surface tension of solids," *Proceedings of the Physical Society of London Section B*, vol. 63, p. 374, 1950.
- [6] G. G. Stoney, "The tension of metallic films deposited by electrolysis," *Proceedings of the Royal Society of London Series a-Containing Papers of a Mathematical and Physical Character*, vol. 82, pp. 172-175, May 1909.
- [7] R. C. Cammarata and K. Sieradzki, "Surface and interface stresses," *Annual Review of Material Science*, vol. 24, pp. 215-234, 1994.
- [8] H. Ibach, "The role of surface stress in reconstruction, epitaxial growth and stabilization of mesoscopic structures," *Surface Science Reports*, vol. 29, pp. 193-263, 1997.
- [9] R. V. Kukta, D. Kouris, and K. Sieradzki, "Adatoms and their relation to surface stress," *Journal of the Mechanics and Physics of Solids*, vol. 51, pp. 1243-1266, Jul 2003.
- [10] M. Pierre and S. Andrés, "Elastic effects on surface physics," *Surface Science Reports*, vol. 54, pp. 157-258, 2004.
- [11] A. E. Love, *Treatise on the mathematical theory of elasticity*, 4 ed.: Dover Publications, 1944.

- [12] N. V. Lavrik, M. J. Sepaniak, and P. G. Datkos, "Cantilever transducers as a platform for chemical and biological sensors," *Review of Scientific Instruments*, vol. 75, pp. 2229-2253, 2004.
- [13] R. Berger, E. Delamarche, H. P. Lang, C. Gerber, J. K. Gimzewski, E. Meyer, and H.-J. Güntherodt, "Surface stress in the self-assembly of alkanethiols on gold probed by a force microscopy technique," *Applied Physics A*, vol. 66, pp. S55-S59, 1997.
- [14] P. Datkos and I. Sauer, "Detection of 2-mercaptoethanol using gold-coated micromachined cantilevers," *Sensors and Actuators B*, vol. 61, pp. 75-82, 1999.
- [15] M. A. Abraham, J. Andonian-Haftvan, C. M. Du, V. Diart, G. S. Whiting, J. W. Grate, and R. A. McGill, "Hydrogen bonding. Part 29. Characterization of 14 sorbent coatings for chemical microsensors using a new solvation equations," *Journal of Chemistry of Solids*, vol. 2, pp. 369-378, 1995.
- [16] J. W. Grate and S. J. Patrasch, "Selective vapor sorption by polymers and cavitands on acoustic wave sensors: Is this molecular recognition," *Analytical Chemistry*, vol. 68, pp. 913-916, 1996.
- [17] S.-C. Ha, Y. Yang, Y. S. Kim, Soo-Hyun Kim, Y. J. Kim, and S. M. Cho, "Environmental temperature-independent gas sensor array based on polymer composite," *Sensors and Actuators B*, vol. 108, pp. 258-264, 2005.
- [18] A. Hirlemann, E. T. Zellers, and A. J. Ricco, "Use of linear energy relationships for modeling responses from polymer-coated acoustic sensors," *Analytical Chemistry*, vol. 73, pp. 3458-3466, 2001.
- [19] J. Janata, *Chemical sensors*. Portland: Springer, 1989.
- [20] D. L. McCorkle, R. J. Warmack, S. V. Patel, T. Mlsna, S. R. Hunter, and T. L. Ferrell, "Ethanol vapor detection in aqueous environments using micro-capacitors and dielectric polymer," *Sensors and Actuators B*, vol. 107, pp. 892-903 2005.
- [21] D. Then, A. Vidic, and C. Ziegler, "A highly sensitive self-oscillating cantilever array for the quantitative and qualitative analysis of vapor mixtures," *Sensors and Actuators B*, vol. 117, pp. 1-9, 2006.

- [22] S. Hermes, F. Schroder, R. Chelmoski, C. Woll, and R. A. Fischer, "Selective nucleation and growth of metal-organic open framework thin films on patterned COOH/CF₃-terminated self-assembled monolayers on Au(111)," *Journal of the American Chemical Society*, vol. 127, pp. 13744-13745, 2005.
- [23] E. A. Wachter and T. Thundat, "Micromechanical sensors for chemical and physical measurements," *Review of Scientific Instruments*, vol. 66, pp. 3662-7, 1995.
- [24] R. Jumpertz, A. V. D. Hart, O. Ohlsson, F. Saurenbach, and J. Schelten, "Piezoresistive sensors on AFM cantilevers with atomic resolution," *Microelectronic Engineering*, vol. 41-42, pp. 441-4, 1998.
- [25] O. Nakabeppu, K. Hijikata, M. Chandrachud, J. Lai, and A. Majumdar, "Microscale temperature measurement using an atomic force microscope," *Nippon Kikai Gakkai Ronbunshu. B Hen (Transactions of the Japan Society of Mechanical Engineers. Part B)*, vol. 62, pp. 284-290, 1996.
- [26] J. Lai, T. Perazzo, Z. Shi, and A. Majumdar, "Infrared photodetection in the picowatt range using uncooled micromechanical sensors. ," in *Micro-Electro-Mechanical Systems (MEMS) International Mechanical Engineering Congress and Exposition*, 1996, pp. 55-9.
- [27] K. Eckhard, C. Kranz, H. Shin, B. Mizaikoff, and W. Schuhmann, "Frequency dependence of the electrochemical activity contrast in AC-scanning electrochemical microscopy and atomic force microscopy-AC-scanning electrochemical microscopy Imaging," *Analytical Chemistry*, vol. 79, pp. 5435-5438, 2007.
- [28] M. Sepaniak, P. Datskos, N. Lavrik, and C. Tripple, "Microcantilever transducers: A new approach to sensor technology," *Analytical Chemistry*, vol. 74, pp. 568-575, 2002.
- [29] J. Thaysen, "Cantilever for biochemical sensing integrated in a microhandling system," in *Mikroelektronik Centret Orsted's: University of Denmark*, 2001.
- [30] J. Thaysen, A. D. Yalcinkaya, R. K. Vestergaard, S. Jensen, M. W. Mortensen, P. Vettiger, and A. Menon, "SU-8 based piezoresistive mechanical sensor," in *Fifteenth IEEE International Conference on Micro Electro Mechanical Systems*, Las Vegas, NV, 2002, pp. 320-3.

- [31] T. Thundat, P. I. Oden, and R. J. Warmack, "Microcantilever sensors," *Microscale Thermophysical Engineering*, vol. 1, pp. 185-199, 1997.
- [32] T. Volden, "CMOS- Integrated cantilevers for biosensing and probe microscopy," in *Natural Sciences*. vol. Doctor of Natural Sciences Zurich: Swiss Federal Institute of Technology, 2005.
- [33] K. M. Hansen and T. G. Thundat, "Microcantilever biosensors," *Methods*, vol. 37, pp. 57-64, 2005.
- [34] S. R. Manalis, E. B. Cooper, P. F. Indermuhle, P. Kernen, P. Wagner, D. G. Hafeman, S. C. Minne, and C. F. Quate, "Microvolume field-effect pH sensor for the scanning probe microscope," *Applied Physics Letters*, vol. 76, pp. 1072-1074, 2000.
- [35] R. Marie, H. Jensenius, J. Thaysen, C. B. Christensen, and A. Boisen, "Adsorption kinetics and mechanical properties of thiol-modified DNA-oligos on gold investigated by microcantilever sensors," *Ultramicroscopy*, vol. 91, pp. 29-36, 2002.
- [36] A. W. McFarland and J. S. Colton, "Chemical sensing with micromolded plastic microcantilevers," *Journal of Microelectromechanical Systems*, vol. 14, 2005.
- [37] M. Morata, J. Amirola, F. Figueras, L. Fonseca, J. Santander, I. Gracia, M. Dominquez, A. Rodriguez, M. Horrillo, and C. Cane, "Micro-cantilevers for gas sensing," in *Spanish Conference on Electron Devices*, Tarragona, 2005.
- [38] C. Zeigler, "Cantilever-based biosensors," *Analytical and Bioanalytical Chemistry*, vol. 379, pp. 946-959, 2004.
- [39] J. K. Gimzewski, C. Gerber, E. Meyer, and R. R. Schlittler, "Observation of a chemical reaction using a micromechanical sensor," *Chemical Physics Letters*, vol. 217, pp. 589-594, 1994.
- [40] A. W. McFarland, M. A. Poggi, M. J. Doyle, L. A. Bottomley, and J. S. Colton, "Influence of surface stress on the resonance behavior of microcantilevers," *Applied Physics Letters*, vol. 87, p. 3, 2005.
- [41] T. Thundat, R. J. Warmack, G. Y. Chen, and D. P. Allison, "Thermal and ambient - induced deflections of scanning force microscope cantilevers," *Applied Physics Letters*, vol. 64, pp. 2894-2903, 1994.

- [42] J. Teng and P. D. Prewett, "Focussed ion beam fabrication of thermally actuated bimorph cantilevers," *Sensors and Actuators A*, vol. 123-124, pp. 608-613, 2005.
- [43] R. Raiteri, M. Grattarola, H.-J. Butt, and P. Skladal, "Micromechanical cantilever based biosensors," *Sensors and Actuators B*, vol. 79, pp. 115-126, 2001.
- [44] J. Pei, F. Tian, and T. G. Thundat, "Glucose biosensor based on the microcantilever," *Analytical Chemistry*, vol. 76, pp. 292-297, 2004.
- [45] A. M. Moulin, S. J. O'Shea, R. A. Bradley, P. Doyle, and M. E. Welland, "Measuring surface induced conformational changes in proteins," *Langmuir*, vol. 15, pp. 8776-8779, 1999.
- [46] J. Fritz, M. K. Baller, H. P. Lang, H. Rothuizen, P. Vettiger, E. Meyer, H.-J. Güntherodt, C. Gerber, and J. K. Gimzewski, "Translating biomolecular recognition into nanomechanics," *Science*, vol. 288, pp. 316-318, 2000.
- [47] G. Wu, H. Ji, K. Hansen, T. Thundat, R. Datar, R. Cote, M. Hagan, A. Chakraborty, and A. Majumdar, "Origin of nanomechanical cantilever motion generated from biomolecular interactions," *PNAS*, vol. 98, pp. 1560-1564, 2001.
- [48] Y. Kanda, "Piezoresistance effect in silicon," *Sensors and Actuators A*, vol. 28, pp. 83-91, 1991.
- [49] G. C. Kuczynski, "Effect of elastic stain on the electrical resistance of metals," *Physical Review*, vol. 94, pp. 61-64, 1954.
- [50] M. J. Madou, *Fundamentals of microfabrication*, 1 ed. Boca Raton: CRC Press, 2000.
- [51] S. D. Senturia, *Microsystem design*. New York: Springer-Verlag, 2000.
- [52] L. Yin and W. Wun, "Design, optimisation and fabrication of surface micromachined pressure sensors," *Mechatronics*, vol. 8, pp. 505-519, 1998.
- [53] X. X. Li, X. M. Chen, Z. H. Song, P. T. Dong, Y. L. Wang, J. W. Jiao, and H. Yang, "A microgyroscope with piezoresistance for both high-performance coriolis-effect

- detection and seesaw-like vibration control," *Journal of Microelectromechanical Systems*, vol. 15, pp. 1698-1707, Dec 2006.
- [54] "<http://www.hitachimetals.com/product/sensors/mems/piezoresistive.cfm>," Hitachi 3-axis accelerometer (October, 2007).
- [55] C. S. Smith, "Piezoresistance effect in Germanium and Silicon," *Physical Review*, vol. 94, pp. 42-48, 1954.
- [56] O. N. Tufte and E. L. Stelzer, "Piezoresistive properties of heavily doped n-type silicon," *Physical Review*, vol. 166, pp. A1705-A1716, 1964.
- [57] Y. Kanda, "A graphical representation of the piezoresistance coefficients in silicon," *IEEE Transactions on Electron Devices*, vol. 29, pp. 64-70, 1982.
- [58] K. Matsuda, Y. Kanda, K. Yamamura, and K. Suzuki, "Nonlinearity of piezoresistance effect in p-type and n-type silicon," *Sensors and Actuators a-Physical*, vol. 21, pp. 45-48, Feb 1990.
- [59] K. Matsuda, K. Suzuki, K. Yamamura, and Y. Kanda, "Nonlinear piezoresistance effects in silicon," *Journal of Applied Physics*, vol. 73, pp. 1838-1847, Feb 1993.
- [60] Y. Kanda and A. Yasukawa, "Optimal design consideration for piezoresistive pressure sensors," *Sensors and Actuators A*, vol. 62, pp. 539-542, 1997.
- [61] J. Thaysen, A. D. Yalcinkaya, R. K. Vestergaard, S. Jensen, M. W. Mortensen, P. Vettiger, and A. Menon, "SU-8 based piezoresistive mechanical sensor," in *Fifteenth IEEE International Conference on Micro Electro Mechanical Systems*, Las Vegas, NV, 2002, p. 320.
- [62] T. Volden, "CMOS-Integrated cantilevers for biosensing and probe microscopy," Zurich: Swiss Federal Institute of Technology, 2005.
- [63] P. Li and X. Li, "A single-sided micromachined piezoresistive SiO₂ cantilever sensor for ultra-sensitive detection of gaseous chemicals," *Journal of Micromechanics and Microengineering*, pp. 2539-2546, 2006.

- [64] J. Gere and S. Timoshenko, *Mechanics of materials*, Fourth ed. Boston: PWS Publishing Company, 1997.
- [65] J. Thaysen, A. D. Yalcinkaya, P. Vettiger, and A. Menon, "Polymer-based stress sensor with integrated readout," *Journal of Applied Physics D: Applied Physics*, vol. 35, pp. 2698–2703, 2002.
- [66] H. P. Lang, M. Hegner, and C. Gerber, "Cantilever sensor arrays," *Materials Today*, vol. 8, 2005.
- [67] T. C. Pearce, S. S. Schiffman, H. T. Nagle, and J. W. Gardner, *Handbook of Machine Olfaction*: WileyOVCH, 2003.

CHAPTER 3

MATERIAL DESIGN AND NOISE ISSUES

The previous chapter discusses the background associated with the use of microcantilevers for chemical sensing and current work on chemical sensing with piezoresistive microcantilever systems. This chapter discusses material related issues in the design of piezoresistive microcantilevers for surface stress sensing. All existing microcantilever surface stress sensors that are based on single-crystal silicon use p-doped piezoresistors. In this work, the advantages of using n-doped silicon piezoresistors for surface stress sensing have been demonstrated. Also, estimates of Johnson, Hooge and thermal vibration noise in the piezoresistive microcantilever leads to recommendations for operating frequencies to minimize noise and to estimate of minimum detectable stress.

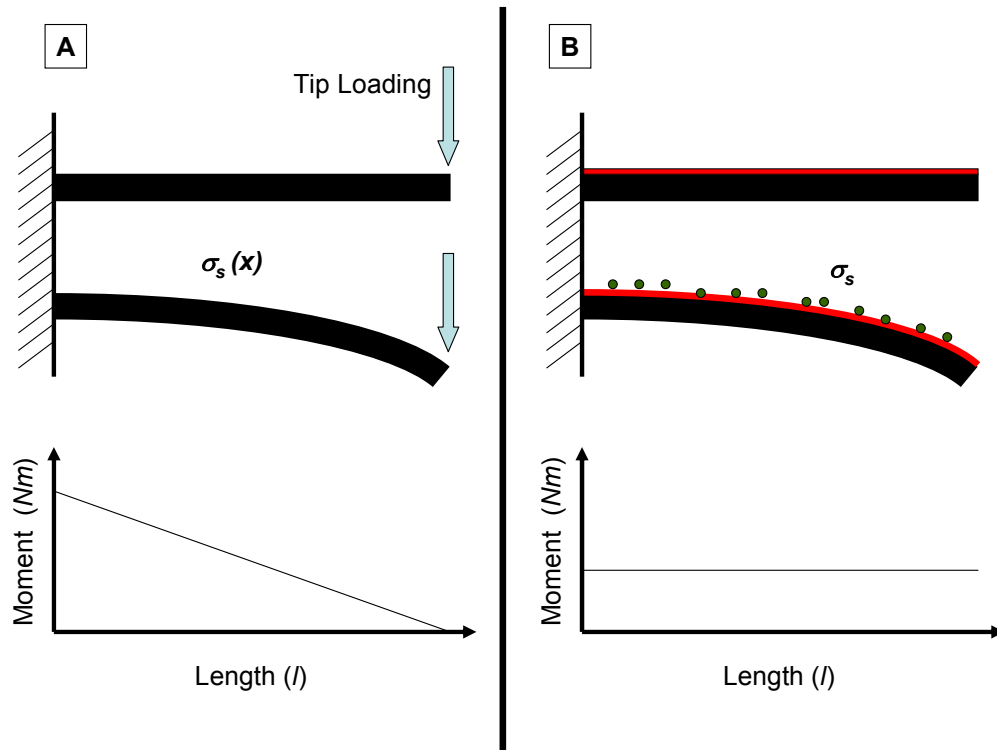


Figure 3.1 Comparison of loading effects in A. AFM-type cantilever and B. surface-stress based cantilevers. The cantilever deflects due to surface stress associated with analyte binding.

3.1 Elements of Piezoresistive Microcantilever Design

Design of the P μ CA involves choice of cantilever geometry, materials, array design and choice of operating conditions that enable high sensitivity and low-noise measurement for low detection limit measurement of the chosen analyte (selectivity is, for most part, determined by the functionalization of the cantilever surface and not the focus of this dissertation).

A significant error in most current work is that piezoresistive microcantilevers for surface stress- based sensing are designed on the lines of piezoresistive microcantilevers for AFM probes. AFM probes are designed for measurement of tip loading. Figure 3.1 shows how the largest moments are generated at the clamped end of an AFM probe. Hence piezoresistors are built at the clamped end of the cantilever where the highest stresses due to tip-loading occur. Uniform surface stresses on a cantilever, however, results in a uniform moment throughout the cantilever. There is no well-defined region of maximum surface stress. Also since the surface stresses are local, they may not affect a response in a piezoresistor distant from the location of surface stress. Hence design requirements of piezoresistive microcantilevers for surface stress measurement are:

- The piezoresistor must be placed in the region of surface stress.
- The piezoresistive response ($\frac{\Delta R^s}{R}$) should be maximized.

While most current work recognizes the importance of resistor placement, no existing cantilever devices fully addresses various aspects of maximizing piezoresistive response. Design of the piezoresistive microcantilever such that the piezoresistive response is large may achieved by appropriate design of doping and geometry for silicon piezoresistors. This chapter deals with the former while issues related to design of geometry are taken up in Chapter 4.

3.1.1 Geometry of the Piezoresistive Microcantilevers

A P μ CA consisting of ten rectangular cantilevers has been designed. Figure 3.2 shows the geometric parameters of a single cantilever. Piezoresistive cantilever designs based on all-silicon cantilevers are created by doping a selected region of the cantilever. However, in this work, the piezoresistors were created by doping and patterning the SCS

layer of a silicon-on-insulator (SOI) wafer. Hence the piezoresistors occupy a distinct layer within the multilayered structure. An important parameter to note is δ , the distance of the piezoresistor from the clamped end (Figure 3.2).

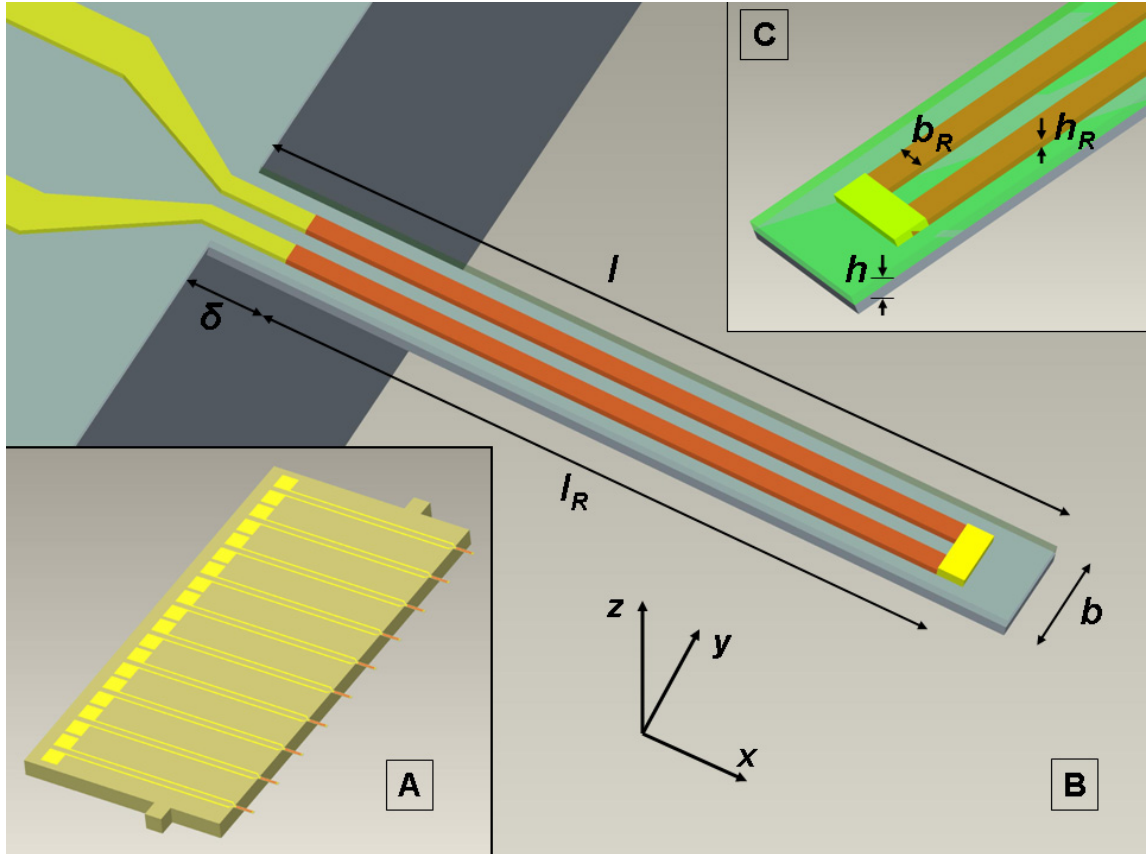


Figure 3.2 P μ CA schematic and geometric parameters. (A) A ten-cantilever array. (B) An individual cantilever. (C) Close-up of the piezoresistor.

3.2 Material Design

The large gauge factors of silicon make it an ideal candidate for use in various forms of stress measurement. Smith's seminal work on piezoresistive constants of silicon [1] led to a realization of its applicability to various forms of pressure, deformation, and stress sensing. Work by Tufte et al. [2] and Kanda [3, 4] has led to the development of models for piezoresistance in p-type and n-type silicon. Piezoresistance has been used in numerous applications; e.g., accelerometers, gyroscopes, dynamometers [5]. Also, in recent years, it has been used in microcantilever-based measurement in AFM probes [6] and surface stress sensors.

The effect of doping on surface stress sensitivity is a crucial element in the design of SCS-based piezoresistive microcantilevers but has been ignored until recently. Recent work by Rasmussen et al. [7] suggests that n-type piezoresistors have higher effective gauge factors than p-type piezoresistors for surface-stress-based piezoresistive cantilever sensors. In this work we will demonstrate further advantages of using n-type silicon for detection based on surface stress.

3.2.1 State of Stress in the Microcantilever

To demonstrate the effect of doping type on surface stress sensitivity, let us consider the surface stress response of the piezoresistor in a multilayered cantilever. The orientation of the axes is shown in Figure 3.2. In all the work that follows, we will assume that the longitudinal direction of the cantilever is along the x -axis and that the transverse direction is along the y -axis.

For a piezoresistor with resistance R , resistivity ρ , length l , width w and thickness t , the relative change in piezoresistance ($R = \rho l / wt$) is given by [4]

$$\frac{\Delta R^s}{R} = \frac{\Delta l}{l} - \frac{\Delta w}{w} - \frac{\Delta t}{t} + \frac{\Delta \rho}{\rho} = \varepsilon_x - \varepsilon_y - \varepsilon_z + \frac{\Delta \rho}{\rho} \quad (3.1)$$

For plain stress ($\sigma_z = 0$), the relative change in piezoresistance of a silicon piezoresistor, with Young's modulus E and Poisson ratio ν , is given by [8]

$$\frac{\Delta R^s}{R} = (\varepsilon_x - \varepsilon_y - \varepsilon_z) + \sigma_x \pi_x + \sigma_y \pi_y \quad (3.2)$$

$$\text{Also, } \varepsilon_x = \frac{1}{E}(\sigma_x - \nu \sigma_y), \varepsilon_y = \frac{1}{E}(\sigma_y - \nu \sigma_x), \varepsilon_z = -\frac{\nu}{E}(\sigma_x + \sigma_y) \quad (3.3)$$

$$\text{Therefore, } \frac{\Delta R^s}{R} = \sigma_x \left(\frac{1+2\nu}{E} + \pi_x \right) + \sigma_y \left(-\frac{1}{E} + \pi_y \right) \quad (3.4)$$

Near the clamped end $\varepsilon_y = 0$ and $\sigma_y = \nu \sigma_x$. Hence,

$$\left. \frac{\Delta R^s}{R} \right|_{\text{Clamped End}} = \left(\frac{1+\nu}{E} + \pi_x + \nu \pi_y \right) \sigma_x = S_{\text{clamped}} \sigma_x \quad (3.5)$$

Far from the clamped end of the cantilever, $\sigma_x \approx \sigma_y$. Therefore,

$$\left. \frac{\Delta R^s}{R} \right|_{Free\ End} = \left(\frac{2\nu}{E} + \pi_x + \pi_y \right) \sigma_x = S_{free} \sigma_x \quad (3.6)$$

3.2.2 Effect of Doping on Piezoresistor Response

The effect of p-type and n-type doping on the surface stress sensitivities, $S_{clamped}$ and S_{free} , is tabulated in Table 3.1. The results presented in this section are based on piezoresistive constants for a doping level of 10^{16} cm^{-3} (Table 3.1).

Table 3.1. Longitudinal (π_x) and transverse (π_y) piezocoefficients in [110] silicon^a. Surface stress sensitivities for various boundary conditions show the advantage of n-type doping.

Doping	p-type	n-type
π_x (10^{-11} Pa^{-1})	72	-31
π_y (10^{-11} Pa^{-1})	-66	-18
$S_{clamped}$	54.93	-36.61
S_{free}	6.31	-49.32

^a Source: O. N. Tufte and E. L. Stelzer, "Piezoresistive properties of heavily doped n-type silicon", Physical Review, vol. 166, A1705-A1716, 1964

As can be seen from Table 3.1, far from the clamped end, where chemical sensing occurs, n-type piezoresistors have higher strain sensitivity than p-type piezoresistors. The results also suggest that the effective gage factors for a piezoresistor will change based on its length. Stresses in the longitudinal and transverse directions of a $200 \times 50 \mu\text{m}$ cantilever, that had a layer structure similar to that of the P μ CA, were evaluated using ANSYSTM (Figure 3.3).

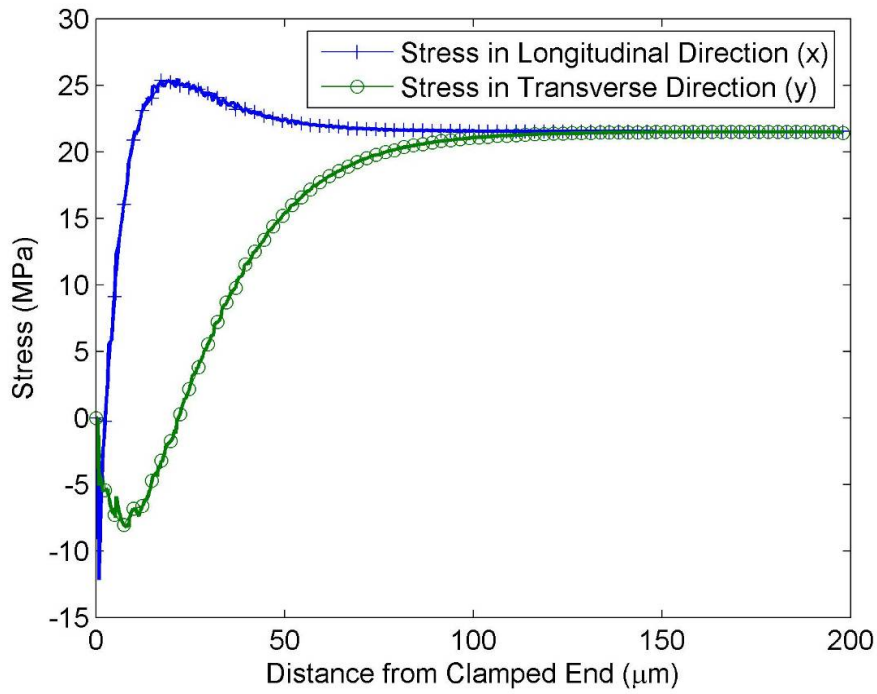


Figure 3.3 Longitudinal and transverse stress (in the piezoresistor) along the length of a $200 \times 50 \mu\text{m}$ microcantilever under uniform surface stress of 60 N/m .

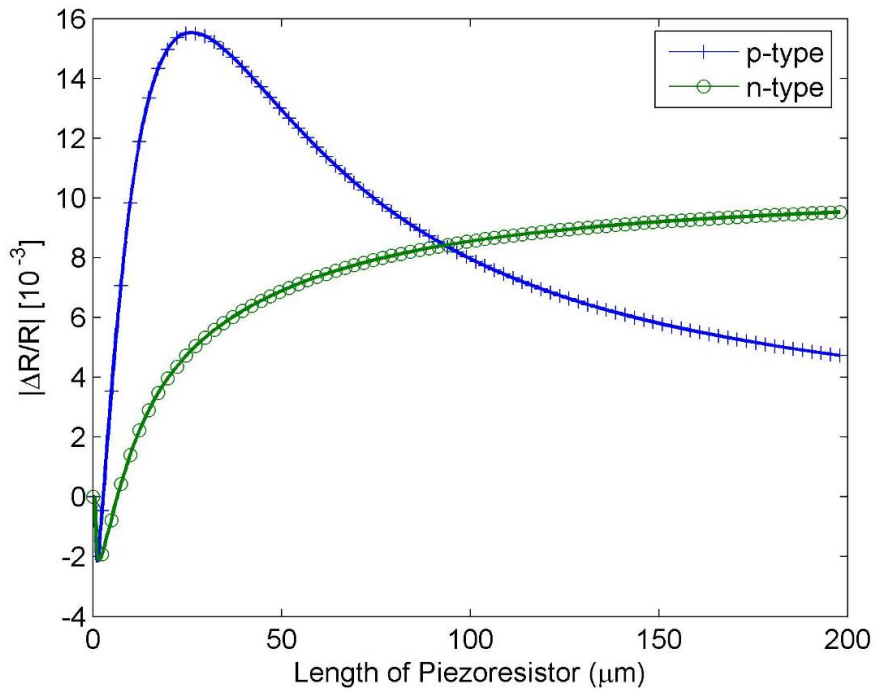


Figure 3.4 Piezoresistor response for different resistor lengths (l_R). Here $\delta = 0$. Use of n-type silicon is advantageous for $l_R > 93.6 \mu\text{m}$.

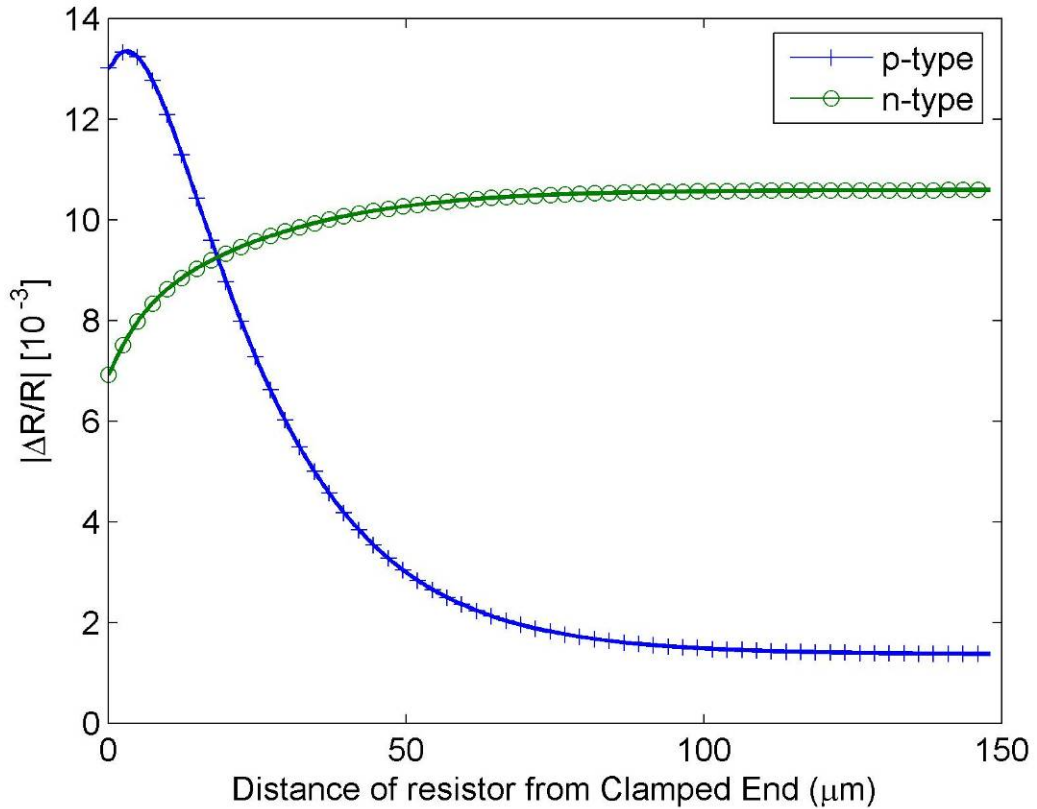


Figure 3.5 Piezoresistor response for different resistor positions (δ) with a fixed resistor length ($l_R = 50 \mu\text{m}$). Use of n-type silicon piezoresistors is advantageous for $\delta > 18.4 \mu\text{m}$.

The piezoresistor response, $\frac{\Delta R^s}{R}$, for this stress-strain profile is shown in Figure 3.3. We see that n-type doping is more effective if the piezoresistor is longer than a critical length (Figure 3.4). However, the response is significantly enhanced if the piezoresistor is positioned at some distance (δ) from the clamped end of the cantilever. For this simple cantilever structure, the enhancement in response of n-type over p-type for a resistor $50 \mu\text{m}$ long is significant (Figure 3.5). If $\delta > 50 \mu\text{m}$, an n-type piezoresistor is approximately five times more sensitive than a p-type piezoresistor. We also notice that the surface stress sensitivity is nearly constant for $\delta > 50 \mu\text{m}$. This result is very significant because it implies that the surface stress sensitivity remains unaffected by small deviations in the actual clamping distance (δ') from the designed clamping distance (δ), potentially due to variations in the bulk etch of the silicon (this is discussed in greater detail in Chapter 5). While the critical lengths evaluated are valid only for this

particular cantilever geometry (Figure 3.4 and Figure 3.5), the trends shown here are true for all cantilever devices, and the results show the benefits of n-type piezoresistors for sensing based on surface stress.

This analysis suggests that n-doped silicon piezoresistors are superior to p-doped piezoresistors for surface stress sensing applications. Also appropriate design of the parameter δ can result in a significant improvement in piezoresistive microcantilever response.

3.3 Sources of Noise in Piezoresistive Microcantilevers

In the measurement of surface stress using piezoresistive readout, the resolution of the measurement is limited by sources of noise in the piezoresistive microcantilever system. While system noise and noise during analyte measurement in a flow environment are considerable, this section deals only with noise in the piezoresistive microcantilever. The sources of noise in the cantilever are electrical- Johnson noise and Hooge noise, and thermomechanical or vibration noise.

3.3.1 Johnson Noise

Johnson noise is caused by thermal fluctuation of carriers in the resistor. The Johnson noise voltage power for a resistor is

$$\langle V_J^2 \rangle = 4k_B TR\Delta f \quad (3.7)$$

where k_B is the Boltzmann constant, T the Kelvin temperature, R the resistance of the cantilever and $\Delta f = f_{max} - f_{min}$ is the bandwidth of measurement. Since $R = \frac{\rho l_R}{h_R w_R}$,

$\langle V_J^2 \rangle$ is directly proportional to resistor length, and inversely proportional to resistor thickness and resistor width.

3.3.2 Hooge Noise

The Hooge noise, also referred to as $1/f$ noise, in a resistor is the frequency dependent noise. The spectral density of $1/f$ noise is given by

$$S_H = \frac{\alpha V_s^2}{fN} \quad (3.8)$$

The noise voltage power associated with Hooge noise is

$$\langle V_H^2 \rangle = \frac{\alpha V_s^2}{N} \log \left(\frac{f_{\max}}{f_{\min}} \right) \quad (3.9)$$

where α is a material constant, V_s is the supply voltage and $N = nl_R h_R w_R$ and n is the carrier concentration in the resistor. α has been shown to be a function of doping and annealing conditions [9]. Hence Hooge noise is inversely proportional to the volume of the cantilever.

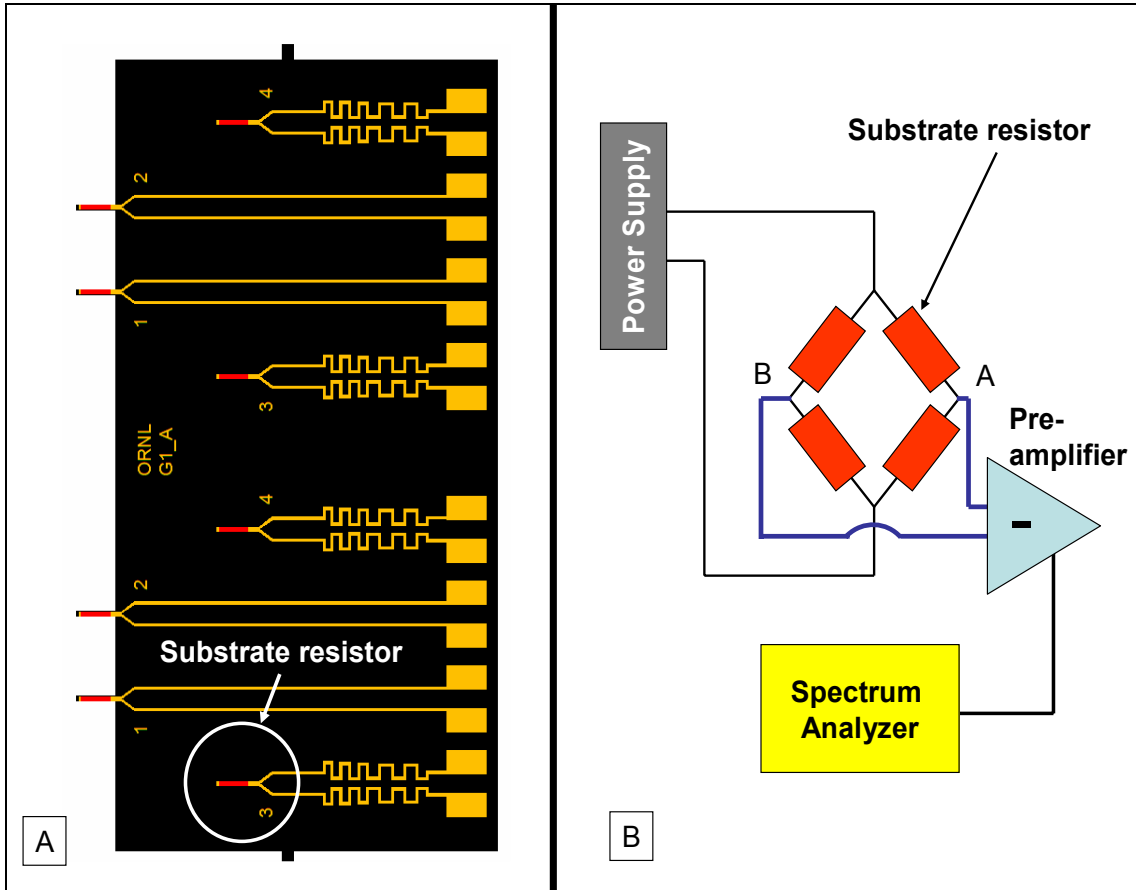


Figure 3.6 A. Device with four substrate resistors used for measurement of $1/f$ noise. B. Schematic of circuit used for measurement of $1/f$ noise.

The material constant α was determined by measuring Hooge noise in silicon resistors manufactured in the same process as the $P\mu CA$. Figure 3.6 shows the device that was used for this experiment. The device has four silicon resistors on the substrate were used in a Wheatstone bridge. A Tektronix PS2520G programmable power supply

(Tektronix Inc., Beaverton, OR) was used as the voltage source. The output from the Wheatstone bridge was amplified using a SR560 low-noise preamplifier (Stanford Research Systems, Sunnyvale, CA) and spectral analysis was performed using a SR785 dynamic signal analyzer (Stanford Research Systems, Sunnyvale, CA).

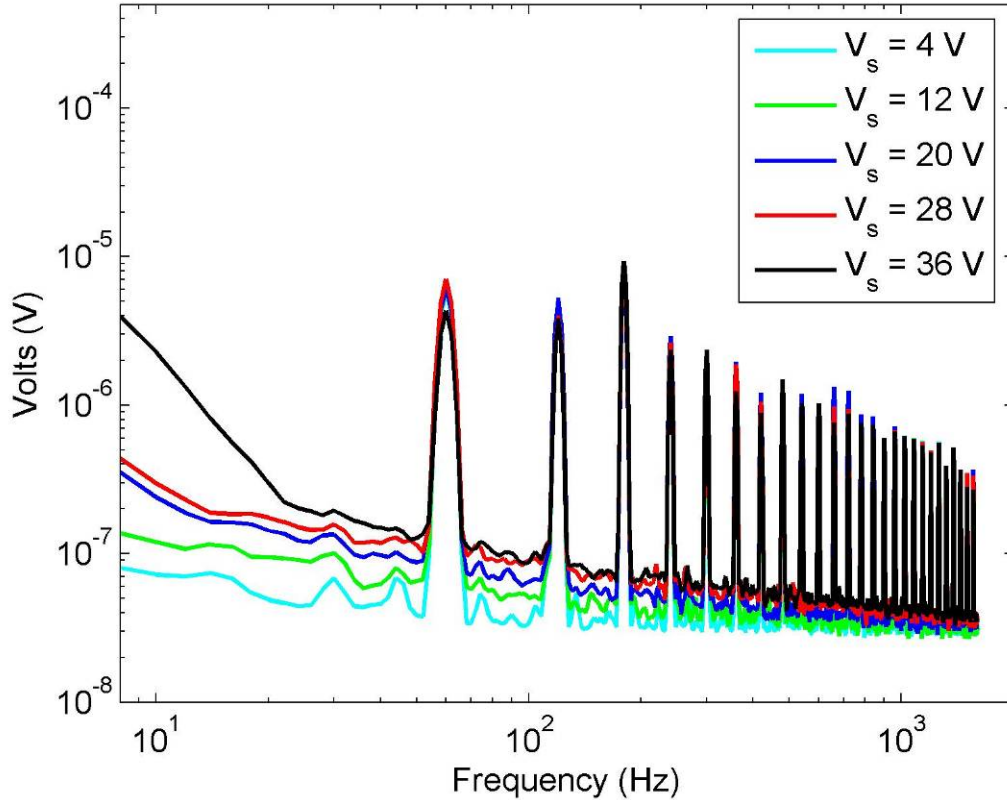


Figure 3.7 $1/f$ noise spectrum measured using substrate resistors.

The $1/f$ noise was measured for different values of supply voltage and these are plotted in Figure 3.7. The large frequency peaks are associated with 60 Hz noise. Comparing the data to (3.9), we can examine the extent of agreement. The noise measured in Figure 3.7 is much greater than predicted by $1/f$ noise theory (3.9). If the value of α is evaluated using (3.9), the value obtained is of the order of 10^{-1} while the range for doped silicon has been shown to be between 10^{-3} and 3×10^{-6} [9, 10] for the doping and annealing conditions in this work.

The value of α used for estimation of noise in the system is 3.2×10^{-3} , which is based on the corner frequency observed in our measurement (approximately 2 kHz). This

value is also in agreement with the experimentally obtained value for a doping level of $3 \times 10^{-19} \text{ cm}^{-3}$ and annealing at $1050 \text{ }^\circ\text{C}$ for 30 minutes [10]. The error in the measurement of α is possibly due to the strong presence of 60 Hz noise in the spectrum which is unrelated to device operation.

3.3.3 Vibration Noise

An important source of noise in a free-standing cantilever is vibration noise. This is evaluated by summing up over all the vibrational modes of the cantilever. Thaysen [10] suggests that the measurement noise associated with this vibration is given by

$$\langle V_{noise}^2 \rangle = \frac{k_B^2 T l^2}{27 k l_R \left(1 - \frac{1}{2} \frac{l_R}{l}\right)^2} \frac{\Delta f}{f_{res}} \quad (3.10)$$

Some other expressions of this form are presented in literature [11-13] but all of these are based on stress generation in the cantilever which is used in an atomic force microscope (AFM). Since the probe experiences a point load in this case, the stress developed in the cantilever over its length is a function of the distance of the point of contact from the fixed end of the cantilever. On the other hand, in a piezoresistive microcantilever for measurement of surface stress, stresses are uniform over the length of the cantilever and the equations for measurement noise due to cantilever vibration must be developed differently.

3.3.3.1 Vibration Noise in a Microcantilever-based Piezoresistive Surface Stress Sensor

For a cantilever beam of length l , width w and thickness h , the transverse vibration of a cantilever beam is described by the equation:

$$\frac{d^2 z}{dt^2} + \frac{Eh^2}{12\rho} \frac{d^4 z}{dt^4} = 0 \quad (3.11)$$

The density of the cantilever beam material is ρ and E is the Young's modulus. The boundary conditions for a free cantilever beam are

$$\Phi(0) = 0, \quad \frac{d\Phi(0)}{dx} = 0 \quad (3.12)$$

and
$$\frac{d\Phi^2(l)}{dx^2} = 0, \frac{d\Phi^3(l)}{dx^3} = 0 \quad (3.13)$$

The first two conditions state that amplitude and inclination of the beam at the clamped end are zero. The last two conditions state that external shear force and external moment at the free end of the cantilever are zero.

The solution for this system of equations is a measure of the thermomechanical vibration noise in a cantilever [14]:

$$z = \sum_{i=1}^{\infty} q_i \Phi_i \quad (3.14)$$

where

$$\Phi_i = (\sin \alpha_i + \sinh \alpha_i) \left(\cos \frac{\alpha_i}{l} x - \cosh \frac{\alpha_i}{l} x \right) - (\cos \alpha_i + \cosh \alpha_i) \left(\sin \frac{\alpha_i}{l} x - \sinh \frac{\alpha_i}{l} x \right) \quad (3.15)$$

where if ω_i is the i^{th} fundamental frequency of the cantilever beam,

$$\alpha_i = \frac{12\rho\omega_i^2 l^4}{Eh^2} \quad (3.16)$$

Butt et al. [14] have shown, using the equipartition theorem,

$$\langle q_i^2 \rangle = \frac{3k_B T}{\alpha_i^2 k (\sin \alpha_i + \sinh \alpha_i)^2} \quad (3.17)$$

3.3.3.2 Noise in Piezoresistive Readout

The thermomechanical noise in a cantilever results in noise in the piezoresistive response of the piezoresistive region of the silicon cantilever. Now, in the piezoresistive surface stress sensitive cantilever,

$$\frac{\Delta V}{V_s} = B \frac{\Delta R}{R} = -BS_{R\sigma} \bar{\sigma} \quad (3.18)$$

B is the factor associated with measurement using a differential bridge ($B = 4$ for a full differential bridge and $B = 2$ for a half bridge), $\bar{\sigma}$ is the average stress over the length of the cantilever developed as a result of the interaction between the analyte and

the top surface and V_s is the supply voltage. $S_{R\sigma}$ is the transfer function that relates the surface stress to the piezoresistive response.

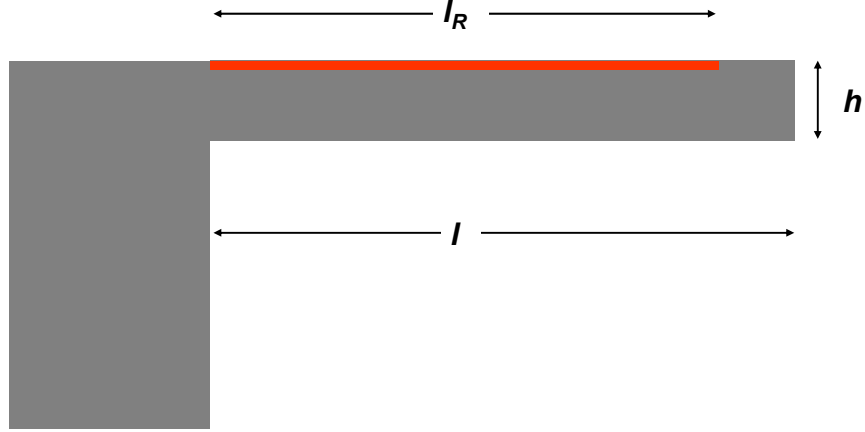


Figure 3.8 Schematic of piezoresistive microcantilever beam

Assuming stresses only along the longitudinal direction (x -direction) of the beam, for a surface stress sensitive microcantilever with a thin piezoresistor at the top (Figure 3.8), $S_{R\sigma} = \pi_{eff}$, where π_{eff} maybe be evaluated as

$$\pi_{eff} = \frac{\frac{1}{l_R} \int_0^{l_R} \pi(x) \sigma(x) dx}{\frac{1}{l_R} \int_0^{l_R} \sigma(x) dx} \quad (3.19)$$

Now,

$$\frac{\Delta R}{R} = \frac{1}{l_R} \int_0^{l_R} -\pi_{eff} \sigma_s(x) dx = \frac{\pi_{eff}}{l_R} \int_0^{l_R} E \frac{\partial^2 z}{\partial x^2} \frac{h}{2} dx = \pi_{eff} \frac{Eh}{2l_R} \frac{\partial z(l_R)}{\partial x} \quad (3.20)$$

where σ_s is the surface stress at a given location on the cantilever. The lower limit of the integration is zero based on the boundary conditions. For a perfectly nulled Wheatstone bridge,

$$V_{out} = B\pi_{eff} V_s \frac{Eh}{2l_R} \frac{\partial z(l_R)}{\partial x} = B\pi_{eff} V_s \frac{Eh}{2l_R} \sum_{i=1}^{\infty} q_i \frac{\partial \Phi_i(l_R)}{\partial x} \quad (3.21)$$

$$\Rightarrow \langle V_{i,\text{piezonoise}}^2 \rangle = \left(B\pi_{\text{eff}} V_s \frac{Eh}{2\lambda} \right)^2 \langle q_i^2 \rangle \left(\frac{\partial \Phi_i(l_R)}{\partial x} \right)^2 \quad (3.22)$$

$$\Rightarrow \langle V_{i,\text{piezonoise}}^2 \rangle = \left(B\pi_{\text{eff}} V_s \frac{Eh}{2\lambda} \right)^2 \left(\frac{3k_B T}{\alpha_i^2 k (\sin \alpha_i + \sinh \alpha_i)^2} \right) \left(\frac{\partial \Phi_i(l_R)}{\partial x} \right)^2 \quad (3.23)$$

Now let,

$$\frac{\partial \Phi_i(l_R)}{\partial x} = -\frac{\alpha_i}{l} J_i(l_R) \quad (3.24)[11]$$

where,

$$J_i(l_R) = (\sin \alpha_i + \sinh \alpha_i) \left(\sin \frac{\alpha_i l_R}{l} + \sinh \frac{\alpha_i l_R}{l} \right) + (\cos \alpha_i + \cosh \alpha_i) \left(\cos \frac{\alpha_i l_R}{l} - \cosh \frac{\alpha_i l_R}{l} \right) \quad (3.25)$$

From these relations, we obtain

$$\frac{\langle V_{\text{piezonoise}}^2 \rangle}{\langle V_s^2 \rangle} = \frac{3k_B T}{k} \left(B\pi_{\text{eff}} \frac{Eh}{2l_R} \right)^2 \frac{1}{l^2} \sum_{i=1}^{\infty} \frac{J_i^2(l_R)}{\alpha_i^2 (\sin \alpha_i + \sinh \alpha_i)^2} \quad (3.26)$$

The summation converges to $\frac{l_R}{l}$ [11]. Since the spring constant of the cantilever is

$$k = \frac{3Ewh^3}{l^3},$$

$$\frac{\langle V_{\text{piezonoise}}^2 \rangle}{\langle V_s^2 \rangle} = \frac{3k_B T}{k} \left(B\pi_{\text{eff}} \frac{Eh}{2l_R} \right)^2 \frac{1}{l^2} \frac{l_R}{l} = \frac{3k_B T E B^2 \pi_{\text{eff}}^2}{l_R w h} \quad (3.27)$$

This relation proves that for the system described before, noise in piezoresistive readout is also inversely proportional to length and width of the resistor. The noise in piezoresistive readout in a silicon cantilever for $V_s = 1$ V under ambient conditions is shown in Figure 3.9.

3.3.4 Total System Noise

Total noise in the piezoresistive microcantilever may be evaluated as:

$$\langle V_{Total\ noise}^2 \rangle = \langle V_J^2 \rangle + \langle V_H^2 \rangle + \langle V_{piezonoise}^2 \rangle \quad (3.28)$$

Figure 3.10 shows the different noise components for cantilever measurement as a function of silicon piezoresistor length at 25 °C with a frequency of measurement of 10 kHz and a bandwidth of 10 Hz (conditions under which measurements were made- refer Chapter 6) as a function of resistor length.

For a piezoresistive cantilever 500 μm long with a piezoresistor length of 400 μm , the variation of noise in the piezoresistive response with frequency is shown by Figure 3.11.

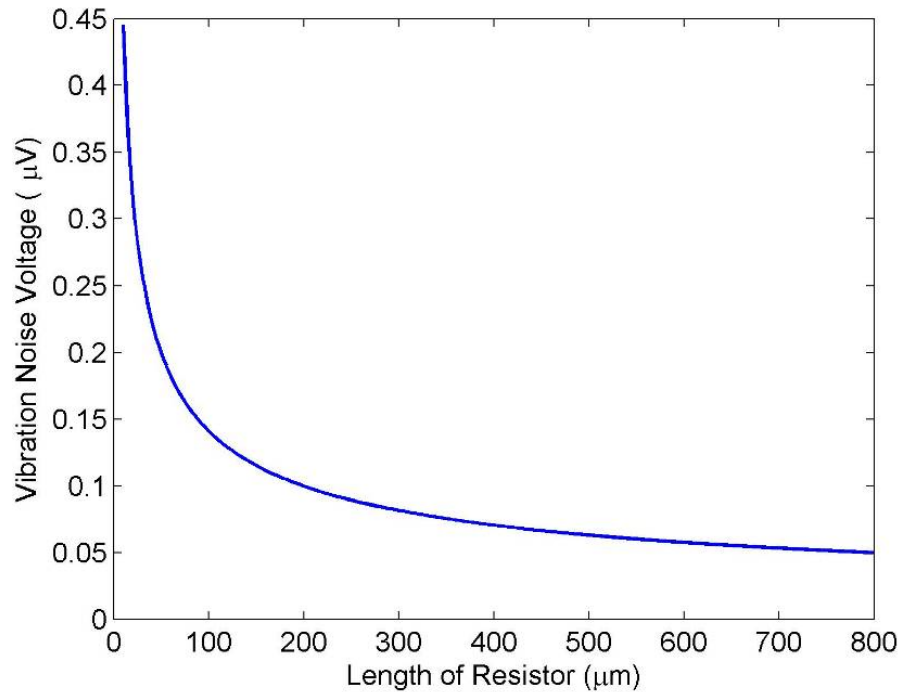


Figure 3.9 Variation of vibration noise with length of the piezoresistor (l_R).

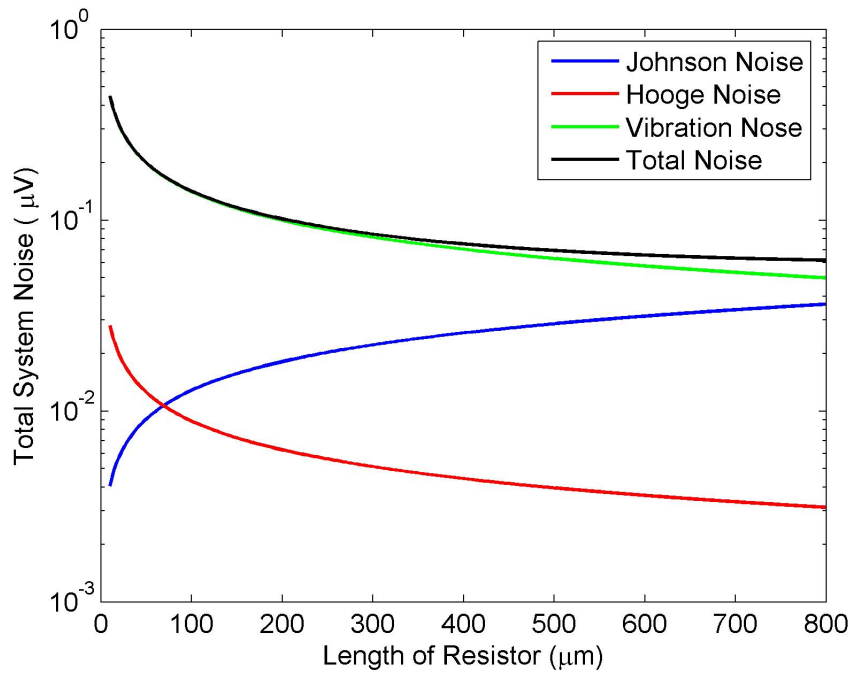


Figure 3.10 Variation of various noise sources with resistor length at 10 kHz with a bandwidth of 10 Hz.

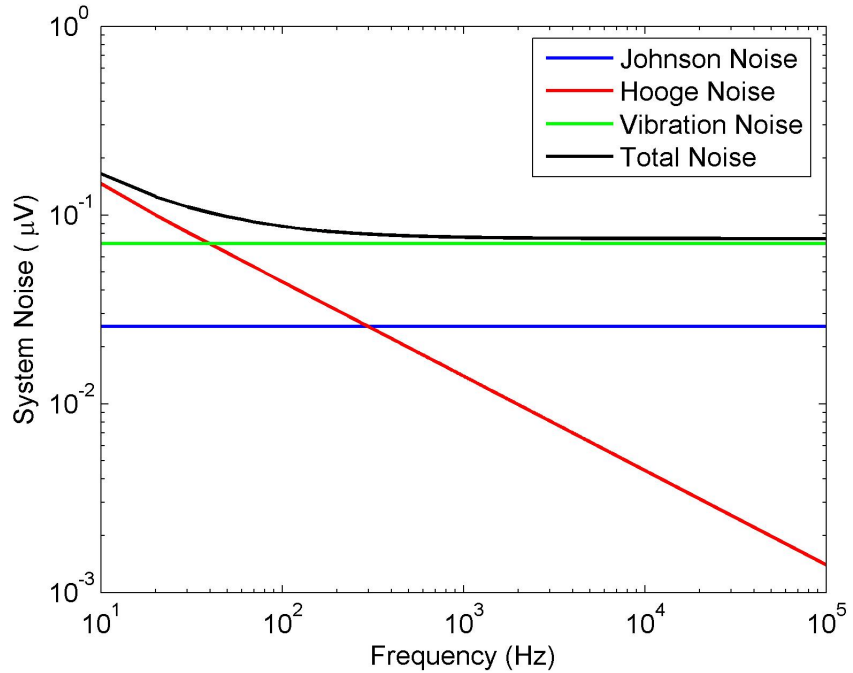


Figure 3.11 Variation of noise sources with frequency of electrical excitation of the piezoresistive microcantilever.

The noise analysis shows that cantilever noise decreases with increase in length of the piezoresistor. Further $1/f$ noise effects in the piezoresistor are negligible beyond the corner frequency of approximately 2 kHz.

Thermomechanical vibration noise associated with Brownian motion is very small in magnitude and has almost no effect on the total noise in the piezoresistive microcantilever. In a real microcantilever that is deployed in a flow environment, thermomechanical noise can be very large. Filtering of such noise effect can be effected by use of reference cantilevers.

3.4 Effect of Doping Parameters

Doping level has little effect on the relative position and length of the piezoresistors from the perspective of maximizing surface stress sensitivity. It does however have an important contribution to the magnitude of piezoresistive coefficient and temperature coefficient of resistance (TCR) of the piezoresistor. Figure 3.12 shows the change in piezoresistive coefficients with doping level and temperature for n-type silicon.

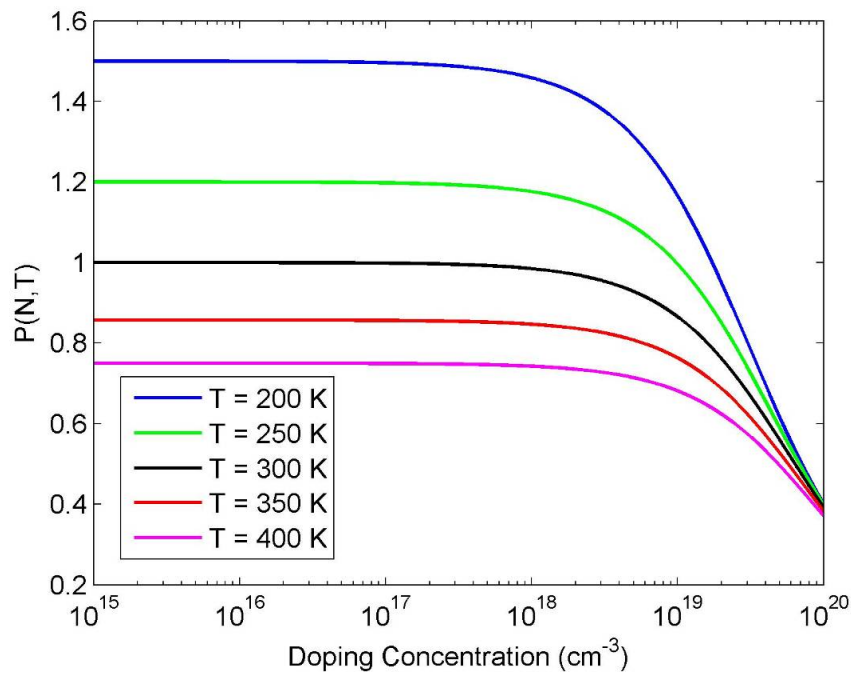


Figure 3.12 Effect of doping level and temperature on n-doped silicon [3].

3.4.1 Minimum Detectable Stress in Piezoresistive Microcantilevers

The effect of doping level on piezoresistive response and noise has been discussed in § 3.2.2 and § 3.3.4 respectively.

The minimum detectable stress in the piezoresistive microcantilevers may be evaluated from the studies on surface stress sensitivity and noise. The analytical model presented in § 4.2 provides a measure of the surface stress sensitivity of the cantilever sensors. All results presented in this section are based on the layer structure of the cantilevers that have been used in this work (refer Figure 4.14).

The piezoresistive response for a microcantilever placed a fully differential Wheatstone bridge may be related to the voltage response as

$$\frac{1}{4} \frac{\Delta V}{V} = \frac{\Delta R}{R} = S_{cantilever} \sigma_{surface\ stress} \quad (3.29)$$

The minimum detectable stress ($\sigma_{minimum\ stress}$), for an input voltage of 1 V, maybe be evaluated in terms of the total noise in the piezoresistive sensor as

$$\sigma_{minimum\ stress} = \frac{1}{4} \frac{V_{Total\ noise}}{V S_{cantilever}} \quad (3.30)$$

The variation of minimum detectable stress as a function of piezoresistor length is shown in Figure 3.13. Since the minimum detectable stress is a function of $S_{cantilever}$ which depends on the doping level of the cantilever, it is important to understand how doping level affect minimum detectable stress. Figure 3.14 shows that the doping beyond $3 \times 10^{19} \text{ cm}^{-3}$ does not produce any appreciable benefit from the perspective of improving minimum detectable stress.

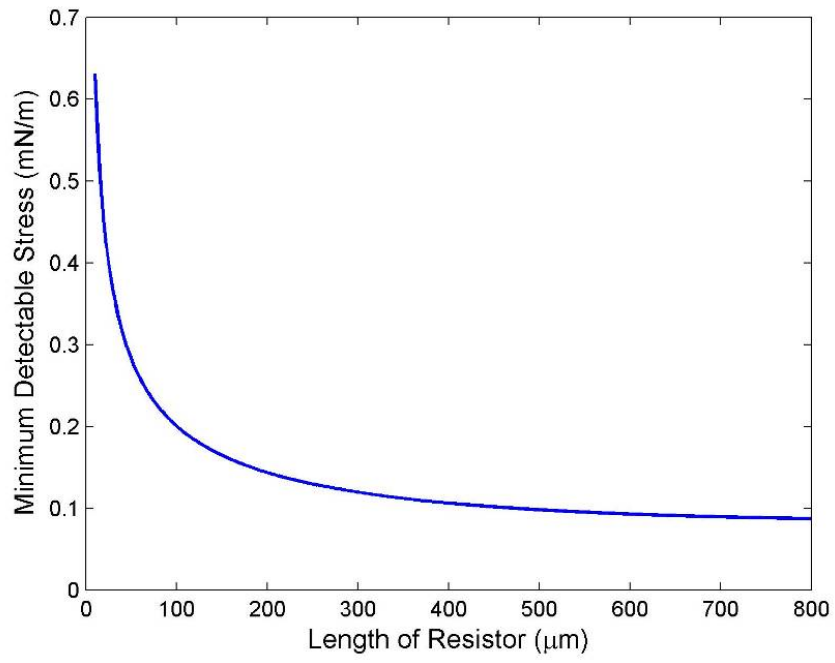


Figure 3.13 Minimum detectable surface stress as a function of piezoresistor length (l_R).

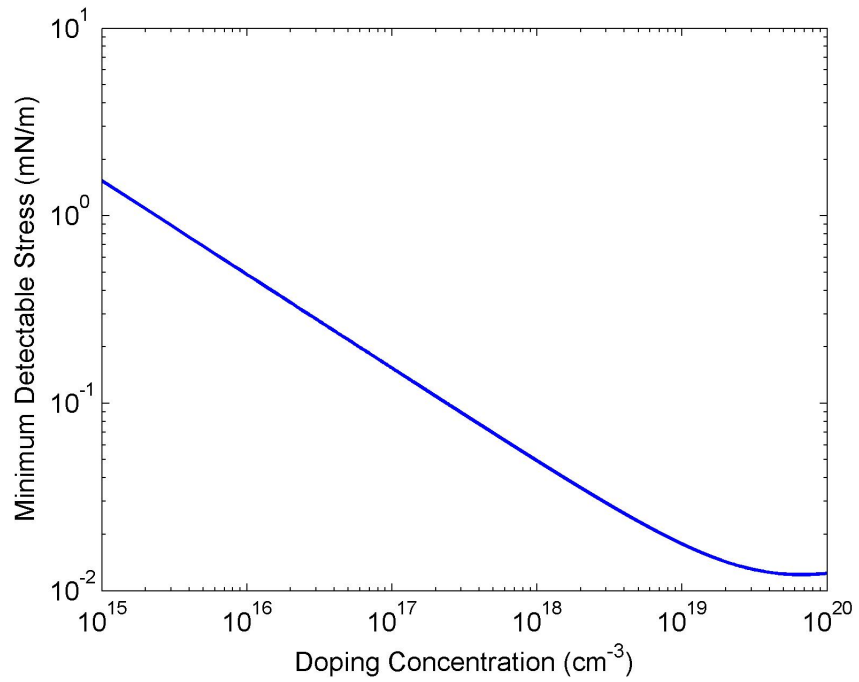


Figure 3.14 Variation of minimum detectable stress with doping concentration.

3.5 Conclusions

The noise and doping analysis in this chapter led to several conclusions are regards design of the P μ CA. The analyses in § 3.3.4 and § 3.4.1 suggest that a longer piezoresistive sensor has lower device noise. § 3.2.2 suggests that if a longer cantilever is chosen then n-type doping is preferable for surface stress measurement. For these reasons in this work, n-doped piezoresistors have been used. The complete matrix of designs used in this work is discussed in § 4.5.2.

The choice of the doping level affects piezoresistive constant and noise in the cantilever sensor. Also when using longer piezoresistors, low doping can result in large piezoresistance values which were not desirable. Hence in this work a doping level of $2.2 \times 10^{19} \text{ cm}^{-3}$ has been chosen.

3.6 References

- [1] C. S. Smith, "Piezoresistance effect in Germanium and Silicon," *Physical Review*, vol. 94, pp. 42-48, 1954.
- [2] O. N. Tufté and E. L. Stelzer, "Piezoresistive properties of heavily doped n-type silicon," *Physical Review*, vol. 166, pp. A1705-A1716, 1964.
- [3] Y. Kanda, "A graphical representation of the piezoresistance coefficients in silicon," *IEEE Transactions on Electron Devices*, vol. 29, pp. 64-70, 1982.
- [4] Y. Kanda, "Piezoresistance effect in silicon," *Sensors and Actuators A*, vol. 28, pp. 83-91, 1991.
- [5] S. D. Senturia, *Microsystem design*. New York: Springer-Verlag, 2000.
- [6] R. Jumpertz, A. V. D. Hart, O. Ohlsson, F. Saurenbach, and J. Schelten, "Piezoresistive sensors on AFM cantilevers with atomic resolution," *Microelectronic Engineering*, vol. 41-42, pp. 441-4, 1998.
- [7] P. A. Rasmussen, O. Hansen, and A. Boisen, "Cantilever surface stress sensors with single-crystalline silicon piezoresistors," *Applied physics letters*, vol. 86, p. 203502, 2005.

- [8] J. Gere and S. Timoshenko, *Mechanics of materials*, Fourth ed. Boston: PWS Publishing Company, 1997.
- [9] L. K. J. Vandamme and S. Oosterhoff, "Annealing of ion-implanted resistors reduces the 1/ f noise," *Journal of Applied Physics*, vol. 59, pp. 3169-3174, 1986.
- [10] J. Thaysen, "Cantilever for biochemical sensing integrated in a microhandling system," in *Mikroelektronik Centret Orsted's*: University of Denmark, 2001.
- [11] O. Hansen and A. Boisen, "Noise in piezoresistive atomic force microscopy," *Nanotechnology*, vol. 10, pp. 51-60, 1999.
- [12] J. A. Harley and T. W. Kenny, "1/f noise considerations for the design and process optimization of piezoresistive cantilevers," *Journal of Microelectromechanical Systems*, vol. 9, pp. 226-235, June 2000.
- [13] T. Volden, "CMOS- Integrated cantilevers for biosensing and probe microscopy," in *Natural Sciences*. vol. Doctor of Natural Sciences Zurich: Swiss Federal Institute of Technology, 2005.
- [14] H. J. Butt and M. Jaschke, "Calculation of thermal noise in atomic force microscopy," *Nanotechnology*, vol. 6, pp. 1-7, Jan 1995.

CHAPTER 4

DESIGN OF THE P μ CA

The previous chapter illustrated the value in careful choice of doping and some geometric parameters associated with design of the piezoresistive microcantilevers. This chapter presents further theoretical considerations in the design of highly sensitive, low-noise piezoresistive microcantilevers.

To this end a new model for surface-stress measurement, based on classical laminated plate theory, is presented. This model allows for estimation of deformation and piezoresistive response of a multilayered plate to surface stresses during analyte measurement and residual stresses in the structural layers due to fabrication processes. Also, the model accounts for bending-stretching coupling in the response to these stresses.

Evaluation of the effect of geometric parameters on piezoresistive surface stress response, based on finite element analysis, is presented. Also, design of the flow cell for analyte measurement and other design issues are discussed. Finally, in § 4.6, the concept and theoretical ramifications of an alternative scheme of surface stress measurement-double-sided sensing are discussed.

4.1 Surface Stress Sensitivity

The surface stress on a cantilever is evaluated based on the measured piezoresistive response of the cantilever using the equation

$$\frac{\Delta R^s}{R} = S_{cantilever} \sigma_{surface\ stress} \quad (4.1)$$

Here $S_{cantilever}$ is the surface stress sensitivity of the cantilever. In all existing work on surface stress measurement with piezoresistive microcantilevers, the surface stress sensitivity of the cantilever is approximated to that of the free end of the cantilever (S_{free} , refer Table 3.1). Figure 3.5 shows the variation in piezoresistive response as function of δ , the distance of the piezoresistor from the clamped end. Since all existing piezoresistive microcantilever systems are based on designs with $\delta = 0$, the surface stress

sensitivity of the cantilevers $S_{cantilever} < S_{free}$. This results in underestimation of the surface stress that develops on the cantilever surface.

Surface stress sensitivity is measured in all existing literature based on beam or plate bending models. For a cantilever beam, though, the surface stress sensitivity varies a function of location on the cantilever beam. Hence, the ‘true surface stress sensitivity’ of a piezoresistive microcantilever, which will be referred to as the surface stress may be evaluated as shown in (3.19).

4.2 A New Cantilever Bending Model

Plate models used for various applications use various assumptions to simplify the mathematics involved while accurately modeling plate deformation. An often-used simplification is to assume that the 3-D plate can be modeled as a 2-D beam. Another simplification of the model is possible if the strains associated with the axial moments and bending moments on the plate can be decoupled (i.e., ε_0 and χ can be solved independently). As will be discussed later, this assumption implies that $\mathbf{B} = 0$. Another point of interest when using plate models is whether large deformations need to be considered. If large deformations are present, higher-order terms must be included in the definition of strains.

Several models have been presented in the literature to relate surface stress on the cantilever and the associated bending of the cantilever. In some reports [1], the phenomenon has been modeled as a plate-bending problem in which a biaxial modulus of elasticity is used. Typically in these models, the curvature due to surface stress, evaluated with the Stoney equation [2], is related to deflection at the cantilever tip. However, the effect of cantilever stretching due to surface stress is not accounted for. In other work, the solutions of bending and stretching problems have been superimposed to yield in a more accurate representation of the cantilever response to surface stress [3]. However, none of these models has accounted for the coupling of stretching and bending in a multilayered microcantilever.

The effect of residual stresses in thin films on deformation of structures is well documented. A number of applications control the curvature of microelectromechanical systems (MEMS) devices by careful control of intrinsic stresses [4]. Further, some

applications, such as bending of micromirrors, actuation of valves, and flow and pressure sensing, result in large deformation of some device components. Modeling of such devices requires that higher-order deformation effects be accounted for. This requirement is not needed for surface-stress-based bending, where deflection is typically on the order of a few hundred nanometers [1, 5].

In this work, a unified model of cantilever bending, which accounts for the effect of intrinsic stresses and surface stresses, is presented. It is based on classical laminated plate theory [6]. Large deformation effects have not been included in this model for the present. Also, material properties of each layer have been assumed to be isotropic. However, the form of the equations can easily be modified to allow for anisotropic materials.

Consider a laminated plate structure with N plates, each of uniform thickness. The strain at any point in the laminated cantilever can be described as

$$\boldsymbol{\varepsilon}(x, y, z) = \boldsymbol{\varepsilon}^0(x, y) + z\boldsymbol{\chi}(x, y) \quad (4.2)$$

where

$$\boldsymbol{\varepsilon}^0 = \begin{bmatrix} \varepsilon_x^0 \\ \varepsilon_y^0 \\ \varepsilon_{xy}^0 \end{bmatrix}, \boldsymbol{\chi} = \begin{bmatrix} \chi_x \\ \chi_y \\ \chi_{xy} \end{bmatrix} \quad (4.3)$$

For small deformation of the cantilever plates, higher-order effects can be neglected and

$$\varepsilon_x^0 = \frac{\partial u}{\partial x}, \varepsilon_y^0 = \frac{\partial v}{\partial y}, \varepsilon_{xy}^0 = \frac{\partial u}{\partial y} + \frac{\partial v}{\partial x} \quad (4.4)$$

and

$$\chi_x = -\frac{\partial^2 w}{\partial x^2}, \chi_y = -\frac{\partial^2 w}{\partial y^2}, \chi_{xy} = -2\frac{\partial^2 w}{\partial x \partial y} \quad (4.5)$$

Stress in the k^{th} layer of the laminated cantilever is described as

$$\boldsymbol{\sigma}_k = \begin{bmatrix} \sigma_x \\ \sigma_y \\ \sigma_{xy} \end{bmatrix}_k = \tilde{\mathbf{Q}}_k(\boldsymbol{\varepsilon}^0 + z\boldsymbol{\chi}) + \boldsymbol{\sigma}_{i,k} + \boldsymbol{\sigma}_s \quad (4.6)$$

where

$$\tilde{\mathbf{Q}}_k = \frac{E_k}{1-\nu_k^2} \begin{bmatrix} 1 & \nu_k & 0 \\ \nu_k & 1 & 0 \\ 0 & 0 & \frac{1-\nu_k}{2} \end{bmatrix} \quad (4.7)$$

The intrinsic stresses in each layer and the surface stresses are assumed to be isotropic. Hence,

$$\boldsymbol{\sigma}_{i,k} = \begin{bmatrix} \sigma_i \\ \sigma_i \\ 0 \end{bmatrix}_k, \quad \boldsymbol{\sigma}_s = \begin{bmatrix} \sigma_s(z) \\ \sigma_s(z) \\ 0 \end{bmatrix} \quad (4.8)$$

The surface stress is modeled as [7]

$$\sigma_s(z) = \sigma_s^+ \delta(z - h/2) + \sigma_s^- \delta(z + h/2) \quad (4.9)$$

where $\delta(z)$ is the Dirac-delta function. The axial forces and the planar moments may be evaluated as

$$\mathbf{N} = \int_{-h/2}^{h/2} \boldsymbol{\sigma} dz, \quad \mathbf{M} = \int_{-h/2}^{h/2} \boldsymbol{\sigma} z dz \quad (4.10)$$

The force and moment equations may be written as

$$\mathbf{N} = \mathbf{A}\boldsymbol{\varepsilon}^0 + \mathbf{B}\boldsymbol{\chi} + \mathbf{N}_i + \mathbf{N}_s \quad (4.11)$$

and

$$\mathbf{M} = \mathbf{B}\boldsymbol{\varepsilon}^0 + \mathbf{D}\boldsymbol{\chi} + \mathbf{M}_i + \mathbf{M}_s \quad (4.12)$$

where

$$\mathbf{A} = \int_{-h/2}^{h/2} \tilde{\mathbf{Q}}_k dz = \sum_{k=1}^n \tilde{\mathbf{Q}}_k h_k \quad (4.13)$$

Now,

$$\mathbf{B} = \int_{-h/2}^{h/2} \tilde{\mathbf{Q}}_k z dz = \sum_{k=1}^n \tilde{\mathbf{Q}}_k h_k z_k \quad (4.14)$$

and

$$\mathbf{D} = \int_{-h/2}^{h/2} \tilde{\mathbf{Q}}_k z^2 dz = \sum_{k=1}^n \tilde{\mathbf{Q}}_k \left[z_k^2 + \frac{1}{3} \left(\frac{h_k}{2} \right)^2 \right] h_k \quad (4.15)$$

Using (4.8) and (4.9) in (4.10), we can write $\mathbf{N}_s =$

$$\begin{bmatrix} \sigma_s^+ + \sigma_s^- \\ \sigma_s^+ + \sigma_s^- \\ 0 \end{bmatrix} \quad (4.16)$$

and

$$\mathbf{M}_s = \begin{bmatrix} \frac{h}{2}(\sigma_s^+ - \sigma_s^-) \\ \frac{h}{2}(\sigma_s^+ - \sigma_s^-) \\ 0 \end{bmatrix} \quad (4.17)$$

Also,

$$\mathbf{N}_i = \int_{-h/2}^{h/2} \boldsymbol{\sigma}_{i,k} dz, \quad \mathbf{M}_i = \int_{-h/2}^{h/2} \boldsymbol{\sigma}_{i,k} z dz \quad (4.18)$$

The system of equations obtained for deformation of the multilayered cantilever is

$$\begin{bmatrix} \mathbf{N} \\ \mathbf{M} \end{bmatrix} = \begin{bmatrix} \mathbf{A} & \mathbf{B} \\ \mathbf{B} & \mathbf{D} \end{bmatrix} \begin{bmatrix} \boldsymbol{\varepsilon}^0 \\ \boldsymbol{\chi} \end{bmatrix} + \begin{bmatrix} \mathbf{N}_i \\ \mathbf{M}_i \end{bmatrix} + \begin{bmatrix} \mathbf{N}_s \\ \mathbf{M}_s \end{bmatrix} \quad (4.19)$$

In order to evaluate curvature induced by intrinsic stress and surface stress in the absence of external forces and moments, the equilibrium equations are written as

$$\begin{bmatrix} \mathbf{A} & \mathbf{B} \\ \mathbf{B} & \mathbf{D} \end{bmatrix} \begin{bmatrix} \boldsymbol{\varepsilon}^0 \\ \boldsymbol{\chi} \end{bmatrix} + \begin{bmatrix} \mathbf{N}_i \\ \mathbf{M}_i \end{bmatrix} + \begin{bmatrix} \mathbf{N}_s \\ \mathbf{M}_s \end{bmatrix} = \mathbf{0} \quad (4.20)$$

Finally, strain in the cantilever is obtained as

$$\begin{bmatrix} \boldsymbol{\varepsilon}^0 \\ \boldsymbol{\chi} \end{bmatrix} = - \begin{bmatrix} \mathbf{A} & \mathbf{B} \\ \mathbf{B} & \mathbf{D} \end{bmatrix}^{-1} \left(\begin{bmatrix} \mathbf{N}_i \\ \mathbf{M}_i \end{bmatrix} + \begin{bmatrix} \mathbf{N}_s \\ \mathbf{M}_s \end{bmatrix} \right) \quad (4.21)$$

This complete cantilever deformation model allows for a measure of strain associated with surface stresses and residual stresses in the cantilever structural layers. The model will be used in the current work to determine the thickness and stress required in some structural layers to control curvature of the cantilever (§ 5.4.1).

4.3 Effect of Geometric Parameters on Surface Stress Response

The effect of doping and geometric factors l_r and δ were discussed in § 3.2.2. The finite element model used indicates the trends in p-type and n-type doping. This analysis does not however aid in design decisions on width of the piezoresistor w_r , gap between the piezoresistive paths g or understand the effect of length of the cantilever l

(see Figure 3.2). In order to develop a set of design rules for location of the piezoresistor analysis of spatial distribution of stress in a cantilever is required.

4.3.1 Surface Stress Distribution in ANSYS Model

In order to develop this set of design rules, a microcantilever model was created in ANSYS™ using shell elements (SHELL181). The cantilever length is 450 μm and the cantilever width is 100 μm. The layer structure was as indicated in Figure 4.14 and a tensile stress of 20 MPa was applied to the 50 nm thick gold layer. The axis directions for the analysis presented are as shown in Figure 3.2. This mimics a surface stress of 1 N/m on the microcantilever. Figure 4.1 show the stress in the x -direction in the piezoresistive layer and the y -direction stresses are shown in Figure 4.2.

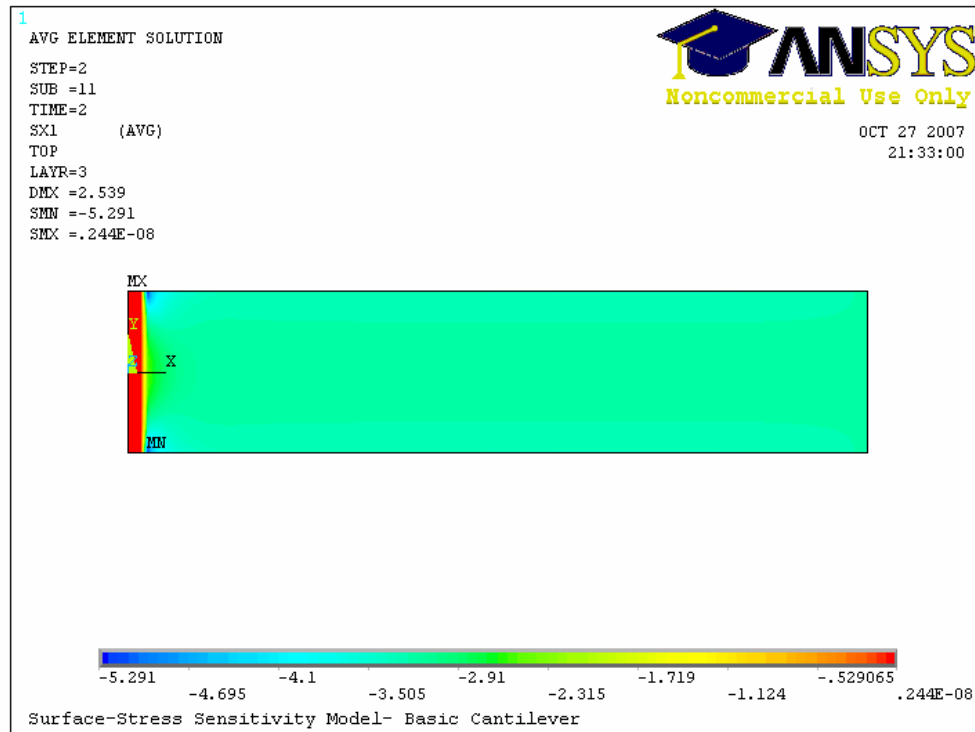


Figure 4.1 Stress in the x -direction in the silicon piezoresistor cause by a surface stress of 1 N/m in the gold layer. The first 10 μm of the cantilever (left) is clamped. All units are in MPa.

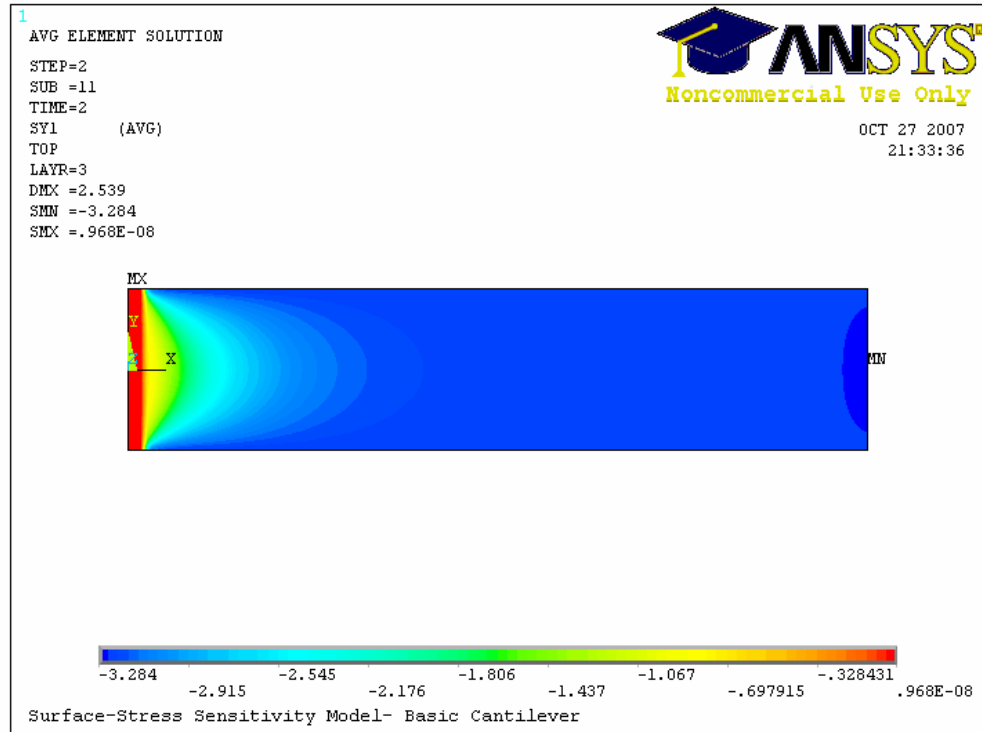


Figure 4.2 Stress in the y - direction in the silicon piezoresistor cause by a surface stress of 1 N/m in the gold layer. The first 10 μm of the cantilever (left) is clamped. All units are in MPa.

The surface stress sensitivity for p-type (Figure 4.3) and n-type (Figure 4.4) doping is calculated for each location on the cantilever, from the spatial distribution of stress, as

$$\frac{\Delta R^s}{R} = \sigma_x \pi_x + \sigma_y \pi_y \quad (4.22)$$

As observed in the simpler analysis performed in § 3.2.2, surface stress sensitivity for n-type silicon is larger than for p-type silicon by a factor of almost 3 at locations distance from the clamped end of the cantilever.

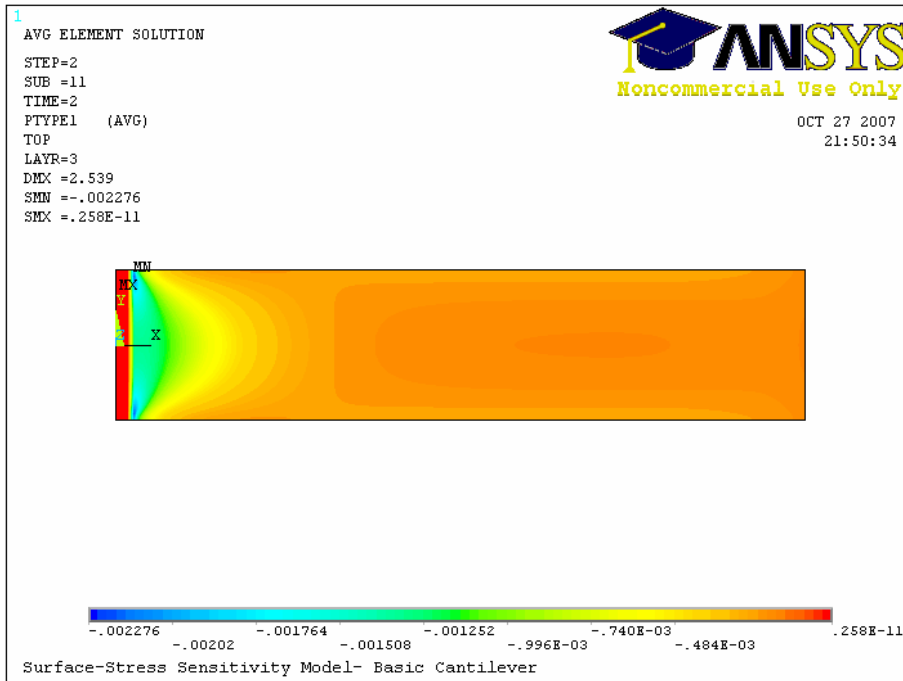


Figure 4.3 Surface stress sensitivity for p-type silicon piezoresistors.

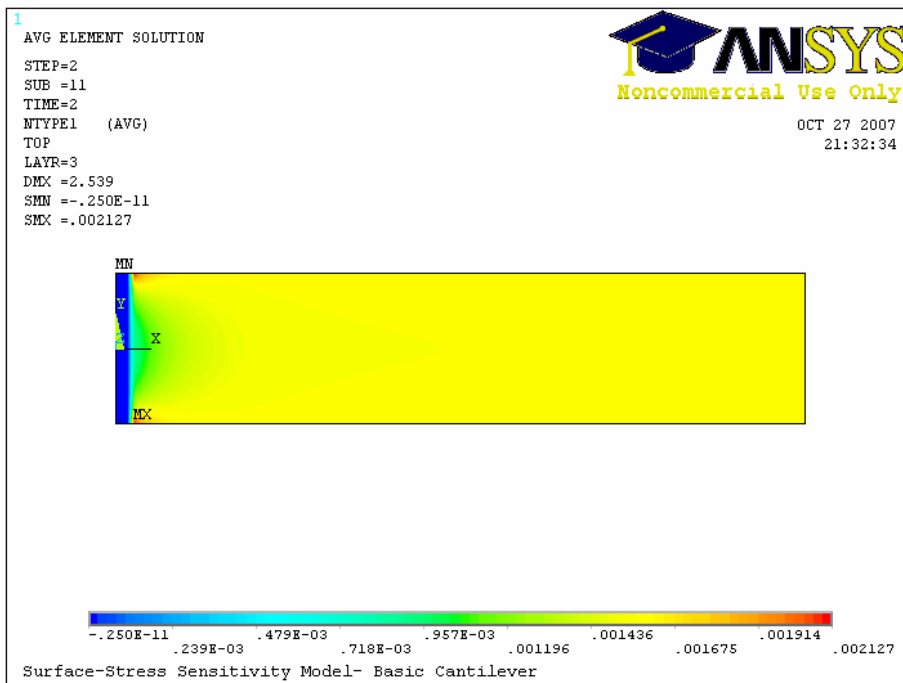


Figure 4.4 Surface stress sensitivity for n-type silicon piezoresistors.

4.3.2 Effect of Geometric Parameters on Surface Stress Response

Evaluation of the effect of geometric parameters was performed by evaluating the average value of surface stress sensitivity for n-type silicon over piezoresistors defined by varying the different geometric factors shown in Figure 4.5.

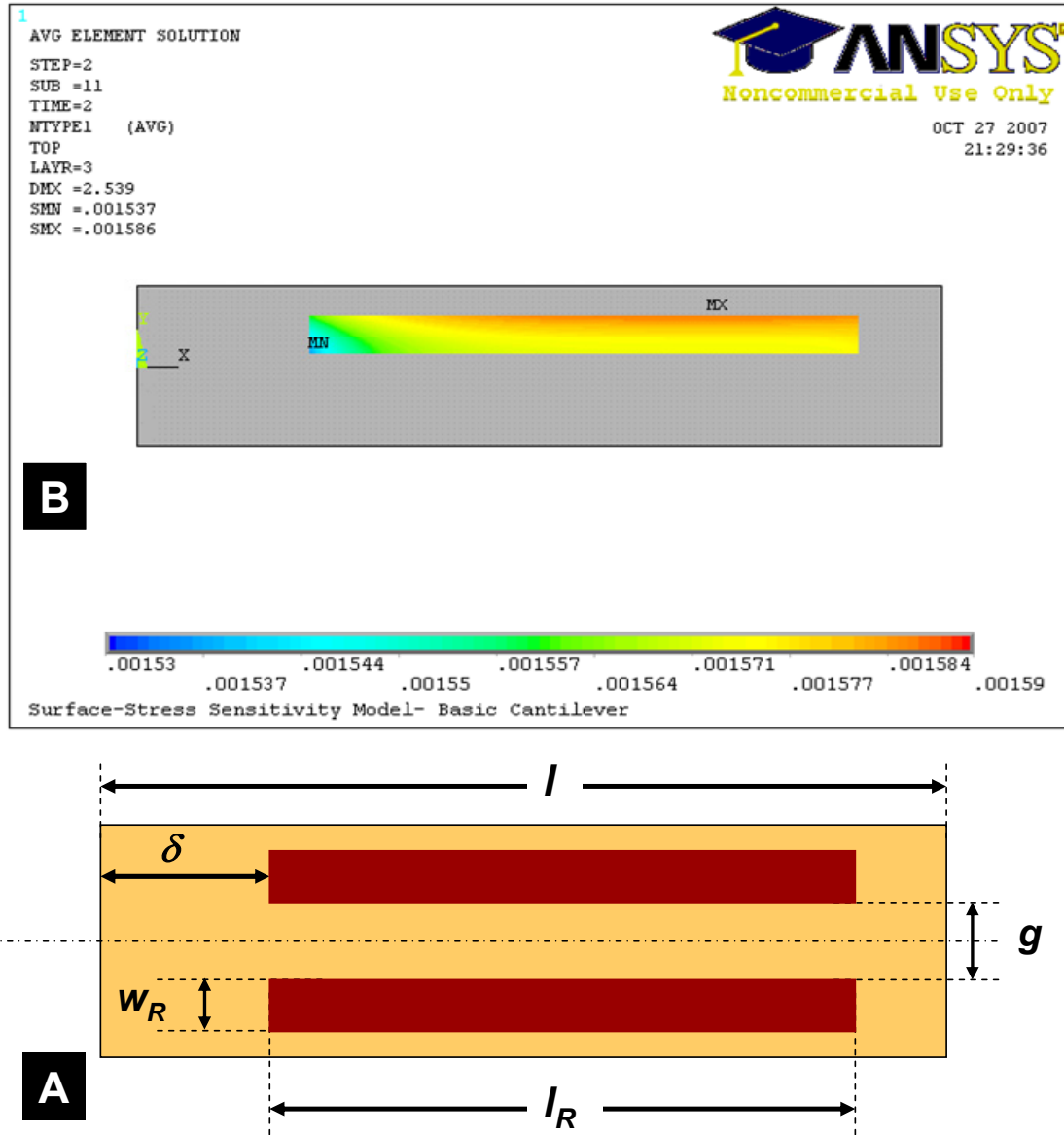


Figure 4.5 A. Parameters that were varied to evaluate the effect of resistor placement and geometry on surface stress sensitivity. B. A finite element plot showing n-type surface stress sensitivity in the region chosen for evaluation of effect of geometric parameters (all units in MPa).

- Effect of l_R was evaluated for $l = 450 \mu\text{m}$, $w_R = 20 \mu\text{m}$, $\delta = 0 \mu\text{m}$ and $g = 20 \mu\text{m}$.

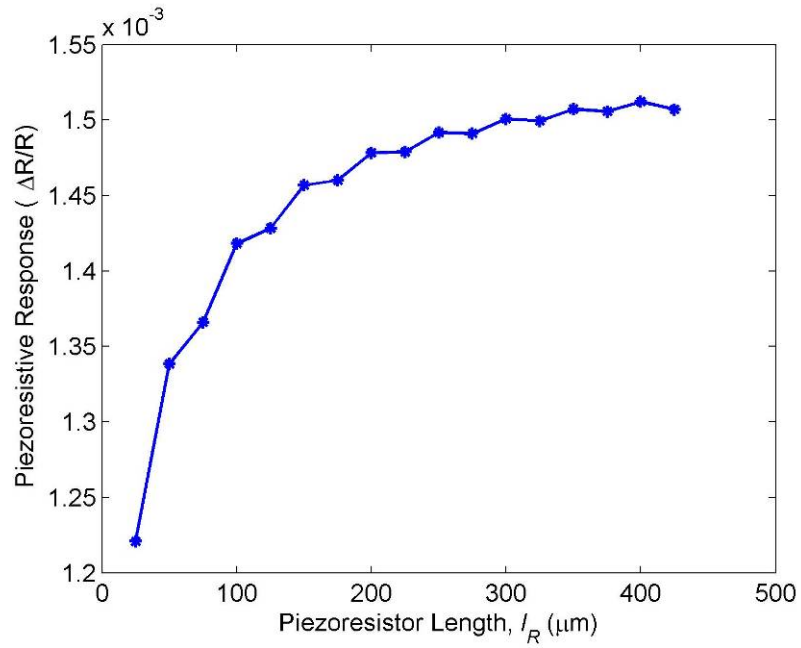


Figure 4.6 Effect of piezoresistor length on surface stress response.

- Effect of δ was evaluated for $l = 450 \mu\text{m}$, $l_R = 300 \mu\text{m}$, $w_R = 20 \mu\text{m}$, $g = 20 \mu\text{m}$.

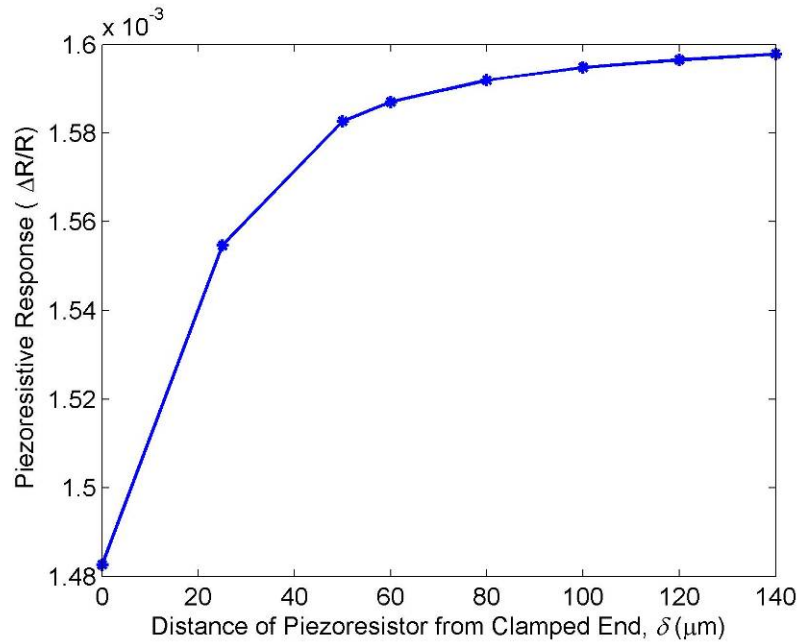


Figure 4.7 Effect of piezoresistor distance from the clamped end of the cantilever on surface stress response.

- Effect of w_R was evaluated for $l = 450 \mu\text{m}$, $l_R = 300 \mu\text{m}$, $\delta = 100 \mu\text{m}$ and $g = 20 \mu\text{m}$.

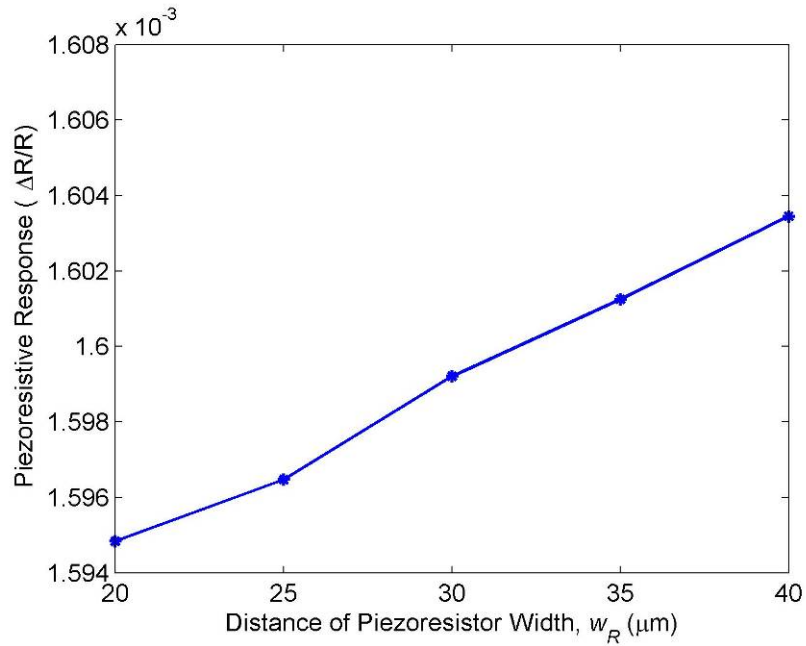


Figure 4.8 Effect of piezoresistor width on surface stress response.. Large piezoresistor width creates a larger piezoresistive response.

- Effect of g was evaluated for $l = 450 \mu\text{m}$, $l_R = 300 \mu\text{m}$, $w_R = 20 \mu\text{m}$, $\delta = 100 \mu\text{m}$.

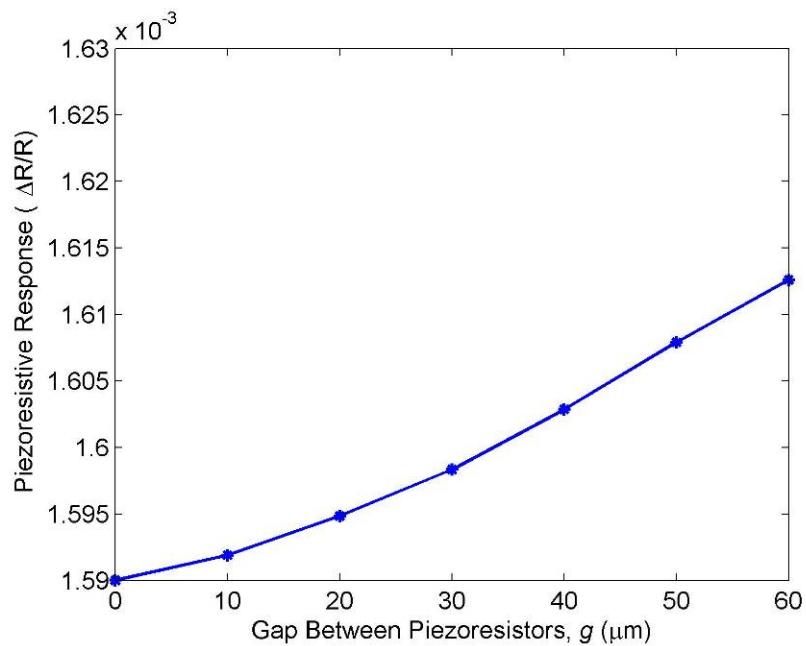


Figure 4.9 Effect of variation of gap between piezoresistors.

- The effect of l was evaluated for $l_R = 250 \mu\text{m}$, $w_R = 20 \mu\text{m}$, $\delta = 0 \mu\text{m}$ and $g = 20 \mu\text{m}$. Finite element models for cantilevers lengths ranging from $250 \mu\text{m}$ to $450 \mu\text{m}$ were evaluated and the effect of varying the cantilever length was investigated for a fixed set of the other geometric parameters. The principal point of interest here is whether a variation in cantilever length changes the surface stress profile such that the piezoresistive response from a piezoresistor (of fixed length) changes.

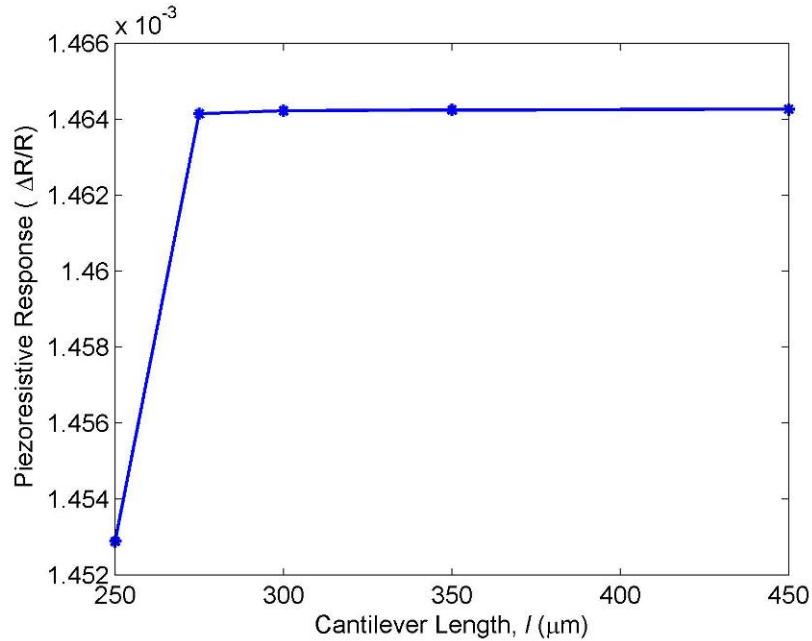


Figure 4.10 Effect of variation of cantilever length for the same length of the piezoresistors. If $l \approx l_R$, the piezoresistive response is reduced to fringe effects in the stress profile in the piezoresistor.

4.3.3 Design Rules for Piezoresistive Microcantilevers

The finite element results suggest that the following trends that may be used as guidelines for design of piezoresistive microcantilevers for surface stress measurement.

- Larger response is obtained for larger piezoresistor length
- Cantilever length has a no effect on the response if $l \ll l_R$. The surface stress response decreases if $l \approx l_R$ due to fringe effects associated with the stress profile developed.
- Piezoresistive response is larger for a larger resistor width and for larger gap between the piezoresistor. This is due to the higher local surface stress sensitivity towards the outer side of the microcantilever.

- Clamping distance should be $\delta \geq w_c$, where w_c is the width of the cantilever. This ensures that clamping effects do not lead to a reduction of piezoresistive response.

4.4 Microfluidic Design

Design of the flow cell used in this work was carried out based on simple design considerations of laminar flow. 2-D finite element models were created in Fluent to evaluate the flow patterns. For a complete analysis of optimal design of the flow cell, issues such as mass transport also need to be considered in the design of the flow volume and placement of the piezoresistive microcantilevers in the flow [8, 9].

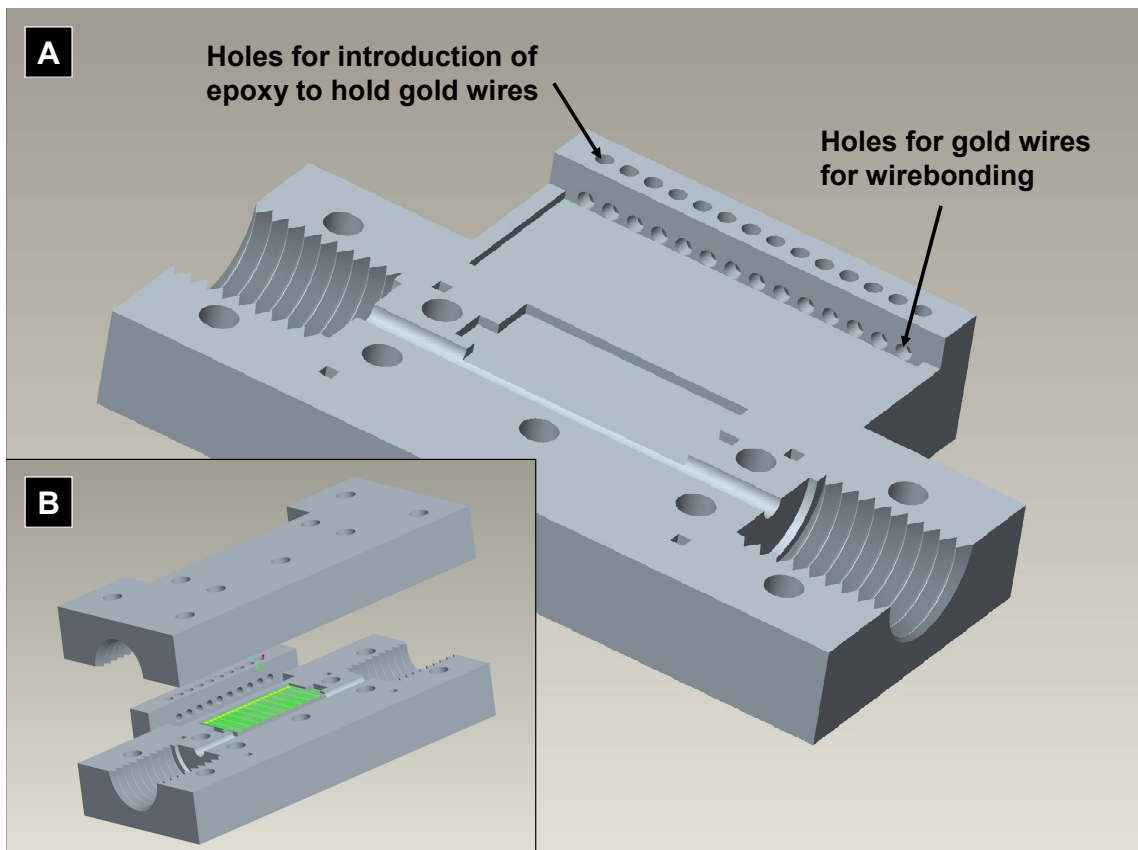


Figure 4.11 A. Base of flow cell used for integration of the P μ CA. B. CAD image of the two halves fo the flow cell with the integrated P μ CA.

4.4.1 Design of Flow Cell

The CAD layout of the flow cell used in this work is shown in Figure 4.11 and the manner in which the P μ CA was integrated into the flow cell. Further specifics of the

dimensions of the cell are included in Appendix A. Also, the use of this cell for flow measurements has been discussed in Chapter 7.

The cell consists of two halves that are screwed together using bolts before testing. The cross-section of the flow channel is a circle of radius 1 mm. The cantilevers experience transverse flow of the analyte. The volume flow rates used in this work were between 2 sccm and 10 sccm. This corresponds to flow velocities from 63.7 cm s^{-1} to 318.3 cm s^{-1} . To ensure the steady flow in the flow channel in the vicinity of the cantilever, the entry length of the flow cell is calculated based on laminar flow theory. The minimum length for laminar flow was found to be 3.3 mm for 10 sccm flow. The entry length designed for the flow cell is 10 mm.

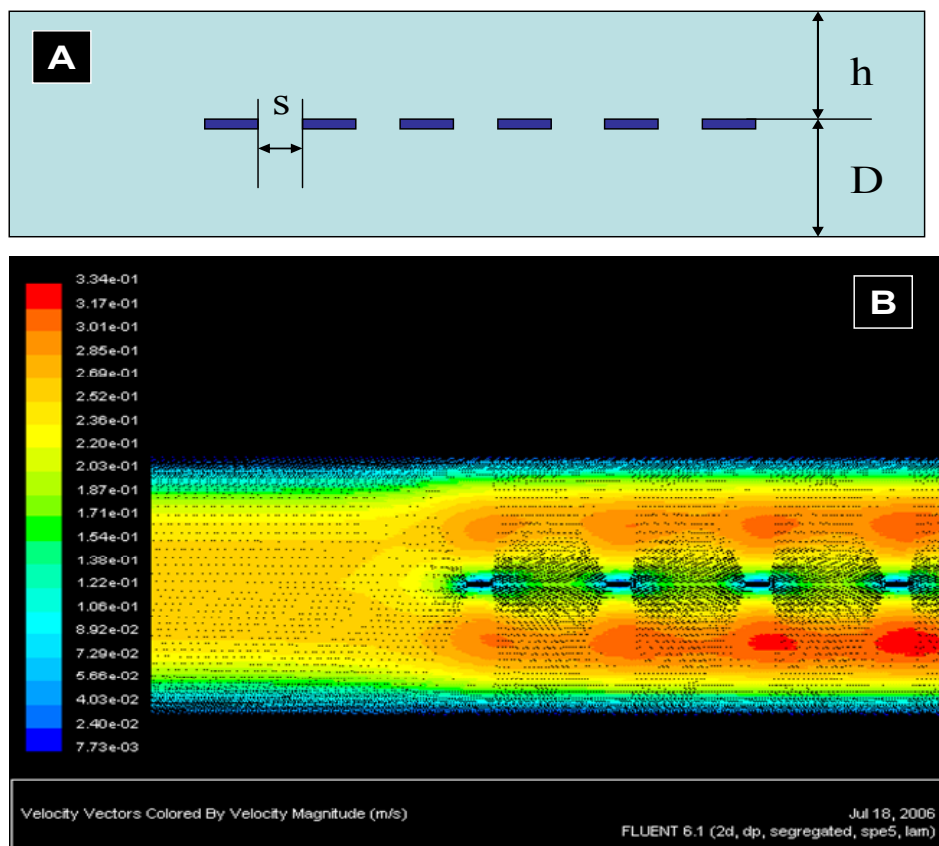
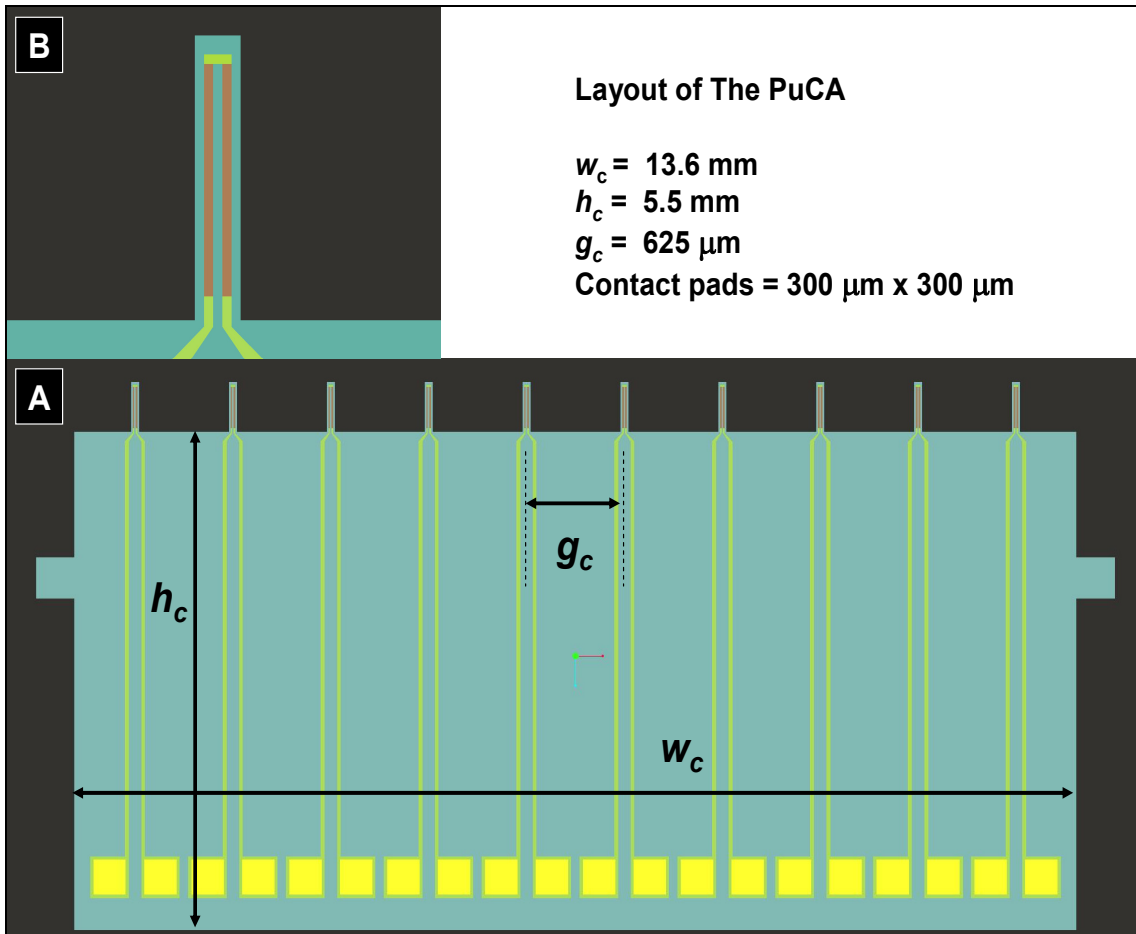


Figure 4.12 A. Schematic for flow model, B. Results of flow of air in the flow channel at 19.8 cm s^{-1} . The flow profile at the inlet was uniform.

4.4.2 Other Considerations

A qualitative analysis was performed using a finite element model in fluent. The parameters investigated are shown in Figure 4.12. In this 2D model the spacing between the cantilevers s and the position of the cantilever in the flow were varied and the flow profiles in different flow velocities were analyzed. The objective of this analysis was to evaluate the spacing between the cantilevers that would ensure that the flow regime around all the 10 cantilevers was near identical. This analysis suggested that for the flow velocities in question, a spacing $s > 400 \mu\text{m}$ for cantilevers $10 \mu\text{m}$ thick would fulfill the objective. In reality the cantilevers used in this work are about $1.085 \mu\text{m}$ thick and a small spacing should suffice for the purposes listed. However in this design considerations of wirebonding and packaging dictated a cantilever spacing of $625 \mu\text{m}$. This is clearly more than adequate for a uniform flow profile around the cantilevers.



4.5 Final Device Design

4.5.1 Design of Piezoresistive Microcantilever Array

The P μ CA was designed with 10 cantilevers. The variations in cantilever parameters are shown in Table 4.1. The overall shape and dimension of the chip are shown in Figure 4.13.

4.5.2 Matrix of Device Designs

In order to evaluate the effect of geometric parameters on surface stress response, a large matrix of designs was implemented. Table 4.1 lists the various designs that have been fabricated in this work. The parameters that were varied in this work were cantilever length l , piezoresistor length l_R , and distance from the clamped end δ . The parameters that were not varied were piezoresistor width, $w_R = 20 \mu\text{m}$, and gap between the piezoresistors, $g = 20 \mu\text{m}$.

Table 4.1 Matrix of cantilever designs. Cantilever length, piezoresistor length and distance from the clamped end of the cantilever were varied.

	$l = 150 \mu\text{m}$	$l = 300 \mu\text{m}$	$l = 450 \mu\text{m}$	$l = 600 \mu\text{m}$	$l = 700 \mu\text{m}$
$l_R / \delta (\mu\text{m})$	75/0,30,60	150/0,30,60	225/0,30,60	300/0,30,60	375/0,30,60
	100/0,30	200/0,30,60	300/0,30,6	400/0,30,60	550/0,30,60
	125/0	250/0,30	375/0,30,60	500/0,30,60	725/0

A copy of masks designed for the fabrication process is included in Appendix A.

4.6 Double-Sided Surface Stress Measurement

4.6.1 Concept of Double-Sided Sensing

In all existing work on surface stress-based chemical sensing with microcantilevers, only one side of the cantilever is functionalized. Surface stress associated with analyte binding results in deflection of the cantilever. This deflection may be measured using optical, capacitive, magnetic or other methods.

Chemical sensing with piezoresistive microcantilevers using single-sided sensing can, however, result in erroneous measurement of surface stress since surface stresses on the non-functionalized surface of the cantilever are not accounted for. One method of solving this problem is to functionalize both surfaces of the cantilever (double-sided stress measurement). In this case, both sides of the cantilever are functionalized. In the absence of a non-functionalized surface, erroneous measurement due to non-specific binding on the non-functionalized surface cannot occur. Double-sided surface stress, in a symmetric cantilever structure, results in an elongation or compression of the cantilever beam (Figure 4.15). These changes are more easily measured using piezoresistive techniques as compared to optical or capacitive methods.

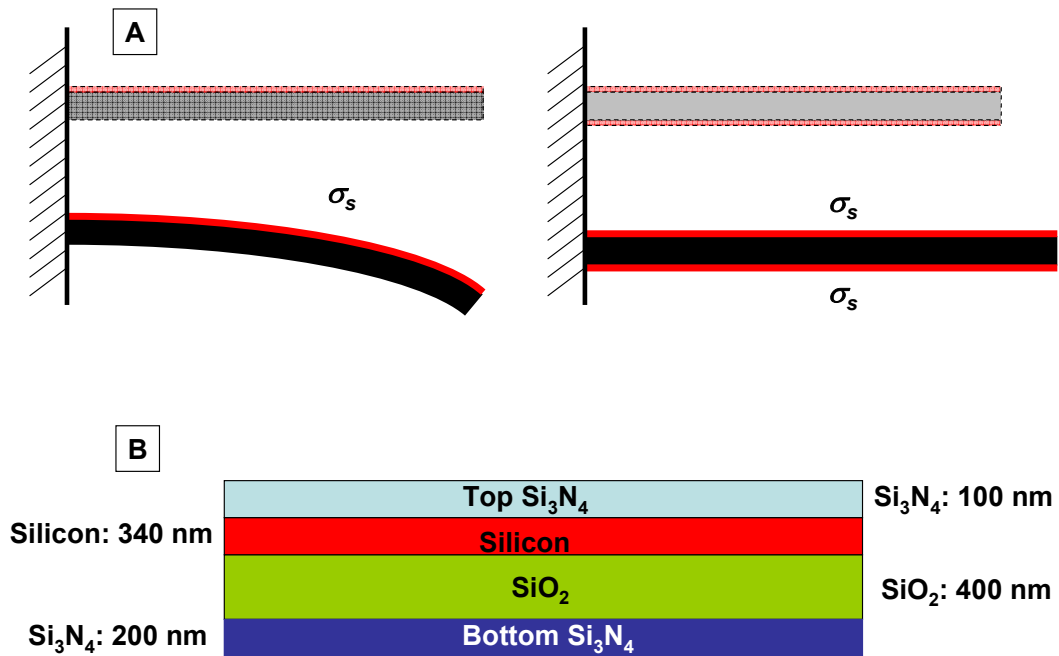


Figure 4.14 A. Cantilever deformation under SSS and DSS, B. Layer structure of cantilever beam structure used in this work. (σ_s - surface stress)

Rasmussen et al. [10] showed, theoretically, that DSS measurement achieves higher stress sensitivities than SSS for piezoresistive cantilevers (all layers were assumed to have the same Young's modulus). However no experimental verification of this sensing principle exists in current literature.

4.6.2 Design Issues

The surface stress sensitivity for DSS and SSS measurement in a multilayered cantilever (Figure 4.15) was evaluated using an analytical model [11]. A comparison of DSS and SSS surface stress sensitivities showed that higher surface stress sensitivities can be achieved with DSS measurement for low nitride encapsulation thicknesses. However if fabrication or measurement issues mandate a thicker nitride encapsulation, SSS surface stress sensitivities may be larger. This analysis was performed for cantilever structures with no silicon dioxide layer.

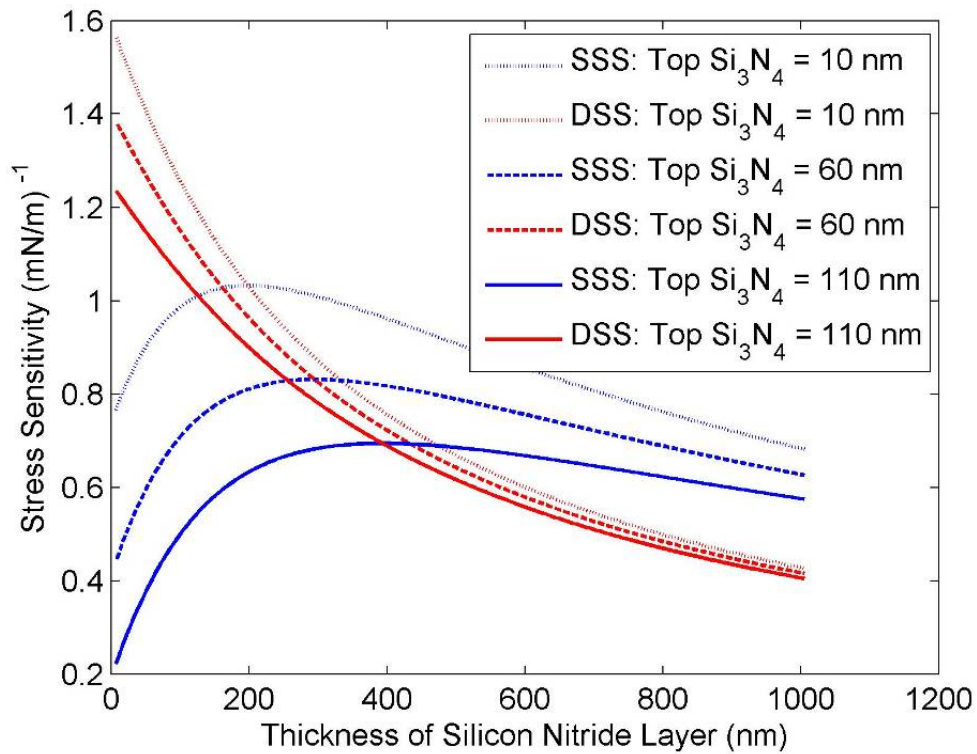


Figure 4.15. Calculated SSS and DSS surface stress sensitivity for varying bottom nitride thickness.

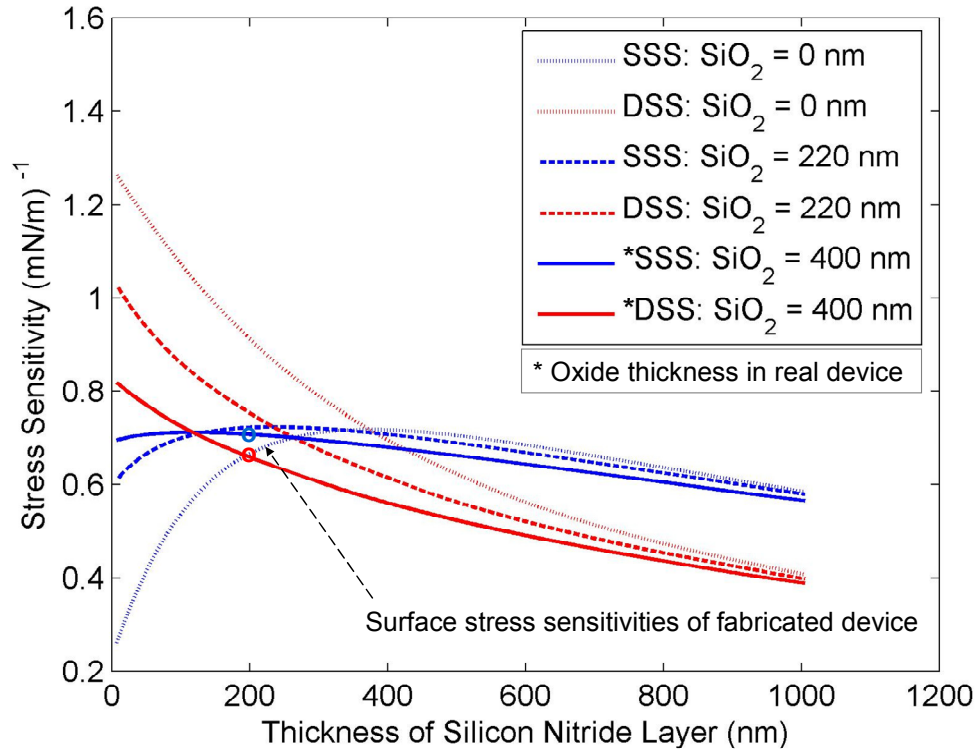


Figure 4.16. Calculated SSS and DSS surface stress sensitivity for different oxide layer thickness. Surface stress sensitivity of the fabricated microcantilevers are indicated.

In the experiments with DSS and SSS sensing, sensors optimized for SSS sensing [12] were used. DSS and SSS surface stress sensitivities for this cantilever structure are of comparable value (Figure 4.16).

4.7 Conclusion

This chapter presents some novel aspects of design and application of piezoresistive microcantilevers:

- A new surface stress model has been presented for evaluation of the effect of surface stress and intrinsic stresses in the layers of the cantilever.
- A new model for thermomechanical vibration noise in piezoresistive microcantilevers for surface stress has been developed.
- Analysis of double-sided measurement for surface stress measurement has been performed.

In addition to the above some ground rules for design of piezoresistive microcantilevers for surface stress measurement have been formulated. Based on these rules a piezoresistive microcantilever has been designed. The aspects of width of the resistor and gap between the resistors have not been included in the design of the piezoresistive microcantilevers used in this work. The fabricated devices have been tested to corroborate some of the findings of the parameter analysis in this chapter.

Further discussion on the analysis in this chapter is taken up in chapter 9.

4.8 References

- [1] R. Raiteri, M. Grattarola, H.-J. Butt, and P. Skladal, "Micromechanical cantilever based biosensors," *Sensors and Actuators B*, vol. 79, pp. 115-126, 2001.
- [2] G. G. Stoney, "The tension of metallic films deposited by electrolysis," *Proceedings of the Royal Society of London Series a-Containing Papers of a Mathematical and Physical Character*, vol. 82, pp. 172-175, May 1909.
- [3] P. A. Rasmussen, J. Thaysen, O. Hansen, and A. Boisen, "Optimised cantilever biosensor with piezoresistive read-out," *Ultramicroscopy*, vol. 97, pp. 371-376, 2003.
- [4] J. S. Pulskamp, A. Wickenden, R. Polcawich, B. Piekarski, M. Dubey, and G. Smith, "Mitigation of residual film stress deformation in multilayer microelectromechanical systems cantilever devices," *Journal of Vacuum Science and Technology B*, vol. 21, pp. 2482-2486, 2003.
- [5] K. M. Hansen and T. G. Thundat, "Microcantilever biosensors," *Methods*, vol. 37, pp. 57-64, 2005.
- [6] J. M. Whitney, *Structural analysis of laminated anisotropic plates*. Lancaster: Technomic Publishing Company, Inc., 1987.
- [7] J. E. Sader, "Surface stress induced deflections of cantilever plates with applications to the atomic force microscope: Rectangular plates," *Journal of Applied Physics*, vol. 89, pp. 2911-2921, 2001.
- [8] D. W. Dareing, F. Tian, and T. Thundat, "Effective mass and flow patterns of fluids surrounding microcantilevers," *Ultramicroscopy*, vol. 106, pp. 789-794, 2006.

- [9] C. Phillips, M. Jakusch, H. Steiner, B. Mizaikoff, and A. G. Fedorov, "Model-based optimal design of polymer-coated chemical sensors," *Analytical Chemistry*, vol. 75, pp. 1106-1115, 2003.
- [10] P. A. Rasmussen, A. V. Grigorov, and A. Boisen, "Double sided surface stress cantilever sensor," *Journal of Micromechanics and Microengineering*, vol. 15, pp. 1088-1091, 2005.
- [11] A. Choudhury, P. J. Hesketh, Z. Hu, and T. G. Thundat, "Single and double sided chemical sensing with piezoresistive microcantilevers," in *IEEE Sensors 2007 Atlanta*: IEEE, 2007.
- [12] A. Choudhury, P. J. Hesketh, Z. Hu, and T. G. Thundat, "Design and fabrication of a piezoresistive microcantilever array," in *208th Meeting of the ECS, Los Angeles, CA*, 2005.

CHAPTER 5

FABRICATION OF THE P μ CA

The previous chapter detailed the design of the piezoresistive microcantilever array. In this chapter issues related to fabrication and functionalization of the piezoresistive microcantilever array are discussed. Device fabrication was carried out at the Microelectronics Research Center at Georgia Tech based on the mask designs described in the previous chapter.

5.1 Materials and Process Flow

Fabrication of the P μ CA was carried out using standard MEMS batch fabrication processes. An SOI wafer (SOITEC, Bernin, France) was chosen for device fabrication. The wafer specifications are listed in Table 5.1.

Table 5.1. Specifications for SOI wafer.^a

Layer	Layer thickness	Specifications
Device silicon layer	340 nm	(100) SCS, p-type, 5-25 Ω -cm
Buried oxide	400 nm	Thermal oxide
Handle wafer	525 μ m	(100) prime grade silicon

^a Wafer made using the SmartcutTM process.

5.2 P μ CA Fabrication

The fabrication of the P μ CA consisted of four essential steps. The fabrication process flow is shown in Figure 5.1.

1. Resistor doping: The SOI wafers were doped by ion implantation with phosphorus (doping conditions: dose: $7 \times 10^{14}/\text{cm}^2$, energy: 120 keV) at Core Systems Inc. (Sunnyvale, CA) to create n-doped piezoresistors. To activate the dopant, the SOI wafers were annealed at 1050 °C, in a tube furnace, in N₂ for 48 min. The resistivity of the silicon (measured by four-point probe measurement) was approximately $3.4 \times 10^{-3} \Omega$ -cm. The thickness of the buried oxide and device silicon layers of the SOI wafer (Table 5.2) were verified with a Nanospec 3000 refractometer (Nanometrics, Milpitas, CA). Initial

experiments on cantilever fabrication were carried out a SOI wafer (SIMGUI Technology Co. Ltd., Shanghai, China). The wafer had a buried oxide layer thickness of 300 nm and a device silicon layer thickness of 205 nm. To evaluate the doping and annealing conditions, the doping profile was measured using spread resistance analysis (Solecon Laboratories, Reno, NV). Figure 5.2 show a comparison between the measured doping profile and the one expected from modeling using MicroTec (Siborg Systems Inc., Ontario, Canada)- a software package for two-dimensional process and device simulation. The measured value of resistivity of the doped region (for the wafer from SIMGUI Corp.) is approximately $2.05 \times 10^{-3} \Omega\text{-cm}$.

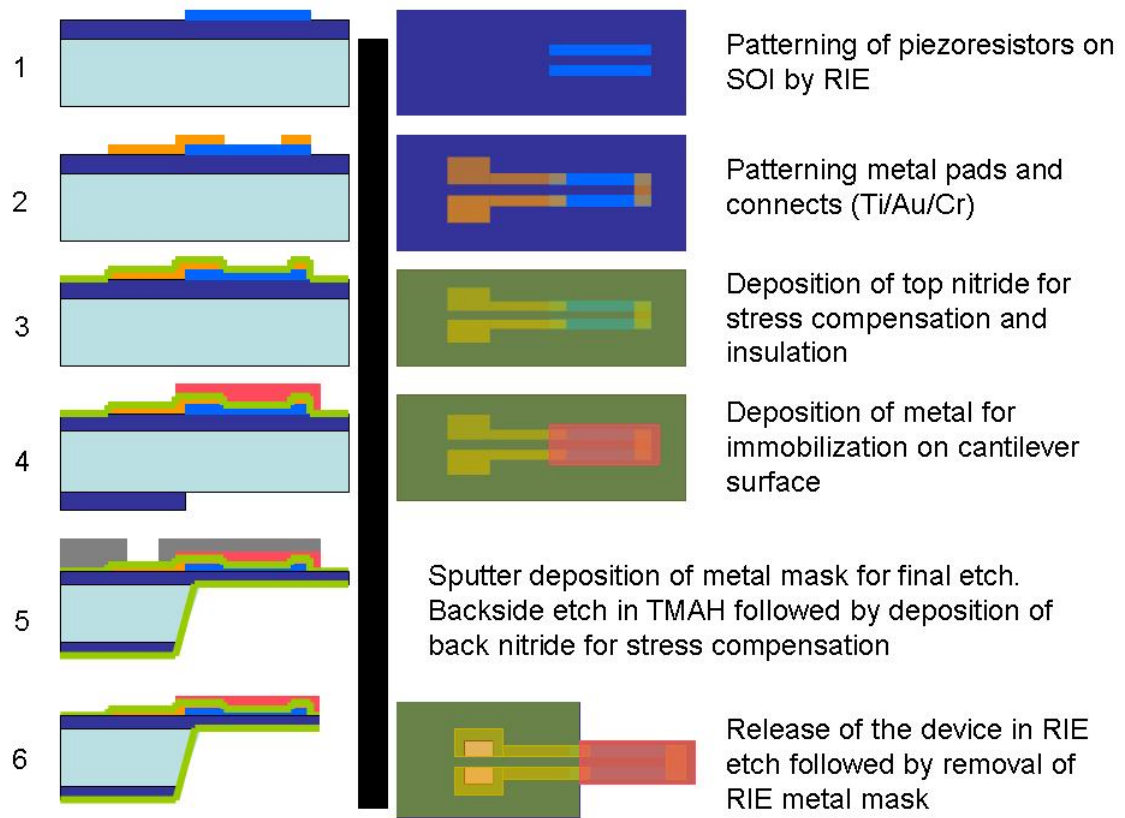


Figure 5.1. P μ CA fabrication process flow.

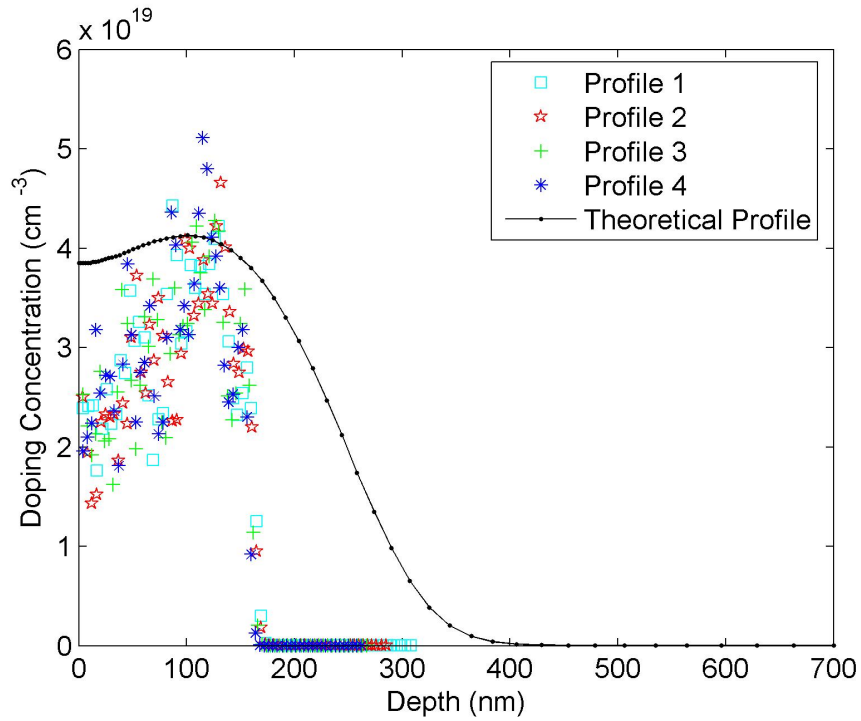


Figure 5.2 Doping profile of SOI wafer after doping and annealing. The measured profiles are compared to the profile evaluated theoretically.

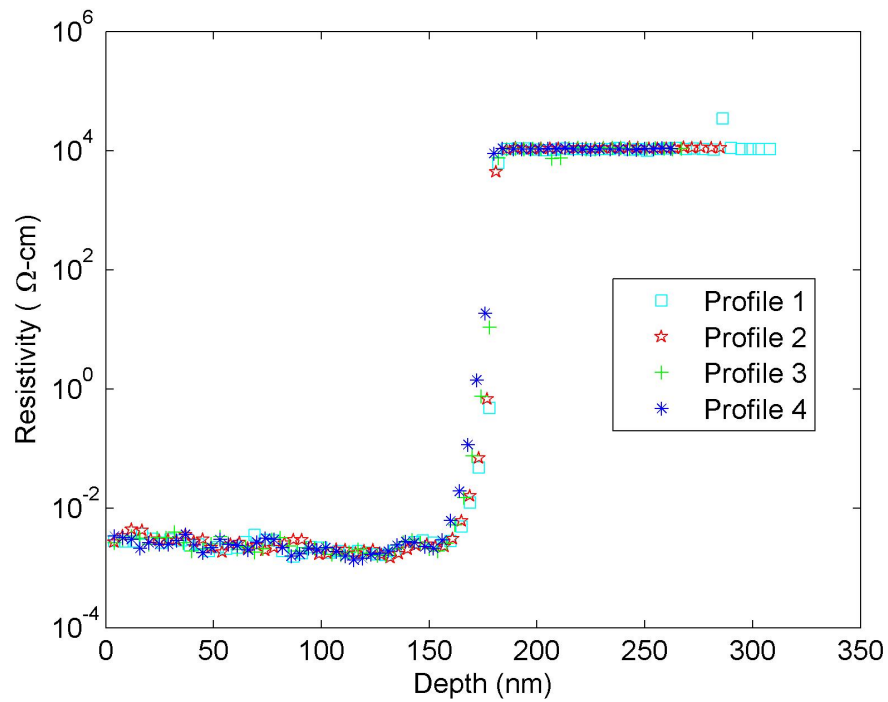


Figure 5.3. Resistivity measured from the doping profile measurement made using spreading resistance analysis (SRA).

At a later stage of this work wafers from SOITEC were used as the wafers from SIMGUI Corp. were found to unsuitable for the fabrication process described here. This was because the wafers were prepared in a SIMOX (silicon implanted oxide) process. This results in a low doping of the bulk silicon under the buried oxide layer. The final silicon etch is carried out in TMAH in this work. The oxide doping of the bulk silicon prevented this final etch and proved untenable for the design fabrication process.

The doping and annealing of the SOI wafers from SOITEC were designed such that resistivity of the device silicon layer was $3.4 \times 10^{-4} \Omega\text{-cm}$.

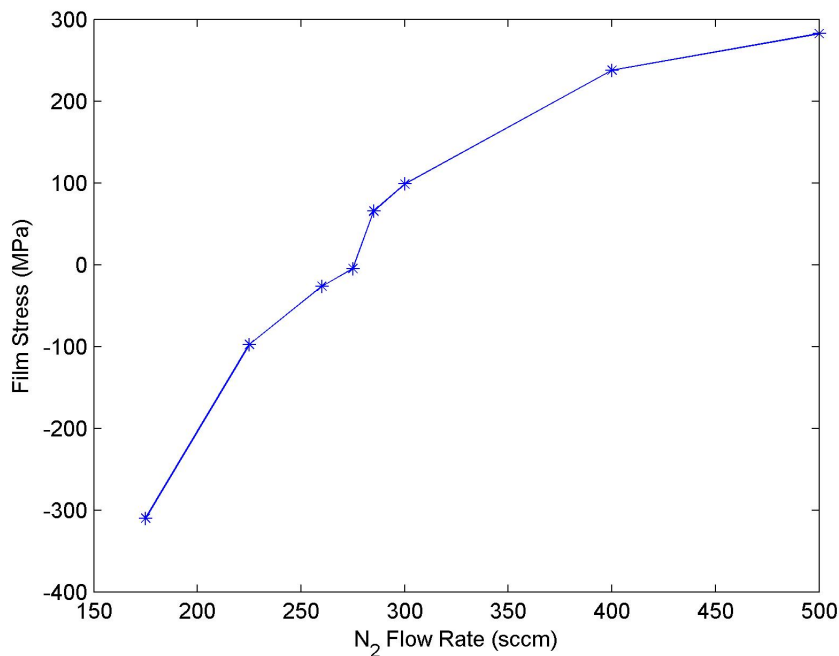


Figure 5.4. Change in silicon nitride stress with N₂ flow rate on Unaxis PECVD system.

2. Device definition: The silicon piezoresistors were defined by reactive ion etching (RIE) the SOI wafers in an SF₆/O₂ plasma. Since the etch rate of SiO₂ is negligible in such a plasma, the wafer was overetched to ensure that the silicon piezoresistors were well defined. A 3000-Å layer of gold was sputter-deposited and defined to create contacts to the piezoresistors (a 100-Å adhesion layer of titanium was used). A layer of silicon nitride was used to encapsulate the device (this will be referred to as “top nitride”). The top nitride layer was carefully chosen to have a compressive stress of -300 MPa (Figure 5.4). As will be discussed later, the coating is important in the scheme of stress compensation that was evolved to create “flat” cantilevers. An aluminum layer was

sputter-deposited and patterned to create a mask for definition of the cantilevers and the chip.

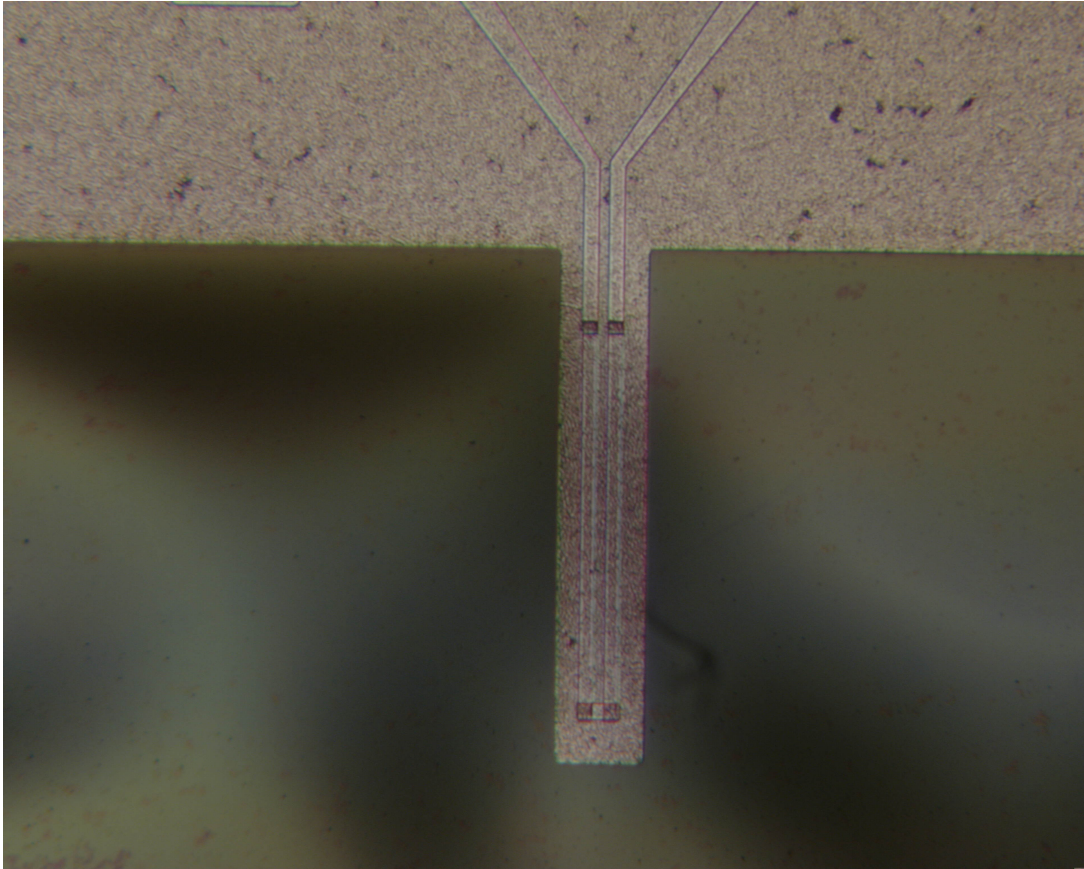


Figure 5.5. Piezoresistive microcantilever embedded in membrane released by TMAH etch.

3. Membrane release: A 1.4- μm layer of low-stress silicon nitride (~ 30 MPa) was deposited on top of the aluminum mask, effectively burying the mask under a thick layer of silicon nitride. The nitride layer serves to strengthen the membrane area upon release. This step was followed by definition of the backside oxide and deep RIE of the wafer in a Plasmatherm inductively coupled plasma system (Unaxis, St. Petersburg, FL). Since the buried SiO_2 is not a sacrificial layer but an integral part of the cantilever structure, it is not desirable to expose it to the DRIE etch plasma. The etch rate of SiO_2 is approximately 5 nm/cycle. Exposure to the DRIE plasma can alter the thickness of the 400-nm-thick SiO_2 layer and thus alter the mechanical characteristics of the cantilever. Also, it is nearly impossible to ensure uniformity of the wafer etch. To circumvent these issues, the backside silicon etch was stopped 10 to 20 μm short of reaching the oxide layer, and the

remainder of the silicon was etched in a TMAH bath (10 wt % at 70 °C). A single-sided holder (AMMT, Frankenthal, Germany) was used to ensure that the aluminum mask was not attacked during this process. At the end of this step, the cantilever chip was defined and the cantilevers were embedded in the released membrane (Figure 5.5).

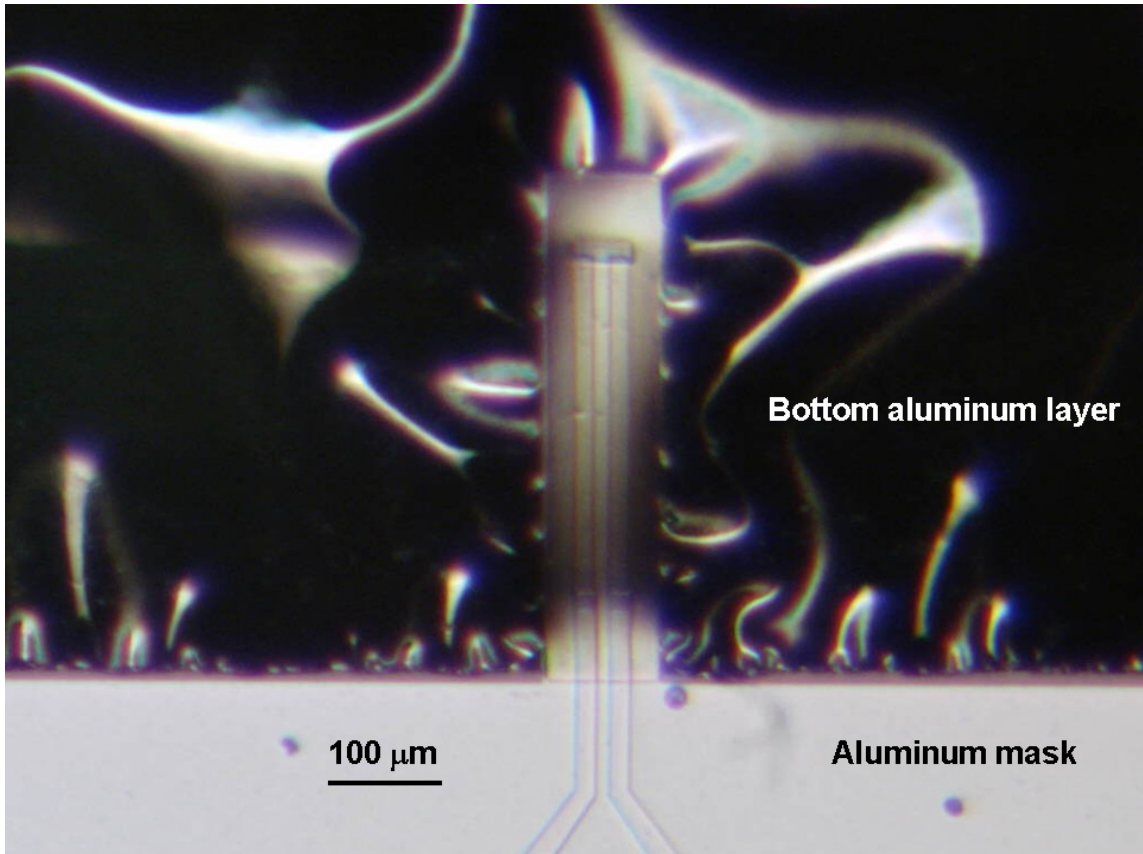


Figure 5.6. Microcantilever definition is performed using the buried aluminum mask. The bottom aluminum layer prevents etching of the underside of the cantilever in the nitride etch plasma.

4. Device release: After the wafer was rinsed in distilled water and carefully dried in a convection oven at 115 °C for 30 minutes, a layer of tensile silicon nitride was deposited from the backside of the wafer (referred to as “bottom nitride”). This layer is the last component of the stress-compensation scheme. A layer of aluminum (2500 Å) was deposited onto the back of the wafer. The nitride membrane was then etched from the top by RIE. The buried aluminum mask acts both to define the cantilevers and to open access to the gold contact pads. In the remainder of the membrane region, the aluminum layer deposited from the back serves to protect the backside of the cantilever from being etched

in the final membrane etch step (Figure 5.6). The aluminum layers on the top and the back are etched in aluminum etchant (Transene Inc., Danvers, MA) at 70 °C, after which the devices are rinsed, first in distilled water and then in methanol, and allowed to air-dry. This last step is to ensure that the cantilevers do not break due to surface-tension effects. The fabricated piezoresistive microcantilevers and the P μ CA are shown in Figure 5.7 and Figure 5.8.

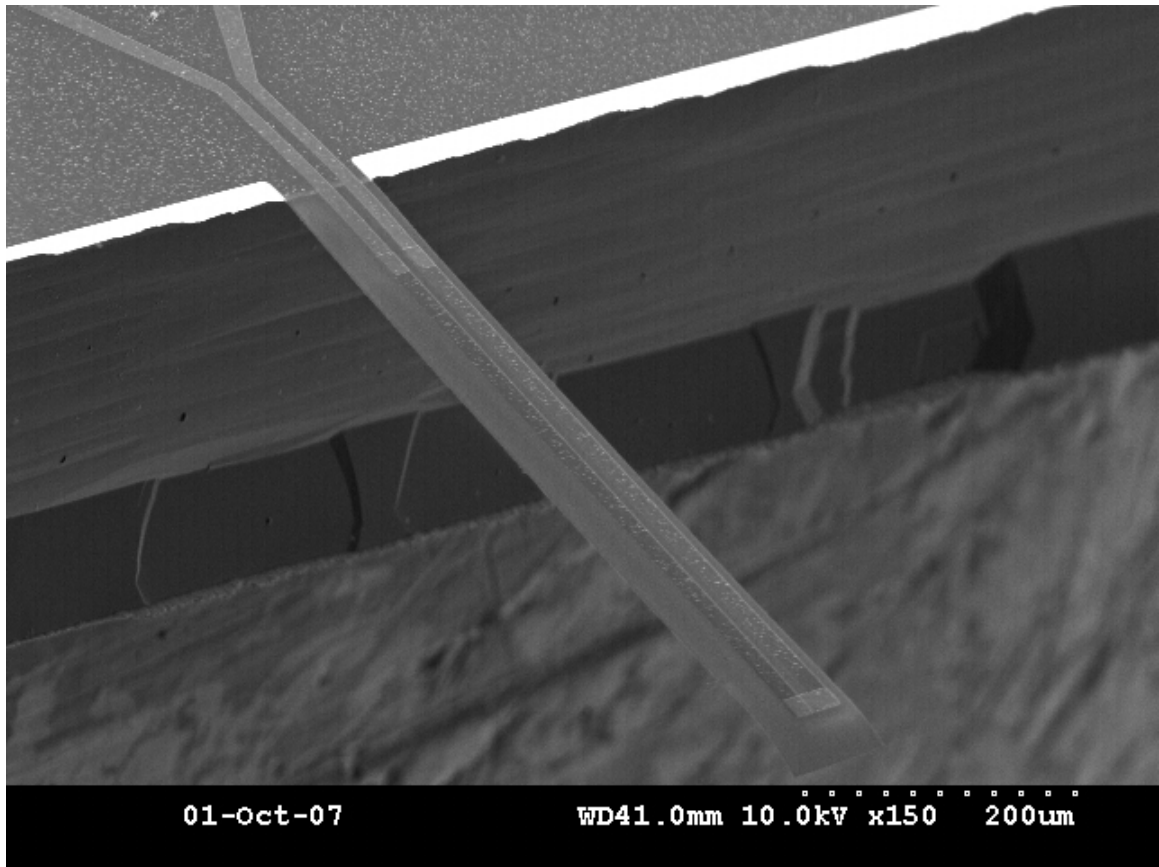


Figure 5.7 Piezoresistive microcantilever in the P μ CA. The distance from the clamping point (δ) is 250 μ m in this cantilever.

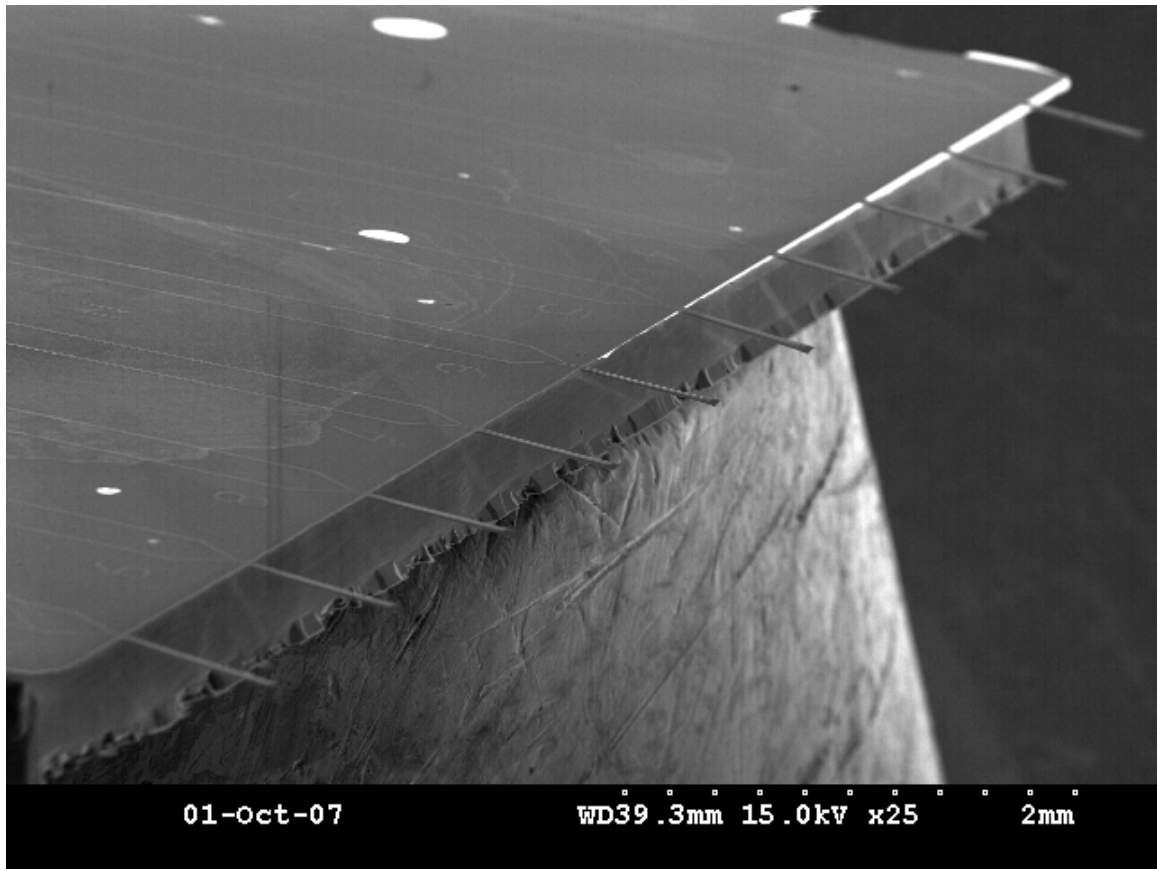


Figure 5.8 The ten-cantilever piezoresistive microcantilever array (P μ CA). Evidence of TMAH etching can be seen in the edge of the silicon portion of the chip.

5.3 Salient Features of P μ CA Fabrication Process

5.3.1 Tight control on layer dimensions

Several fabrication processes require wet/dry etch of the SCS or oxide layers. Since these etches are often not limited by an etch-stop layer, variations in etch depth occur among different batches of wafers or even in the same wafer if the etching conditions are not uniform. In the fabrication process presented, the device dimensions depend on the initial thicknesses of the SCS, buried oxide, and nitride layers (see Figure 5.9). The nitride layer deposition has been calibrated; uniformity across the deposition platen is within 1%. The deposition rate is also well-calibrated. The back-side etch in DRIE is stopped 10 to 20 μm short of the buried oxide layer to prevent etch of the layer in the DRIE plasma. The remainder of the silicon is etched in TMAH. In TMAH, the etch rate of silicon is almost four orders of magnitude higher than that of SiO_2 [1]. Hence the

change in SiO₂ layer thickness is very small, and the fabrication process is easily controlled.

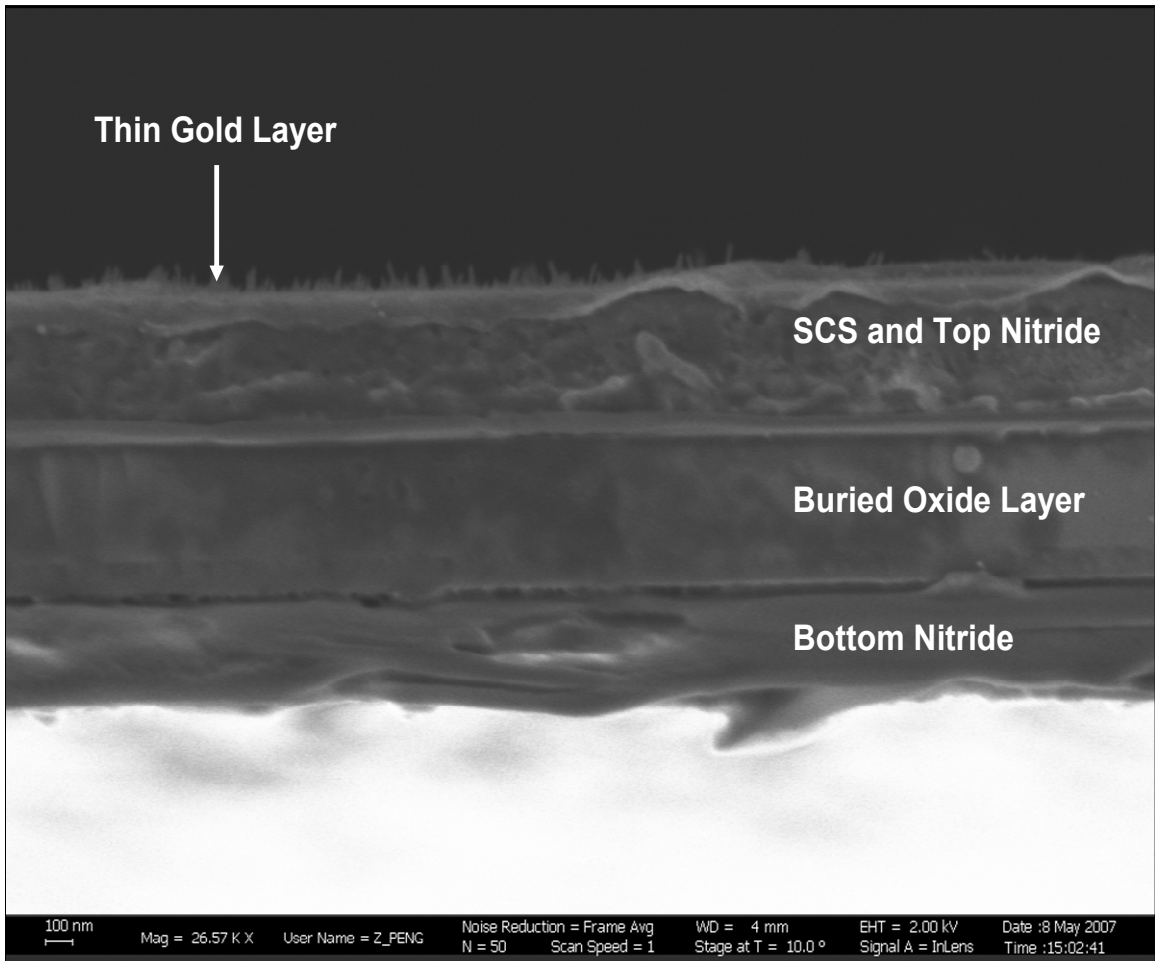


Figure 5.9. Cross section of the cantilever, showing the layer structure (with the piezoresistor).

5.3.2 Robust design

In all current AFM and surface stress cantilever designs, the piezoresistors are at the clamped end ($\delta = 0 \mu\text{m}$). In processing associated with these designs, it is crucial to ensure that the definition of the edge of the device (the clamped end of the cantilever) is accurate to within a few microns. This can give rise to numerous yield issues. Often very small batches of devices have to be etched to obtain the required uniformity. The design of the P μ CA cantilevers with $\delta > 50 \mu\text{m}$ makes the sensors insensitive to the exact position of the clamped end. If δ is designed correctly, an error in the definition of the

clamped end ($|\delta - \delta'|$) of up to 10 μm is acceptable (Figure 5.10). Also, overetching of the bulk silicon layer can be carried out with no detrimental effects on the device sensitivity. This is done to ensure all the bulk silicon under the cantilever is removed.

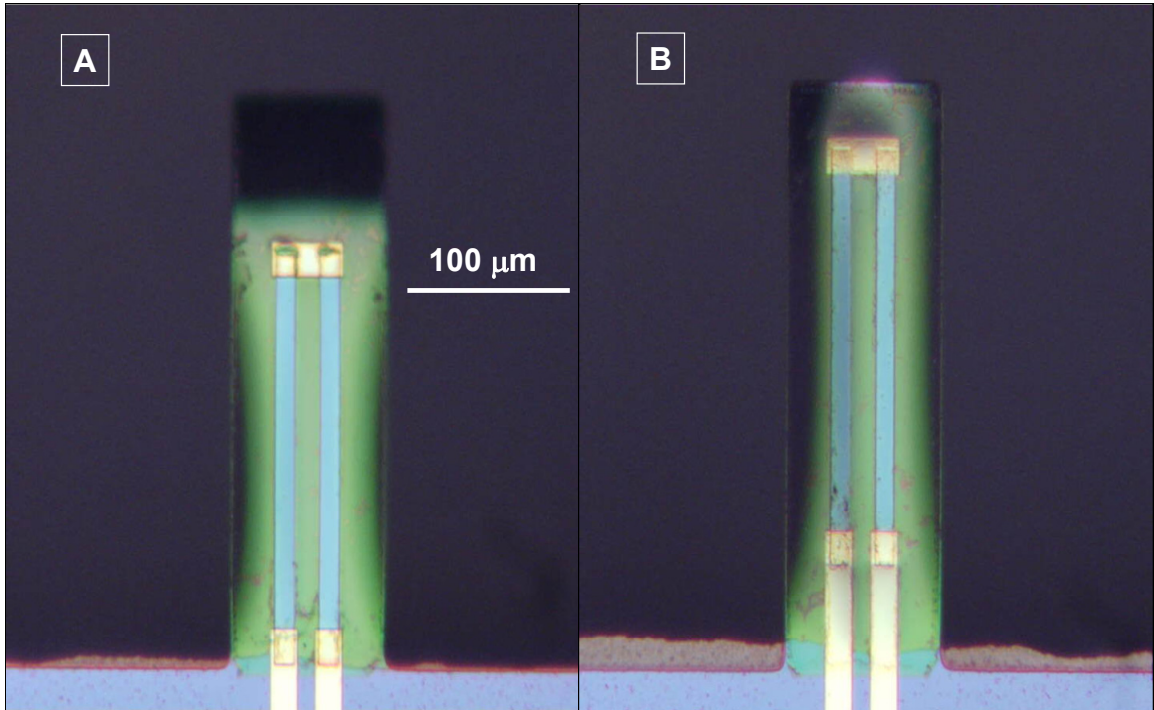


Figure 5.10. P μ CA microcantilever. A. $\delta = 0 \mu\text{m}$ and $\delta' \sim 0 \mu\text{m}$, B. $\delta = 50 \mu\text{m}$ and $\delta' = 10\text{-}15 \mu\text{m}$. Correct design of the cantilever parameter, δ , ensures that the surface stress sensitivity of the cantilever shown in B is unaffected by small errors in etching of the bulk silicon ($|\delta - \delta'| < 10 \mu\text{m}$).

The robust design and fabrication process lead to yields of as high as 80%. Currently, the critical-point dryer is not used for final device release, and several cantilevers break because of issues related to surface tension. Use of the critical-point dryer will improve yields further.

5.4 Fabrication Issues

5.4.1 Scheme of Stress Compensation.

Figure 5.11.A shows the structure of the cantilever with the top and bottom nitride layers. Early attempts at fabrication resulted in highly curved cantilevers (Figure 5.11.B).

This was due to residual stresses in the layers of the cantilever device. While a large curvature in no way compromises the functionality or sensitivity of the P μ CA, functionalization of such cantilevers by way of spotting, using systems such as the NanoeNabler™ (BioForce Nanosciences Inc., Ames, Iowa), or metal deposition is extremely difficult. Hence a scheme for curvature compensation was devised to allow for reduction in curvature of the cantilever. Since the stress in the SCS and SiO₂ layers of the wafer depend on the way that the wafer is manufactured, we sought to control the curvature of the cantilevers by controlling the stresses in the remainder of the layers.

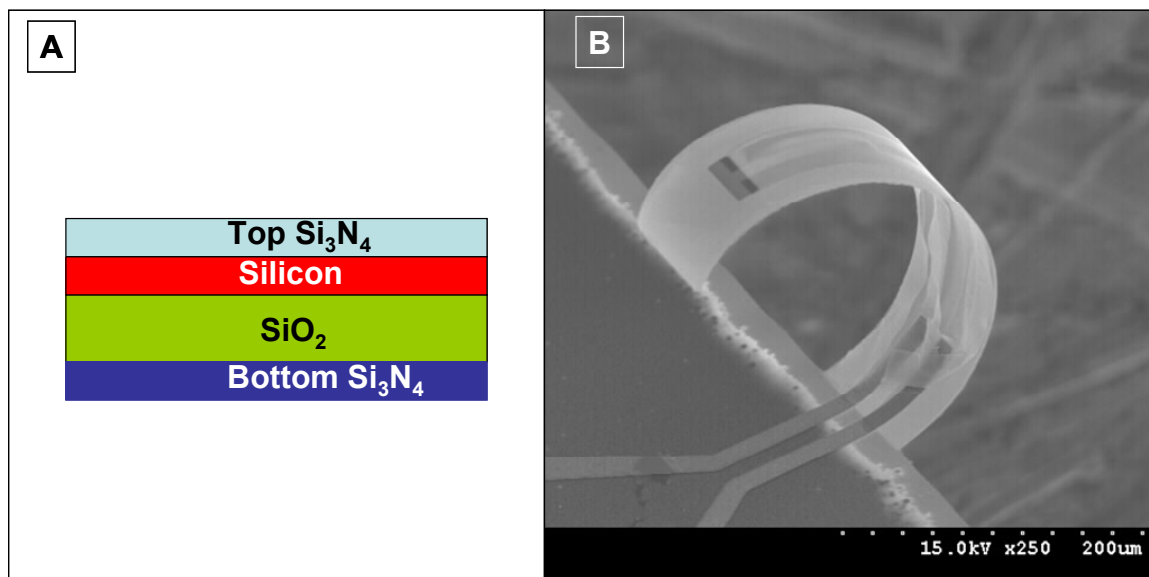


Figure 5.11. A. Layer structure of the cantilever. B. Curvature of a cantilever fabricated without the appropriate stress compensation for flat cantilevers.

The stress in the silicon nitride film grown by plasma-enhanced chemical vapor deposition (PECVD) (Unaxis 7900 PECVD, St. Petersburg, FL) can be controlled by changing the nitrogen flow rate during deposition (Figure 5.4). These stresses were evaluated using the Stoney equation [2]. A known thickness of silicon nitride was deposited on a silicon wafer for various nitrogen flow rates. The curvature of the wafer was measured on a Tencor KLA profilometer (KLA-Tencor Corp., San José, CA) before and after deposition, and the stress in the film was estimated.

The stress compensation scheme could have been implemented with a single layer of nitride on the top; however, adding a nitride layer on the back serves two purposes. It ensures that neither of the nitride layers has very large stresses. Also, by using a thinner

top nitride layer and a thicker bottom nitride layer, the neutral axis of the cantilever is lowered, and the surface stress sensitivity of the cantilever increases with bottom nitride thickness up to approximately 130 nm (Figure 5.12). Stress in the thermal SiO₂ layer was based on values found in the literature. Stresses in the gold layers deposited on the cantilever via sputter deposition were estimated using the method described above.

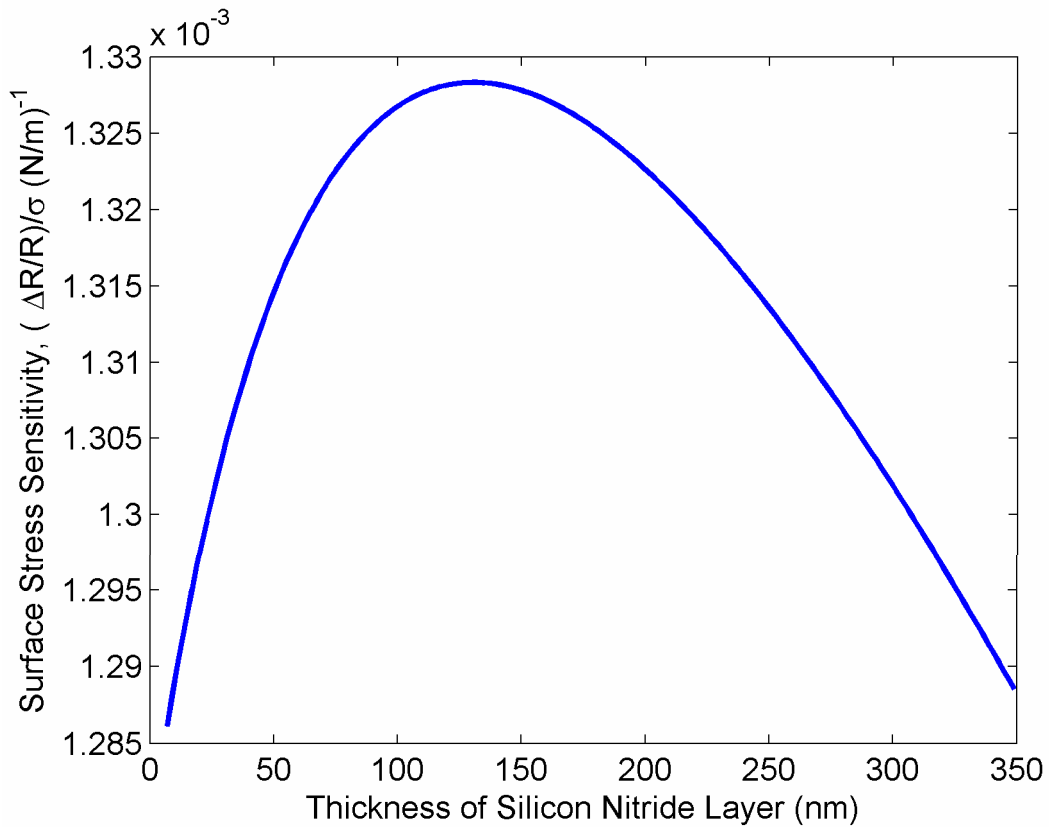


Figure 5.12. Variation of surface stress sensitivity with thickness of bottom nitride layer.

Compensation of the residual stresses in the films to control curvature of the cantilever was performed by carefully choosing the appropriate thickness and stress in the top and bottom nitride layers. The cantilever curvature model described earlier was implemented in MATLAB™. Table 5.2 lists the values of the mechanical properties of the various layers that were used in the implementation of this model.

Table 5.2. Mechanical properties and residual stress in various layers of the cantilever.

Layer	Si ₃ N ₄ (top)	SCS	SiO ₂	Si ₃ N ₄ (bottom)
Young's modulus (MPa)	160	169	75	160
Poisson ratio	0.24	0.27	0.17	0.24
Thickness (nm)	100	340	400	200
Residual stress (MPa)	-300	200	-270	270

Using (4.21), assuming that no surface stresses are present and that all curvature is on account of intrinsic stresses in the cantilever, we can write

$$\begin{bmatrix} \varepsilon^0 \\ \chi \end{bmatrix} = - \begin{bmatrix} \mathbf{A} & \mathbf{B} \\ \mathbf{B} & \mathbf{D} \end{bmatrix}^{-1} \left(\begin{bmatrix} \mathbf{N}_i \\ \mathbf{M}_i \end{bmatrix} + \begin{bmatrix} \mathbf{N}_s \\ \mathbf{M}_s \end{bmatrix} \right) = - \begin{bmatrix} \mathbf{A} & \mathbf{B} \\ \mathbf{B} & \mathbf{D} \end{bmatrix}^{-1} \begin{bmatrix} \mathbf{N}_i \\ \mathbf{M}_i \end{bmatrix} \quad (5.1)$$

Using the values from Table 5.2,

$$\mathbf{A} = \begin{bmatrix} 143804.8 & 34210.0 & 0 \\ 34210.0 & 143804.8 & 0 \\ 0 & 0 & 54797.4 \end{bmatrix}, \mathbf{B} = \begin{bmatrix} 0.0055 & 0.00204 & 0 \\ 0.00204 & 0.0055 & 0 \\ 0 & 0 & 0.00173 \end{bmatrix}, \mathbf{D} = \begin{bmatrix} 15.2 & 3.72 & 0 \\ 3.72 & 15.2 & 0 \\ 0 & 0 & 5.74 \end{bmatrix} \times 10^{-9} \quad (5.2)$$

and

$$\mathbf{N}_i = \begin{bmatrix} -11 \\ -11 \\ 0 \end{bmatrix} \text{N}, \mathbf{M}_i = \begin{bmatrix} -1.13 \\ -1.13 \\ 0 \end{bmatrix} \times 10^{-6} \text{N-m} \quad (5.3)$$

Curvature of the cantilever in the longitudinal direction is approximately -28 mm (the negative sign shows the direction of curvature; in this case, the minus sign indicates a downward curve). Also, using (4.2) and setting $z = z_R$, we find that the strain in the piezoresistor is underestimated by 2.5% (for this set of residual stresses) if the coupling term \mathbf{B} is ignored. While the curvature in this case is designed to be large (for flat cantilevers), it is apparent that curvature of the cantilever is a function of the mechanical properties of the layers and residual stresses. The curvature of the cantilever for a given set of layer materials can be changed by changing the layer thicknesses or residual stresses or both. Figure 5.13 shows the change in curvature of the cantilever for different bottom nitride thicknesses for fixed residual stresses in the layers (see Table 5.2). The

cantilever is completely flat for a bottom nitride thickness of approximately 195.8 nm under the said conditions. (The residual stress in the SCS layer was evaluated from the curvature model in an earlier iteration wherein all other stresses and film thicknesses were known.) Also, different regions of the cantilever have different layer structures. However, based on our experience, the curvature of the cantilever is fairly accurately modeled by approximating the entire cantilever to the structure in Figure 5.11.A.

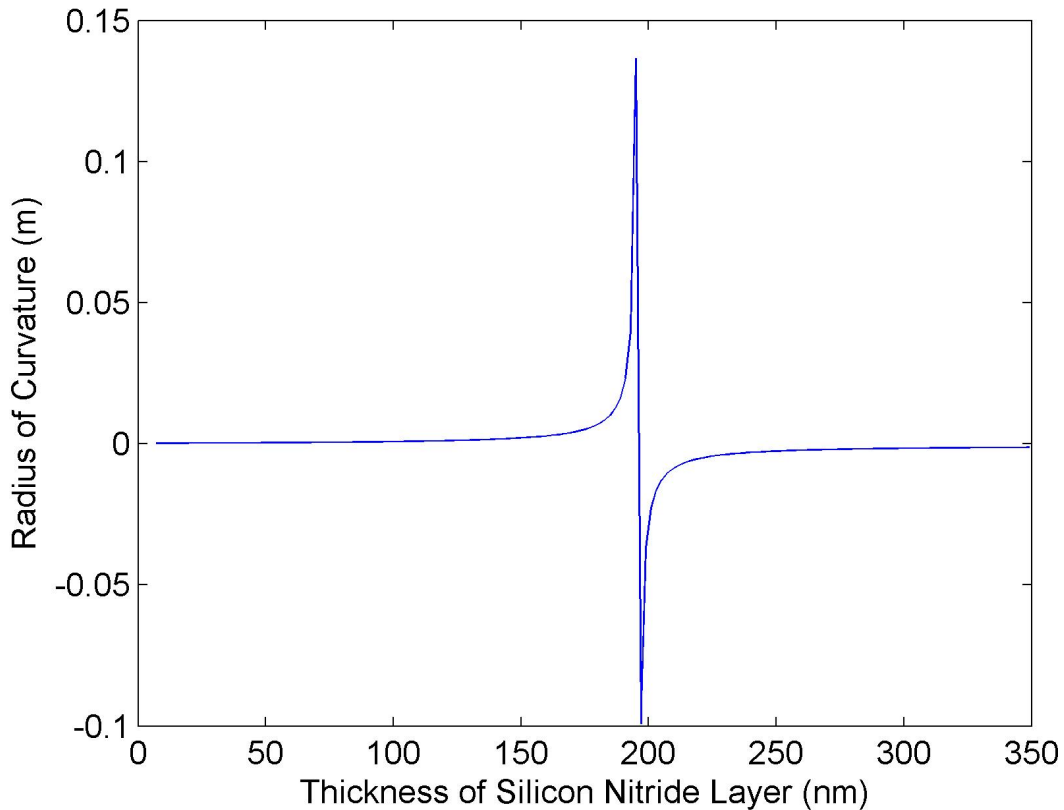


Figure 5.13. Change in radius of curvature with increasing thickness of bottom (tensile) nitride layer. At approximately 200 nm, it approaches infinity; i.e., the cantilever is almost flat.

5.4.2 Functionalization of Cantilevers.

Our current experiments with P μ CAs involved using a cantilever functionalized with gold (50 nm) on the top surface to detect 6-mercapto-1-hexanol. In the past, various groups have functionalized cantilever surfaces with materials such as metals, polymers, and DNA [3]. The fabrication process developed allows for deposition of metals on the cantilever during the cantilever fabrication. However, poor adhesion of the gold was

noticed in some devices. The likely reason for the delamination of the gold functionalization layer is the high interface stresses that develop during the processing.

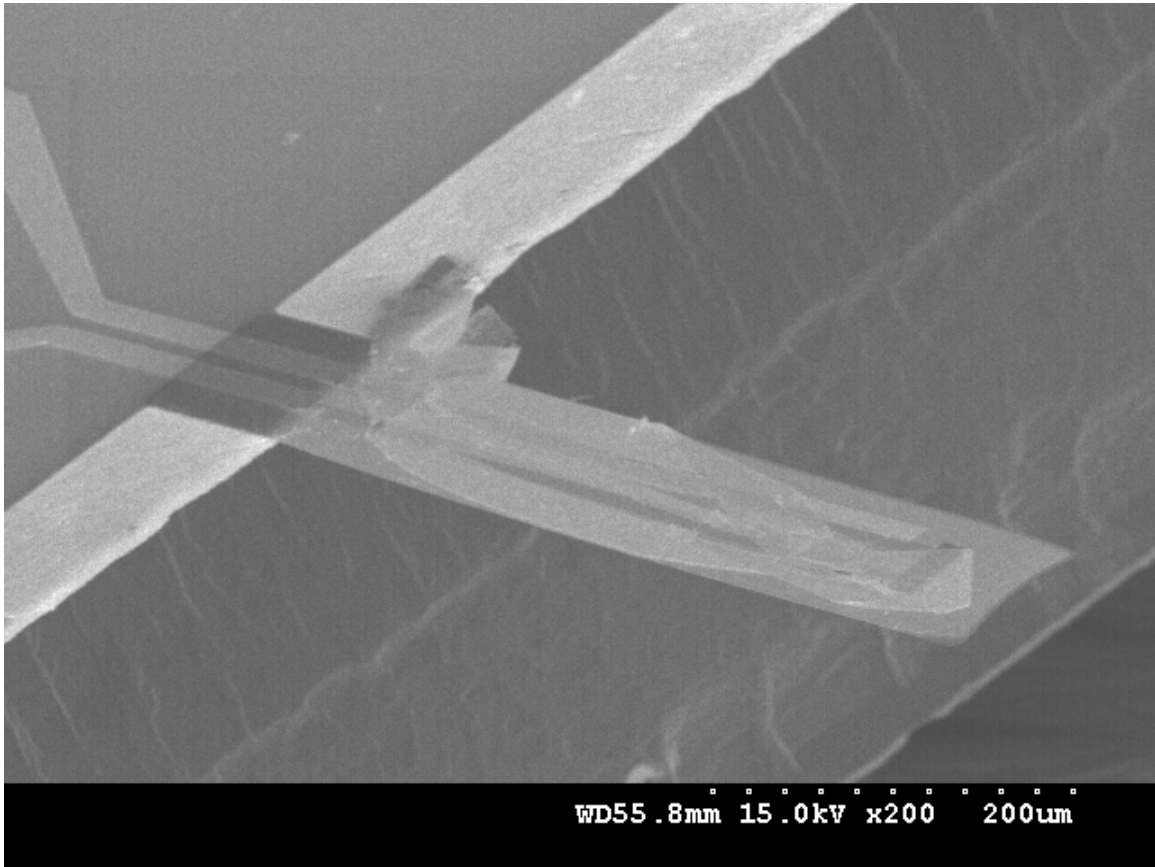


Figure 5.14 Delamination of gold from cantilever surface due to large interfacial stresses.

An alternative method that has been implemented is the use of a shadow masking process for the deposition of metals. A shadow mask was made by using stereolithography (SLA) [4]. The mask was designed to allow for easy alignment and selective metallization of the cantilevers in a sputtering system. Figure 5.15 shows the manner in which the two halves of the mask are placed around the P μ CA. The device is placed on the lower half and fixed in place with double-sided sticky tape. Alignment is carried out once the top mask is put on to ensure the cantilevers to be coated are in the line-of-sight. The holes over the cantilevers that are to be left uncoated are either blocked with a specially designed SLA cover or with tape.

Preparation of samples for double-sided measurement was carried out in the same manner. The SLA mask shown in Figure 5.15 has holes for metallization on both top and

bottom halves. Devices used for double-sided measurement were taken through two cycles of coating, ensuring at all times that the reference cantilevers are not coated.

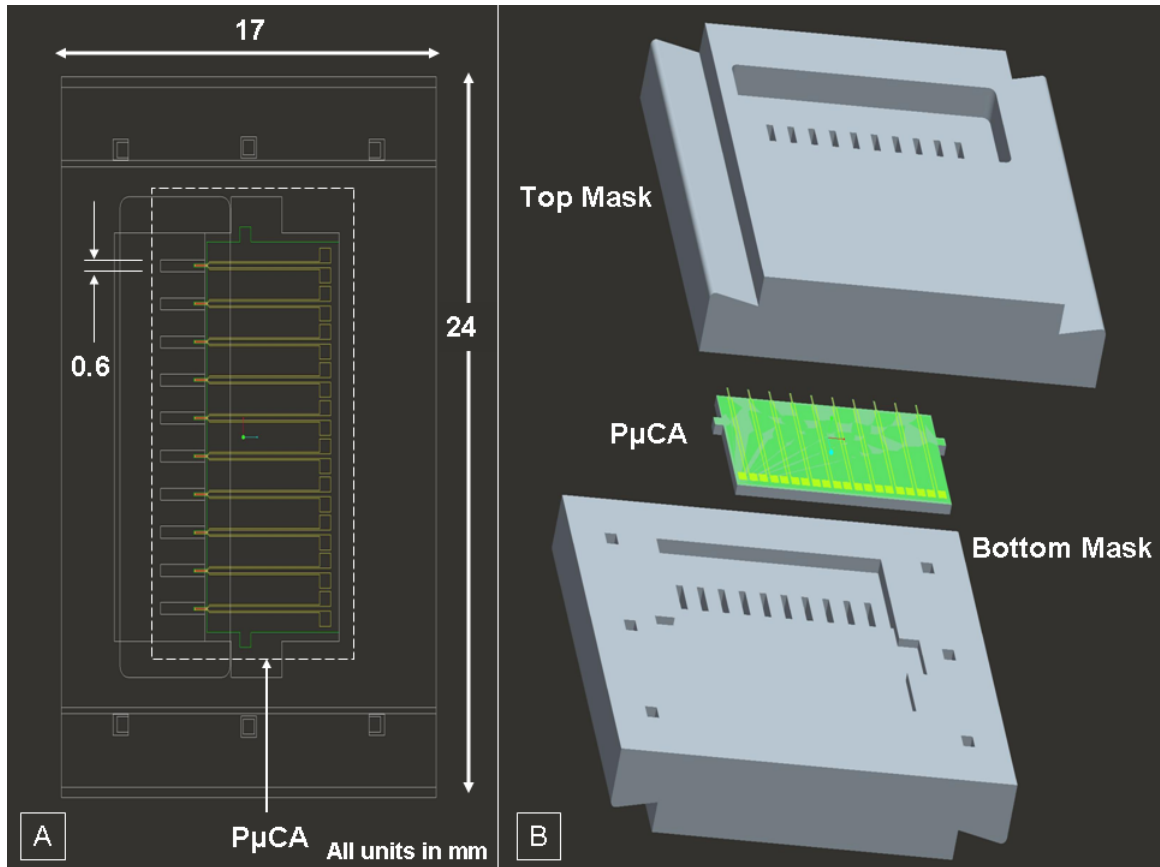


Figure 5.15. Scheme for metallization of the piezoresistive microcantilevers after fabrication.

5.5 Conclusions

A robust method of fabrication of the piezoresistive microcantilever devices has been developed. Cleanliness of the sample, the device surface and, often, the equipment used for fabrication has been found to be crucial in ensuring good contact of electrical purposes and good adhesion of various layers in this fabrication process.

The analytical model for surface stress developed in Chapter 4 may be used to control the curvature of the cantilever based on the stresses in the various layers. Some issues of delamination of gold from the cantilever surface are not completely understood. These are possibly due to large interfacial stresses and could potentially be resolved by choosing alternative materials or deposition processes.

The chapters that follow discuss issues of characterization and testing of the P μ CA that has been fabricated.

5.6 References

- [1] M. J. Madou, *Fundamentals of microfabrication*, 1 ed. Boca Raton: CRC Press, 2000.
- [2] G. G. Stoney, "The tension of metallic films deposited by electrolysis," *Proceedings of the Royal Society of London Series a-Containing Papers of a Mathematical and Physical Character*, vol. 82, pp. 172-175, May 1909.
- [3] N. V. Lavrik, M. J. Sepaniak, and P. G. Datkos, "Cantilever transducers as a platform for chemical and biological sensors," *Review of Scientific Instruments*, vol. 75, pp. 2229-2253, 2004.
- [4] P. F. Jacobs, *Stereolithography & other RP&M technologies: From rapid prototyping to rapid tooling* Dearborne: Society of Manufacturing Engineers, 1996.

CHAPTER 6

MECHANICAL AND THERMAL CHARACTERIZATION

In the previous chapter issues related to fabrication and functionalization of the P μ CA was discussed. This chapter investigates the mechanical and thermal characteristics of the cantilevers fabricated. Issues related to electrical characterization of the cantilevers and electronic noise issues have been discussed in the relevant portions of Chapters 3, 4 and 5. Mechanical and thermal characterization has aided understanding of the operational characteristics of these cantilevers and selection of the appropriate range of operation of these sensors.

6.1 Mechanical Characterization

6.1.1 Measurement of Natural Frequency of Cantilevers

The natural frequency of the piezoresistive microcantilevers was evaluated using a Digital Instruments Multimode AFM (Veeco Inc., Santa Barbara, CA). The 10-cantilever P μ CA was diced into individual 1.5 mm x 2.5 mm dies to allow it to be used on the AFM. The entire device was coated with photoresist that was baked at 80 °C for 2 hours to ensure the cantilevers did not break in the dicing process. Measurements were made under ambient conditions.

The natural frequency measurement with a cantilever with a free length (length from the clamping point) of 517 μ m long piezoresistor is shown in Figure 6.1. The natural frequency was evaluated at 50.59 kHz. A second measurement with a cantilever with a shorter free length of 321 μ m yielded a natural frequency of 117.16 kHz.

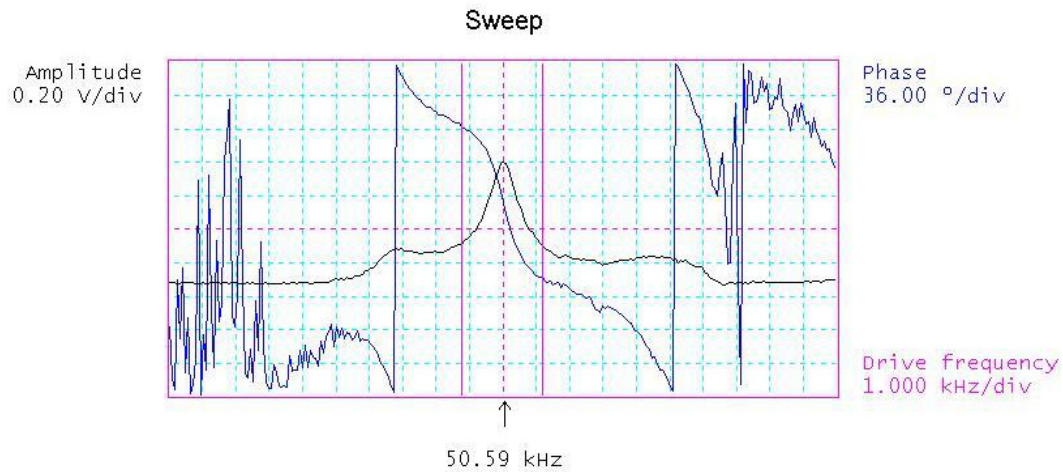


Figure 6.1 Measurement of natural frequency of a 517 μm cantilever. Phase response of the cantilever is overlain in the plot.

6.1.2 Measurement of Gauge Factor of Cantilevers

The gauge factor of the single crystal silicon of the cantilevers was required for an accurate measure of the surface stress sensitivity of the cantilever. In order to evaluate the gauge factor, the deflection sensitivity of the surface stress sensitive microcantilever was evaluated.

6.1.2.1 Calculation of Gauge Factor

In piezoresistive microcantilever probes used on AFM systems, the piezoresistor is placed at the clamped end since this represents the region of maximum stress. The effect of tip deflection of the cantilever can be calculated using a simple equation for moment generated at the clamped end of the cantilever [1]. In the surface stress sensitive microcantilevers used in this work, the piezoresistive response to tip deflection is evaluated by calculating the average stress over the length of the piezoresistor (Figure 6.2).

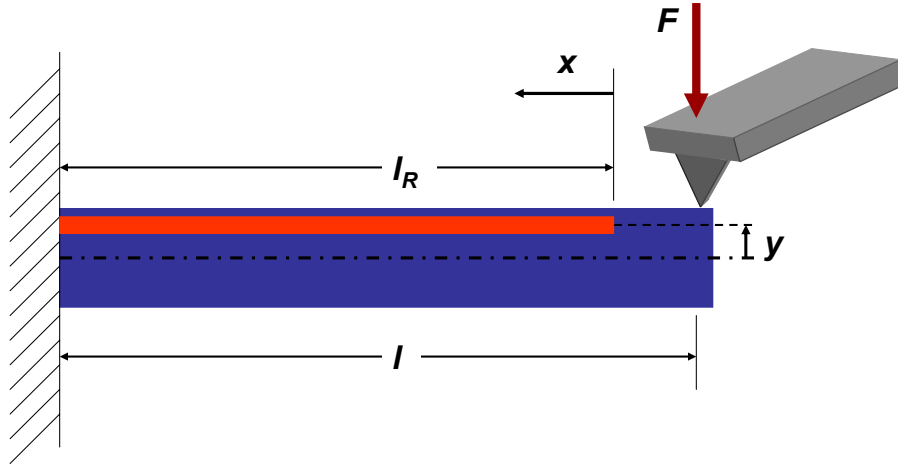


Figure 6.2 Schematic showing cantilever cross-section and the method of deflection of piezoresistive microcantilever. A known deflection is achieved by using a stiff AFM probe.

If a force of F applied at the cantilever tip, the moment (M_x) at a distance x from the tip of the piezoresistor of length l_R on a cantilever of length l (Figure 6.2), is given by

$$M_x = F(l - l_R + x) \quad (6.1)$$

The resultant surface stress at a piezoresistor placed at a distance y above the neutral axis of the cantilever cross-section, with an area moment of inertia of I , is

$$\sigma_x = \frac{M_x y}{I} \quad (6.2)$$

The average stress experienced by the piezoresistor is

$$\langle \sigma \rangle = \frac{\int_{x=0}^{l_R} \sigma_x dx}{l_R} \quad (6.3)$$

$$\Rightarrow \langle \sigma \rangle = \frac{F \left(l_R l - l_R^2 + \frac{l_R^2}{2} \right) y}{l l_R} = \frac{F \left(l - \frac{l_R}{2} \right) y}{I} \quad (6.4)$$

If deflection of the cantilever with spring constant $k_{cantilever}$ is Δz , $F = k_{cantilever} \Delta z$ and the piezoresistive response of the cantilever, based on the longitudinal piezoresistive coefficient, is given by

$$\frac{\Delta R}{R} = \pi_{longitudinal} \langle \sigma \rangle = \pi_{longitudinal} k_{cantilever} \left(\left(l - \frac{l_R}{2} \right) \frac{y}{I} \right) \Delta z \quad (6.5)$$

The spring constant of the cantilever, $k_{cantilever} = \frac{3(EI)_{cantilever}}{l_R^3}$, $(EI)_{cantilever}$ is the flexural rigidity of the cantilever based on the material properties of the multilayered cantilever [1]. The stiffness of the cantilever has been calculated based on the length of the piezoresistor (l_R) as opposed to the length of the cantilever (l). This is an acceptable approximation since in all the experiments performed the point of application of force was the tip of the piezoresistor.

Incorporating the expression for spring constant, the piezoresistive response to tip deflection may be written as

$$\frac{\Delta R}{R} = \pi_{longitudinal} \langle \sigma \rangle = 3 \frac{(EI)_{cantilever}}{l_R^3} \pi_{longitudinal} \left(\left(l - \frac{l_R}{2} \right) \frac{y}{I} \right) \Delta z \quad (6.6)$$

An effective Young's modulus E' is evaluated as $E' = \frac{(EI)_{cantilever}}{I}$ and the piezoresistive response may be expressed as

$$\frac{\Delta R}{R} = \pi_{longitudinal} \langle \sigma \rangle = 3E' \pi_{longitudinal} \left(\frac{\left(l - \frac{l_R}{2} \right)}{l_R^3} y \right) \Delta z \quad (6.7)$$

The gauge factor, $K = E' \pi_{longitudinal}$ may be evaluated from (6.7). This expression also shows that the deflection sensitivity of the cantilever for surface stress detection decreases with increase in length of the piezoresistor length.

6.1.2.2 Experimental Evaluation of Deflection Sensitivity

Experiments for deflection sensitivity were performed on a Veeco Dimension 3100 AFM (Veeco Inc., Santa Barbara, CA). A stiff AFM probe with a spring constant of 40 N/m (Nanoprobes Inc., Yaphank, NY) was used to deflect a piezoresistive microcantilever at a frequency of 7 Hz with a peak-to-peak deflection amplitude of 2 μm . As mentioned in the previous section, in all experiments the point of the interaction of the AFM probe tip and the piezoresistor was the tip of the piezoresistor. The layer structure of the cantilever has been described in Chapter 5. The dimensions of the cantilever used in this experiment were $l = 450 \mu\text{m}$, $l_r = 400 \mu\text{m}$ and $y = 325 \text{ nm}$.

The nominal resistance of the cantilever was 3.46 k Ω . Measurement of deflection sensitivity was performed using a 10-channel CMOS chip developed at Oak Ridge National Laboratories [2]. The voltage-resistance characteristics of the CMOS chip is shown in Figure 6.3.

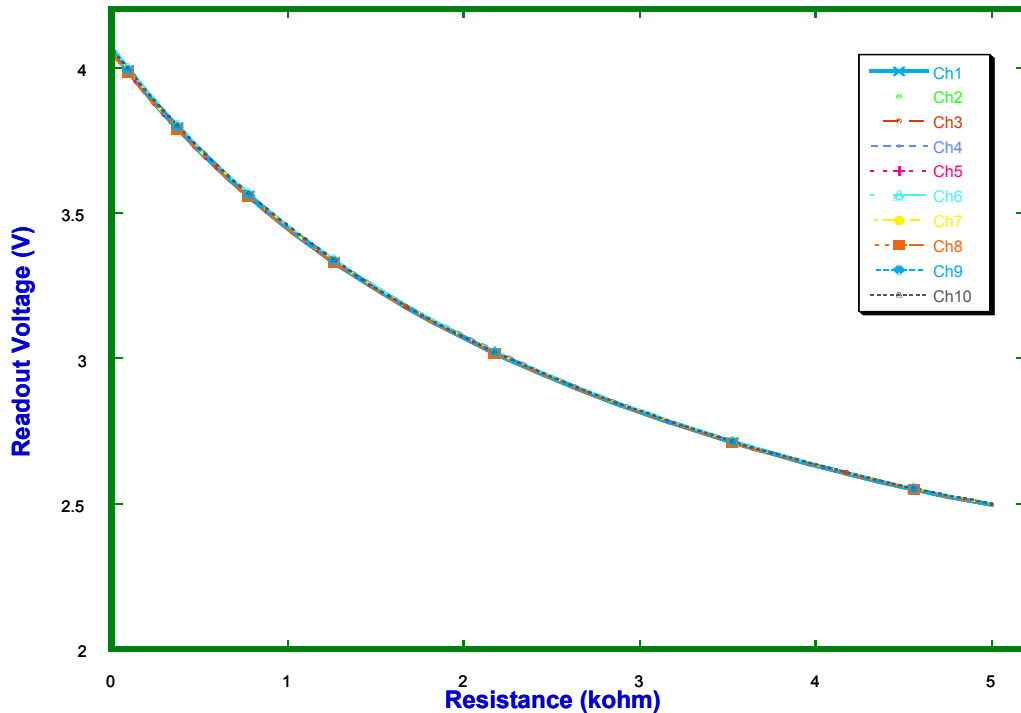


Figure 6.3 Voltage sensitivity of the 10-channel CMOS chip to resistance change in the piezoresistive microcantilever [2]. The voltage sensitivity at 3.46 k Ω is $4.4 \times 10^{-4} \text{ V}/\Omega$.

The peak-to-peak amplitude of the voltage response to the 2 μm deflection was approximately 200 μV , which is equivalent to a resistance change of 0.45 Ω . This leads to an estimate of gauge factor of $K = -49.58$. Typically silicon gauge factors are in the range of -100 to -140 [3, 4]. However the gauge factor evaluated here is for a highly doped silicon piezoresistor which is incorporated in a silicon cantilever. Hence the effect gauge factor of the sensor is lower than for single crystal silicon.

6.2 Thermal Characterization

6.2.1 Introduction

Thermal characterization of the piezoresistive microcantilevers was performed for two distinct reasons. As will be discussed in Chapter 7, resistance measurement in this work has been performed using PSD techniques. Since this involves excitation of the cantilevers with AC signals, it was important to evaluate the response of the cantilevers to such excitation and to determine if thermal variations were introduced in the cantilever by the AC signals. The concern was that cantilever resistance might vary significantly due to AC excitation. This could lead to erroneous measurement. The second reason for these experiments was that thermal characterization of the cantilever would allow for temperature control during chemical measurement. This could, potentially, be used to measure kinetics of the analyte binding or dissociation process.

The following issues have been taken up for study in this work:

1. Modeling of the cantilevers to predict cantilever response.
2. Characterization of the temperature coefficient of resistance of the silicon piezoresistors.
3. Response of the cantilevers to DC and sinusoidal excitation.
4. Evaluation of microscale convection heat transfer coefficients.
5. Operation of heated cantilever array.

6.2.2 Background

Thermal models to predict the thermal response of microcantilever and microheater systems have been developed [5, 6]. These frequency-response based models

can only predict the thermal response once steady-state has been achieved. Prediction of the initial transients is possible only with a time-domain based model. This is particularly important in understanding the rate and nature of chemical reactions because in several systems the reaction is complete before system comes to steady-state thermal operation.

A crucial component of the development of a thermal model is to understand the magnitude and the nature of heat transfer from the heated microdevice. Heat transfer relations for macro-scaled devices based on natural convection suggest heat transfer coefficients of the order of $10 \text{ W/m}^2\text{K}$. However work by several groups [5-7] suggests heat transfer coefficients are much higher at micron scales. Further Guo et al. [8] have suggested that heat transfer to air at micron length-scales occurs by way of conduction rather than natural convection. However, for the purposes of modeling, the heat transfer to air may be expressed as an effective heat transfer coefficient (h_{eff}) which can then be used to evaluate thermal properties of the surrounding air (or fluid medium). In the rest of this document this ' h_{eff} ' is referred to simply as ' h '.

The current work seeks to develop a thermal model for a piezoresistive microcantilever and evaluate the values of h_{eff} over a range of temperature of ambient to $150 \text{ }^\circ\text{C}$ since these are the expected working conditions of the piezoresistive cantilevers in use in this work. Another reason for development of the thermal model is to able to evaluate the appropriate operational range of the piezoresistive microcantilevers such that electrical excitation does not cause large thermal oscillations in the microcantilevers. Finally the model could be used as tool for open or closed loop control of temperature in the microcantilever.

6.2.3 Model for Heat Transfer from Piezoresistive Microcantilevers

In order to create a model to accurately predict thermal behavior of the cantilever, the following assumptions were made:

- The cantilever is assumed to have a rectangular cross-section.
- The clamped end of the cantilever is at ambient temperature (T_{amb}).
- The free end is adiabatic (area of heat transfer at the free end is 0.1% of total surface area).
- Temperature across each cross-section of the cantilever is uniform ($Bi \sim 7 \times 10^{-3}$).

- There is no heating in sections where the piezoresistor does not extend.
- All material properties are temperature independent.

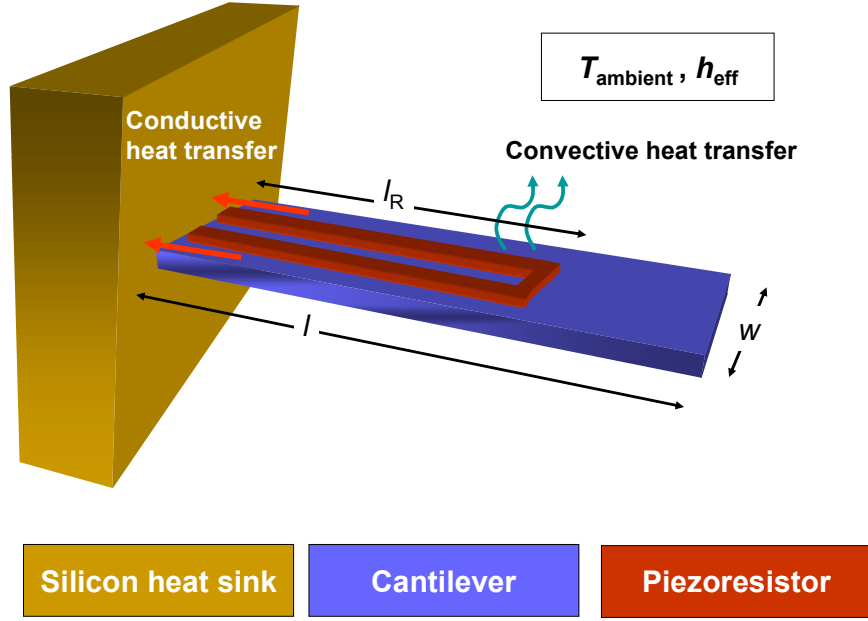


Figure 6.4 Schematic of heat transfer from a piezoresistive microcantilever.

The simple PDE describing the cantilever section with the doped silicon piezoresistor is,

$$\frac{\partial \theta}{\partial t} = a \frac{\partial^2 \theta}{\partial x^2} + b\theta + c\dot{Q} \quad (6.8)$$

where,

$$a = \frac{\sum_{Layer 1}^{Layer N} k_i v_i}{\sum_{Layer 1}^{Layer N} \rho_i c_{p,i} v_i}, \quad b = -\frac{2h_{eff} w}{A_c \sum_{Layer 1}^{Layer N} \rho_i c_{p,i} v_i} \quad \text{and} \quad c = \frac{2}{A_c A_p \sum_{Layer 1}^{Layer N} \rho_i c_{p,i} v_i} \quad (6.9)$$

ρ_i is the density, k_i is the thermal conductivity and v_i the volume fraction of the i^{th} material layer. A_c and A_p are the cross-section of the cantilever and the piezoresistor respectively.

Also, the ohmic heating term, $\dot{Q} = I_c^2 s(\theta)$

$$I_c = \frac{V_c}{R_c(\theta)} = \frac{V_{in}}{R_c(\theta) + R_{ballast}} \quad (6.10)$$

Here $\theta(x,t) = T(x,t) - T_{amb}$, $s(\theta)$ is the temperature dependent resistivity of the piezoresistor and V_c is the voltage across the cantilever. The boundary conditions associated with this model are:

$$\theta(0,t) = 0, \theta(x,t) = 0 \text{ and } \frac{\partial \theta(l,t)}{\partial x} = 0 \quad (6.11)$$

The first two boundary condition states that temperature at the clamped end is always at ambient temperature and the second that at $t = 0$, the entire cantilever is at ambient temperature. The third boundary condition establishes an adiabatic boundary condition at the free end of the cantilever.

The schematic in Figure 6.4 shows the heat transfer phenomena associated with cantilever operation. Heat generation occurs only in the region with the piezoresistor. The finite element model accounts for this effect and heating is limited to the portion of the cantilever with the piezoresistor. In the unheated portion of the cantilever, $c = 0$. All material properties used in (6.9) were based on values reported in literature [4, 9-11].

An analytical solution was developed for this system (Appendix C). This closed form solution can be obtained only if the cantilever resistance in (6.10) and the heat transfer coefficient in (6.9) are constants. In order to model the cantilever heating better, a finite difference solution was developed to include the instantaneous cantilever resistance, $R_c(\theta)$. The finite difference solution may be written in the form,

$$\frac{\theta_u^{\tau+1} - \theta_u^\tau}{\Delta t} = a \left[\frac{\theta_{u+1}^\tau - 2\theta_u^\tau + \theta_{u-1}^\tau}{\Delta x^2} \right] + b \theta_u^\tau + c [C_0 + C_1 \theta_u^\tau] \quad (6.12)$$

where C_0 and C_1 are constants associated with the thermal dependence of cantilever resistance on temperature such that $R_c(T) = C_0 + C_1(T)$ and T is temperature of the piezoresistor in degrees centigrade. The resistance of the cantilever, based on the thermal profile developed due to ohmic heating, is given by:

$$R_c(t) = R_0 + \frac{2}{A_p} \int_0^{l_c} s(\theta(x,t)) dx \quad (6.13)$$

While an implicit finite difference formulation could have been used for the case when heat transfer coefficient is constant, this is not possible when a thermal dependence

on temperature, $h = h(\theta)$, is assumed. In order to evaluate the accuracy of finite difference solution, for a constant heat transfer coefficient (h) and input voltage (V_{in}), it was compared with an analytical solution (Appendix C) to (6.8) and found to agree within 0.6% with a time step (Δt) of 1 μ s and step length (Δx) of 6 μ m. Higher accuracy may be achieved by smaller time and spatial steps but this increases the simulation time significantly. All work presented here was based on an explicit finite difference formulation.

6.2.4 Device Details

In order to evaluate the effect of various design parameters, cantilevers with different cantilever and resistor lengths were design and fabricated. In our current measurements were made with two chips. The design parameters associated with these devices are listed in Table 6.1. The materials properties of the multilayered cantilever and cantilever dimension define the heat capacity of the cantilever while the heat flux is related to the length of the cantilever resistor. Since the specific resistivity and cross-section of the silicon piezoresistor are the same for all the cantilever designs, the length of the resistor is the measure of the heat dissipated by the cantilever.

Table 6.1 Design parameters of cantilever chips used in experiments. Cantilevers have been referred to as ‘Cant’ in this table. All dimensions are in microns.

Device No.	Cant 1	Cant 2	Cant 3	Cant 4	Cant 5	Cant 6
Device 1: $l_R = 400,$ $\delta = 0$	$l = 475$	$l = 425$	$l = 625$	$l = 575$	X	X
Device 2: $l = 750,$ $\delta = 0$	$l_R = 650$	$l_R = 550$	$l_R = 460$	$l_R = 725$	$l_R = 550$	$l_R = 375$

6.2.5 Experimental Design

The initial measurements on temperature coefficient on resistance were made on two separate chips to ensure electrical properties did not show large variation over the wafer. Once this was established, subsequent DC characterization experiments were carried out with a single chip (device 2) with six different cantilever designs. This

allowed for evaluation of heat transfer properties at the length scales associated with the cantilevers. The cantilever thermal characteristics were found to be very repeatable and strongly correlated with the cantilever geometry. This justified the use of a single cantilever to perform the thermal characterization experiments to evaluate frequency response of the cantilever to various sinusoidal inputs.

6.2.6 Measurement Setup

The P μ CA was wire-bonded onto a gold package and the selected cantilever was placed in series with a carbon ballast resistor of 4.130 k Ω ($\pm 1\%$). A DS345 signal generator (SRS Instruments, Sunnyvale, CA) was used to apply a voltage $V_{in}(t)$ across the circuit (Figure 6.5). The output voltage, $V_{out}(t)$, was measured, across the ballast resistor, on a TDS3032 oscilloscope (Tektronix, Richardson, TX). The voltage across the piezoresistor, $V_c(t) = V_{in}(t) - V_{out}(t)$. Each waveform was averaged 2,500 times, using a program written in LabVIEW, to reduce measurement noise.

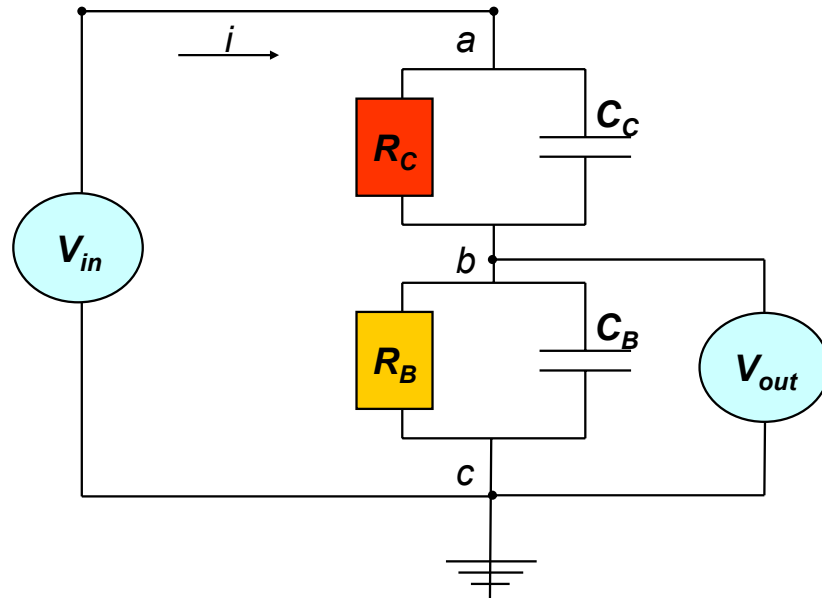


Figure 6.5 Circuit for measurement of cantilever resistance. The circuit capacitances were evaluated using impedance analysis.

6.2.7 Characterization of Measurement Setup

6.2.7.1 Characterization of the Input Source

In order to evaluate the relationship between input voltage and cantilever thermal response, it was important to verify the power being delivered to cantilever by the input power supply- a DS345 signal generator (Stanford Research Systems, Sunnyvale, CA). Hence spectral analysis of the cantilever input was carried out. At frequencies lower than 100 kHz, the harmonic distortion in the DS354 is less than 55 dB [12]. Figure 6.6 shows the frequency spectrum associated with a representative input voltage. Harmonics noticed in the spectrum were 3 orders of magnitude lower than the principal input frequency. If these are ignored in measurement of resistance, errors in measurement of resistance of the order of 5-10 Ω are possible.

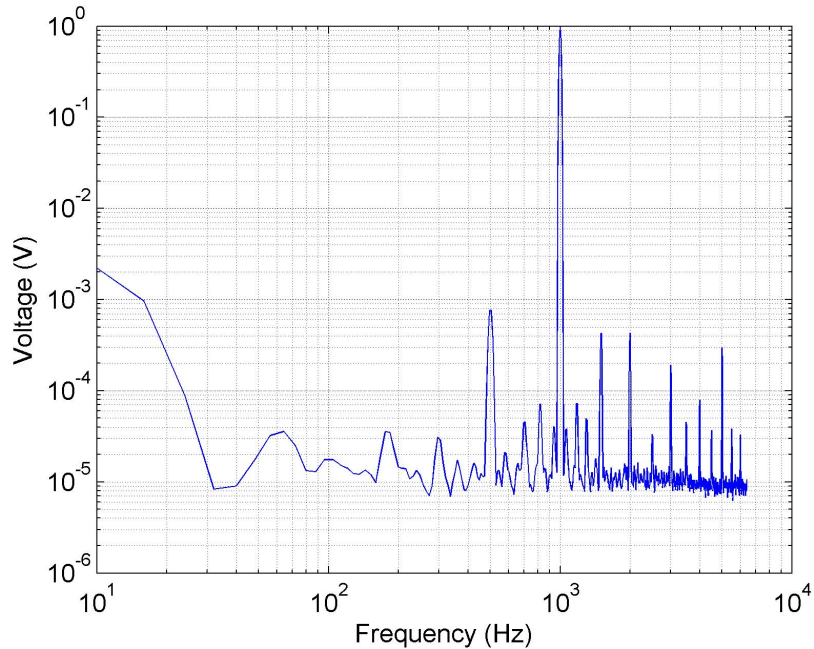


Figure 6.6 Frequency spectrum of the signal generator output for a 1V output at 1 kHz.

6.2.7.2 Characterization of the Ballast Resistor

At very low frequencies, resistance of the cantilever at any time, t , is given by

$$R_c(t) = (V_{in}(t)/V_{out}(t) - 1)R_b \quad (6.14)$$

However this relation is valid only for a limited frequency range in which the reactance of the ballast resistor is small. The ballast resistor impedance was evaluated using a Solartron SI 1260 impedance analyzer (Solartron, Hamshire, UK). The impedance plot suggests that (6.14) is not valid for frequencies of 10 kHz and higher. The ballast resistor impedance could be modeled as resistor (R_b) and a capacitor (C_b) in parallel (Figure 6.5). In a similar fashion, impedance analysis of the cantilever showed that the piezoresistor can be modeled as a resistor (R_c) and capacitor (C_c) in parallel. Impedance analysis of connectors and wiring in the measurement circuit suggested that these impedances were negligible. Hence these were ignored in the complete circuit shown in Figure 6.5. The values of the circuit parameters evaluated were $R_B = 4316 \Omega$ and $C_B = 79.63 \text{ pF}$ (Figure 6.7). Impedance analysis of the cantilever used for AC characterization was performed at several different amplitudes ranging from 0.1 V to 3 V and in each case we found the cantilever capacitance could be modeled effectively with $C_C = 9.76 \text{ pF}$.

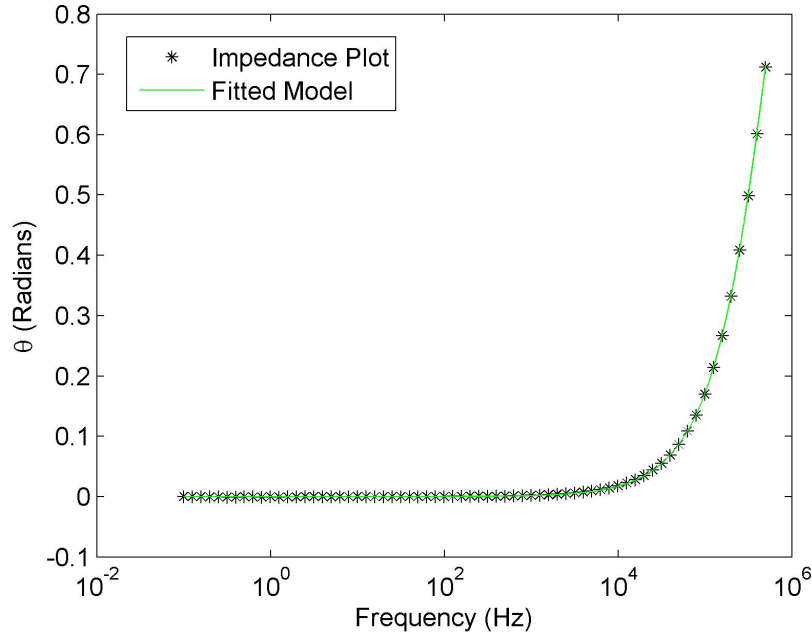


Figure 6.7 Impedance characteristics of ballast resistor.

6.2.8 Measurement of Cantilever Resistance

At frequencies higher than 10 kHz, impedance characteristics of the measurement circuit and the cantilever piezoresistor must be accounted for in order to measure cantilever resistance. The current flowing in the resistance measurement circuit (Figure 6.5) is described by the equation,

$$i = \frac{V_{ab}}{R_C} + C_C \frac{dV_{ab}}{dt} = \frac{V_{bc}}{R_B} + C_B \frac{dV_{bc}}{dt} \quad (6.15)$$

where,
$$V_{bc} = V_{out}, V_{ab} = V_{in} - V_{out} \quad (6.16)$$

Two distinct methods were used to measure resistance:

1. Measurements were made using the raw data obtained from experiment. V_{in} and V_{out} are obtained from the experiment. Using the relations (6.15) and (6.16), the cantilever resistance as a function of time, R_C , can be obtained directly. The issue with this approach is the measurement of derivatives V_{ab} and V_{bc} . The derivative is measured as $\frac{dV}{dt} = \frac{\Delta V}{\Delta t}$.

As pointed out earlier, the oscilloscope used for measurement had a resolution of 1 mV. This resulted in measurements with associated quantization errors. Also there were numerous high frequency components in the spectra of both V_{in} and V_{out} . In order to reduce the noise associated with the measurement of the derivative, Δt was chosen such that $\Delta t = \frac{k}{f_s}$ where k is an integer constant and f_s is the sampling frequency associated with the measurement. Choosing a large k reduces measurement noise. However this method also serves to filter the measured signal with a low pass filter with a cutoff frequency of $\frac{f_s}{k}$. In some measurements $k > 10$ were required to reduce measurement noise. However a significant noise level in the measurements, associated with the noise floor, remains. For an excitation frequency of 1 kHz, for the sampling period used in these experiments, the sampling frequency was 5 MHz.

2. A second method of measurement was developed, based on the inspection of the spectra V_{in} and V_{out} . Figure 6.6 shows the noise in the measurement is principally due to the existence of significant subharmonic and harmonic components. However beyond

3ω , where ω is the excitation frequency, these have a very limited influence on the heating and therefore resistance of the piezoresistor. Hence the input and output waveforms, V_{in} and V_{out} , were fit in MATLAB with a Fourier series of the form:

$$V(t) = a_0 + a_1 \cos\left(\frac{1}{2}\omega t\right) + b_1 \sin\left(\frac{1}{2}\omega t\right) + a_2 \cos(\omega t) + b_2 \sin(\omega t) + a_3 \cos(2\omega t) + b_3 \sin(2\omega t) + a_4 \cos(3\omega t) + b_4 \sin(3\omega t) \quad (6.17)$$

The Fourier fit ignores the effects of noise over a large range of frequencies acts to filter noise associated with the noise floor. It does however account for all the significant harmonics and subharmonics associated with the physical phenomenon at hand. However it should be noted this may only be done if the SNR is large. Using this form of the equation and the relations described in (6.15) and (6.16), cantilever resistance was evaluated as function of time. In this work, this method has been used to evaluate cantilever resistance with various excitation frequencies.

6.2.9 Thermal Characterization of Microcantilevers

6.2.9.1 Thermal Calibration of Devices

In order to evaluate the relationship between cantilever resistance (R_c) and cantilever temperature (T_c), calibration of the cantilevers was carried out. The P μ CA was glued to a gold package with a silver thermal epoxy (SPI Supplies, Chester, PA) and the chip temperature was monitored using a J-type thermocouple bonded to the package using the thermal epoxy. Cantilever resistance was measured with a Keithley 2400 Sourcemeter (Keithley Instruments Inc., Cleveland, OH) with source current of 10 μ A. The package was placed on a hotplate and the temperature was slowly ramped to 150 $^{\circ}$ C. Figure 6.8 shows plots of the temperature-resistance calibration for device 2 (table 1).

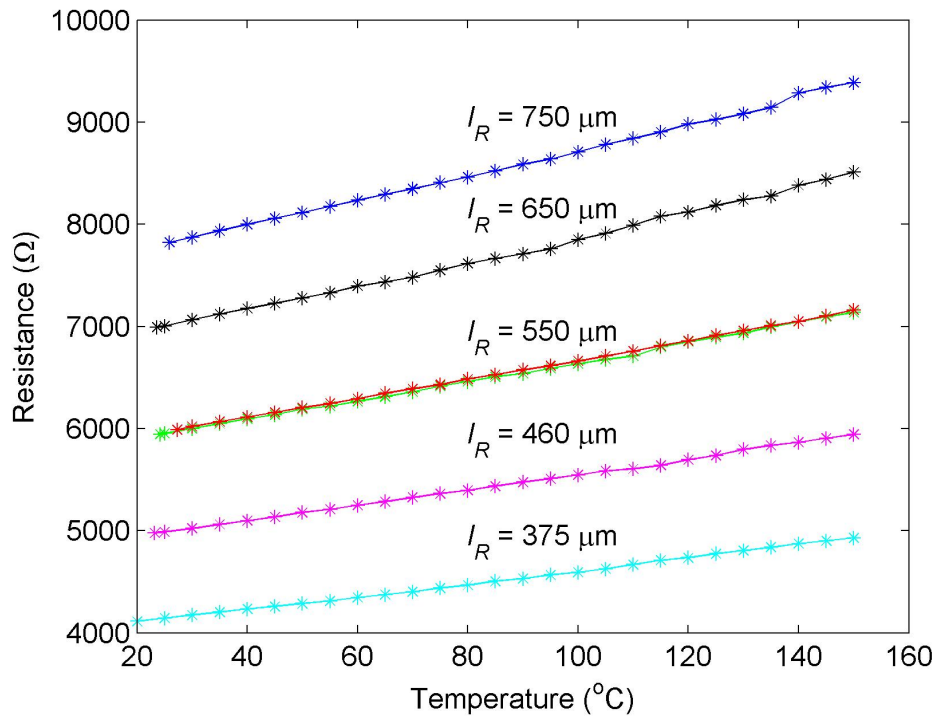


Figure 6.8 Temperature-resistance calibrations of cantilevers with different resistor lengths.

Thermal calibration of the cantilevers on device 1 was also carried out. This device consists of cantilevers of the same resistor length and different cantilever lengths and the calibration curves of these cantilevers were near identical. The average temperature coefficient of resistance of these curves is $6.525 \text{ } \Omega/\text{K}$ with a standard deviation of $0.19 \text{ } \Omega/\text{K}$. In order to evaluate the effect of resistor length, further experiments were carried out on device 2 (different piezoresistor lengths).

The temperature coefficient of resistivity of the piezoresistors associated with the different cantilever designs is shown in Figure 6.9. The temperature coefficient of resistivity predicted based on work by Reggiani et al. [13] for the doping conditions used is $5.495 \times 10^{-8} \text{ } \Omega\text{-m}/\text{K}$. Measured values of temperature coefficient of resistivity were within 13.9 % of the predicted value. Discrepancies in this value may have arisen from small differences in the doping profile (from that predicted by the model; refer Chapter 5), actual geometric parameters of the piezoresistor (from designed values) and errors in the thermal calibration process.

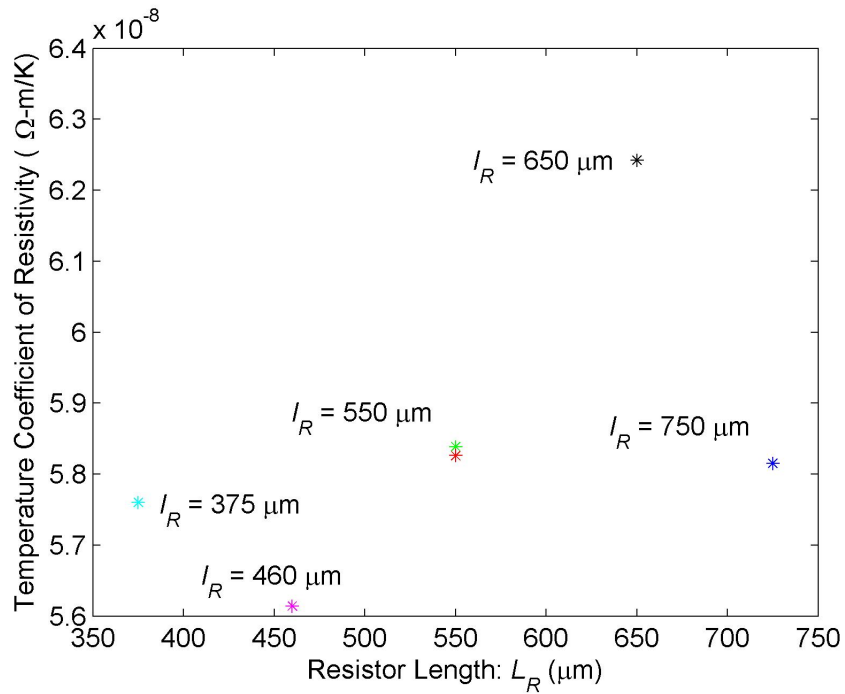


Figure 6.9 Temperature coefficient of resistivity of the cantilevers.

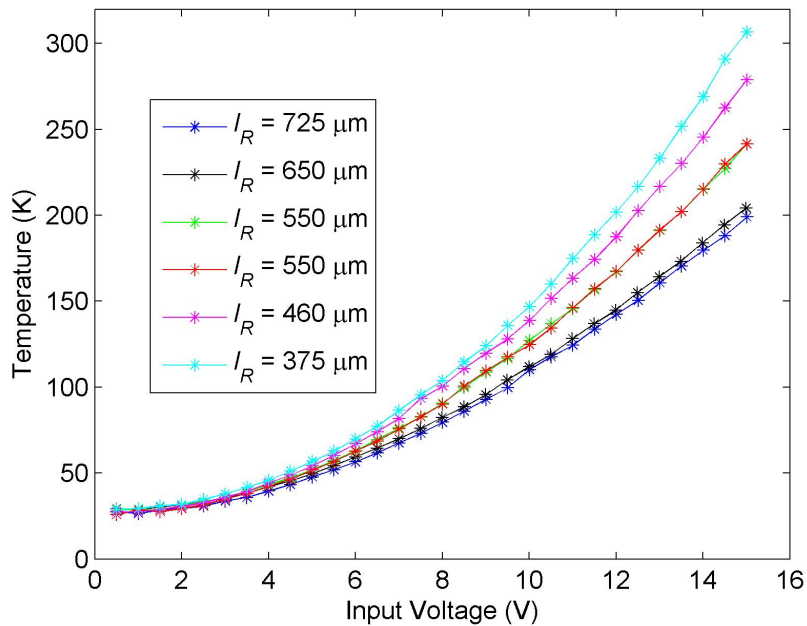


Figure 6.10 Cantilever average temperatures for various voltage inputs. Since thermal calibration was performed up to 150 °C, voltage values that are associated with higher temperatures are not shown.

6.2.9.2 DC Calibration

In order to evaluate the DC response of the cantilevers, the cantilevers on device 2 (Table 6.1) were placed in the calibration circuit and the cantilever response to different DC input voltages was evaluated. In Figure 6.10 the temperature associated with ohmic heated is presented. This was evaluated using the calibration curves in Figure 6.8. The cantilever temperature is proportional to power delivered to the device. Also the identical cantilevers (length: 550 μm) showed near identical response as expected.

6.2.9.3 Evaluation of Effective Heat Transfer Coefficient

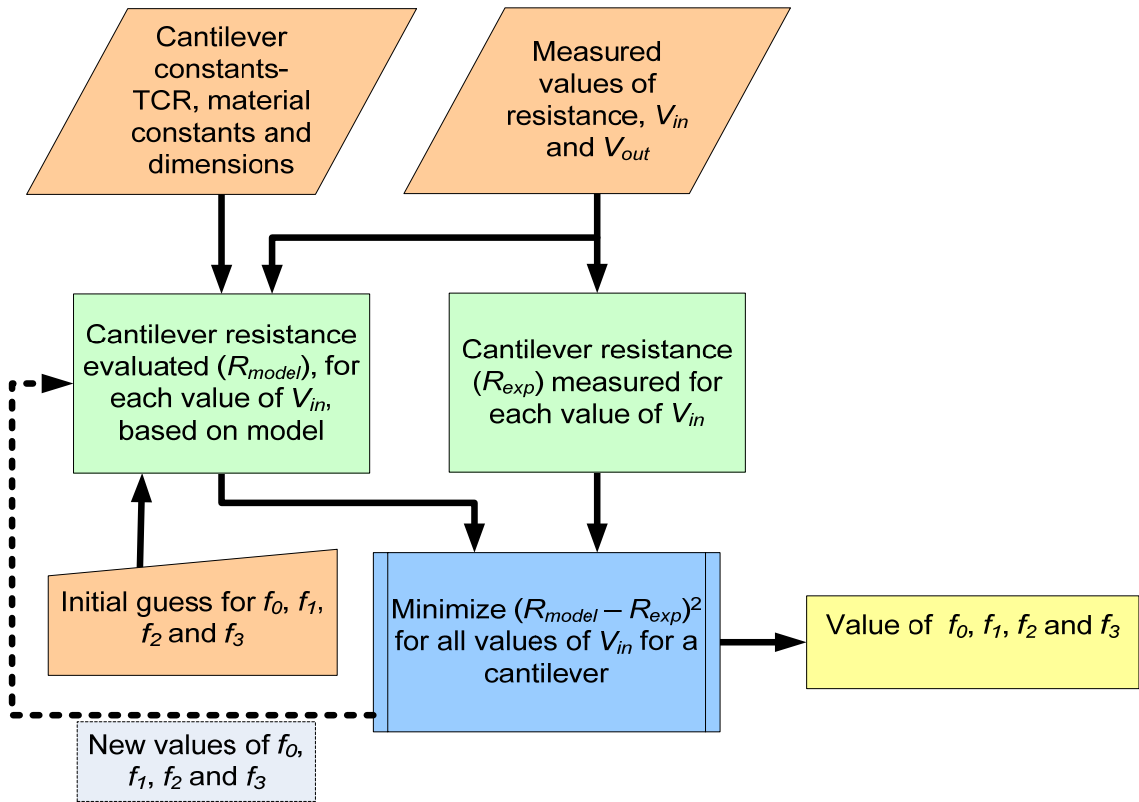


Figure 6.11 Flow-chart for minimization routine used to evaluate thermal dependence of heat transfer coefficient.

The finite difference thermal model (6.12) was coupled with a temperature-dependent heat transfer coefficient of the form $h(\theta) = f_0 + f_1 \theta + f_2 \theta^2 + f_3 \theta^3$. The data presented in Figure 6.10 was used to evaluate the constants f_0, f_1, f_2 and f_3 . A minimization algorithm was implemented in MATLAB™ to evaluate the constants. The

logic flow of the algorithm is shown in Figure 6.11. The criterion for minimization was that the value of resistance evaluated based on $h(\theta)$ and the thermal model was within 0.2 % of the measured value of resistance for a given voltage input.

Figure 6.12 shows nature of the thermal dependence of heat transfer coefficient on cantilever local temperature. The nature of the plot suggests that the heat transfer coefficient is not independent of the piezoresistor length. However the equations of heat transfer do not suggest any definitive relationship between the heat transfer coefficient evaluated and the length of the piezoresistor.

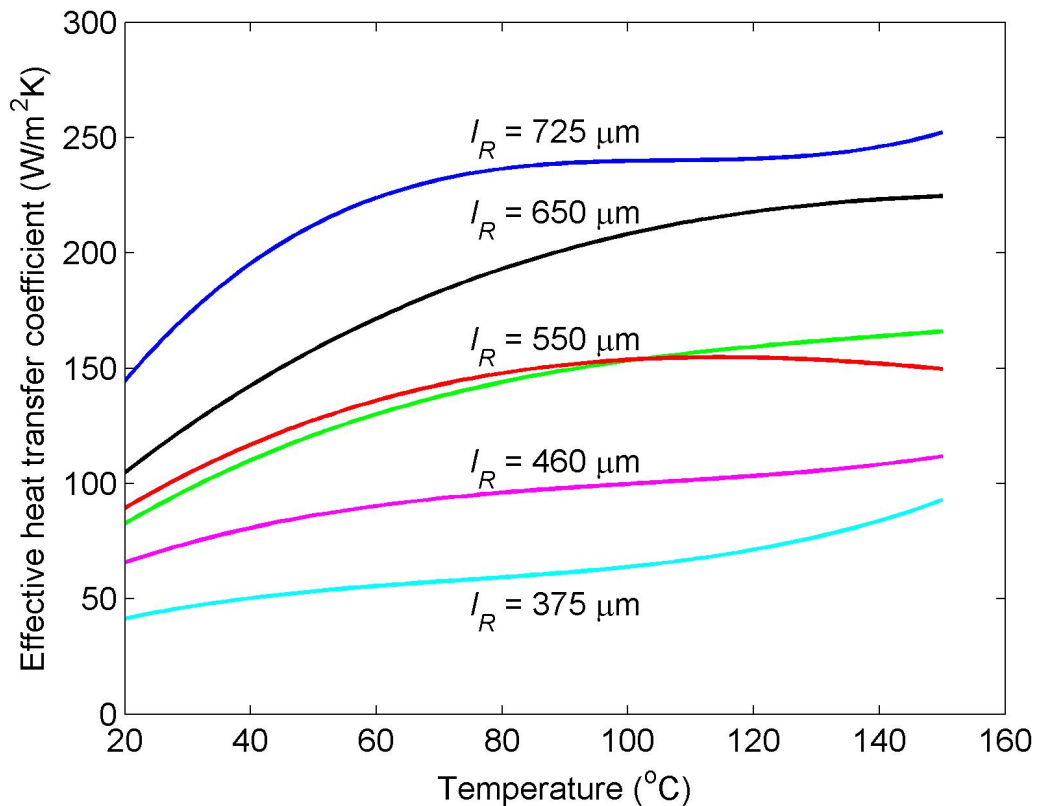


Figure 6.12 Temperature dependence of heat transfer coefficient for different piezoresistor lengths.

It should be noted that the thermal model used in this work does not account for the thermal dependence of material properties over the temperature range investigated in this work (20 °C – 150 °C). The material properties associated with the model are calculated based on volume fractions of various materials; this may account for the dependence of heat transfer coefficient on the geometry of the piezoresistive

microcantilever (Figure 6.12). No physical explanation of the results is offered in this work.

6.2.9.4 Cantilever Response to Sinusoidal Inputs

The cantilever was excited with various input voltages at frequencies ranging from 25 Hz to 100 kHz and the average resistance and resistance amplitude corresponding to this excitation was evaluated. All measurements on response to sinusoidal inputs were performed on the cantilever with $l_R = 650 \mu\text{m}$. Figure 6.13 and Figure 6.14 show the cantilever response to sinusoidal inputs at different RMS voltages.

The sinusoidal response at 5 V-rms and 7 V-rms was simulated with the thermal model for the microcantilever. In each case, the input excitation consisted of an AC and DC component. This was to ensure that current in the measurement is always non-zero. This allows for an evaluation of resistance using the equations outlined at all times.

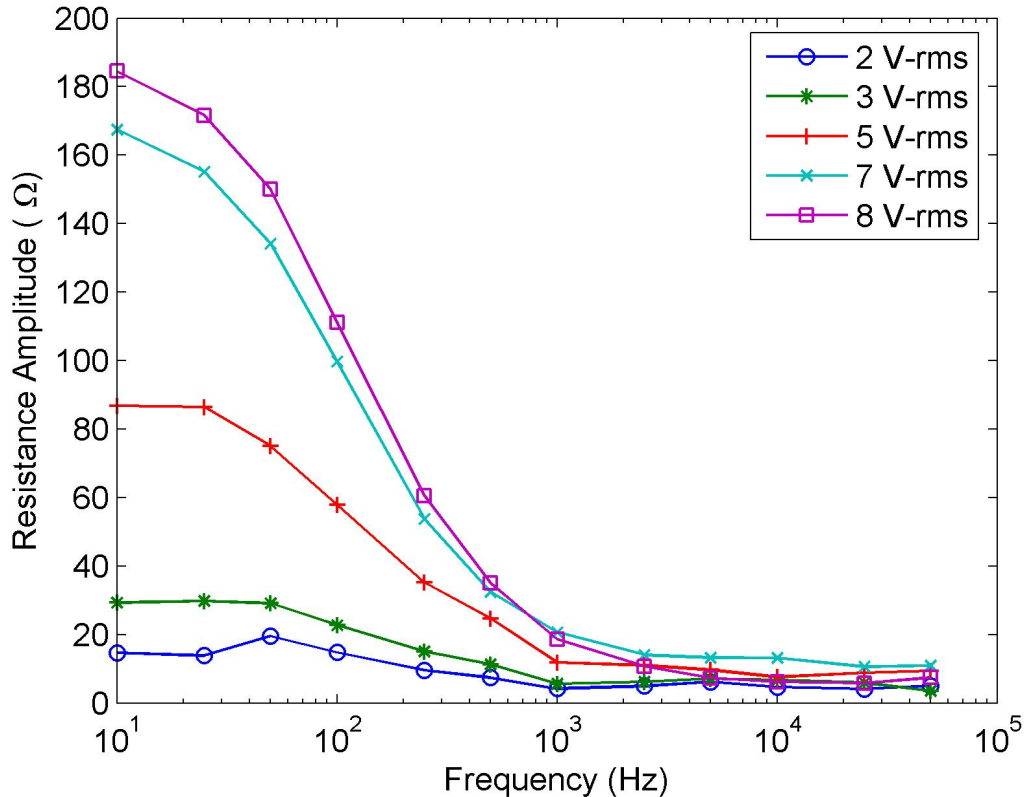


Figure 6.13 Amplitude of resistance response at different excitation frequencies.

Figure 6.15 shows a comparison of the resistance amplitude and resistance mean of the cantilever over the range of frequencies investigated. The simulated response matches up with measured values of resistance average and amplitude extremely well. The error in simulation of resistance amplitude at frequencies lower than 1 kHz is within 15 Ω . Errors in simulation of average resistance were smaller. Measurement of resistance at frequencies higher than 1 kHz falls within the range of quantization error of the oscilloscope use for data acquisition (Tektronix TDS 3012B, Tektronix Inc., Richardson, TX).

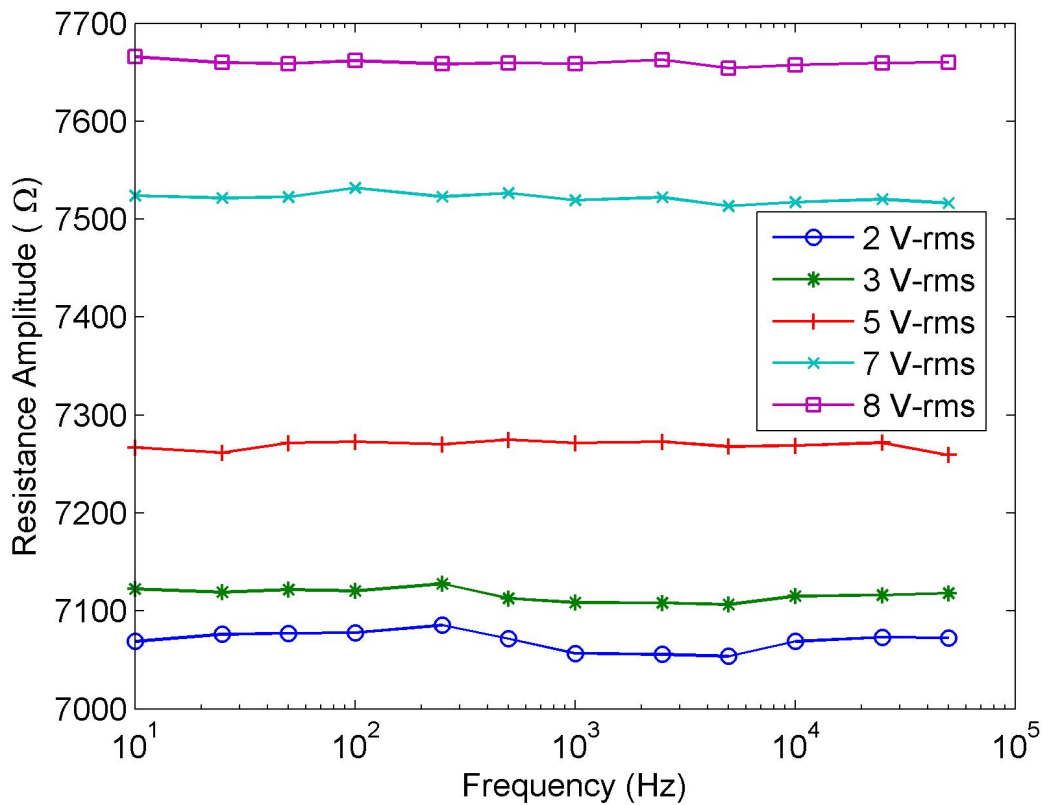


Figure 6.14 Average resistance of the piezoresistor for resistive heating at different frequencies.

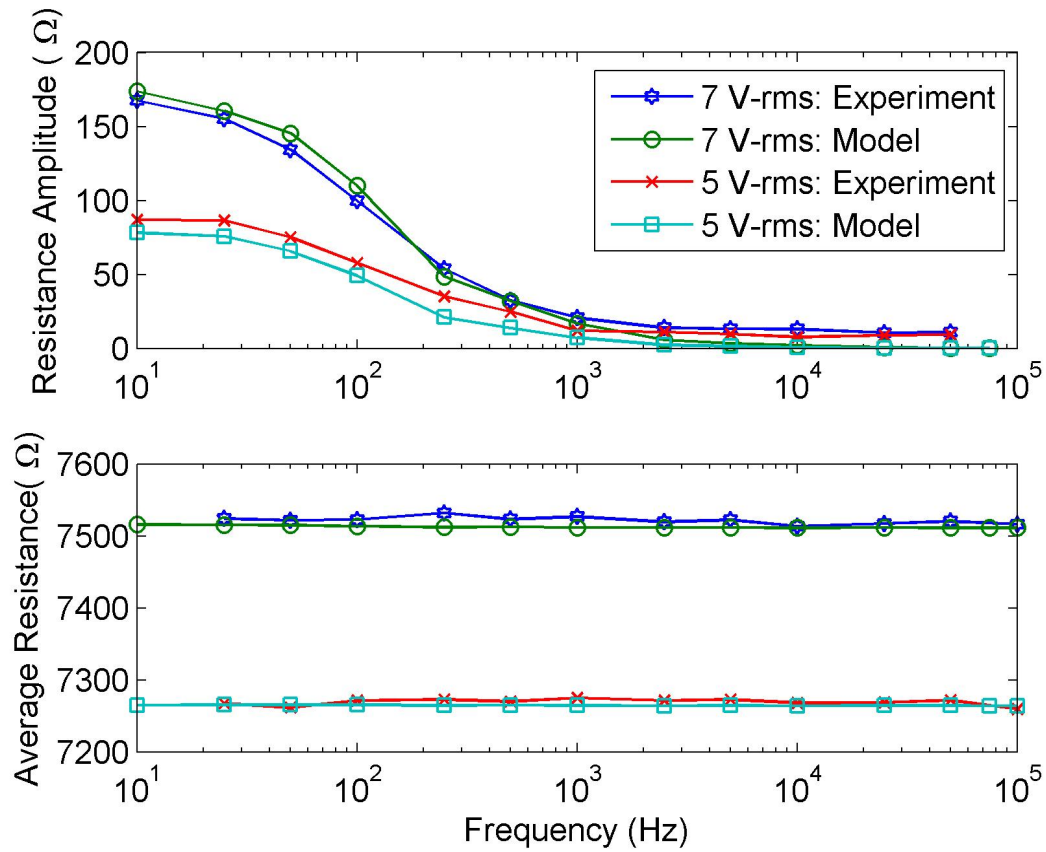


Figure 6.15 Comparison of simulation results with experimentally measured values. Top: Resistance amplitude of the piezoresistor. Bottom: Average resistance of the piezoresistor.

6.2.9.5 Analysis of Sinusoidal Response

The results from the thermal analysis show that the piezoresistor acts like a first order thermal filter. At low frequencies large resistance amplitudes (implying large amplitude of temperature change) are seen which suggest that the piezoresistor follows the input excitation frequency closely. At frequencies higher than 500 Hz (this corresponds, roughly, to the measured time constant for the cantilever), the amplitude of oscillation decreases. This is due to the cantilever is not being able to respond thermally to electrical excitation at higher frequencies.

6.2.10 Measurement in Flow Conditions

During analyte measurement with the P μ CA in the flow setup (§ 7.2), conditions around the cantilever are different from those in which the thermal measurements

presented above were made. To evaluate the effect of flow on the thermal behavior of the cantilever, the P μ CA was mounted on a flow cell and DC calibration measurements were made at various flow rates of N₂ gas. Figure 6.16 shows the thermal behavior of the cantilever under these conditions. These measurements were made with a single cantilever (cantilever 2 on device 1- refer Table 6.1). As expected the thermal response of the cantilever at high flow rates is fairly limited. The heat transfer coefficients evaluated in this work are valid for ambient conditions. The thermal dependence of the heat transfer coefficient under flow conditions may be evaluated using the same techniques.

The experiment was repeated with helium gas at the same flow rates and a different set of thermal response curves was obtained. This suggests the cantilever can be used to identify different carrier gases and flow rate conditions. Also by repeating the analysis carried out at ambient conditions valuable information on heat transfer coefficient of the gases under different flow conditions can be evaluated.

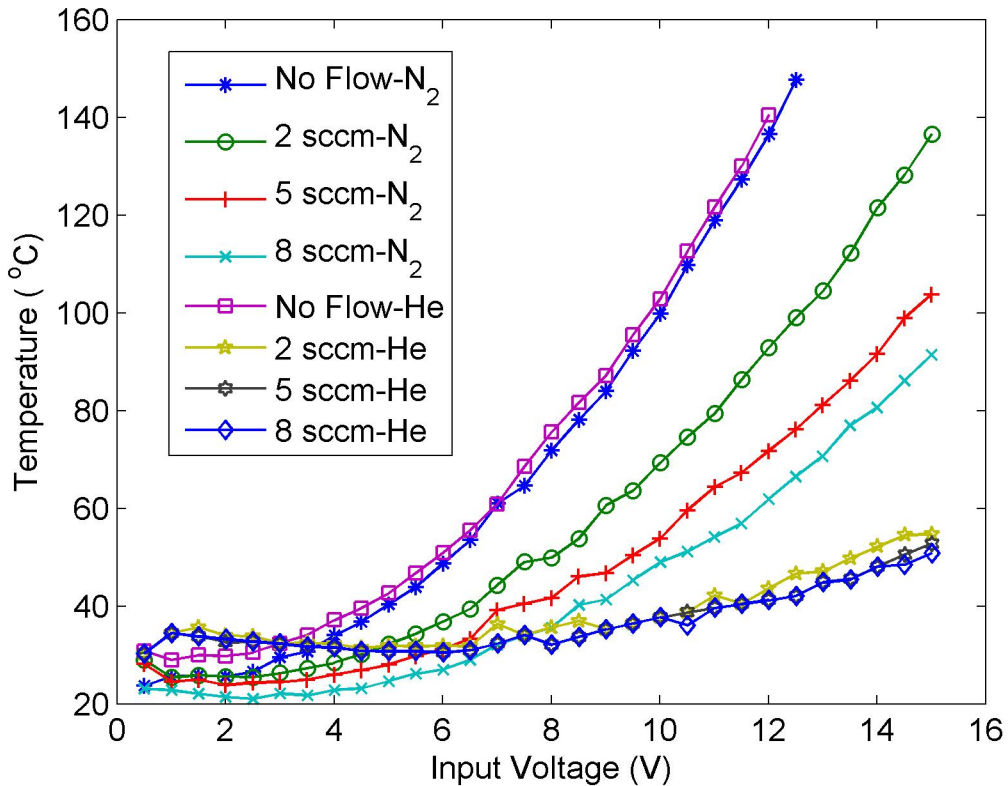


Figure 6.16 Thermal response of the cantilever, in the flow measurement setup, to DC excitation at different flow rates.

6.2.11 Array Operation

6.2.11.1 Demonstration of Array Operation

The P μ CA used in this work has 10 cantilevers. In order to evaluate whether the cantilever array could be used as an array of sensors at different operational temperatures, the cantilevers were heated with three separate power supplies as shown in Figure 7.2 and measurements were made on an Infrascopes II infrared camera (Quantum Focus Instruments Corp., Vista, CA). The measurement showed the expected result which was that different cantilever temperatures and, in this particular experiment, different zones of thermal interrogation can be set up during analyte measurement. Experiments of this nature are discussed in Chapter 8.

6.2.11.2 Thermal Cross-talk in Array

An important issue to evaluate when using the P μ CA as a thermal cantilever array is the effect of heating of a cantilever on other cantilevers in the array. In order to investigate this, measurements were made on a cantilever chip. The cantilever was heated with a DC power supply so that the temperature of the cantilever was maintained at 100 °C under ambient conditions. Resistance of adjacent cantilevers was interrogated with a Keithley 2400 Sourcemeter (Keithley Instruments Inc., Cleveland, OH) with a source current of 10 μ A (Figure 6.17). Heating associated with this value of current is negligible. Resistance change, under these experimental conditions, in the immediately adjacent cantilever was approximately 1 Ω . This corresponds to a temperature rise of approximately 0.1 °C. Also in the experiment, cantilevers at the center and edge of the array were heated and the same effect was noticed. Cantilevers not immediately adjacent to the heated cantilever did not show any change in resistance. Hence these may be assumed to be unaffected by the thermal effects in the heated cantilever.

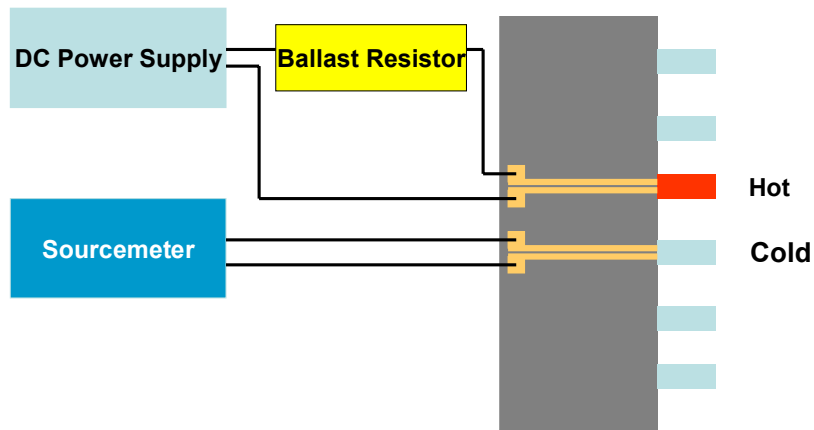


Figure 6.17 Measurement setup for investigation of effect of heating on adjacent cantilevers.

6.3 Measurement Space for Piezoresistance Measurement

The mechanical and thermal calibration studies of the P μ CA serve as indicators of the appropriate range of operation. In Chapter 7, the method of electrical resistance measurement of the piezoresistive microcantilevers is discussed. Measurement of resistance is made, in this work, using small AC voltages. The choice of the excitation voltage and frequency may be made based on device characteristics and limitations of the measurement system.

The mechanical characterization indicated that natural frequencies of the cantilevers are higher than 30 kHz for the longest cantilevers (700 μ m in length). It has been seen that electrical excitation of a mechanical system near its fundamental frequency can result in large oscillation. Hence measurement must be made at frequencies that are either higher or lower than the fundamental frequency of the cantilever.

Thermal characterization studies show that operation of the cantilevers (with AC excitation) at high frequencies results in large attenuation of the amplitude of thermal oscillation. Hence from this perspective a high frequency of AC resistance measurement is desirable. Figure 6.18 and Figure 6.19 show the variation of resistance amplitude and average resistance with frequency of electrical excitation of 0.25 V-pk across the piezoresistive microcantilever. This plot was made using the thermal model described

earlier. The average resistance does not vary much after 1 kHz and the resistance amplitude is smaller than 0.1Ω (roughly equivalent to $0.01 \text{ }^\circ\text{C}$ of thermal variation) for frequencies higher than 1 kHz.

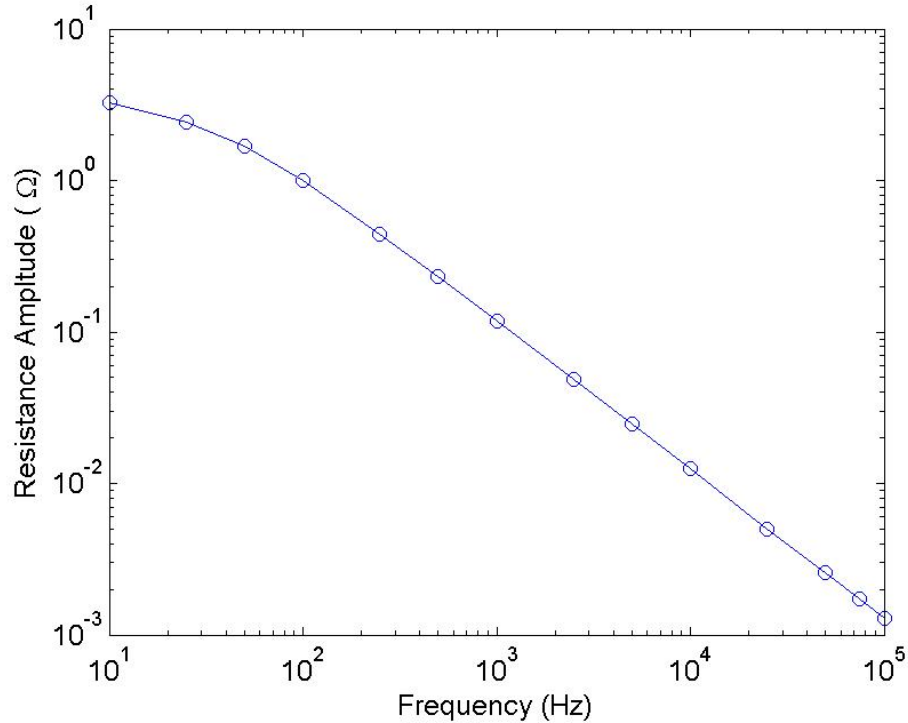


Figure 6.18 Prediction of variation of resistance amplitude with excitation frequency for a voltage amplitude of 0.25 V across the piezoresistor. The prediction was based on the thermal model.

The final consideration in choice of the measurement space is the limitation of our measurement technique and setup. The impedance characteristics of the ballast resistor and measurement techniques required for measurement at high frequencies have been discussed in § 6.2.7.2. The impedance becomes large beyond 25 kHz and measurement of resistance cannot be carried out using a simple resistive model.

With these characteristics and limitations in mind, all measurements in this work have been made with a voltage amplitude of 0.5 V (across the Wheatstone bridge) at 10 kHz.

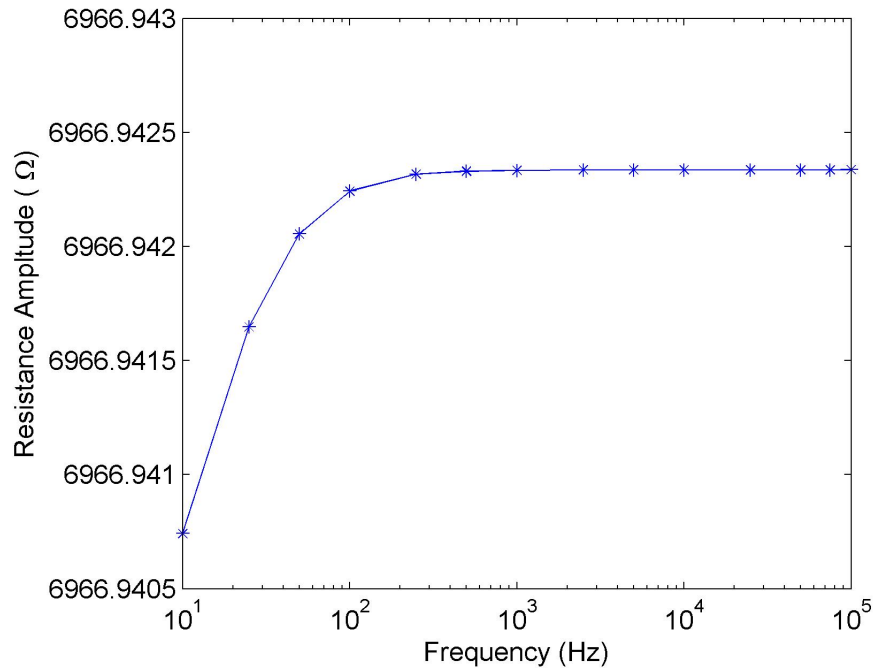


Figure 6.19 Prediction of variation of average resistance with excitation frequency for a voltage amplitude of 0.25 V across the piezoresistor. The prediction was based on the thermal model.

6.4 References

- [1] J. Gere and S. Timoshenko, *Mechanics of materials*, Fourth ed. Boston: PWS Publishing Company, 1997.
- [2] Z. Hu, W. Qu, N. Islam, S. Islam, A. Choudhury, and T. Thundat, "High sensitivity multi-channel piezoresistive cantilever CMOS readout systems," in *208th Meeting of the ECS*, 2005.
- [3] R. Hull, *Properties of single crystal silicon*: Inspec, 1999.
- [4] L. A. Window, "Strain gauge technology," Second ed: Springer, 1992.
- [5] X. Hu, A. Jain, and K. E. Goodson, "Investigation of the natural convection boundary condition in microfabricated structures," in *ASME Summer Heat Transfer Conference*, San Francisco, CA, 2005.

- [6] K. Park, J. Lee, Z. M. Zhang, and W. P. King, "Frequency-dependent electrical and thermal reponse of heated atomic force microscope cantilevers," *Journal of Microelectromechanical Systems*, vol. 16, pp. 213-222, 2006.
- [7] R. P. Maginell, D. A. Rosato, D. A. Benson, and G. C. Frye-Mason, "Finite element modeling of a microhotplate for microfluidic applications," in *International Conference on Modeling and Simulation of Microsystems, Semiconductors, Sensors and Actuators*, San Juan, Puerto Rico, 1999, pp. 663-666.
- [8] Z. Y. Guo and Z. X. Li, "Size effect on microscale single-phase flow and heat transfer," *International Journal of Heat and Mass Transfer*, vol. 46, pp. 149-159, 2003.
- [9] M. J. Madou, *Fundamentals of microfabrication*, 1 ed. Boca Raton: CRC Press, 2000.
- [10] M. Gad-el-Hak, *The MEMS Handbook*: CRC Press, 2002.
- [11] "MEMS Clearinghouse," <http://www.memsnet.org/material/>.
- [12] J. Teng and P. D. Prewett, "Focussed ion beam fabrication of thermally actuated bimorph cantilevers," *Sensors and Actuators A*, vol. 123-124, pp. 608-613, 2005.
- [13] S. Reggiani, M. Valdinoci, L. Colalongo, M. Rudan, G. Bacarani, A. D. Stricker, F. Illien, N. Felber, W. Fichtner, and L. Zullino, "Electron and hole mobility in silicon at large operating temperatures—Part I: bulk mobility," *IEEE Transactions on Electron Devices*, vol. 49, pp. 490-499, 2002.

CHAPTER 7

MEASUREMENT SETUP

In the previous chapter, the thermal and mechanical calibration of the 10-cantilever P μ CA was discussed. This chapter details the methods and apparatus used for chemical detection with the microcantilever array. The twin elements of the measurement scheme, used in this work, are the electrical measurement setup for low-noise measurement of piezoresistance change in the cantilevers, and the flow setup for controlled exposure of the P μ CA to the chosen analyte.

7.1 Electrical Measurement

Piezoresistance change, in piezoresistive microcantilever systems, is typically measured using DC methods. DC electrical measurement, while simple, is associated with several sources of noise- both internal to the electrical device and external. The principal sources of noise in DC measurement are white noise, $1/f$ noise [1], and signal drift. Commonly used techniques of reduction of measurement noise are [2]:

1. Phase-sensitive detection (PSD): Limiting the bandwidth of measurement can significantly improve SNR due to the reduction in noise associated with white noise. Also by choosing an appropriate frequency of measurement, noise from external electrical instrumentation and $1/f$ can be virtually eliminated [3]. PSD detection is achieved by modulating the measurand at a discrete frequency. The modulated signal is then detected synchronously using the reference signal. The modulated signal is multiplied by the reference signal and the DC component of the product is obtained using a low-pass filter. The bandwidth of the filter sets the time constant associated with PSD.

2. Multiple-time averaging (MTA): MTA is performed by averaging multiple traces associated with an electrical phenomenon or cyclic measurement. Typically this can be used to eliminate drift in the measure and leads to a reduction in white noise error. The white noise error σ_n for n_t traces each with a time resolution of T_{res} is given by

$$\sigma_n = k(n_t T_{res})^{-\frac{1}{2}} \quad (7.1)$$

where k is a function of the pulse rate of the signal.

3. Signal filtering: Signal filtering methods to eliminate the effect of chosen region of the frequency spectra can help eliminate the effect of noise sources in the environment or other electromagnetic instrumentation.

The use of these techniques depends on the nature of the measurement being made. If a steady-state measurement is being made, all of these techniques can be used. In measurements that are cyclic in nature such as temperature cycling of the cantilever structure, filtering using a band-pass filter or time averaging on a computer or the oscilloscope can help reduce noise dramatically. When real-time measurements that are not cyclic are being made, filtering and the use of PSD aid in reducing noise. With PSD, real-time analysis of the data can be carried out. However such a measurement is possible only if the time constant of the lock-in amplifier filter (τ_{filter}) is much larger than the time constant of the excitation frequency ($\tau_{filter} \gg \tau_{excitation}$). Also it is required that $\tau_{response} \gg \tau_{filter}$. This is to ensure that there are no aliasing errors with measurement.

7.1.1 PSD Methods for Noise Reduction

Phase-sensitive measurement of resistance was implemented with a resistive circuit. Figure 7.1 show the normalized voltage noise measured using a DC Wheatstone bridge using a 3 k Ω thin film resistor. The differential output of the bridge was measured using a SR745 spectral analyzer (SRS Instruments, Sunnyvale, CA). The supply voltage was 5 V. The spectral view of the voltage output shows high $1/f$ noise as is typical of most electrical measurement. If the noise associated with a PSD-type measurement at 10 kHz with a measurement bandwidth of 172 Hz is compared with noise associated with a low-pass filter with a filter cut-off of 128 Hz, the noise for the low-pass measurement is higher by upto 5 orders of magnitude. This implies a huge loss in SNR using DC or low-pass filter based measurement as compared with PSD measurement.

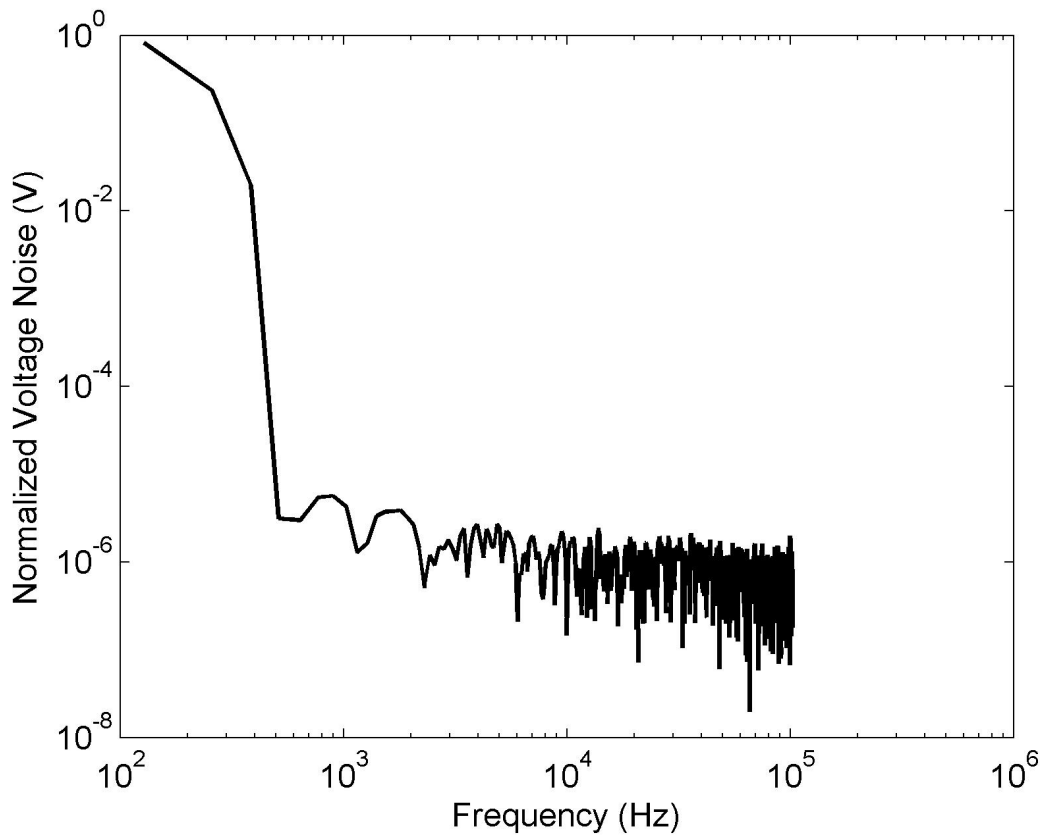


Figure 7.1 Normalized noise spectrum measured from a thin film resistor. $1/f$ noise at low frequencies is very high.

7.1.1.1 Noise Measurement with PSD Methods

Device noise issues due to doping conditions of the piezoresistors have been discussed in § 3.3. Also based on the noise spectrum the SNR is much higher with PSD measurement at high frequencies. In most practical cases of resistance measurement though, the noise due to the instrumentation is much larger than device noise and the difference in the noise levels for DC and PSD measurements are not as large. Signal conditioning with DC measurement

Measurements were made with a 10-channel, constant current CMOS readout chip designed at Oak Ridge National Laboratories for measurement of the 10-cantilever P μ CA [4]. Measurements made with a thin film resistors and the P μ CA, with a time constant of 100 ms, showed a floor noise level of greater than 20 μ V.

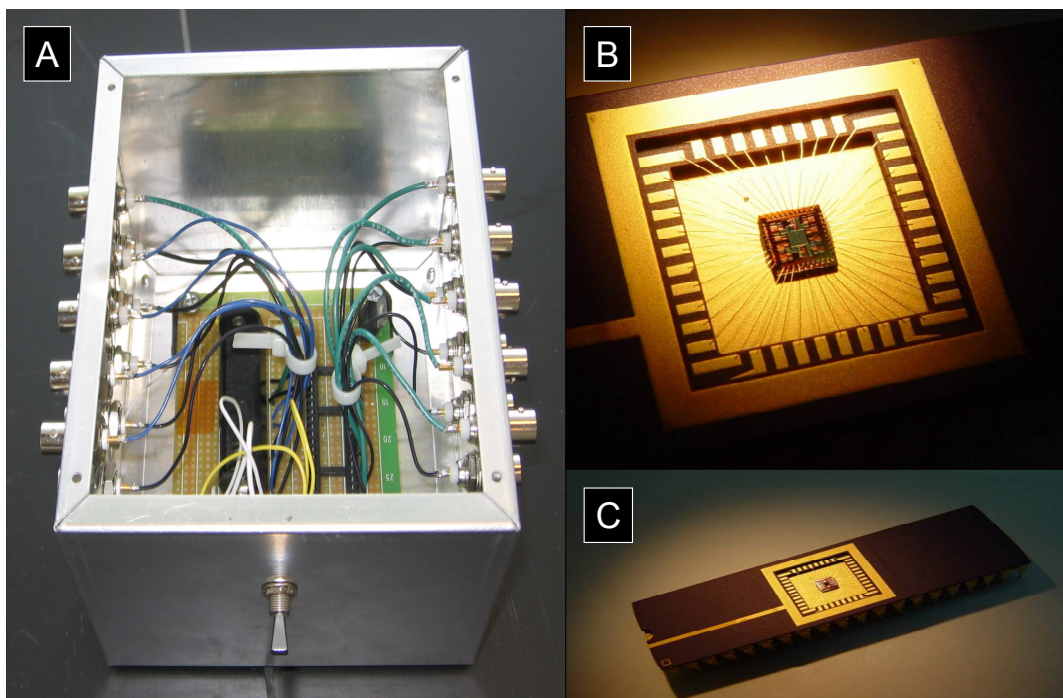


Figure 7.2 A. Measurement box used for measurement with 10-channel CMOS chip, B. Close-up of CMOS chip wirebonded on a DIP package [4], C. DIP package that is used with the measurement box [4].

Measurements made with a single piezoresistor on a simpler version of the system shown in Figure 7.3 with a single measurement channel, made at 10 kHz with a time constant of 300 ms, allowed for measurement with a floor noise of approximately $1 \mu\text{V}$. If a longer time constant is used, the noise level can be improved further. However, as explained earlier, the choice of the time constant depends on the time scale of the sensor response to the chemical analyte.

7.1.2 Electrical Measurement Setup

A schematic of the electrical measurement setup for resistance measurement is shown in Figure 7.3. Currently this system is limited to simultaneous measurement of six cantilevers. Each microcantilever of the $\text{P}\mu\text{CA}$ is placed on a single Wheatstone bridge (Figure 7.3 B). The differential voltage across the Wheatstone bridge is measured by the lock-in amplifier. Since the lock-in amplifier (SR830, Stanford Research Instruments, Sunnyvale, CA) can only measure a single Wheatstone bridge at one time, the multiplexer unit (SIM 925, Stanford Research Instruments, Sunnyvale, CA) is used to

scan through the six channels making it possible to interrogate the piezoresistance of the six cantilevers.

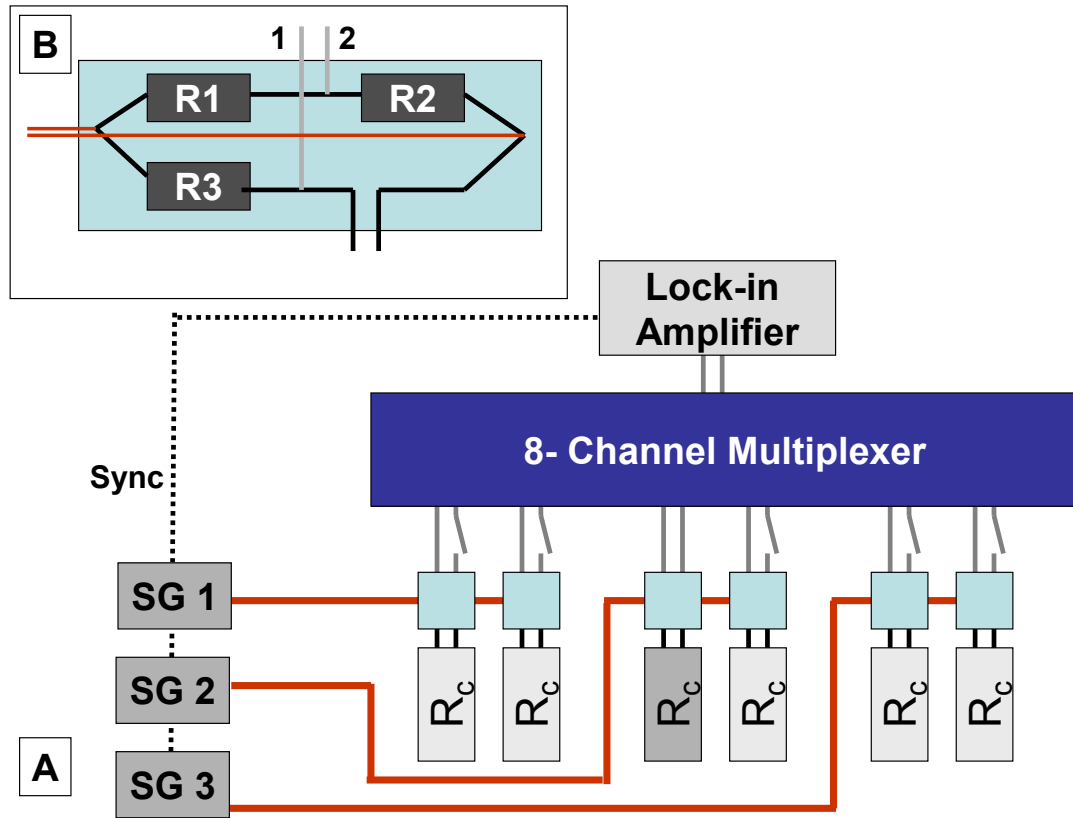


Figure 7.3 System for measurement of resistance from the cantilevers using PSD. A. The three independent power supplies (SG1-3) allow for heating of the cantilevers to different temperatures (each signal generator can have a different DC bias), B. Each cantilever is placed on a 3/4th Wheatstone bridge, represented here by the blue rectangle.

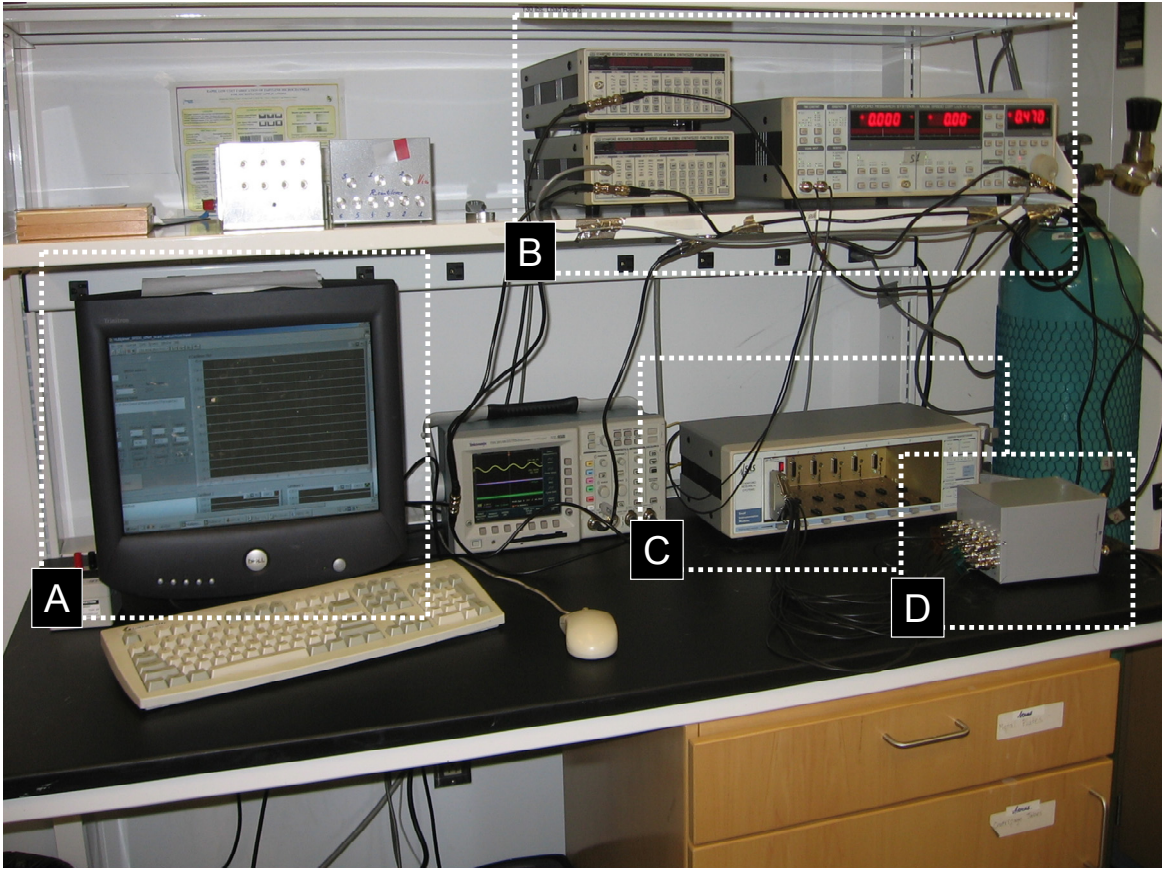


Figure 7.4 Instruments used for resistance measurement: A. Computer with LabVIEW for data acquisition, B. Signals generators and lock-in amplifier, C. SIM 925 multiplexer which is connected to D. Measurement box with Wheatstone bridge circuits.

A $3/4^{\text{th}}$ Wheatstone bridge has been implemented for each cantilever on the measurement box (Figure 7.5). This enables high sensitivity measurement of each cantilever. Resistors for the $3/4^{\text{th}}$ bridge implemented in the measurement box are chosen so that they are very close to the cantilever being measured on a particular channel. A zero-insertion-force (ZIF) connector has been used to facilitate easy change of the resistors when testing the different cantilever designs, all of which have different nominal resistance values. On one end the box connects to the piezoresistors and on the other to the multiplexer module (a schematic of the circuit layout included in Appendix D).

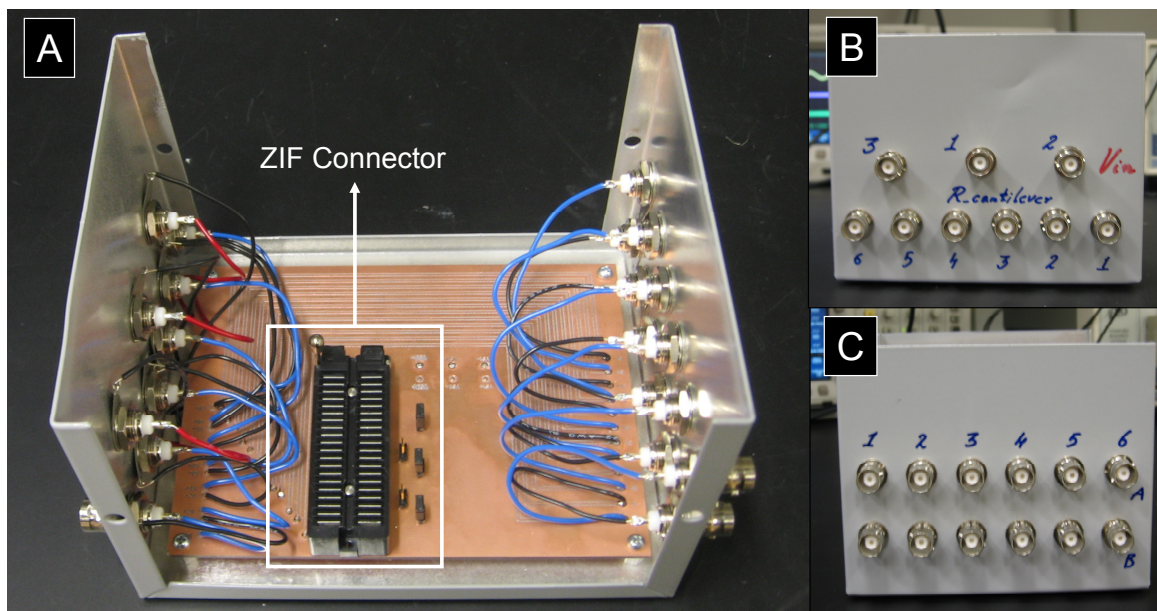


Figure 7.5 Measurement box used for implementation of Wheatstone bridge circuits and to heat cantilevers to different temperatures. A. ZIF connector and internals of the measurement box, B. BNC connectors for connection to piezoresistors and power supply to the Wheatstone bridge circuits. Three independent power supplies with different DC bias may be used. C. BNC connectors for connection to SIM 925 multiplexer. Each channel has an A and B line for differential measurement at the lock-in amplifier.

High measurement resolution is possible on all channels with the current setup. If a single cantilever being measured, the lock-in can be used to measure cantilever resistance with low-noise and high resolution. This is achieved by use of the ‘offset’ and ‘expand’ functions of the lock-in. This technique allows for high resolution measurement around the average value of resistance. When using the multiplexer with six cantilevers however, a single set of the offset and expand settings lead to poor measurement resolution. To overcome this shortcoming, a LabVIEW program was created that allows for setting of the offset and expand of each channel separately when the multiplexer scans over the six cantilevers (Figure 7.6). However, the use of a single lock-in for measurement of multiple cantilevers using a multiplexer does limit sampling frequency of the measurement. The highest sampling frequency that the lock-in amplifier allows is 512 Hz. When using the multiplexed system, however, the lock-in takes 2 seconds to lock-in after the channel switch. The exact settling time depends on the filter and time constant settings chosen. For the measurement setting chosen (Chapter 6), the sampling frequency was 0.5 Hz and the entire set of six cantilevers are scanned over 12 seconds.

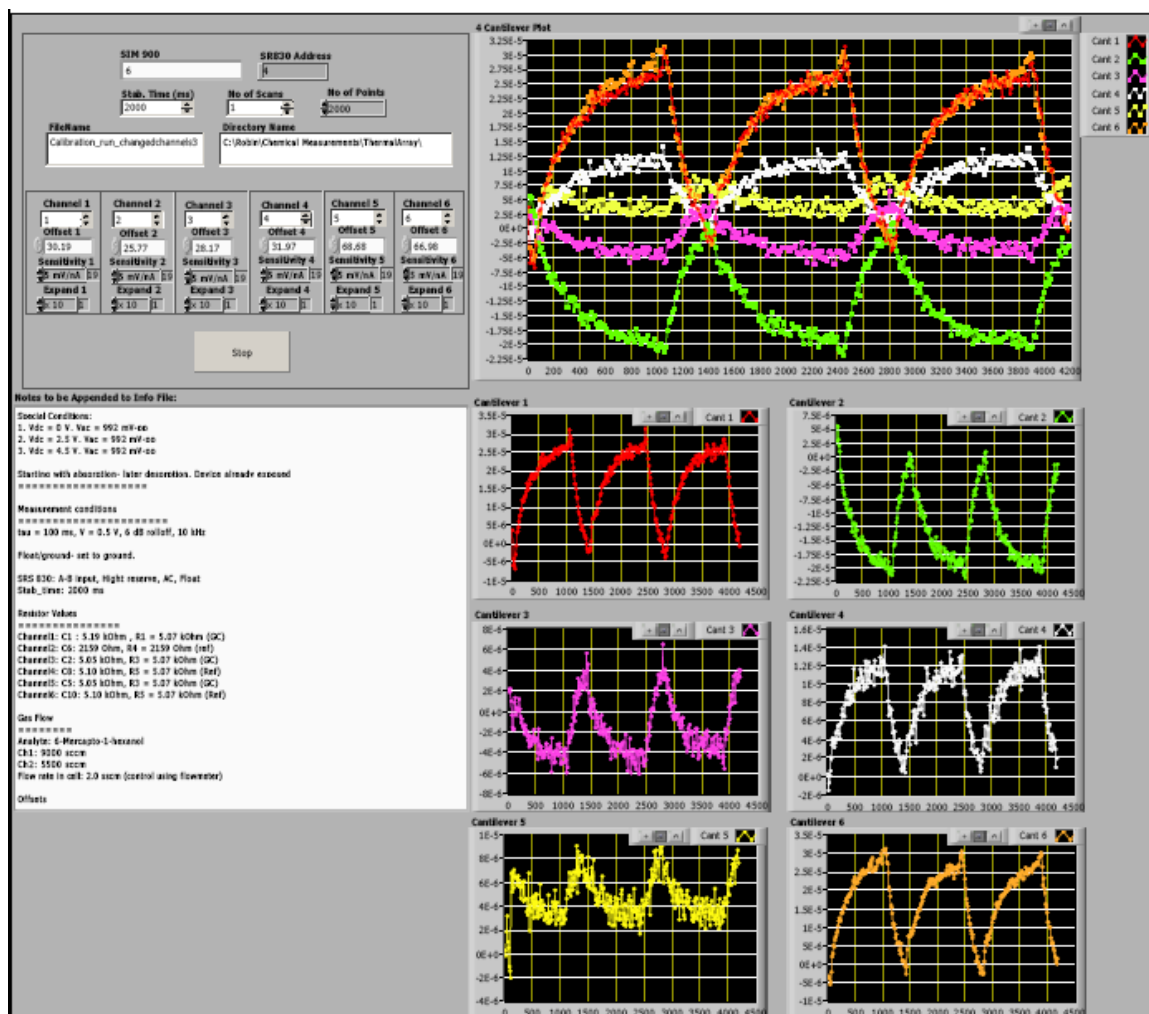


Figure 7.6 Screenshot of LabVIEW program used for data acquisition and control of the multiplexer.

7.1.3 External Noise Sources

All experiments for chemical analyte detection were carried out in Room 319 of the Erskine J. Love Building at Georgia Tech. During calibration measurement runs to evaluate the efficacy of the measurement setup, harmonics of a 1.25 mHz ($\tau = 800$ seconds) frequency, a noise pickup were repeatedly seen in the measurements. The nature of the noise curve resembles a capacitive charging-discharging phenomenon (Figure 7.7). The amplitude of this signal was 1-2 orders of magnitude higher than the noise in the measurement setup described above. This clearly limits the detection limit of the setup. In several cases the amplitude of the noise signal seemed to increase with the differential voltage input associated with lock-in measurement.

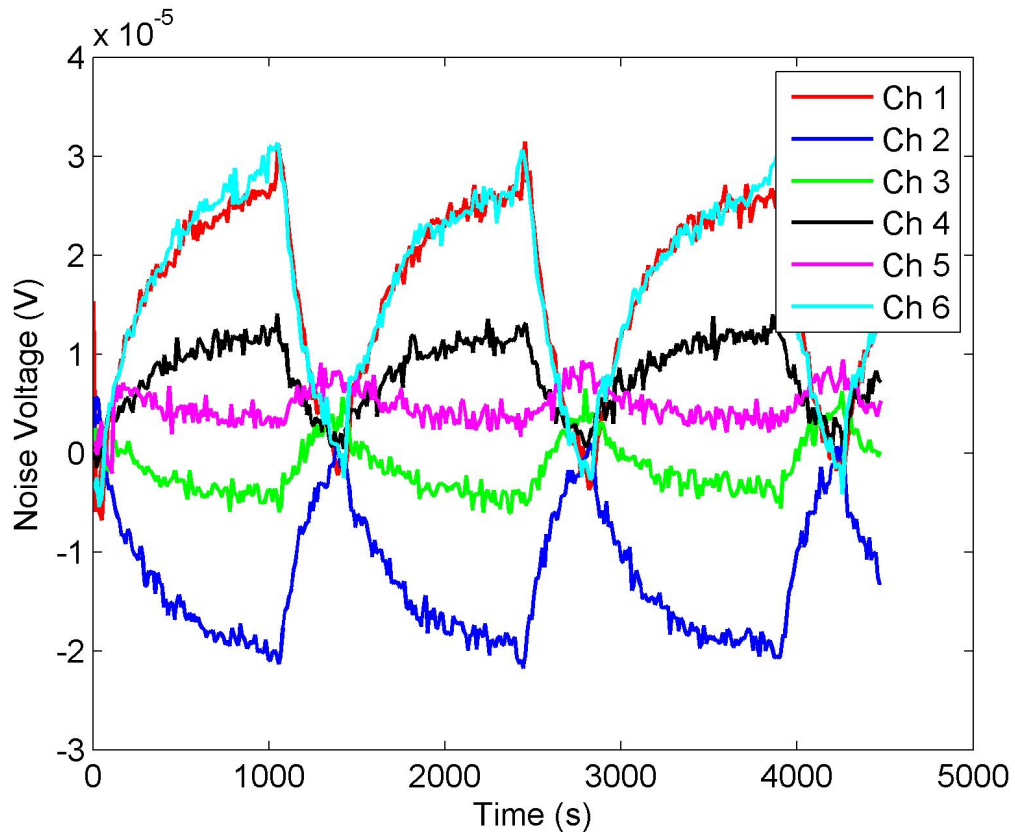


Figure 7.7 Noise measured on the various channels of the data acquisition setup with thin films resistors. The time period of this noise signal is approximately 1600 seconds.

Such a noise signal has also been reported during measurements on a porous silicon gas sensor [5]. Extensive measurements were made with the lock-in amplifier setup on a mobile setup that was taken to various part of the building and similar signals were seen at all locations though the frequency of the noise signal varied by as much as 50%. Noise measurements were made using each module of the low-noise setup. The noise signal measured is likely to be due a large electromagnetic pulse in the building. A seasonal dependence has also been noticed. This noise source seems to be more prevalent in the winter months of the year, probably due to heating systems being operated in the building.

A Faraday cage was built around the sensor and numerous changes in cables and connectors were made to reduce noise pickup in the measurement. These improvements did not change the pickup in the instrumentation. Finally a differential measurement was made of two signal generator outputs, that were synchronized and in phase, using the

lock-in amplifier. This eliminates the effect of the instrumentation of associated with the resistance measurement. Once again a 1.25 mHz signal was seen. The voltage of the differential input was approximately 200 mV-rms. The amplitude of the noise signal associated with this measurement was approximately 225 μV -ppk. Measurements were also made with a single input on the lock-in amplifier and the same pick-up and frequency were observed.

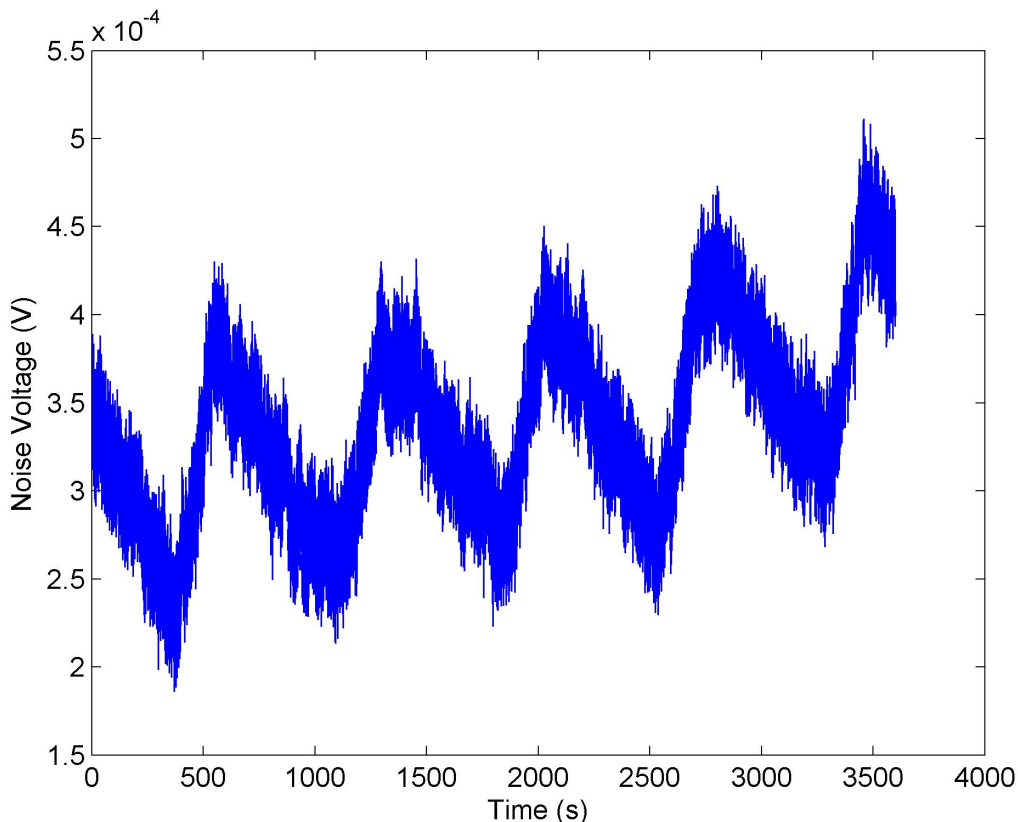


Figure 7.8 1.25 mHz noise signal measured using two signal generator sources with the lock-in amplifier.

7.2 Chemical Flow Setup

Effective measurement of piezoresistive response to various chemical analytes required a system that allowed for good control of analyte concentration and flow rates. The schematic of the chemical measurement setup used for exposure of the cantilevers to the chosen analyte is shown in Figure 7.9. The analyte was placed in an effusion vial (VICI Metronics, Santa Clara, CA). This in turn was placed inside a mixing chamber (Sigma-Aldrich, St. Louis, MO). Mass flow controllers (MFCs) from MKS Instruments

Inc. (Wilmington, MA) were used to control the flow of high purity N₂ (Airgas South Inc., Atlanta, GA) in the two lines shown in Figure 7.9.

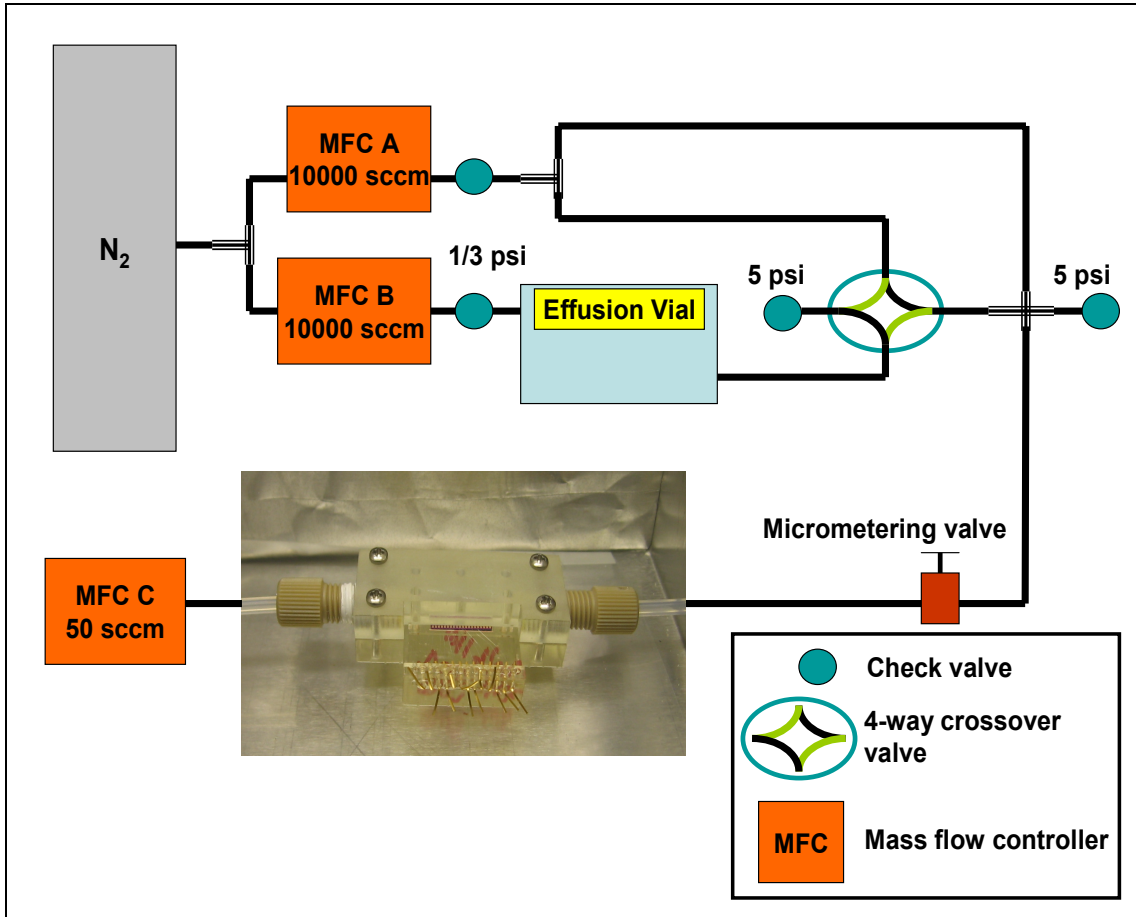


Figure 7.9 The chemical testing setup for exposure of the cantilevers in the SLA package to controlled concentrations of the analyte.

The rate of analyte effusion from the effusion vial is given by

$$r = 1.90 \times 10^4 T D_0 M \frac{A}{L} \log \left(\frac{P}{P - \rho} \right) \quad (7.2)$$

where, r = rate of diffusion (ng/min)

T = temperature of vapor (°K)

D_0 = diffusion coefficient (cm²/sec) at 25 °C, 1 atm

M = molecular weight (g/mole)

A = cross-sectional area of the capillary (cm²)

L = length of diffusion path (mm Hg)

P = atmospheric pressure (mm Hg)

ρ = vapor pressure of chemical at temperature T (mm Hg)

The molar concentration of the analyte, C in ppm, is given by

$$C = \frac{\frac{r \times 10^{-9}}{R_A + R_B} \times 10^6}{22400} \quad (7.3)$$

where R_A is the flow rate of N_2 from MFC A (sccm) and R_B is the flow rate of N_2 from MFC B (sccm). The vapor pressure of the analyte may be calculated using the equation:

$$\log p = A - \frac{B}{t + C} \quad (7.4)$$

where A , B and C are constants that have been obtained from literature [6, 7], for analytes used in this work.

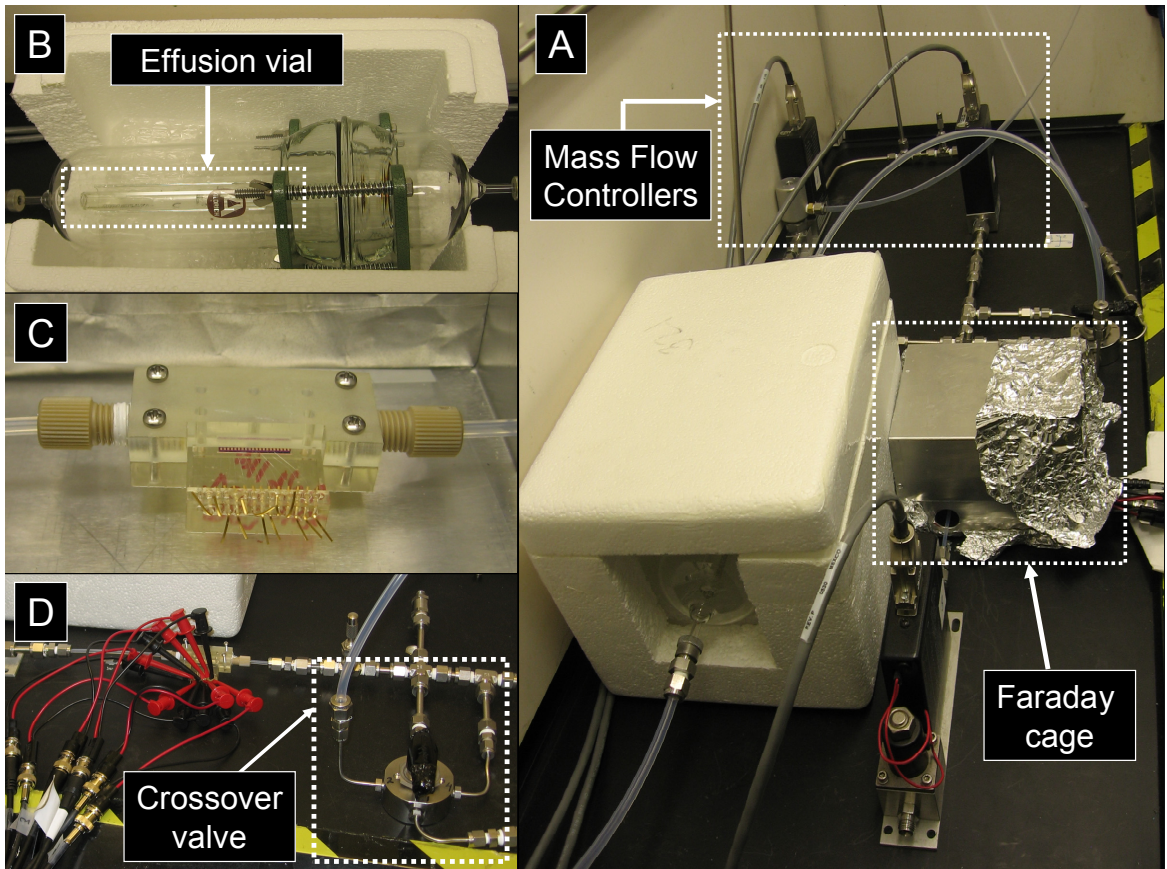


Figure 7.10 A. The complete flow setup used for control of analyte concentration, B. Mixing chamber with the effusion vial, C. Flow cell inside the Faraday cage and D. Flow cell with clips for connection to measurement box, and 4-way crossover valve.

The flow-rate of the mass flow controllers is set using a 247D power supply unit (MKS Instruments, Wilmington, MA). A 4-way crossover valve (Swagelok Inc. Suppliers: Georgia Valve and Fitting Co., Alpharetta, GA) enabled controlled exposure of the cantilevers to the analyte. In a typical measurement run, the cantilevers were first measured in a pure nitrogen flow (referred to as purge flow) for approximately 10 minutes. This enabled evaluation of the baseline for the measurements. After this, the cross-over valve was switched to expose the cantilevers in the chemical flow cell to the analyte. A 5 psi check valve placed at the intersection of the different gas lines (Figure 7.9) ensured that the pressure drop associated with the switch in the flow was minimal. Figure 7.10 shows individual components of the flow setup used for chemical measurement.

7.2.1 Chemical Flow Cell

The chemical flow cell was designed to accommodate the 10-cantilever P μ CA. The flow cell was designed in ProEngineer™ and fabricated in the Rapid Prototyping and Manufacturing Institute (RPMI) at Georgia Tech. The cell was coated with approximately 20 μ m of parylene on a PDS 2010 Labcoter (Specialty Coating Systems, Indianapolis, IN).

Issues related to the entry length and flow channel diameter have been discussed in Chapter 4. Figure 7.11 shows the flow cell design that was used towards to end of this work. The ends were threaded to allow easy interfacing with the flow setup using a PEEK™ fluidic union (Upchurch Scientific, Oak Harbor, WA) to ensure low risk of contamination due to the material of the union.

Gold leads were glued in using a photocurable epoxy- Dymax 9-3095-GEL (Dymax Corp., Torrington, CT)- on a Dymax Light-Welder PC-3D system (Figure 7.11). The contact pads of the piezoresistive microcantilevers were wirebonded to the leads for ease of measurement of the cantilever resistance.

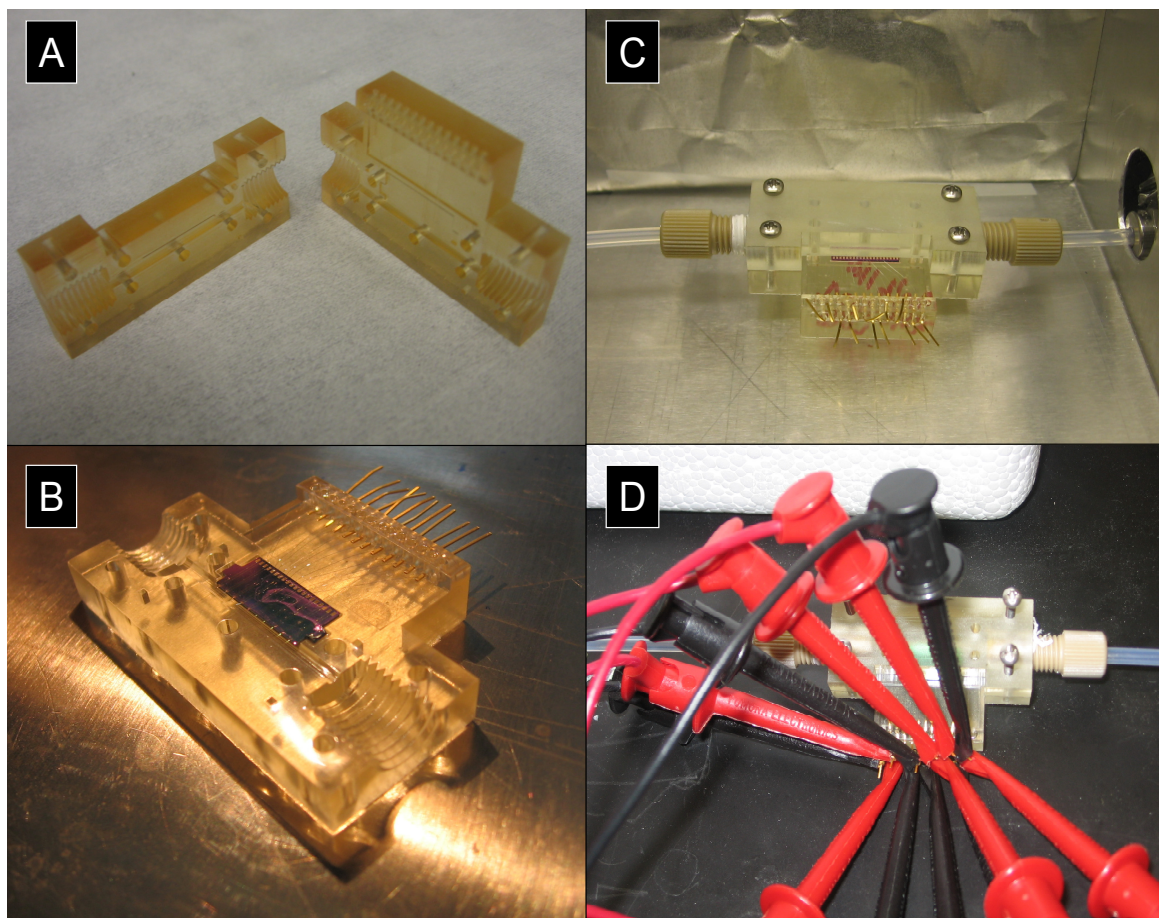


Figure 7.11 A. SLA flow cell top and base, B. PuCA wirebonded on the flowcell base, C. Flow cell placed connected to flow system and placed inside Faraday cage, D. Connection of flowcell leads to measurement box.

7.3 Experimental Protocol

Measurement of various analytes with the instrumentation setup described earlier involves the following steps:

4. Electrical setup: All electrical components are connected as described in Figure 7.3. Resistors are chosen for each channel of the measurement box such that they form a well-balanced Wheatstone bridge with the cantilever piezoresistors.
5. Flow system setup: Flow mixing chamber is cleaned using soap solution and any fluid in the effusion vial (from a previous experimental run) is removed. This is done to ensure there is no water in the mercaptohexanol solution. Every few runs, the Teflon tubing (Figure 7.10) that connects to the flow cell is changed to ensure limited contamination from any mercaptohexanol adsorbed on the tube surface. Also, the

effusion vial is refilled with 5 ml of mercaptohexanol. The flow rate on the 247D power supply unit is set based on the desired analyte concentration.

1. Device setup: The P μ CA was glued on the flowcell base using double-sided sticky tape. This was found to be the most convenient approach especially when the device was to be taken out of the flow cell after the chemical exposure for further experiments on thermal calibration, analysis of surface properties, etc. The P μ CA was then wirebonded to the gold leads on the flow cell (Figure 7.11). Finally the flow cell is placed inside the Faraday cage, which is grounded to the instrument ground, and the gold leads to the piezoresistors are connected to the measurement box.

2. Device preparation: The method of functionalization of the cantilevers has been described in Chapter 5. In several cases it was noticed that resistance of cantilevers measured after deposition of the functional gold layer dropped to the 30-80 Ω region. If the cantilevers are then excited with a 3-5 V-ppk voltage at 10-25 kHz, the resistance goes back to the nominal designed value of piezoresistance. Also before the start of the experiment, the cantilever was heated to around 80-100 $^{\circ}$ C, based on calibration techniques described in Chapter 6, to remove any adsorbed water on the cantilever surface. This can be done before the cell is introduced into the flow setup or it can be done while purging the cell with N₂. Heating of the cantilevers in the purge N₂ was typically done for 10 minutes before the experiment was started.

7.4 Conclusions

This chapter presented the measurement and flow setup used in this work. The method of resistance measurement allows for low-noise measurement of resistance-approximately 20-30 times lower than with specialized CMOS instrumentation for similar applications. The lock-in amplifier is, however, susceptible to electromagnetic noise in the environment as has been shown in § 7.1.3 and the noise pick-up can limit the effectiveness of the low-noise measurement. The flow setup used for the present allows for a fairly wide range of flow velocities and concentrations- ranging from 30 ppb to around 400 ppb of mercaptohexanol.

Improvements to the current flow setup and measurement system will be discussed in Chapter 9.

7.5 References

- [1] J. A. Harley and T. W. Kenny, "1/f noise considerations for the design and process optimization of piezoresistive cantilevers," *Journal of Microelectromechanical Systems*, vol. 9, pp. 226-235, June 2000.
- [2] T. H. Wilmhurst, *Signal Recovery from Noise in Electronic Instrumentation*: Adam Hilger Ltd, 1985.
- [3] D. P. Blair and P. H. Sydenham, "Phase sensitive detection as a means to recover signals buried in noise," *Journal of Physics E: Scientific Instruments*, vol. 8, pp. 621-627, 1975.
- [4] Z. Hu, W. Qu, N. Islam, S. Islam, A. Choudhury, and T. Thundat, "High sensitivity multi-channel piezoresistive cantilever CMOS readout systems," in *208th Meeting of the ECS*, 2005.
- [5] J. R. DeBoer, "Evaluation methods for porous silicon gas sensors." Master of Science Atlanta: Georgia Institute of Technology, 2004.
- [6] A. G. Osborn and D. R. Douslin, "Vapor pressure relations of 36 sulphur compounds present in petroleum," *Thermodynamic Testing and Correlations*, vol. 11, pp. 502-509, 1966.
- [7] C. L. Yaws, K. Narasimhan Prasad, and C. Gabbula, *Yaws' handbook of Antoine coefficients for vapor pressure*: Knovel, 2005.

CHAPTER 8

CHEMICAL SENSING EXPERIMENTS

The last chapter discussed the specifics of the measurement system and setup used in this work. This chapter deals with testing of the P μ CA to confirm several design approaches presented in the chapters on design and to evaluate the feasibility to different testing schemes. Limitations of the current devices and the measurement scheme implemented are also discussed. All graphs in this chapter show the actual change in voltage and the piezoresistive response calculated. The piezoresistive response plotted shows is averaged (moving average) over ten points.

8.1 Background

8.1.1 Surface Stress on Gold

A large volume of literature exists on adsorption of thiolated compounds on gold. Gold is an excellent choice for surface functionalization since it is believed to be extremely inert and can therefore remain unaffected by most chemicals under ambient conditions. Some studies do, however, suggest there is evidence of degradation in the sensor response with increasing time between deposition of the gold layer and measurement with the sensor [1].

Liquid and vapor phase adsorption of alkanethiols, mercaptanols and similar thiolated compounds (HS-(CH₂)_{n-1}-X) have been used to create self-assembled monolayers (SAMs) on gold [1-10]. The sulfur end of the alkanethiols binds to the gold while the functional group X populates the outer surface of the adsorbed layer. The self-assembly process on alkanethiols has an enthalpy of adsorption $\Delta E \approx -150 \text{ kJ mol}^{-1}$ [11]. Surface stress associated with this binding process is generally compressive. Berger et al. have shown that the magnitude of this surface stress depends on the length of the carbon chain for alkanethiols of the form HS-(CH₂)_{n-1}-CH, where n is the number of carbon atoms in the chain. The nature (polarity) and size of the functional group X has also been

seen to have an effect on the surface stress generated on the functionalized surface [8, 11]. Other factors that affect the magnitude of surface stress associated with adsorption of thiolated compounds are method of deposition of gold (this includes variation in grain size and uniformity of the gold film) and condition of the gold layer (presence of pre-absorbed water vapor or other analytes) [4]. Recent work suggests that surface morphology of the gold does not play a significant role in the magnitude of surface stress measured but it does, however, affect the reaction kinetics of adsorption and desorption [7].

8.1.2 Reaction Kinetics of Alkanethiols on Gold

The analyte used for measurement in this work is 6-mercapto-1-hexanol. The adsorption and desorption reaction kinetics of mercaptanols are very similar to those observed in alkanethiols since the reaction is driven by binding of the sulfur to the gold of the functionalized surface [3, 4].

Detection of alkanethiols on gold has been performed in vapor phase and liquid phase (typically in solution with water or organic solvents such as ethanol). Reports suggest that the formation of monolayers or multi-layers depends on the solvation energies associated with the binding, i.e, they depend on the medium in which detection is carried out [2, 4]. In several cases multi-layers are formed and after reconstruction over several hours, a single monolayer is seen on the gold surface [3]. Shadnam et al. [6] studies the desorption kinetics of alkanethiols monolayers from gold at temperatures ranging from 383 K to 653 K and found evidence of two consecutive first order kinetic mechanisms with activation energies of 29.9 and 32.7 kcal mol⁻¹. They also showed that the desorption reaction was faster and more complete in liquids.

8.2 Chemical Sensing with Microcantilevers

8.2.1 General Microcantilever Response

The measurement setup described in § 7.1.2 allows for simultaneous measurement of six cantilevers. Hence three cantilevers of the P μ CA were functionalized with 40 nm of gold with a 10 nm adhesion layer of titanium. Issues related to method of

functionalization and packaging have been discussed in § 5.4.2 and § 7.2.1 respectively. Each gold-coated cantilever was paired with an identical reference cantilevers on the P μ CA for measurement. Other elements of the measurement setup such as the power supply, lock-in amplifier settings, analyte flow control, and data acquisition have been described in Chapter 7. All measurements described here were made with 6-mercapto-1-hexanol.

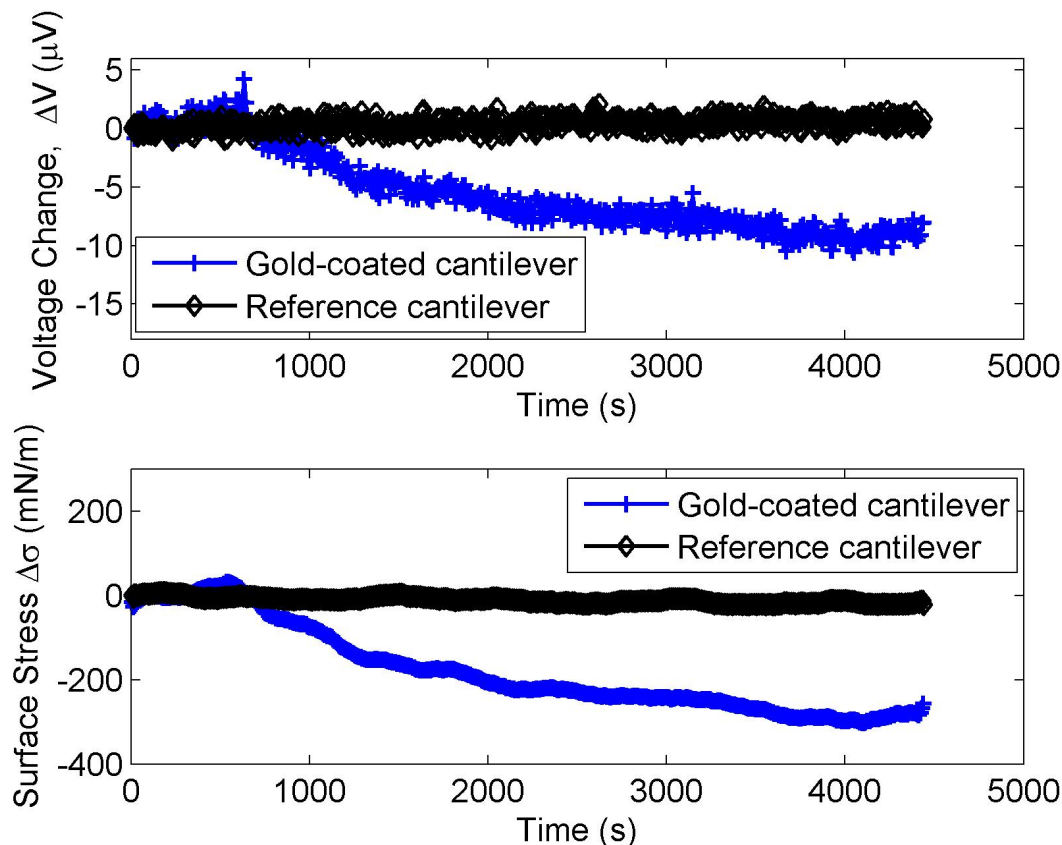


Figure 8.1 Response from a gold-coated and uncoated reference cantilever when both are exposed to 55 ppb of mercaptohexanol (flowrate 2sccm).

8.2.1.1 Response to 6-Mercapto-1-hexanol

The concentration of the analyte was controlled by control of the mass flow rates of N₂ in mass flow meters 1 and 2 (refer Figure 7.9). Figure 8.1 shows a typical response from the gold-coated and reference cantilevers. The voltage output has been converted into a surface stress response for each of the two cantilevers using the equation

$$\Delta V = V_{in} \left(\frac{R_{cantilever}}{R + R_{cantilever}} - \frac{1}{2} \right) \quad (8.1)$$

where ΔV is the voltage change observed and V_{in} is the input voltage to the Wheatstone bridge circuit (refer Figure 7.3). This equation is used in favor of the more standard equation for a Wheatstone bridge response due the nonlinear behavior of the bridge.

The drift in the measurement is associated with noise issues discussed in Chapter 7. The presence of the reference cantilever though can help filter out noise due to flow fluctuations and drift in the measured response. The response after subtracting the response of the reference cantilever is shown in Figure 8.2. The cantilever is exposed to the analyte at 400 seconds. The ‘dip’ in the response prior to the exposure is due to noise in the measurement. Subtraction from a reference can in some cases accentuate this noise response.

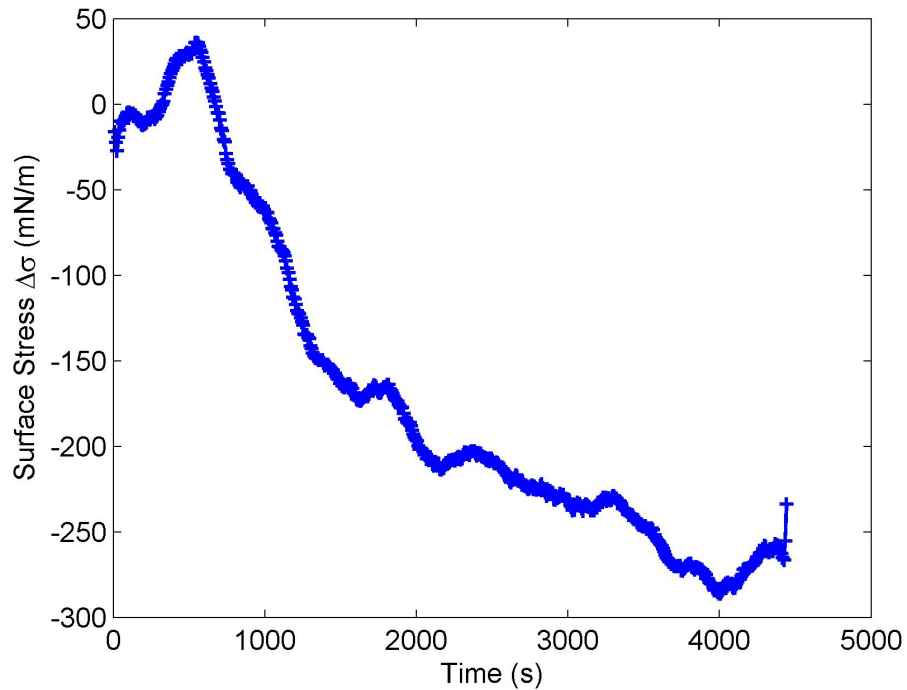


Figure 8.2 Differential measurement of surface stress by subtracting surface stress response of gold-coated cantilever from reference cantilever. This plot is generated by subtracting the surface stress response of the gold-coated cantilever from that of the reference cantilever in Figure 8.1.

A typical measurement consists of an initial period of measurement of the cantilever response in dry nitrogen for 10 minutes. This allows to evaluation of the baseline of the experiment, noise in the measurement and drift in the measurement, if present. After this time the 4-way crossover valve is switched and the cantilevers are exposed to the analyte for the duration of exposure desired after which the flow is switched back to dry nitrogen. At certain settings of the mass flow meters, a small change in the flow is noticed. This is particularly true if a high flow (higher than 10 sccm) is desired in the flow cell. At lower flow rates (around 2 sccm), no resistance change associated with change in flow-rate is seen. The flow switch occurs due to a large change in the pressure at the four-way crossover valve. A mass flow controller has been placed at the outlet of the flow cell (refer Figure 7.9) that ensures flowrate is always kept at 2 sccm. However at the time of the flow switch, flowrates may vary from the flow setting for upto 5 seconds. At the end of the experiment a change in the piezoresistance of the gold-coated cantilever is seen (Figure 8.3).

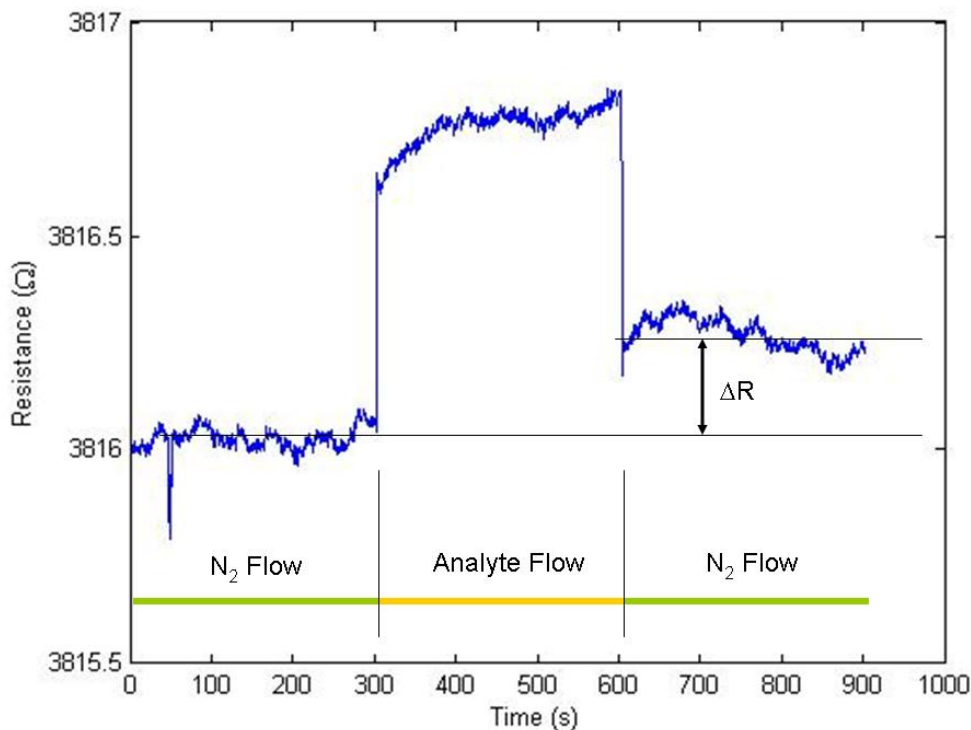


Figure 8.3 Response curve associated with analyte absorption at 55 ppb at 10 sccm for a short time. The jump in resistance of the piezoresistor at the start and end of analyte flow is due to a change in flow rate in the system. The piezoresistance changes at the end of analyte exposure.

8.2.2 Effect of Cantilever Geometry on Surface Stress Response

The matrix of designs to evaluate the effects of various parameters on geometry has been described in Chapter 4. Cantilever response experiments for different combinations of microcantilevers were conducted to verify the analysis presented in Chapter 3. In this section results on effect of clamping distance and cantilever length are presented. Tests for evaluation of effect of resistor length were not very conclusive for reasons that are explained later in this section.

8.2.2.1 Effect of Clamping Distance

Two cantilever pairs were exposed to 55 ppb of mercaptohexanol to evaluate the effect of delta. As seen in Figure 8.4, the cantilever response for large distance from the clamping point was larger.

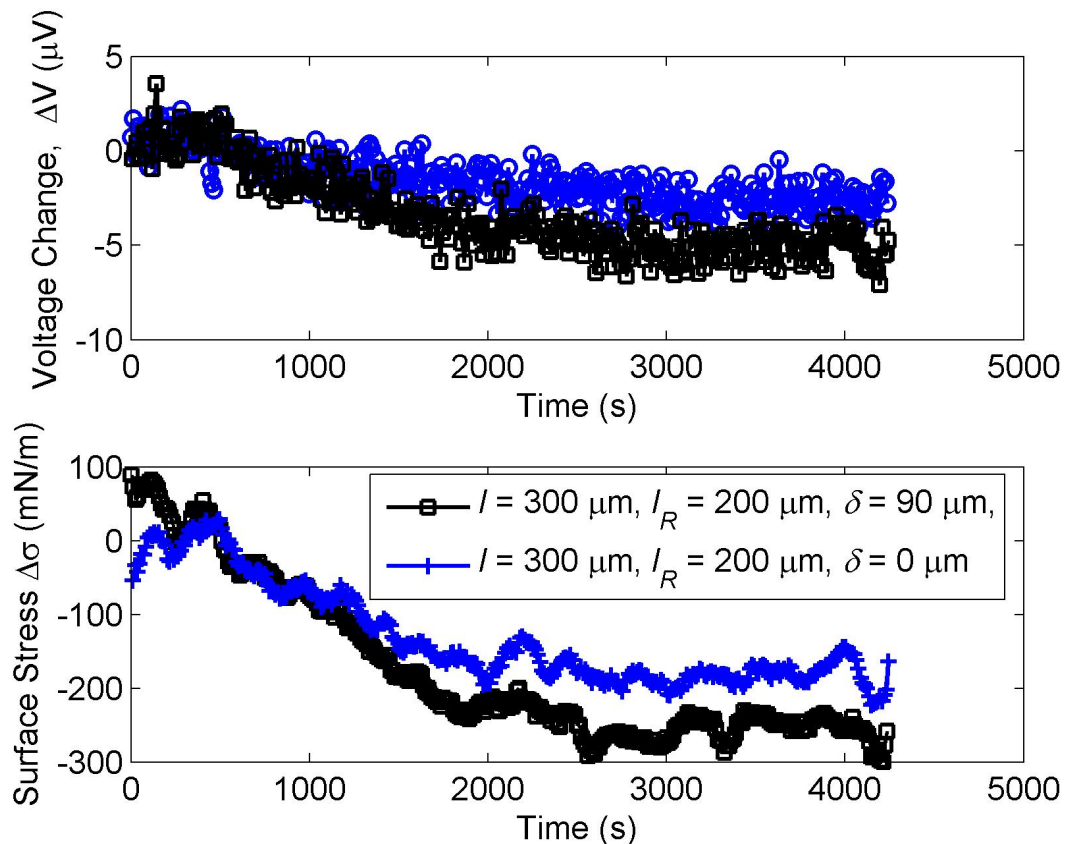


Figure 8.4 Effect of clamping distance (δ): The seemingly smaller response for $\delta = 0 \mu\text{m}$ is due to use of incorrect surface stress sensitivity. Analyte concentration: 55 ppb, flowrate: 2 sccm.

While this is as expected from the design analysis (Chapter 3), an important point to ponder here is that while both cantilevers are exposed to the same analyte concentration, the surface stress that is evaluated is different (Figure 8.4). This is because of the use of the same value of surface stress sensitivity in Figure 8.4 to evaluate surface stress response with both cantilever designs. For the cantilever with $\delta = 90 \mu\text{m}$, the surface stress sensitivity of $7.05 \times 10^{-4} (\text{N/m})^{-1}$. However for the second cantilever with $\delta = 0 \mu\text{m}$, the stress distribution at the clamped end of the cantilever reduces surface stress sensitivity (refer § 3.2.2). If this correction is made, both cantilevers will show the same surface stress response. To evaluate the surface stress sensitivity of each cantilever as a function of δ a finite element model could be used. All results reported in this work are based on $S_{\text{cantilever}} = 7.05 \times 10^{-4} (\text{N/m})^{-1}$. The real cantilever surface stress for the mercaptohexanol reaction on gold is given by the design with $\delta = 90 \mu\text{m}$ - approximately -280 mN/m. This cantilever is unaffected by clamped-end boundary conditions that lower the surface stress sensitivity of the piezoresistive microcantilever.

The design analysis (Figure 3.5) suggests that the ratio of surface stress sensitivities of the two cantilevers is 1.53. The ratio of surface stress sensitivities evaluated from the response curve in Figure 8.4 is approximately 1.51, indicating good agreement with theoretical predictions.

8.2.2.2 Effect of Cantilever Length

Cantilever length has a very limited effect on the response unless $l \approx l_R$. In such a case, fringe effects (refer § 4.3.2) change the stress distribution near the piezoresistor and a modification in the cantilever response is seen. In the case presented in Figure 8.5, cantilever length is much greater than resistor length and no fringe effects are expected. Also as expected the cantilever response is the same for both cantilevers.

The surface stress at equilibrium, in this case, is higher than presented in Figure 8.4. This is due to the use of a higher concentration for this particular experiment. This will be discussed in greater detail in § 8.3.2.2.

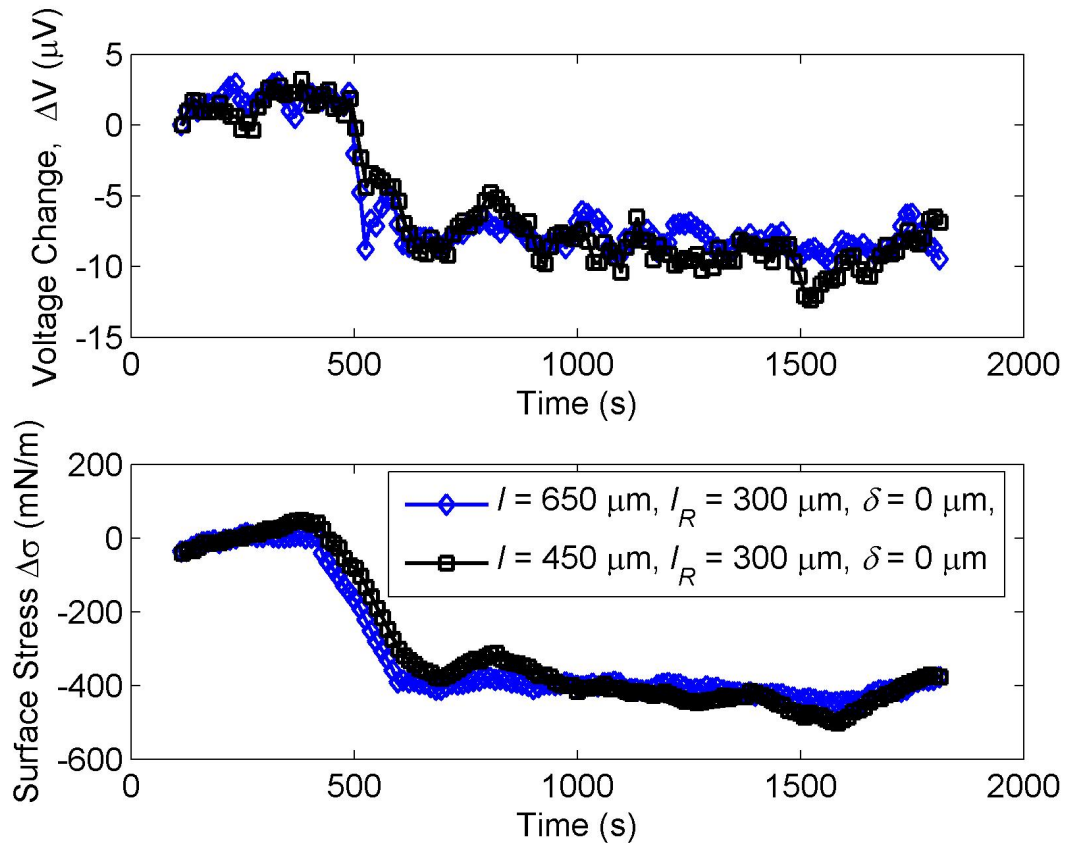


Figure 8.5 Effect of resistor length: The response for the two cantilevers with different cantilever lengths is near identical. The higher stresses here are on account of measurement at a concentration of 400 ppb (flowrate: 2 sccm).

8.2.3 Effect of Resistor Length

A majority of the cantilevers that survived in our processing had resistor lengths in excess of 200 μm and the differences in response with these microcantilevers were not discernable as expected from the design analysis (refer Figure 3.4). The cantilevers designed to evaluate the effect of resistor length, l_R (refer Table 4.1) had a low yield. Hence the effect of variation of resistor length for short cantilevers ($l = 150 \mu\text{m}$, $l_R = 50$ to $125 \mu\text{m}$) could not be evaluated.

8.3 Other Chemical Sensing Schemes

8.3.1 Single and Double-Sided Sensing

The principle of double-sided sensing has been explained in Chapter 4. The specifics of the experiment and results are reported in this section.

Functionalization of the double-sided cantilever sensors has been described in Chapter 5. The test involved exposure of two pairs of cantilevers to mercaptohexanol at 55 ppb with a flow-rate of 2 sccm in the flow cell. One pair consisted of a single-side coated cantilever and an uncoated reference while the second consisted of a double-side coated cantilever and a reference cantilever. The response from the exposure of the two cantilevers is seen in Figure 8.6.

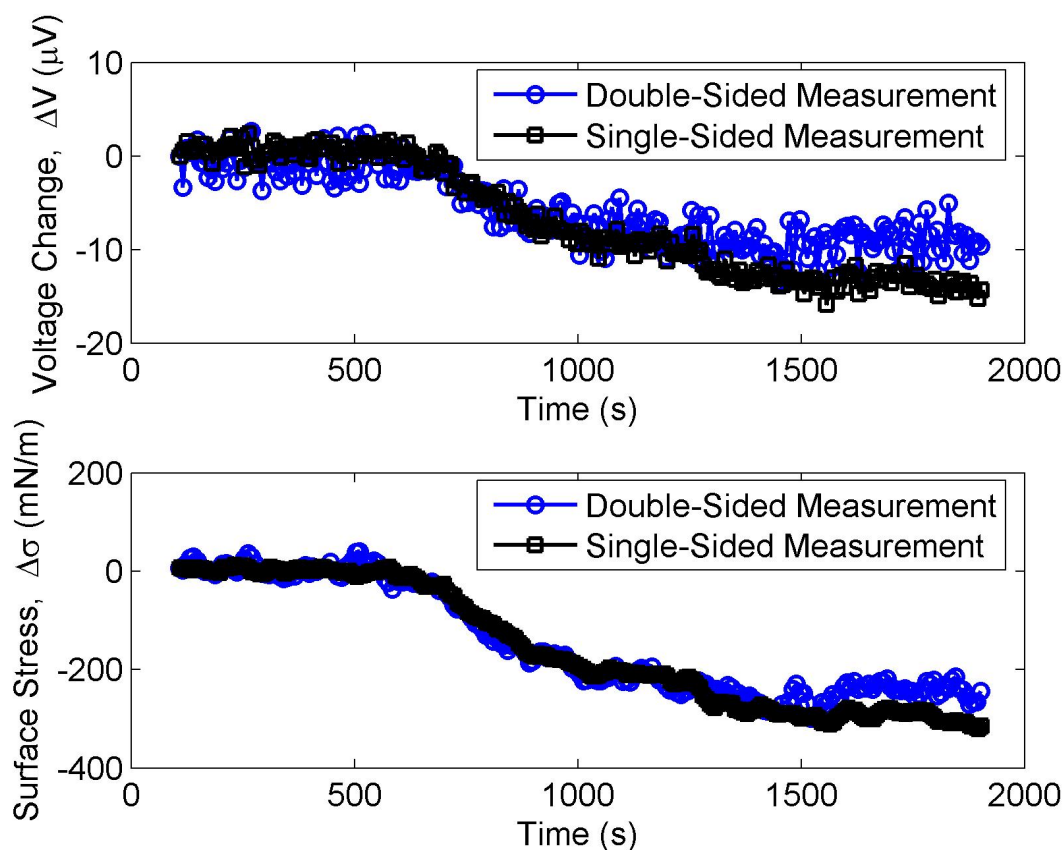


Figure 8.6 The voltage change in the cantilevers (top) and the piezoresistive response (bottom) of single- and double-sided cantilevers to 55 ppb of mercaptohexanol.

Since the cantilevers used in this experiment have a $\delta = 100 \mu\text{m}$, the surface stress response is closer to -280 mN/m . Also we notice that the surface stress response of the double-sided cantilever is lower than the single-sided cantilever. This discrepancy is likely to be due to small errors in the coating of the cantilever or experimental conditions.

This analysis of single and double-sided cantilever sensing suggests that double-sided cantilevers may be used for surface stress sensing applications. Also it suggests that the theoretical background for single and double-sided sensing presented in Chapter 4 is accurate. However, as explained in Chapter 4, the present design of the cantilevers is better suited for single-sided sensing. Design for double-sided cantilever based on trends outlined in § 4.6.2 will result in highly sensitive cantilevers that can be functionalized using liquid or gas phase coatings. Single-sided coating of cantilevers requires specialized instrumentation and coating methods that allow for direct deposition on a single side of the cantilever. Double-sided cantilevers offer greater flexibility from this perspective.

8.3.2 Chemical Sensing with a Thermal Array

In Chapter 6, the possibility of controlling temperature of well-calibrated piezoresistive microcantilevers has been demonstrated. In all existing work on surface stress detection with piezoresistive microcantilevers, temperature change due to current flow, during surface stress measurement with piezoresistive cantilevers, has either been minimized (by using low-power inputs) or has been ignored which results in erroneous measurement. Temperature change of the cantilever can affect analyte binding processes on the surface. This section presents a technique for the evaluation of chemical reaction kinetics and activation constants with a piezoresistive microcantilever array. The work in this section is limited to demonstration of the feasibility of this technique.

8.3.2.1 Background

Existing work on chemical sensing with piezoresistive microcantilevers has demonstrated methods of measuring surface stress due to analyte binding and evaluation of reaction constants at ambient temperatures [7, 12]. Gibbs free energy for the analyte-gold reaction (adsorption-desorption process) for thiolated compounds has been reported

as -34.6 kJmol^{-1} for thiolated DNA [12] and in the range of -13.2 to -14.7 kJmol^{-1} for 1-dodecanethiol (8.4 mM in liquid phase) [7].

The surface stress is a function of the surface coverage (θ) which is related to the chemical reaction via the Langmuir adsorption model, $\theta \propto 1 - \exp(-k_{obs}t)$, where k_{obs} is the observed reaction rate and t is reaction time. Also,

$$k_{obs} = k_{ads}c + k_{des} \quad (8.2)$$

where k_{ads} and k_{des} are reaction rates associated with the analyte adsorption and desorption and c is the concentration of the analyte. The values of k_{obs} may be obtained as a function of concentration for immobilization of thiol-modified double-stranded DNA and the rate constants k_{ads} and k_{des} can be evaluated at room temperature.

In order to assist in discrimination between different analytes, the measurement of an 'effective' activation energy, E_a , associated with surface adsorption reactions can be carried out. Adsorption rates at a given temperature, associated with the analyte binding process, can be evaluated in terms of rate of change of surface stress in the Langmuir adsorption or desorption process. The choice of the adsorption or desorption isotherms depends on the nature of adsorption or desorption phenomenon. An adsorption isotherm that follows a Langmuir relation is associated with a constant rate k_{obs} and is restricted to single monolayer coverage. Typically multilayer coverage is associated with a change in k_{obs} as the coverage proceeds beyond a monolayer. Further, the energy required for reaction on a surface is given by $Q + E_a$ where Q is the heat of adsorption. Also, the heat of adsorption Q decrease and E_a increases with coverage θ . Hence a clear understanding of the nature of the analyte binding on the surface is essential for use of the appropriate adsorption models and the estimation of variation of Q and E_a with θ .

8.3.2.2 Estimation of Reaction Parameters

So far no work has been carried out with cantilever based systems wherein simultaneous surface stress measurements have been made with cantilevers at different temperatures. This will allow for evaluation of the free energies associated with the

adsorption and desorption processes. Further these measurements can be made on a single chip without changing analyte concentration.

For a given temperature (T) of the reaction, the activation energy for desorption (E_a) of the analyte into a medium where the analyte concentration is zero is given by

$$k_{des} = k_0 \exp(-E_a / RT) \quad (8.3)$$

where k_0 is the initial concentration and R is the universal gas constant. If the desorption rates, $k_{T_1,des}$ and $k_{T_2,des}$, are known at two temperatures, T_1 and T_2 , respectively,

$$E_a = R \ln \left(\frac{k_{T_1,des}}{k_{T_2,des}} \right) \left(\frac{1}{T_2} - \frac{1}{T_1} \right)^{-1} \quad (8.4)$$

Further, once the values of k_{ads} are measured from the experiment, the rate constants for adsorption at the two temperatures can be evaluated from (8.2) and the effective activation energy for the adsorption reaction can also be evaluated [13]. In order to implement this technique is important to consider if the reaction is at equilibrium with the concentration in gas phase.

The ability to control the temperature of the cantilever and to make simultaneous measurement of a reaction phenomenon at different temperatures allows for measurement of characteristic parameters for analyte identification. This will provide orthogonal sensing capabilities for existing cantilever-based surface stress sensors and facilitate analyte recognition.

8.3.2.3 Thermal Array Measurement: Results

In order to evaluate the regime in which the reaction is occurs, measurements were made at room temperature (minimal cantilever heating) for two different concentrations- 55 ppb and 400 ppb. Measurement at higher concentration resulted in a higher equilibrium stress on the cantilever. This implies that the reaction is in the mass transport limited regime (Figure 8.7). A similar trend has been reported by Datkos et al. [14].

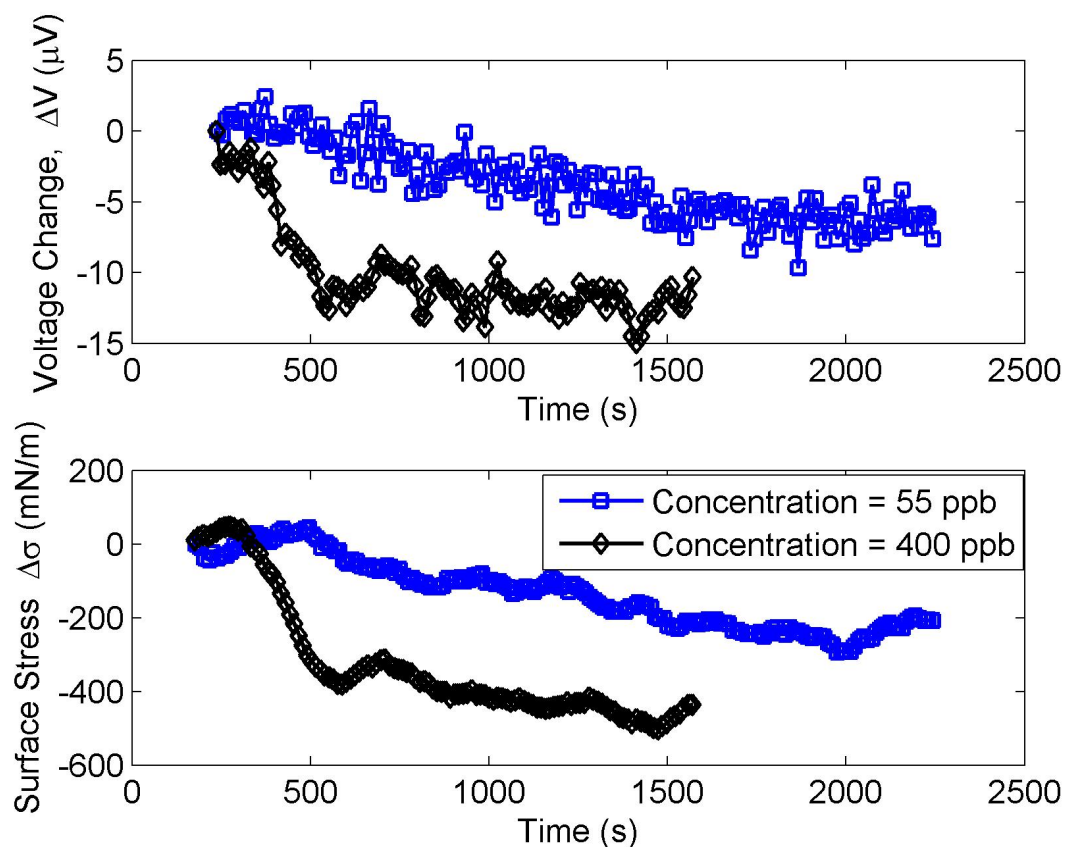


Figure 8.7 Effect of concentration: The equilibrium stress and reaction rate are larger at high concentrations. Flowrate: 2 sccm.

Measurements were made with gold-functionalized cantilevers with 55 ppb (≈ 24.6 nM) of 6-mercapto-1-hexanol at a flow rate of 5 sccm. Two pairs of cantilevers at 21 $^{\circ}\text{C}$ and 50 $^{\circ}\text{C}$ were exposed to the analyte. The cantilevers were heated to different temperatures by applying a different DC bias (the instrumentation has been described in Chapter 7). Each pair consisted of a functionalized cantilever paired with a reference (non-functionalized) cantilever at the same temperature. The cantilever pairs were first exposed to the mercaptohexanol until the response was near saturation.

In a second part of the experiment, the cantilevers were exposed to the analyte for a long time to ensure saturation of the surface. The flow was then switched to a pure N_2 flow and a change in surface stress associated with desorption was observed. An Arrhenius model was fit to the rates observed at the two temperatures. The desorption curves suggest that complete desorption does not occur even after 1600 seconds.

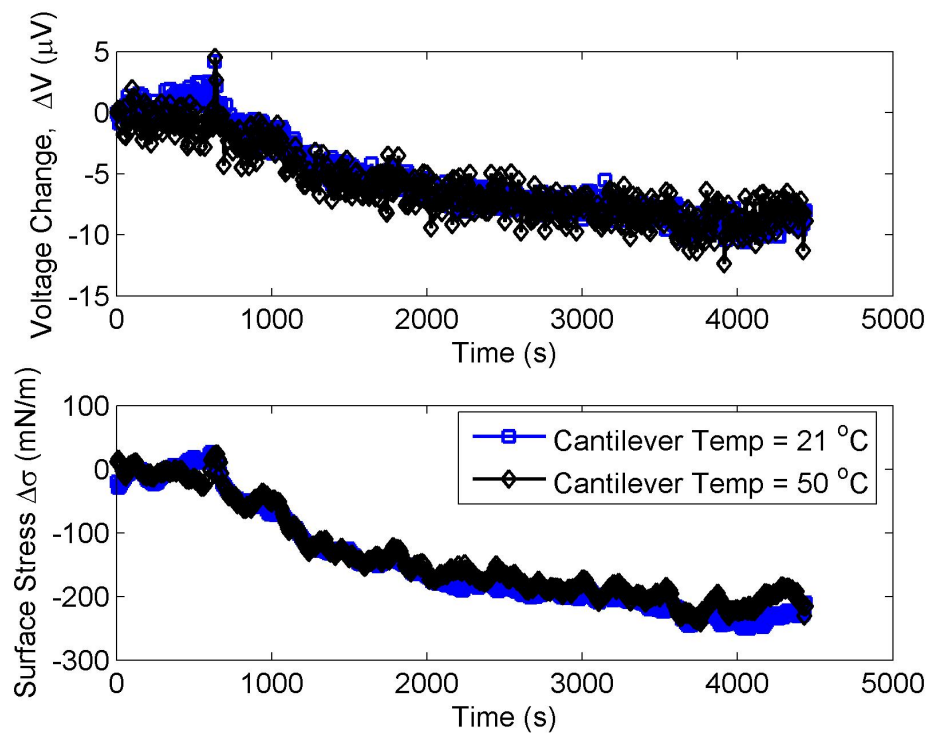


Figure 8.8 Adsorption reactions on the cold and heated cantilevers. The reaction curves are fitted with Langmuir isotherms. These measurements were made at 55 ppb at 5 scfm.

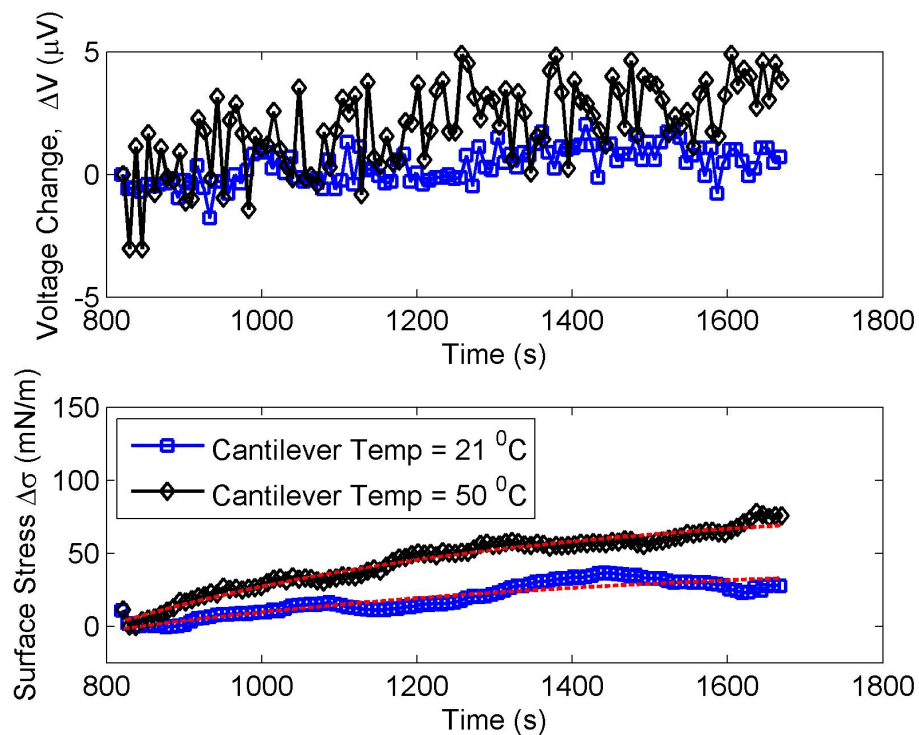


Figure 8.9 Desorption curves for desorption of analyte from the saturated sensors in dry nitrogen. Flow rate: 5 scfm. The red lines indicate fitted Langmuir isotherms.

An important point to note in this measurement is that the assumption that surface stress sensitivity of the cantilevers will stay constant over a wide range of temperatures is not valid. Figure 8.10 shows the effect of doping concentration and temperature on the piezoresistive constants. At a temperature of 50 °C (323 K), the surface stress sensitivity is reduced by a factor of 1.091. This has been factored into the measurements reported in this section.

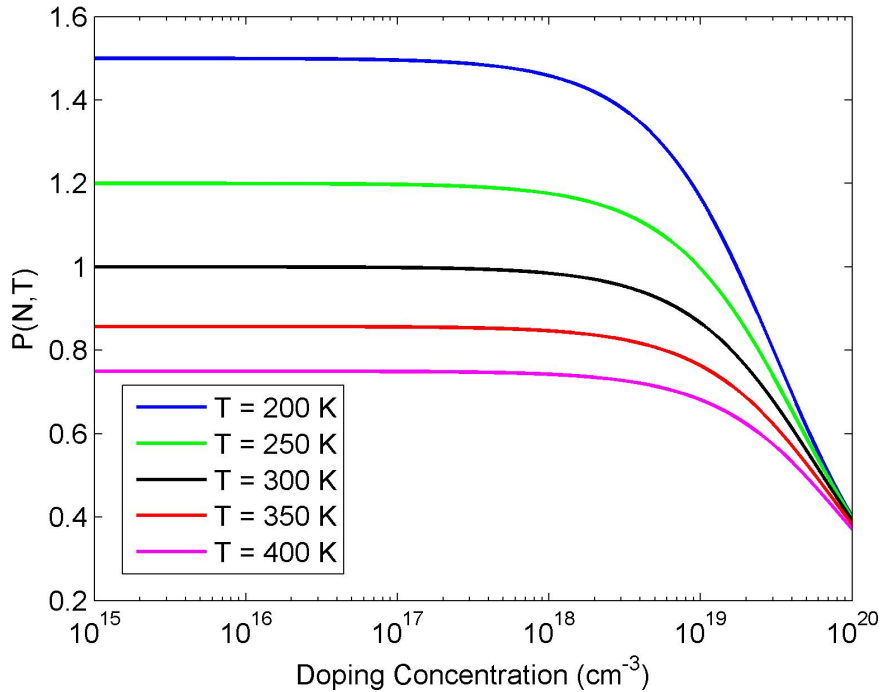


Figure 8.10 Variation of piezoresistive coefficient with doping concentration (for n-type silicon) and temperature. The y-axis plots the ratio of the piezoresistive constant at a given concentration and temperature to piezoresistive constant at 300 K for a doping level of 10^{15} cm^{-3} [15].

8.3.2.4 Thermal Array Measurement: Analysis

Extraction of the Arrhenius and rate constants for the adsorption and desorption curves cannot be performed for the experimental parameters shown because the reaction is proceeding in the mass flow rate limited regime. This implies that the adsorption curve shows the value of stress associated with binding of the analyte to the surface. However since the reaction is mass flow rate limited, the stressogram is a quasi-equilibrium curve. Hence reaction rates cannot be extracted from these data sets in the manner described in § 8.3.2.2.

Desorption rates (in dry nitrogen) were evaluated by fitting the desorption curves (Figure 8.9) with Langmuir isotherms. Desorption rates in nitrogen are estimated at $k_{T=294\text{ K},des} = 1.515 \times 10^{-3} \text{ s}^{-1}$ and $k_{T=323\text{ K},des} = 1.88 \times 10^{-3} \text{ s}^{-1}$. Since the nature of the binding in this reaction is not clear and the reaction (during adsorption is the mass flow rate limited regime, activation energy based on (8.4) are not reported in this work.

Shadnam et al. [6] have shown that the thermal desorption of alkanethiols from gold is associated with a thermodynamic threshold. With 1-heptadecanethiol (HDT) at 383 K, they were able to show that complete desorption does not occur even after two hours. Also they suggest that at 383 K, HDT will not desorb completely even after several hours. At a temperature of 433 K, however, different kinetics are observed and complete desorption occurs in less than 50 minutes. Also the desorption rates they evaluated were different in decalin and in air. This study suggests that heating of the cantilevers to higher temperatures may show evidence of different desorption kinetics and more complete desorption.

So far a limited number of experiments have been performed with the thermal array measurement technique due to noise issues discussed in Chapter 7. Hence extensive verification of the results presented above has not been possible.

8.3.2.5 Thermal Array Measurement: Limitations and Recommendations

A limitation of this technique when used with the P μ CA is the issue of the thermal profile in the cantilever. As shown in Figure 8.11, the thermal profile of the cantilever is not uniform and for an average temperature of 50 °C, the temperature varies from 24 °C to 57 °C. Hence the reaction rate on the cantilever during both adsorption and desorption varies as the temperature profile. The value of activation energy calculated then is based on an averaged value of the rate constant for the cantilever.

Further thermal array measurement with a larger set of cantilevers all at different temperatures seems attractive because it will provide a larger data set and a better measure of activation constants. However use of large temperatures with the current cantilever designs results in large variations in temperature. To remedy this limitation, the cantilever needs to be redesigned (using the thermal model presented in Chapter 6) to achieve a more uniform temperature profile. Use of large values of δ will limit the

amount of heat conduction from the clamped end and aid in this design. In addition, as shown in this work, they also lead in more accurate assessment of surface stress.

Another approach to limiting the spatial variation of temperature is limiting the area of chemical reaction. This can be done by coating a section of the cantilever that has a small variation in temperature.

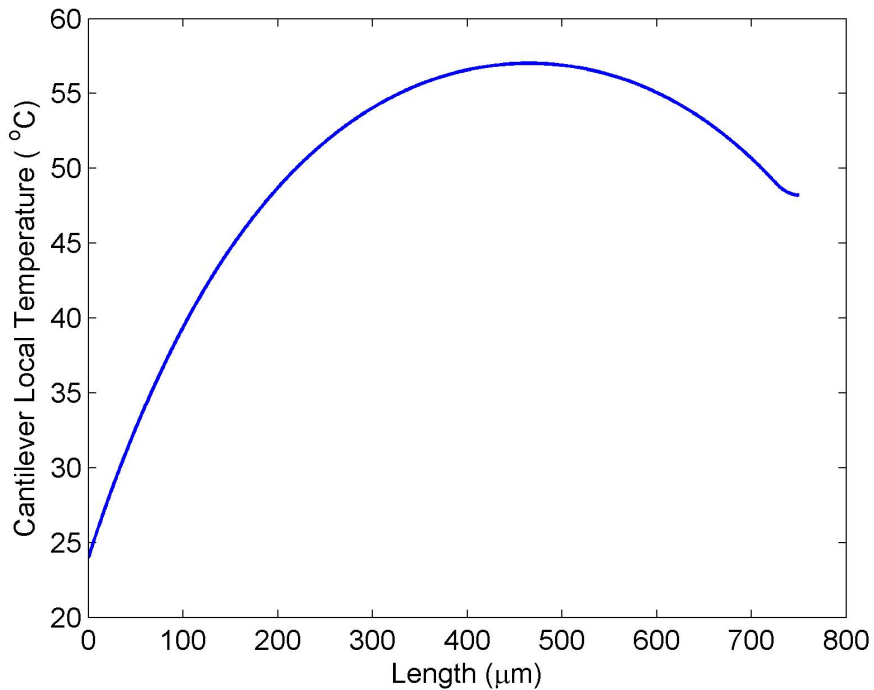


Figure 8.11 Spatial temperature profile of a 750 μm long cantilever with an average temperature of 50 $^{\circ}\text{C}$.

8.4 Conclusions

This chapter served to verify some aspects of the design of the P μ CA. Design of n-doped silicon piezoresistive microcantilevers with large δ has several advantages. It allows of a ‘truer’ measure of surface stress on the cantilever. Also, it ensures a more constant thermal profile on the cantilever in case of thermal array sensing.

The two novel applications of the piezoresistive microcantilevers sensors- double-sided sensing and thermal array sensing could be used to extend the applicability and functionality of piezoresistive microcantilever sensors. The first simplifies methods of functionalization of the cantilevers, potentially reducing costs associated with use of cantilever sensors in field operations, and the second could be used to extend the

functionality of existing piezoresistive microcantilevers sensors. Both methods require that the piezoresistive sensor be design for the application at hand. These will be discussed in more detail in Chapter 9.

8.5 References

- [1] A. G. Hansen, M. W. Mortensen, J. E. T. Andersen, J. Ulstrup, A. Kühle, J. Garnaes, and A. Boisen, "Stress formation during self-assembly of alkanethiols on differently pre-treated gold surfaces," *Probe Microscopy* (ISSN: 1355-185X) , vol: 2, pages: 139-149, 2001, vol. 2, pp. 139-149, 2001.

- [2] R. C. Thomas, L. Sun, and R. M. Crooks, "Real-time measurement for the gas-phase adsorption of n-alkylthiol mono- and multilayers on gold," *Langmuir*, vol. 7, pp. 620-622, 1991.

- [3] W. Pan, C. J. Durning, and N. J. Turro, "Kinetics of alkanethiol adsorption on gold," *Langmuir*, vol. 12, pp. 4469-4473, 1996.

- [4] R. Berger, E. Delamarche, H. P. Lang, C. Gerber, J. K. Gimzewski, E. Meyer, and H.-J. Güntherodt, "Surface stress in the self-assembly of alkanethiols on gold," *Science*, vol. 276, pp. 2021-2024, 1997.

- [5] G. G. Baralia, A.-S. Duwez, B. Nysten, and A. M. Jonas, "Kinetics of exchange of alkanethiol monolayers self-assembled on polycrystalline gold," *Langmuir*, vol. 21, pp. 6825-6829, 2005.

- [6] M. R. Shadnam and A. Amirfazli, "Kinetics of alkanethiol monolayer desorption from gold in air," *Chemical Communications*, pp. 4869-4871, 2005.

- [7] R. Desikan, I. Lee, and T. Thundat, "Effect of nanometer surface morphology on surface stress and adsorption kinetics of alkanethiol self-assembled monolayers," *Ultramicroscopy*, vol. 106, pp. 795-799, 2006.

- [8] D. Lee, T. Thundat, and S. Jeon, "Electromechanical identification of molecules adsorbed on microcantilevers," *Sensors and Actuators B: Chemical* vol. 124, pp. 143-146, 2007.

- [9] X. Y. Ling, L. Malaquin, D. N. Reinhoudt, H. Wolf, and J. Huskens, "An in situ study of the adsorption behavior of functionalized particles on self-assembled monolayers via different chemical interactions," *Langmuir*, vol. 23, pp. 9990-9999, Sep 2007.
- [10] D. K. Peng and J. Lahann, "Chemical, electrochemical, and structural stability of low-density self-assembled monolayers," *Langmuir*, vol. 23, pp. 10184-10189, Sep 2007.
- [11] R. Berger, E. Delamarche, H. P. Lang, C. Gerber, J. K. Gimzewski, E. Meyer, and H.-J. Güntherodt, "Surface stress in the self-assembly of alkanethiols on gold probed by a force microscopy technique," *Applied Physics A*, vol. 66, pp. S55-S59, 1997.
- [12] R. Marie, H. Jensenius, J. Thaysen, C. B. Christensen, and A. Boisen, "Adsorption kinetics and mechanical properties of thiol-modified DNA-oligos on gold investigated by microcantilever sensors," *Ultramicroscopy*, vol. 91, pp. 29-36, 2002.
- [13] J. M. Smith, *Chemical Engineering Kinetics*, Second ed.: McGraw-Hill, Inc., 1970.
- [14] P. Datkos and I. Sauer, "Detection of 2-mercaptoethanol using gold-coated micromachined cantilevers," *Sensors and Actuators B*, vol. 61, pp. 75-82, 1999.
- [15] Y. Kanda, "A graphical representation of the piezoresistance coefficients in silicon," *IEEE Transactions on Electron Devices*, vol. 29, pp. 64-70, 1982.

CHAPTER 9

SUMMARY AND RECOMMENDATIONS

Conclusions of various sections of this work have been presented in the relevant chapters for most part. This chapter serves to list some of the important contributions and limitations of this work and presents ideas to for future work in this area

9.1 Summary

This work presents the design, fabrication and testing of a piezoresistive microcantilever array. Extensive thermal characterization of the piezoresistive microcantilevers has been performed for DC and AC electrical excitation and values of heat transfer coefficient are reported. Also, a method of low-noise measurement of the piezoresistive microcantilever array have been investigated and implemented.

Further, this thesis has investigated the use of two novel techniques of chemical sensing- double-sided sensing and thermal array-based sensing which could potentially extend the applicability and functionality of piezoresistive microcantilever sensors for chemical sensing.

The section that follows lists the contributions of this work. Also a number of recommendations have been made for improvement of the performance of the piezoresistive cantilever sensor presented is this work. Finally, a list of recommendations for future work is presented, based on an understanding of the limitations of the current work and the potential for future research in the directions investigated herein.

9.2 Research Contributions

A number of contributions have been made in this thesis to various aspects of development of piezoresistive microcantilever systems for chemical sensing. These are listed in the sections that follow.

9.2.1 Design

1. The use of n-doped piezoresistor for surface stress sensing applications has been investigated. This study shows that for most cantilever geometries n-type doping results in better surface stress response. Short cantilevers may still benefit from p-type doping. Also it was shown that the electronic noise in the cantilever decreases with length. Hence for surface stress-based measurement with low detection limits, long, n-doped piezoresistive cantilever should be used.
2. The effect of geometric parameters on surface stress sensitivity was investigated. A set of design rules have been established for development of piezoresistive cantilever for surface stress detection. The n-doped piezoresistors should be placed far from the clamped end of the cantilever. Higher surface stress sensitivity is obtained for piezoresistors with large width.
3. Another important contribution of this thesis is the appreciation of the fact that surface stress sensitivity reported in literature is based on sensitivity of the cantilever at the free end. This implies that values of surface stress reported in literature based on these values of surface stress sensitivity without further calibration must be incorrect.
4. Development of a new and complete model for analysis of multilayered plate structures with intrinsic and surface stresses (Chapter 4).
5. Development of a corrected model for noise in piezoresistive readout in microcantilevers for surface stress measurement. Previous models were based on tip loading conditions and therefore incorrect (Chapter 3).

9.2.2 Fabrication

1. Development of a process flow for fabrication of a highly sensitive P μ CA which has high yield and reproducible cantilever characteristics.

2. The robust design of the cantilever ensures a greater uniformity of device performance than possible in designs where the piezoresistor is near the clamped end of the cantilever.
3. Tuning of surface stress in the multilayered cantilever allows for control of curvature of the microcantilevers. Very flat cantilevers were required in this work to allow ease of functionalization of the cantilevers. The technique, however, can be applied to different plate structures to develop geometries with desired radius of curvature.

9.2.3 Thermal Characterization

1. Thermal characterization of piezoresistive microcantilevers for surface stress measurement is generally ignored. This has been performed in this work. The important contributions that accrued from this endeavor were:
 2. Development of an accurate finite difference model for the piezoresistive microcantilevers. This finite difference model allows for prediction of thermal behavior of the cantilever for different electrical excitation (AC and DC).
 3. Evaluation of AC and DC thermal characteristics of the microcantilevers. This work helps understand the thermal behavior of the cantilever for different electrical excitation. It also formed the basis of a comparison with the thermal model.
 4. Evaluation of effective heat transfer coefficient for microcantilevers. This is the first work that reports heat transfer coefficients evaluated from piezoresistive microcantilever systems in a systematic manner. Heat transfer coefficients have been shown to be a function of cantilever geometry and temperature.
 5. A closed-form analytical solution has been developed in this work for evaluation of the temporal response of the microcantilevers (Appendix C). It is limited, though, in terms of their applicability since it assumes heat transfer is independent of temperature.

9.2.4 Measurement

1. Implementation of system of low-noise measurement based on PSD techniques for measurement of cantilever piezoresistance. This technique still has numerous problems associated with pickup of electromagnetic noise that will be discussed later in this chapter.

9.2.5 Application

1. Detection of 6-mercapto-1-hexanol at 55 ppb by two methods of sensing- double-sided sensing and thermal array sensing has been demonstrated.
2. Thermal Array-Based Sensing: The feasibility of thermal array sensing has been investigated with mercaptohexanol. This technique has been used to evaluate activation constants associated with the desorption process. Also it allows for simultaneous measurement of temperature-dependent kinetics and surface stress.

9.3 Recommendations for Improvement of Sensor Performance

While some useful contributions have been made in this work, there are numerous limitations in the current work that need to be addressed to help it achieve its fullest potential and so that it can be used for a wide range of applications. Some important issues that need to be addressed in the current work are:

1. Design
 - i. Some portions of the design analysis of the cantilevers were carried out after mask design had been completed. Incorporation of ideas related to large resistor width and spacing may help further enhance surface stress sensitivity of the cantilevers.
2. Fabrication
 - i. Improvements and simplification of the fabrication process would be extremely beneficial. The current process flow uses TMAH etching and poor quality of the nitride can result in low yield. Moving to a dry process for bulk etching of the handle wafer can significantly improve device yields.
3. Gas flow system
 - i. The current flow system, while adequate for low concentrations of analyte, cannot support concentration of mercaptohexanol in excess of 1 ppm. This might limit the range of investigation of the sensors should investigation of larger concentrations be desired. In such a case, appropriate changes in the flow system will have to be made.
 - ii. Secondary verification of the concentration of the analyte concentration is desirable. Residual gas analysis to determine and corroborate the exact concentration of analyte that the cantilevers are being exposed to would be extremely useful.

- iii. An important concern in the current gas flow system is the possibility of some analyte adsorption on various parts of the flow system. It is possible that during the baseline calibration step, the cantilever is exposed to an unknown concentration of the analyte for the duration of the purge. This is bound to lead to erroneous results. In the current work, an effort was made to counter this problem by frequent change of certain flow-line components. Devising an alternative flow arrangement to prevent the purge and flow lines mixing may eliminate this problem altogether.
4. Resistance measurement setup
 - i. The noise in the resistance measurement setup has been an immense problem in the current work. All investigations point to pick-up of a 1.25 mHz signal at the lock-in amplifier. It is possible this pickup is from somewhere in the building. However for effective use of the P μ CA, this must be eliminated either by placing the entire setup in a Faraday cage or use of instrumentation that is not susceptible to this pickup or by moving this whole experiment to a noise-free location.
5. Testing issues
 - i. In the current work, all measurements have been made with 6-mercapto-1-hexanol in dry nitrogen. A wider range of analytes could be investigated with the current devices. Also the current system could be used for measurement in liquid media and measurement of biological analyte and markers.

9.4 Recommendations for Future Work

This work opens several doors for future work in the direction chemical and biological detection. Some recommendations and possible directions for future work are:

1. Improvement of measurement techniques: Our analysis of device noise shows that the device noise around 2 order of magnitude lower than the lowest noise measurement possible on our current setup. This opens up the door for investigation of methods for extremely low-noise measurement of the P μ CA or related devices.
2. Improvement of measurement setup: Placing the flowcell, Wheatstone bridge circuit and the multiplexer in a single Faraday box may serve to limit some noise effects.
3. Optimal design: While many of the issues related to maximizing sensitivity and reducing noise have been addressed in this work, optimal design of these sensors for

maximum surface stress sensitivity and minimum noise has not been attempted. This could be an interesting and productive study.

4. Microscale thermal issues: In Chapter 6, the heat transfer coefficients for different cantilevers was presented but no explanation was offered for the variation with length of the piezoresistor. Understanding the microscale heat transfer effects associated with cantilever heating and developing analytical or empirical models for the dependence of heat transfer coefficient on various parameters is a very promising area of study. This study will require the development of cantilevers with a more uniform thermal profile for better analysis of heat transfer effects.

5. In the chemical sensing measurements made so far, the measured resistance change is on account of surface stress, thermomechanical noise and heat of reaction associated with the binding event. The thermomechanical noise can be filtered using a reference cantilever, however the change in resistance due change in cantilever temperature (TCR $\sim 8.9 \Omega/K$) induced by the enthalpy of reaction needs to be accounted for.

$$\frac{\Delta R(t)_{Total}}{R} = \frac{\Delta R(t)_{Surface\ Stress}}{R} + \frac{\Delta R(t)_{Thermomechanical}}{R} + \frac{\Delta R(t)_{Reaction}}{R} \Bigg|_{RTD} \quad (9.1)$$

A piezoresistive microcantilever array could be designed with an integrated platinum RTD (TCR $\sim 7.7 \Omega/K$) for temperature measurement (Figure 9.1). This will allow for temperature detection independently of surface stress. By using the temperature measurement from the measuring and reference cantilevers, the third summand in (9.1) can be evaluated as:

$$\frac{\Delta R(t)_{Reaction}}{R} \Bigg|_{RTD} = \frac{\Delta R(t)_{Reaction}}{R} \Bigg|_{RTD}^{measurement} - \frac{\Delta R(t)_{Reaction}}{R} \Bigg|_{RTD}^{reference} \quad (9.2)$$

By creating a piezoresistive microcantilever array with orthogonal thermal sensors, both surface stress and heat of reaction will be measured simultaneous on the same measurement platform and could possibly result in more reliable identification of the analyte. Further this sensor could be used for closed loop control of cantilever temperature.

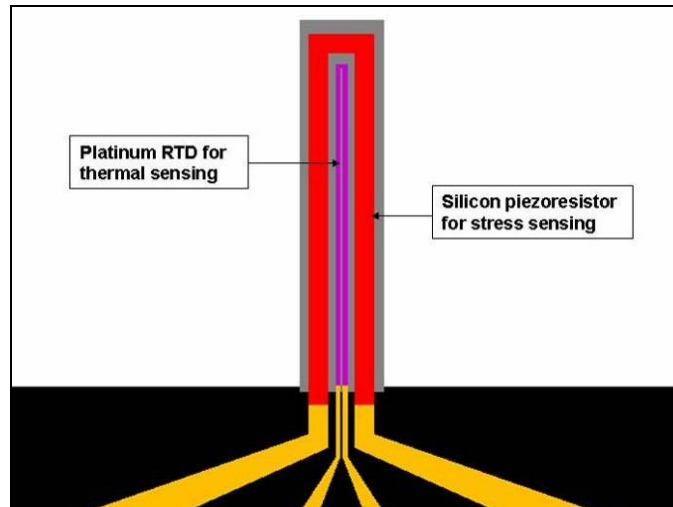


Figure 9.1 Schematic of PT μ CA cantilever. The outer loop is the piezoresistive sensor while the inner loop is the Pt RTD.

6. Integration of a thermal sensor on the cantilever for closed loop control of temperature: The thermal sensor can be doped silicon or a platinum resistance temperature detector (RTD). Further, if the thermal mass of the cantilever is made very small, this may be used to evaluate

7. Novel Functionalization Materials: Use of novel functionalization materials such as metal organic frameworks (MOFs) could extend the applicability of the current sensors to detection of a variety of analytes. Studies on coating of MOF layers on the cantilevers devices developed in this work are being carried out at Sandia National Laboratories (Livermore, CA) [1, 2] (Figure 9.2).

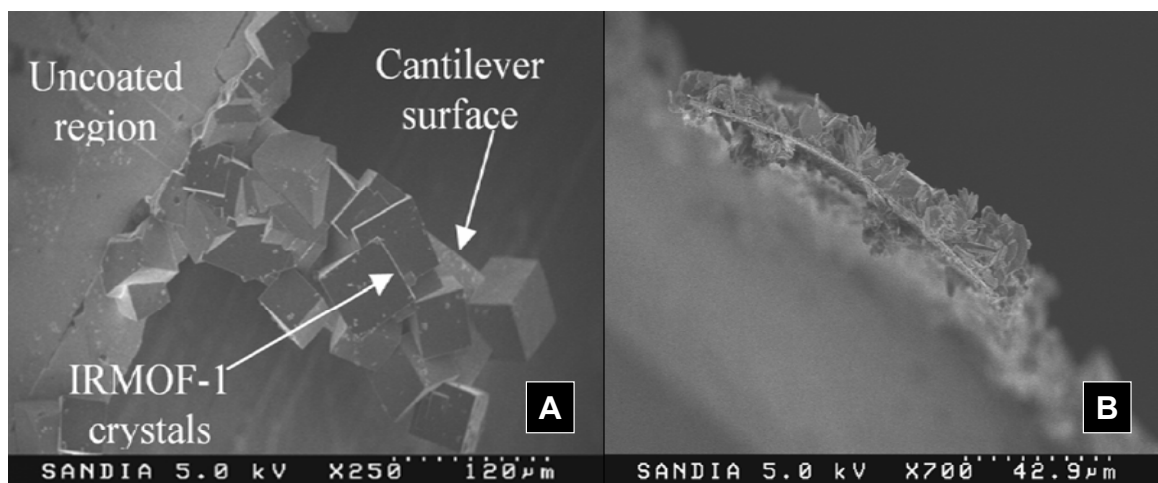


Figure 9.2 MOF coating cantilevers. The MOF used in this coating is MOF-5 [2]. MOFs of different grain sizes have been grown: A- 50 μ m, B- 5 μ m.

8. Double-Sided Measurement: This thesis has demonstrated the feasibility of design and use of double-sided sensing. Also, aspects of design of double-sided cantilevers have been discussed in this work. Cantilevers that are designed for this form of measurement can be up to 50% more sensitive than single-sided cantilever sensors. Further as pointed out double-sided cantilevers may be easier to functionalize making them more attractive for numerous applications.

9.5 References

- [1] R. Shediach, E. Lai, C. Bauer, B. A. Simmons, R. R. Strumpf, A. Choudhury, P. J. Hesketh, and M. D. Allendorf, "Growth of metal organic frameworks on microcantilever substrate materials," in *210th Meeting of the ECS* Cancun, Mexico ECS, 2006.

- [2] A. Choudhury, P. J. Hesketh, Z. Hu, T. G. Thundat, R. Bhakta, R. Houk, A. Skulan, G. Aigeldinger, A. Talin, and M. Allendorf, "Chemical detection with MOF-functionalized piezoresistive microcantilever arrays," in *212th Meeting of the ECS* Washington D.C.: ECS, 2007.

APPENDIX A
DESIGN DETAILS

A.1 Masks Layouts for P μ CA

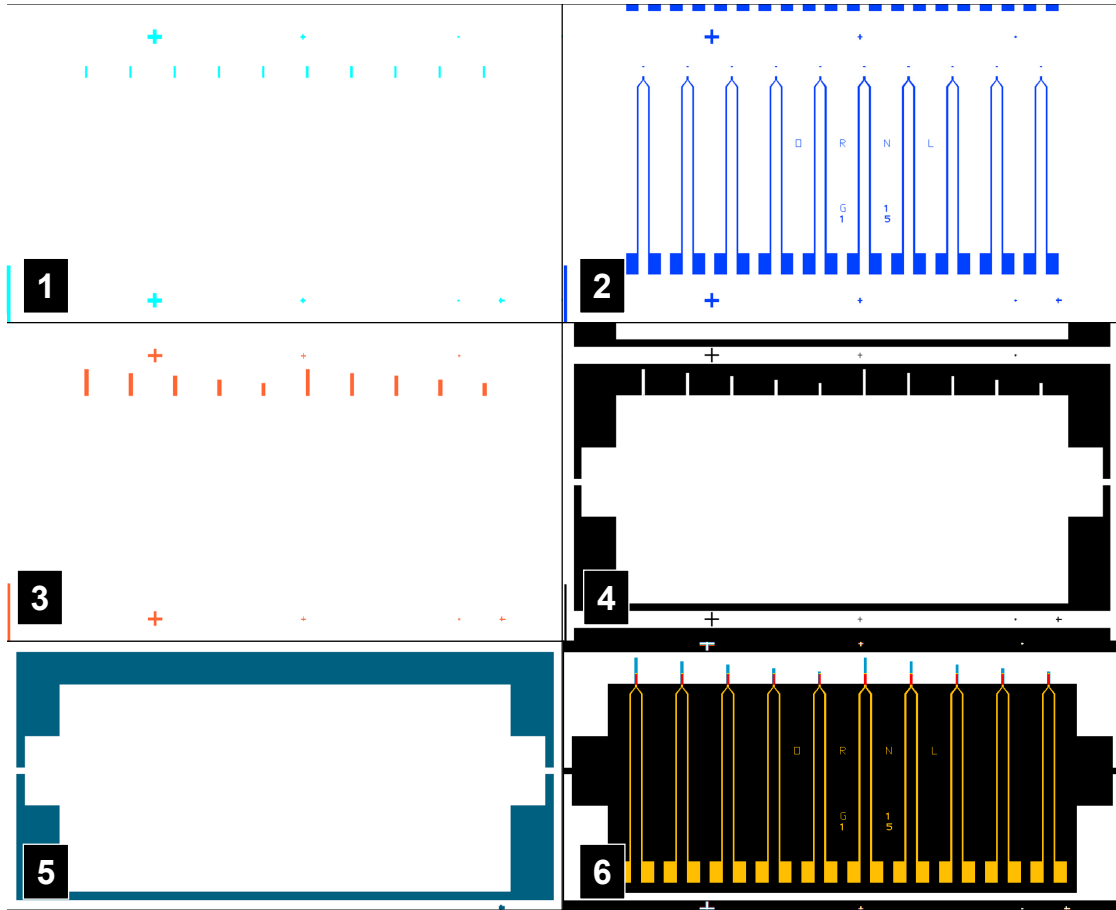


Figure A.1 Masks used in the fabrication process 1-5. The complete device is shown in 6.

Table A. 1 Complete listing of cantilever designs of devices on the mask. Identical colors indicate the same design

Chip No	C 1	C 2	C 3	C 4	C 5	C 6	C 7	C 8	C 9	C 10
1	450/300/100	450/300/100	450/300/100	450/300/100	450/300/100	450/300/100	450/300/100	450/300/100	450/300/100	450/300/100
2	450/300/0	450/300/50	450/300/80	450/300/110	450/300/140	450/300/0	450/300/50	450/300/80	450/300/110	450/300/140
3	450/425/0	450/375/0	450/300/0	450/260/0	450/225/0	450/425/0	450/375/0	450/300/0	450/260/0	450/225/0
4	450/300/0	450/300/30	450/300/60	450/300/90	450/300/120	450/300/0	450/300/30	450/300/60	450/300/90	450/300/120
5	450/300/100	450/300/100	450/300/100	450/300/100	450/300/100	450/300/100	450/300/100	450/300/100	450/300/100	450/300/100
6	750/300/0	650/300/0	550/300/0	450/300/0	350/300/0	750/300/0	650/300/0	550/300/0	450/300/0	350/300/0
7	150/125/0	150/115/0	150/100/0	150/75/0	150/50/0	150/125/0	150/115/0	150/100/0	150/75/0	150/50/0
8	750/725/0	750/650/0	750/550/0	750/460/0	750/375/0	750/725/0	750/650/0	750/550/0	750/460/0	750/375/0
9	625/400/0	575/400/0	525/400/0	475/400/0	425/400/0	625/400/0	575/400/0	525/400/0	475/400/0	425/400/0
10	450/300/0	450/300/50	450/300/80	450/300/110	450/300/140	450/300/0	450/300/50	450/300/80	450/300/110	450/300/140
11	450/425/0	450/375/0	450/300/0	450/260/0	450/225/0	450/425/0	450/375/0	450/300/0	450/260/0	450/225/0
12	450/300/100	450/300/100	450/300/100	450/300/100	450/300/100	450/300/100	450/300/100	450/300/100	450/300/100	450/300/100
13	300/275/0	300/250/0	300/200/0	300/175/0	300/150/0	300/275/0	300/250/0	300/200/0	300/175/0	300/150/0
14	750/725/0	750/650/0	750/550/0	750/460/0	750/375/0	750/725/0	750/650/0	750/550/0	750/460/0	750/375/0
15	750/300/0	650/300/0	550/300/0	450/300/0	350/300/0	750/300/0	650/300/0	550/300/0	450/300/0	350/300/0
16	150/125/0	150/115/0	150/100/0	150/75/0	150/50/0	150/125/0	150/115/0	150/100/0	150/75/0	150/50/0
17	600/550/0	600/500/0	600/400/0	600/350/0	600/300/0	600/550/0	600/500/0	600/400/0	600/350/0	600/300/0
18	450/425/0	450/375/0	450/300/0	450/260/0	450/225/0	450/425/0	450/375/0	450/300/0	450/260/0	450/225/0
19	750/300/0	650/300/0	550/300/0	450/300/0	350/300/0	750/300/0	650/300/0	550/300/0	450/300/0	350/300/0
20	600/550/0	600/500/0	600/400/0	600/350/0	600/300/0	600/550/0	600/500/0	600/400/0	600/350/0	600/300/0
21	450/300/0	450/300/30	450/300/60	450/300/90	450/300/120	450/300/0	450/300/30	450/300/60	450/300/90	450/300/120
22	300/200/0	300/200/25	300/200/50	300/200/75	300/200/90	300/200/0	300/200/25	300/200/50	300/200/75	300/200/90
23	450/300/0	450/300/50	450/300/80	450/300/110	450/300/140	450/300/0	450/300/50	450/300/80	450/300/110	450/300/140
24	300/200/0	300/200/25	300/200/50	300/200/75	300/200/90	300/200/0	300/200/25	300/200/50	300/200/75	300/200/90
25	300/275/0	300/250/0	300/200/0	300/175/0	300/150/0	300/275/0	300/250/0	300/200/0	300/175/0	300/150/0
26	600/550/0	600/500/0	600/400/0	600/350/0	600/300/0	600/550/0	600/500/0	600/400/0	600/350/0	600/300/0
27	450/300/0	450/300/30	450/300/60	450/300/90	450/300/120	450/300/0	450/300/30	450/300/60	450/300/90	450/300/120

Table A. 1 (Continued) Complete listing of cantilever designs of devices on the mask. Identical colors indicate the same design

28	625/400/0	575/400/0	525/400/0	475/400/0	425/400/0	625/400/0	575/400/0	525/400/0	475/400/0	425/400/0
29	750/725/0	750/650/0	750/550/0	750/460/0	750/375/0	750/725/0	750/650/0	750/550/0	750/460/0	750/375/0
30	300/200/0	300/200/25	300/200/50	300/200/75	300/200/90	300/200/0	300/200/25	300/200/50	300/200/75	300/200/90
31	300/275/0	300/250/0	300/200/0	300/175/0	300/150/0	300/275/0	300/250/0	300/200/0	300/175/0	300/150/0
32	625/400/0	575/400/0	525/400/0	475/400/0	425/400/0	625/400/0	575/400/0	525/400/0	475/400/0	425/400/0
33	450/300/100	450/300/100	450/300/100	450/300/100	450/300/100	450/300/100	450/300/100	450/300/100	450/300/100	450/300/100
34	150/125/0	150/115/0	150/100/0	150/75/0	150/50/0	150/125/0	150/115/0	150/100/0	150/75/0	150/50/0

APPENDIX B

FABRICATION DETAILS

B.1 Process Flow

Step No	Description	Machine/Vendor	Process Parameters/ Data	Comments (Date all comments)	Process Time (mins)
1	Doping of wafers	Core Systems Inc	Species: Phosphorus, Dose: 7e14, Energy: 120 keV, Tilt: 7 degrees	Normal lead time of 4-5 days	
2	Annealing of wafers	Lindberg Furnace, Tube 2	Temp 1050C, 48 mins/Ramp1: 20C/min, Dwell time: 0.8 hrs, Ramp2: Sleep	Wafers look pinkish after anneal	240
3	Check resistivity in Four Point Probe	Signatone Probe	Expected resistivity: 3.4 mW-cm		10
4	Piranha clean		Time: 10 mins	Piranha: 7:3 (Peroxide:Sulphuric Acid)	15
5	Deposit backside oxide	Plasmatherm PECVD	Recipe: Aricox, Temp: 300C, Time: 180 mins		180
6	Short BOE for front SOI surface		Time: 10s, 6:1 BOE	Dry after process	0.25
7	Inspection under Nanospec	Nanospec Film Analyser	Use SOI recipe to verify wafer specs	Expect: 400 nm of SiO ₂ & 340 nm of Si	5
8	Dehydration bake	Convection Oven	120C, 5 mins		8

9	Spin resist for resistor patterning	Junior CEE spinner	Resist: Shipley 1827 with HMDS		5
10	Patterning of resistors with SPR220	MA6-Mask Aligner	Resist: SPR 220, Ch2, Time: 20s, Developer 351 (3-5 mins)	Inspect to make sure all the resist is cleanly developed	10
	Mask-G1_M1				
11	Development		Microposit 351 (Water+Developer 1:1)		3
12	Inspection under Nanospec	Nanospec	Ensure SOI recipe works	To ensure complete development	3
13	Descum in RIE for 3 mins	Plasmatherm RIE	Recipe: Rav-des, 3 mins	Inspect to make sure surface is clean. This step is to make sure there are no specks of resist in the open areas	5
14	RIE for patterning of piezoresistors	Plasmatherm RIE	500mTorr, 100W, 4-5 mins, Recipe: Rav_si (silicon piezo etch)	Inspect to see SiO2 showing up.	6
15	Inspection under Nanospec	Nanospec	Inspect to make sure open area is silicon	Measure depth of siO2. Should be approx 400 nm	3
16	Strip resist in acetone/methanol		Strip till it looks clean	Do not do descum after this!!	4

17	Ash wafer	Gastronics Asher	Time: 1 min, standard ashing recipe	Inspect after ashing	3
18	Piranha etch for 15 minutes		15 mins on 80C hotplate	Piranha: 7:3 (Peroxide:Sulphuric Acid)	20
19	Short BOE		Dilution of BOE (110 ml DI + 20 ml 6:1 BOE), Time: 30s	Dry after process	0.25
20	Dehydration bake		Convection oven at 160C for 5 mins		5
21	Sputter of Ti/Au	CVC DC sputterer	Deposition time: Heat(600s, 50% power)/ Delay(300s) /Ti(150s, 7% power)/Au(950s, 7%power)	Put glass slides in to use as reference for etch later	120
22	Spin SPR 220 for patterning contact pads	Junior CEE spinner	HMDS: 3000/500/20, bake at 100C for 60 s, Resist: 4000 rpm /500 rpms/ 40s. Softbake at 115C for 6 mins	SPR 220 with PDMS	10
22	Patterning of contact pads	MA6-Mask Aligner	Ch2, Time: 15s, Developer: 351		15
	Mask: G1 M2				
23	Development		Microposit 351 (Water+Developer 1:1)		3
24	Hardbake	Convection Oven	At 120 C for 15 mins		15
25	Au Etch		KI + Iodine etchant, time: 3 mins	Rinse/dry	4
26	Ti etch		TFTN etch, hotplate at 100C, time: 4-5 mins	Rinse/dry	5
27	Removal using resist	Stripper: 1112A at 85C	Time: 5-7 mins	Rinse well after strip	8

	stripper				
27	Descum for 3-4 minutes	Plasma therm RIE	3 mins at 100W (Rav-des)	Inspect to make sure resist is gone	5
28	Measure contact resistance	Probe Station	Compare with expected values of devices	Critical Step!!!!	30
29	Descum	Plasmatherm RIE	Rav-Pr. High power descum at 250W, 5 mins	Inspect to see if clean. If not do descum at 100W for longer times. Upto 25 mins ok.	30
30	Deposit top nitride (100 nm)	Unaxis PECVD	Recipe: Sin_top, Time: 12.5 mins		15
31	Spin NR5-8000 for cant-metal	Junior CEE spinner	Recipe: 3000/500/40s, Softbake: 150C, 4mins	Hotplate bake	8
32	Lithography for cant-metal	MA-6 Mask aligner	Time: 70s, Ch: 1, Developer: RD6	Critical!! (Post-exposure bake at 100C, 90s)	15
	Mask: G1_M3				
30	Development		Developer RD6, Time: 3 mins	Check to see if the areas for e-beam are clean	4
31	RIE descum	Plasmatherm RIE	Rav-des, 100W, 3-4 mins		5
29	E-beam	CVC E-beam	Pressure < 6e-6 Torr, Ti (100A)/ Au (500A)		45
30	Liftoff		Stripper: RR4	Rinse and dry after process	10

31	Descum	Plasmatherm RIE	Power: 100W, time: 15 mins	Steps of 5 mins	18
32	Sputter deposit Al on front (2500 A)	CVC DC Sputterer	Al deposition		60
33	Spin NR5-8000 on Al	Junior CEE Spinner	Recipe: 3000/500/40s, Softbake: 150C, 4mins	Hotplate bake	8
34	Pattern Al with Chipmask	MA6 Mask aligner	Time: 70s, Ch: 1, Developer: RD6	Critical!! (Post-exposure bake at 100C, 90s)	15
	Mask: G1_M5				
35	Development		Developer RD6, Time: 3 mins		3
35	Descum	Plasmatherm RIE	Time: 5mins		7
36	Hardbake	Convection oven	Temp: 120C, time: 15 mins	Make sure reflow is good	15
37	Al Etch		Al Etchant at 80C, Time: 2-3 mins	Rinse/dry	5
38	Remove resist		RR4 stripper		10
39	RIE of mask	Plasmatherm RIE	Descum at high power (250W for 5 mins)		7
40	Etch SiO2 in RIE	Plasmatherm RIE	Recipe: PM_sin (power: 250W), Time: 12 mins	Keep checking depth in Nanospec	15
41	Make sure surface is clean	Microscope	Else descum more		

42	Deposit 1.4 microns of nitride	Unaxis PECVD	Recipe: Sin_memb, Time: 200 mins	Keep dummy wafer for final etch reference	200
43	Pattern SPR220 for backside definition		2500/200/40, softbake: 115C, 6 mins/ Ch2, Time: 25 secs		20
	Mask: G1_M4				
44	Development		Microposit 351 (Water+Developer 1:1)		4
45	Hardbake	Convection oven	120C, 20 mins		20
46	Wet etch of oxide		10:1 BOE + HF (49%) {4:1}	Done with single sided holder	5
47	Strip backside resist		Stripper 1112A	Rinse and dry	10
48	ICP etch of backside	Plasmatherm ICP	ICP etch through wafer till oxide shows	Mount on second wafer with cool grease	420
49	Remove from mounting wafer		Acetone/Isoprop		20
50	Deposit backside nitride	Unaxis PECVD	Recipe: Sin_bot, Time: 25 mins		30
51	Sputter Al on backside	CVC DC sputterer	Al target (3000A)		45
52	RIE for final definition and release	Plasmatherm RIE	Nitride etch, Recipe: Sin_arn (150W), Time: 20 mins		25

53	Etch Al in wet etch		Al Etch on hotplate at 80C		5
54	Rinse in water and then methanol		Wait for methanol to dry		5

B.2 Important Photoresist Recipes

NR5 (Futurrex NR5-8000)

RPM/Ramp rate/Time: 3000 rpm/500 rpms/ 40s

Softbake Temperature/Time: 150°C/4 mins [Hot Plate]

Exposure (High Vacuum contact mode): (365 nm) Dose 195 mJ/cm²

Post Exposure Bake (temperature/time): 100C/90s [Hot Plate]

Development: Futurrex RD6 Developer- 60s

HMDS

RPM/Ramp rate/Time: 2000 rpm/500 rpms/ 20s

AZ4620 (Clariant AZ 4620)

RPM/Ramp rate/Time: 800 rpm/ 500 rpms/ 40s/3000 rpm/ 10000 rpms/ 3s

Softbake Temperature/Time: 95C/ 15 mins [Oven Bake]

Exposure (High Vacuum contact mode): (405 nm) Dose 1200 mJ/cm²

Development: AZ400K (2.5 water:1 developer) – around 2 minutes

Sh1813 (Shipley 1813)

RPM/Ramp rate/Time: 3000 rpm/ 500 rpms/ 30s

Softbake Temperature/Time: 95C/ 5 mins

Exposure: (405 nm) Dose 180 mJ/cm²

Development: Microposit 354 Developer, Time: 2 mins

Sh1827 (Shipley 1827)

RPM/Ramp rate/Time: 3000 rpm/ 500 rpms/ 30s

Softbake Temperature/Time: 100C/ 2 mins (hotplate)

Exposure: (405 nm) Dose 200 mJ/cm²

Development: Microposit 354 Developer, Time: Around 2-3 mins

SPR 220

RPM/Ramp rate/Time: 4000 rpm/ 500 rpms/ 30s

Softbake Temperature/Time: 115C/ 6 mins (hotplate)

Exposure: (405 nm) Dose 250 mJ/cm²

Development: Microposit 351 Developer, Time: Around 3-4 mins

APPENDIX C

THERMAL MODELS

C.1 Closed-Form Transient Solution for Microcantilever Heating

The simple PDE describing the cantilever of length L with the doped silicon piezoresistor is,

$$\frac{\partial \theta}{\partial t} = a \frac{\partial^2 \theta}{\partial x^2} + b\theta + c\dot{Q} \quad (1)$$

where,

$$a = \frac{\sum_{Layer1}^{LayerN} k_i v_i}{\sum_{Layer1}^{LayerN} \rho_i c_{p,i} v_i}, \quad b = -\frac{2h_{eff} w}{A_c \sum_{Layer1}^{LayerN} \rho_i c_{p,i} v_i} \quad \text{and} \quad c = \frac{2}{A_c A_p \sum_{Layer1}^{LayerN} \rho_i c_{p,i} v_i} \quad (2)$$

Also, the ohmic heating term, $\dot{Q} = I_c^2 s(\theta)$

$$I_c = \frac{V_c}{R_c(\theta)} = \frac{V_{in}}{R_c(\theta) + R_{ballast}} \quad (3)$$

Here $\theta(x, t) = T(x, t) - T_{amb}$. The boundary conditions associated with this model are:

$$\theta(0, t) = 0, \quad \theta(x, t) = 0 \quad \text{and} \quad \frac{\partial \theta(l, t)}{\partial x} = 0 \quad (4)$$

The solution to (1) based on the mixed boundary conditions described is given by [1] is presented in this section. This formulation cannot account for the heated and non-heated sections of the piezoresistive cantilever, though that can easily be implemented. The main limitations of this solution, when compared with the finite difference model that has been used in this work, are that the heat transfer coefficient in this solution has to be a constant and in the term for resistive heating (3), the time dependent value of value of the piezoresistor cannot be used. This implies that that if the cantilever temperature changes form its nominal value, this is not reflected in this solution. This may be acceptable in cases where resistance change is small but was not thought to be

appropriate for this particular work. Hence results presented in this work used a finite difference model described in Chapter 6.

$$\begin{aligned} \theta(x,t) = & \int_0^L f(\xi)G(x,\xi,t)d\xi + \int_0^t \int_0^L \Phi(\xi,\tau)G(x,\xi,t-\tau)d\xi d\tau + a \int_0^t g_1(\tau)\Lambda(x,t-\tau)d\tau \\ & + a \int_0^t g_2(\tau)\Lambda(x,t-\tau)d\tau \end{aligned} \quad (5)$$

where,

$$G(x,\xi,t) = \frac{2}{L} e^{bt} \sum_n^{\infty} \sin\left[\frac{\pi(2n+1)x}{2L}\right] \sin\left[\frac{\pi(2n+1)\xi}{2L}\right] \exp\left[-\frac{a\pi^2(2n+1)^2 t}{4L^2}\right] \quad (6)$$

$$\Lambda(x,t) = \frac{\partial}{\partial \xi} G(x,\xi,t) \Big|_{\xi=0} \quad (7)$$

C.1.1 Sinusoidal input

Let us assume a sinusoidal input of V_{in} is applied across the cantilever resistor.

We can write,

$$V_{in} = V_{DC} + \sum_{i=0}^{N_{\text{sin}}} V_i \sin(\omega_i t) \quad (8)$$

Heat generation in the system is

$$\Phi = c\dot{Q} \quad (9)$$

For the cantilever system, $g_1(t) = g_2(t) = f(x) = 0$ (from the boundary conditions).

Hence the solution (5) simplifies to

$$\theta(x,t) = \int_0^t \int_0^L \Phi(\xi,\tau)G(x,\xi,t-\tau)d\xi d\tau = \sum_{n=0}^{\infty} S_{n,x,t} \quad (10)$$

where

$$S_{n,x,t} = \int_0^t \int_0^L \left\{ \left(\frac{cV_{in}^2(\tau)}{R_o} \right) \frac{2}{L} e^{b(t-\tau)} \sin\left[\frac{\pi(2n+1)x}{2L}\right] \sin\left[\frac{\pi(2n+1)\xi}{2L}\right] \exp\left[-\frac{a\pi^2(2n+1)^2(t-\tau)}{4L^2}\right] d\xi d\tau \right\} \quad (11)$$

Now let

$$\beta = b - \frac{a\pi^2(2n+1)^2}{4L^2} \text{ and } T_{n,t} = \frac{S_{n,x,t}}{\sin\left[\frac{\pi(2n+1)x}{2L}\right]} \quad (12)$$

Then,

$$T_{n,t} = \frac{2}{L} e^{\beta t} \int_0^t \int_0^L \left(\frac{cV_{in}^2(\tau)}{R_o} \right) \sin\left[\frac{\pi(2n+1)\xi}{2L}\right] \exp(-\beta\tau) d\xi d\tau \quad (13)$$

$$\Rightarrow T_{n,t} = \frac{2}{L} e^{\beta t} \int_0^t \left(\frac{cV_{in}^2(\tau)}{R_o} \right) \exp(-\beta\tau) d\tau \left(-\cos\left[\frac{\pi(2n+1)\xi}{2L}\right] \Big|_0^L \right) \left(\frac{2L}{\pi(2n+1)} \right) \quad (14)$$

$$\Rightarrow T_{n,t} = \frac{2}{L} e^{\beta t} \int_0^t \left(\frac{cV_{in}^2(\tau)}{R_o} \right) \exp(-\beta\tau) d\tau \left(-\cos\left[\frac{\pi(2n+1)}{2}\right] - (-1) \right) \left(\frac{2L}{\pi(2n+1)} \right) \quad (15)$$

$$\Rightarrow T_{n,t} = \frac{2}{L} e^{\beta t} \int_0^t \left(\frac{cV_{in}^2(\tau)}{R_o} \right) \exp(-\beta\tau) \left(\frac{2L}{\pi(2n+1)} \right) d\tau \quad (16)$$

Now,

$$V_{in}^2 = V_{DC}^2 + \sum_{i,j=0,i \neq j}^{N_{\text{sine}}} V_i V_j \sin(\omega_i \tau) \sin(\omega_j \tau) + \sum_{j=0}^{N_{\text{sine}}} V_j^2 \sin^2(\omega_j \tau) + 2 \sum_{j=0}^{N_{\text{sine}}} V_{DC} V_j \sin(\omega_j \tau) \quad (17)$$

Rewriting the terms, we get

$$\begin{aligned} V_{in}^2 = & \underbrace{\left(V_{DC}^2 + \frac{1}{2} \sum_{j=0}^{N_{\text{sine}}} V_j^2 \right)}_I + \underbrace{\sum_{i,j=0,i \neq j}^{N_{\text{sine}}} \frac{V_i V_j}{2} (\cos((\omega_i - \omega_j)\tau) - \cos((\omega_i + \omega_j)\tau))}_{II} \\ & - \underbrace{\frac{1}{2} \sum_{j=0}^{N_{\text{sine}}} V_j^2 \cos(2\omega_j \tau)}_{III} + \underbrace{2 \sum_{j=0}^{N_{\text{sine}}} V_{DC} V_j \sin(\omega_j \tau)}_{IV} \end{aligned} \quad (18)$$

Now integrating each of the summands separately,

$$(T_{n,t})_I = \frac{2}{R_o L} e^{\beta t} \int_0^t \left(c \left(V_{DC}^2 + \frac{1}{2} \sum_{j=0}^{N_{\text{sine}}} V_j^2 \right) \right) \exp(-\beta\tau) \left(\frac{2L}{\pi(2n+1)} \right) d\tau \quad (19)$$

$$\Rightarrow (T_{n,t})_I = \frac{2}{R_o L} e^{\beta t} \left(c \left(V_{DC}^2 + \frac{1}{2} \sum_{j=0}^{N_{\text{sine}}} V_j^2 \right) \right) \left(\frac{2L}{\pi(2n+1)} \right) \left(\frac{\exp(-\beta\tau)}{-\beta} \Big|_0^t \right) \quad (20)$$

$$\Rightarrow (T_{n,t})_I = \frac{2}{R_o L} \left(c \left(V_{DC}^2 + \frac{1}{2} \sum_{j=0}^{N_{\text{sine}}} V_j^2 \right) \right) \left(\frac{2L}{\pi(2n+1)} \right) \left(\frac{e^{\beta t} - 1}{\beta} \right) \quad (21)$$

Similarly,

$$(T_{n,t})_{II} = \frac{2}{R_0 L} e^{\beta t} \int_0^t \left\{ \left(c \sum_{i,j=0, i \neq j}^{N_{\text{ sine}}} \frac{V_i V_j}{2} (\cos((\omega_i - \omega_j)\tau) - \cos((\omega_i + \omega_j)\tau)) \right) \left(\frac{2L}{\pi(2n+1)} \right) \exp(-\beta\tau) d\tau \right\} \quad (22)$$

$$\Rightarrow (T_{n,t})_{II} = \frac{2}{R_0 L} \left(\frac{2L}{\pi(2n+1)} \right) e^{\beta t} \times \left(c \sum_{i,j=0, i \neq j}^{N_{\text{ sine}}} \frac{V_i V_j}{2} \left(\frac{((\omega_i - \omega_j) \sin((\omega_i - \omega_j)\tau) - \beta \cos((\omega_i - \omega_j)\tau)) (e^{-\beta\tau}) \Big|_0^t}{\beta^2 + (\omega_i - \omega_j)^2} \right) \right) \quad (23)$$

$$- \frac{2}{R_0 L} \left(\frac{2L}{\pi(2n+1)} \right) e^{\beta t} \times$$

$$\left(c \sum_{i,j=0, i \neq j}^{N_{\text{ sine}}} \frac{V_i V_j}{2} \left(\frac{((\omega_i + \omega_j) \sin((\omega_i + \omega_j)\tau) - \beta \cos((\omega_i + \omega_j)\tau)) (e^{-\beta\tau}) \Big|_0^t}{\beta^2 + (\omega_i + \omega_j)^2} \right) \right)$$

$$\Rightarrow (T_{n,t})_{II} = \frac{2}{R_0 L} \left(\frac{2L}{\pi(2n+1)} \right) \times$$

$$\left(c \sum_{i,j=0, i \neq j}^{N_{\text{ sine}}} \frac{V_i V_j}{2} \left(\frac{((\omega_i - \omega_j) \sin((\omega_i - \omega_j)t) - \beta \cos((\omega_i - \omega_j)t) + \beta e^{\beta t})}{\beta^2 + (\omega_i - \omega_j)^2} \right) \right) \quad (24)$$

$$- \frac{2}{R_0 L} \left(\frac{2L}{\pi(2n+1)} \right) \times$$

$$\left(c \sum_{i,j=0, i \neq j}^{N_{\text{ sine}}} \frac{V_i V_j}{2} \left(\frac{((\omega_i + \omega_j) \sin((\omega_i + \omega_j)t) - \beta \cos((\omega_i + \omega_j)t) + \beta e^{\beta t})}{\beta^2 + (\omega_i + \omega_j)^2} \right) \right)$$

And,

$$(T_{n,t})_{III} = -\frac{2}{R_0 L} \left(\frac{2L}{\pi(2n+1)} \right) e^{\beta t} \int_0^t \left(c \sum_{j=0}^{N_{\text{ sine}}} \frac{V_j^2}{2} \cos(2\omega_j \tau) \right) \exp(-\beta\tau) d\tau \quad (25)$$

$$\Rightarrow (T_{n,t})_{III} = -\frac{2}{R_0 L} \left(\frac{2L}{\pi(2n+1)} \right) e^{\beta t} \times \left(c \sum_{j=0}^{N_{\text{sine}}} \frac{V_j^2}{2} \left(\frac{(2\omega_j \sin(2\omega_j \tau) - \beta \cos(2\omega_j \tau)) (\exp(-\beta \tau)) \Big|_0^t}{\beta^2 + 4\omega_j^2} \right) \right) \quad (26)$$

$$\Rightarrow (T_{n,t})_{III} = -\frac{2}{R_0 L} \left(\frac{2L}{\pi(2n+1)} \right) \times \left(c \sum_{j=0}^{N_{\text{sine}}} \frac{V_j^2}{2} \left(\frac{(2\omega_j \sin(2\omega_j t) - \beta \cos(2\omega_j t) + \beta e^{\beta t})}{\beta^2 + 4\omega_j^2} \right) \right) \quad (27)$$

Finally,

$$(T_{n,t})_{IV} = \frac{2}{R_0 L} \left(\frac{2L}{\pi(2n+1)} \right) e^{\beta t} \int_0^t \left(c \sum_{j=0}^{N_{\text{sine}}} 2V_{DC} V_j \sin(\omega_j \tau) \right) \exp(-\beta \tau) d\tau \quad (28)$$

$$\Rightarrow (T_{n,t})_{IV} = \frac{4V_{DC}}{R_0 L} \left(\frac{2L}{\pi(2n+1)} \right) \left(c \sum_{j=0}^{N_{\text{sine}}} V_j \left(\frac{-\beta \sin(\omega_j t) - \omega_j \cos(\omega_j t) + \omega_j e^{\beta t}}{\beta^2 + \omega_j^2} \right) \right) \quad (29)$$

$$T_{n,t} = (T_{n,t})_I + (T_{n,t})_{II} + (T_{n,t})_{III} + (T_{n,t})_{IV} \quad (30)$$

$$S_{n,x,t} = T_{n,t} \sin \left[\frac{\pi(2n+1)x}{2L} \right] \quad (31)$$

$$\bar{\theta}(t) = \frac{\int_0^L \sum_{n=0}^{\infty} S_{n,x,t} dx}{\int_0^L dx} = \frac{\int_0^L \sum_{n=0}^{\infty} S_{n,x,t} dx}{L} = \frac{\int_0^L \sum_{n=0}^{\infty} T_{n,t} \sin \left[\frac{\pi(2n+1)x}{2L} \right] dx}{L} \quad (32)$$

$$= \frac{\sum_{n=0}^{\infty} T_{n,t} \left(\frac{2L}{\pi(2n+1)} \right)}{L}$$

C.2 References

- [1] A. D. Polyanin and V. F. Zaitsev, Handbook of Linear Partial Differential Equations for Engineers and Scientists. Boca Raton: Chapman & Hall/CRC Press, 2002.

APPENDIX D

ELECTRICAL CIRCUIT LAYOUT

D.1 Electrical Circuit Layout of Measurement Box

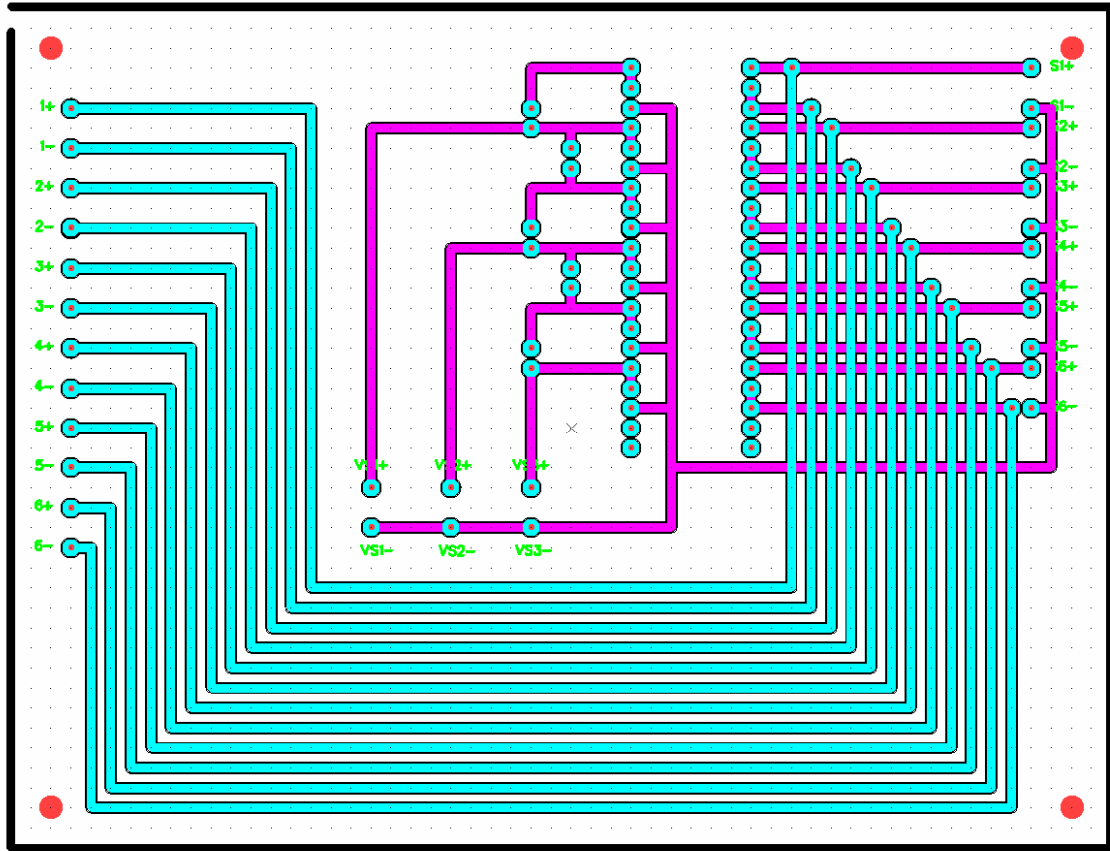


Figure D. 1 Circuit layout for measurement box in § 7.1.2